UNIVERSITÀ DEGLI STUDI DI PALERMO

Dottorato di Ricerca in Ingegneria Civile, Ambientale, dei Materiali

Ingegneria delle Strutture

Dipartimento di Ingegneria

Settore Scientifico Disciplinare ICAR/09

Experimental investigation on the effectiveness of basalt-fibre strengthening systems for confining masonry elements

IL DOTTORE

Ing. Jennifer D'Anna

IL COORDINATORE

Prof. Antonina Pirrotta

TUTORS

Prof. Lidia La Mendola

Dr. Giovanni Minafò, Ph.D

EXTERNAL ADVISORS

Prof. Jian Fei Chen

Dr. Giuseppina Amato, Ph.D

CICLO XXXI

ANNO CONSEGUIMENTO TITOLO 2019

ACKNOWLEDGEMENTS

This thesis is the result of an important path of training and professional growth that lasted three years, during which I was lucky enough to be supported by many people whom I feel like I need to thank.

I greatly appreciate my supervisor Prof. Lidia La Mendola, who gave me the opportunity to undertake this path, believing in me and my potential from the beginning. I am extremely grateful for her teachings and for being a guide and a stable reference point both professionally and ethically, showing the ability to handle every situation with great consistency.

I feel like thanking my supervisor Dr. Giovanni Minafò for the support I received during my research studies. I thank him for having offered me the possibility to clarify doubts and uncertainties. I am also grateful to him for creating the conditions for me to be able to go to the Queen's University of Belfast (UK), where I had an important period of study.

I thank my co-tutor, Dr. Giuseppina Amato, for giving me the opportunity to spend a year at Queen's University of Belfast. Her financial support was essential for the realization of the experimental campaign whose outcomes are one of the most significant parts of this thesis.

I am very grateful to Prof. Jian Fei Chen, my co-tutor, for his great availability and for the advice received during my period of study at Queen's University. I have deep consideration of him, both professionally and humanely.

I would like also to thank the technicians of the Heavy Structure Lab of Queen’s University of Belfast, for their help.

My heartfelt thanks to Prof. Giuseppe Trombino, for the indispensable and unconditional support he gave me during these three years. I am sincerely grateful for his advice and encouragements, and I deeply appreciate his ability to impart the enthusiasm to keep going forward anyway.

I enjoyed the time spent in the company of my colleagues Alessia, Marco, Francesco, Fabio, Gabriele, Vincenzo, Alberto and Salvo, with whom I shared memorable moments.

My special thanks to colleagues and friends I met during the study period in Belfast, who made me feel at home from the first moment. In particular I wish to thank: Annalisa and Panagiotis, for their great support, the advice and the love they have given me and they give me even now; Tatiana, for her kindness and great-heartedness; Raj, for his availability and suggestions; Esmaeel, for his valuable advice during my experimental studies and for the support he gave me; Dimitris, for the good moments we spent together and the laughs.

Finally, I will never thank enough my family, for their unconditional love and for their constant support, which proved to be essential elements for achieving this much desired goal. I dedicate this thesis to them.

RINGRAZIAMENTI

La presente tesi costituisce il risultato di un importante percorso di formazione e crescita professionale durato tre anni, nel corso dei quali ho avuto la fortuna di essere affiancata da molte persone che sento il dovere di ringraziare.

Un profondo ringraziamento va alla mia relatrice, la Prof. Lidia La Mendola, per avermi dato la possibilità di intraprendere questo percorso, credendo in me e nelle mie potenzialità fin dall'inizio. Le sono estremamente grata per i suoi insegnamenti e per essere stata una guida ed un punto di riferimento costante sia professionalmente che moralmente, mostrando la capacità di gestire ogni situazione con grande coerenza.

Sento il dovere di ringraziare il mio relatore Dott. Giovanni Minafò per il supporto datomi nel corso dei miei studi. Lo ringrazio per avermi offerto la possibilità di un confronto diretto per il chiarimento di dubbi e incertezze. Gli sono anche grata per aver creato le condizioni affinché potessi recarmi presso la Queen's University di Belfast, dove ho svolto un importante periodo di studio.

Ringrazio la mia co-tutor, Dott. Giuseppina Amato, per avermi concesso l'opportunità di trascorrere un anno presso la Queen's University di Belfast. Il suo sostegno economico è stato indispensabile per la realizzazione della campagna sperimentale i cui esiti costituiscono una delle parti più significative della presente tesi.

Sono molto grata al Prof. Jian Fei Chen, mio co-tutor, per la sua grande disponibilità e per i consigli ricevuti nel corso del mio periodo di studi alla Queen's University. Nutro profonda stima nei suoi confronti, sia professionalmente che umanamente.

Rivolgo un ringraziamento ai tecnici del Laboratorio di Strutture della Queen's University, per l'aiuto ricevuto.

Un sentito ringraziamento va al Prof. Giuseppe Trombino, per l'indispensabile ed incondizionato supporto datomi nel corso di questi tre anni. Gli sono sinceramente grata per i consigli e gli incoraggiamenti e lo stimo

profondamente per sua capacità di trasmettere ai più giovani l'entusiasmo di andare avanti sempre e comunque.

Ho apprezzato il tempo trascorso in compagnia dei miei colleghi Alessia, Marco, Francesco, Fabio, Gabriele, Vincenzo, Alberto e Salvo, con cui ho condiviso momenti memorabili.

Un ringraziamento speciale va ai colleghi e amici conosciuti durante il periodo di studi a Belfast, i quali mi hanno fatto sentire a casa fin dal primo momento. In particolare tengo a ringraziare: Annalisa e Panagiotis per il loro grande supporto, i consigli e l'amore che mi hanno trasmesso e continuano a trasmettermi tutt'oggi; Tatiana per la sua gentilezza e grandezza d'animo; Raj per la sua disponibilità ed i suggerimenti ricevuti; Esmaeel, per i suoi preziosi consigli durante i miei studi sperimentali e per il supporto datomi; Dimitris per i bei momenti trascorsi assieme e per le risate.

Infine, non ringrazierò mai abbastanza la mia famiglia, per l'amore incondizionato e per il sostegno costante, che si sono rivelati elementi indispensabili per il raggiungimento di questo obiettivo tanto desiderato. Questa tesi è dedicata a loro.

SUMMARY

The use of composite materials for the confinement of masonry columns having weak mechanical characteristics has become a widespread practice during the last decades. This technique, usually realized through the application of Fibre Reinforced Polymer (FRP) externally bonded jackets, has shown good capabilities, being able to significantly improve the load carrying capacity and the ductility of masonry members, thanks to a passive confinement action. However, FRP composites, when applied on masonry substrates, have shown some shortcomings due to the organic nature of the matrix. For this reason, during the last years growing attention has been paid to Fibre Reinforced Cementitious Matrix (FRCM) composites, in which the polymeric matrix is replaced by an inorganic matrix. Moreover, due to the increasing demand for new materials produced with low energy consumption that offer sustainability and good mechanical properties, composites reinforced with basalt fibres have lately attracted interest as material for strengthening masonry structures.

The target of the present thesis is the evaluation of the effectiveness, in terms of strength and deformation capacity, of the confinement action provided by both basalt FRP and FRCM jackets, when the latter are applied on masonry members. In this framework, a detailed experimental investigation is performed by testing FRP and FRCM-confined clay brick masonry cylinders in compression.

A preliminary investigation is carried out on the mechanical properties of constituent materials of masonry, namely bricks and mortar. Moreover, the strengthening systems are deeply analyzed through tests on the mortar matrix of the FRCM and an extensive study on the tensile behaviour of the basalt textile grid used as reinforcement. The mechanical behaviour of the FRCM composite is characterized under tension and the results are discussed in terms of stress-strain curves, evolution of cracks and failure modes. Then, the cylinders reinforced with FRP/FRCM jackets are subjected to uniaxial compressive loads, showing the influence of the key parameters involved in the problem, such as the number of vertical mortar joints in the masonry and the number of wrapping layers. The results in terms of compressive strength increases and corresponding strains

allow drawing some conclusions on the effectiveness of the investigated strengthening systems.

The whole experimental study is carried out employing the Digital Image Correlation (DIC), which is the only monitoring system in some cases and serves as support to traditional systems in other tests, giving information about the displacement fields and the development of cracks during the performed tests.

Finally, analytical formulations useful for the prediction of the compressive behaviour of FRP/FRCM-confined masonry are proposed and compared to the experimental results, allowing some conclusions to be drawn on their reliability for practical design/verification purposes.

SOMMARIO

L'impiego di materiali compositi per il rinforzo di colonne in muratura è diventato una pratica ampiamente diffusa nel corso degli ultimi decenni. Questa tecnica, che consiste generalmente nell'applicazione di materiali polimerici fibrorinforzati (Fibre Reinforced Polymer-FRP), ha mostrato buone potenzialità, essendo in grado di garantire notevoli incrementi di resistenza e duttilità dell'elemento rinforzato, grazie ad un'azione di confinamento passivo. Tuttavia, l'impiego di compositi a matrice polimerica presenta alcuni limiti legati soprattutto alle prestazioni delle resine epossidiche, che a causa della loro natura sintetica danno luogo a problemi di compatibilità con il supporto murario. Per questo motivo, recenti lavori di ricerca hanno avuto l'obiettivo di sviluppare dei materiali di rinforzo non affetti dai problemi connessi all'adozione delle resine epossidiche, portando allo sviluppo dei compositi FRCM (Fibre Reinforced Cementitious Matrix), in cui la matrice polimerica viene sostituita da una matrice di natura inorganica, come una malta cementizia. Inoltre, la crescente domanda di nuovi materiali prodotti con un dispendio minimo di energia in grado di garantire adeguati livelli di sostenibilità, senza però rinunciare a buone prestazioni meccaniche, ha posto l'attenzione sui materiali compositi facenti uso di fibre di basalto per il rinforzo di strutture in muratura.

L'obiettivo della presente tesi è quello di valutare l'efficacia, in termini incrementi di resistenza e duttilità, dell'azione di confinamento fornita da avvolgimenti in FRP o FRCM con fibre di basalto, quando questi sono applicati per il rinforzo di elementi in muratura. Lo studio viene condotto prevalentemente da un punto di vista sperimentale, attraverso la progettazione e realizzazione di una campagna di prove di compressione su cilindri in muratura di mattoni fasciati con FRP o FRCM.

Preliminarmente si presentano i dettagli ed i risultati di un'ampia fase di caratterizzazione dei materiali, finalizzata ad indagare le proprietà meccaniche della malta e dei mattoni che costituiscono la muratura, a caratterizzare la malta impiegata nel rinforzo FRCM e a definire il comportamento in trazione della fibra di basalto impiegata nei sistemi di rinforzo studiati. In una fase successiva si

analizza il comportamento meccanico del rinforzo in FRCM attraverso prove di trazione su strisce di composito, discutendo i risultati in termini di curve tensione-deformazione ed analizzando l'evoluzione del quadro fessurativo e le modalità di rottura. Viene quindi studiato sperimentalmente il comportamento in compressione dei cilindri in muratura confinati con FRP o FRCM, mostrando l'influenza delle principali variabili coinvolte nel problema, come il numero di giunti verticali di malta nella muratura o la percentuale di tessuto presente nel composito. I risultati ottenuti in termini di incrementi di resistenza a compressione e deformazione ultima permettono di formulare alcune considerazioni sull'efficacia dei sistemi di rinforzo studiati.

Tutte le prove condotte sono supportate dalla tecnica della Digital Image Correlation (DIC), che viene impiegata come sistema di misura, integrato talvolta a dispositivi tradizionali, in grado di fornire informazioni sui campi di spostamento e sulla formazione e propagazione delle fessure durante le prove condotte.

Infine, sono proposte alcune formulazioni analitiche per la previsione del comportamento in compressione dei cilindri in muratura rinforzarti con FRP o FRCM. Le espressioni adottate si basano su alcune proposte esistenti in letteratura e vengono confrontate con i risultati sperimentali ottenuti, al fine di trarre alcune conclusioni sulla loro applicabilità nelle pratiche applicazioni.

CONTENTS

INDEX OF SYMBOLS

Uppercase English Letters

A_f	Cross sectional area of bare textile
A_{FRCM}	Full area of FRCM cross-section
A_m	Gross area of the general cross-section of the column
C_{CC}	Cross-Correlation criterion in DIC analysis
C_{SSD}	Sum-Squared Difference criterion in DIC analysis
D	Diameter or diagonal of the confined column with circular or square/rectangular cross-section respectively
E_0	Initial modulus of FRP-confined masonry column
E_I	Tangent modulus relative to the first stage of FRCM constitutive law
E_{II}	Tangent modulus relative to the second stage of FRCM constitutive law
E_{III}	Tangent modulus relative to the third stage of FRCM constitutive law
E_c	Modulus of elasticity of the composite material
E_f	Modulus of elasticity of the fibre
E_h	Hardening modulus of FRP-confined masonry column
E_m	Modulus of elasticity of the matrix of composite material
E_{m0}	Modulus of elasticity of unconfined masonry column
E_{mcs}	Secant modulus of confined column
F_I	Peak load at the end of Stage I in FRCM characteristic curve

F_{II}	Peak load at the end of Stage II in FRCM characteristic curve
F_{III}	Peak load at the end of Stage III in FRCM characteristic curve
L	Distance between subsequent cracks in the FRCM coupon
M	Number of whole pixels from the center to edge of the subset in DIC correlation
P	Displacement along the longitudinal direction of the FRCM coupon
$P(x_0, y_0)$	Subset centre in the reference subset in DIC analysis
$P'(x_0', y_0')$	Subset centre in the deformed subset in DIC analysis
$Q(x_i, y_j)$	General point in the reference subset in DIC analysis
$Q'(x_i', y_j')$	General point in the deformed subset in DIC analysis
R	Shape parameter in the analytical model of Campione and Miraglia (2003)
U	Parameter which rules the slope of the softening branch in the analytical model of La Mendola and Papia (2002)
V_m	Volume fraction of matrix in composite material
V_f	Volume fraction of fibre in composite material

Lowercase English Letters

b	Length of the square/rectangular cross-section of the column
b'	Straight length of the square/rectangular cross-section with rounded corner
d	Height of the square/rectangular cross-section of the column
d'	Straight height of the square/rectangular cross-section with rounded corner

dP	Crack opening in the FRCM coupon
$f_{c,mat}$	Compressive strength of the mortar of FRCM system
f_{fu}	Tensile strength of the fibre
f_l	Lateral confinement pressure
f'_l	Effective lateral confinement pressure
$f_{l,b}$	Confining stress along the cross-section length of square/rectangular column
$f_{l,d}$	Confining stress along the cross-section height of square/rectangular column
f_{m0}	Compressive strength of unconfined masonry column or cylinder
f_{mc}	Compressive strength of confined masonry column or cylinder
$f_{mc,exp}$	Experimental value of compressive strength of confined masonry cylinder
$f_{mc,th}$	Theoretical prediction of compressive strength of confined masonry cylinder
f_r	Effective stress in the composite at failure
$f(x_i, y_j)$	Grey level value at the pixel (x_i, y_j) in the undeformed subset
g_m	Mass density of masonry
$g(x_i', y_j')$	Grey level value at the pixel (x_i', y_j') in the deformed subset
k_1	Experimental coefficient in formulations for the evaluation of the strength of confined masonry column
k_2	Coefficient in Krevaikas and Triantafillou (2005) model for the evaluation of the strain at peak stress
k_e	Horizontal effectiveness coefficient for the evaluation of the effective confinement pressure

k_g	Reduction coefficient for the evaluation of the effective stress in the wrap in the formulation of Corradi et al. (2007)
k_i	Experimental coefficient for the evaluation of the effective stress in the wrap in the formulation of Campione and Miraglia (2003)
k_{mat}	Matrix effectiveness coefficient in Balsamo et al. (2018)
n	Number of reinforcing layers of the composite material
r_c	Corner radius of the square/rectangular cross-section of column
t_f	Equivalent thickness of the fibre
t_{mat}	Thickness of the mortar of FRCM system
u	x-directional displacement component of the reference subset in DIC analysis
v	y-directional displacement component of the reference subset in DIC analysis
y	Longitudinal direction of the FRCM coupon
(x_0, y_0)	Coordinates of the subset centre before deformation in DIC analysis
(x_0', y_0')	Coordinates of the subset centre after deformation in DIC analysis
(x_i, y_j)	Coordinates of a subset point before deformation in DIC analysis
(x_i', y_j')	Coordinates of a subset point after deformation in DIC analysis

Uppercase Greek Letters

Δx	x-directional component of the distance from the center of the subset to the point (x_i, y_j) in DIC analysis

Δy	y-directional component of the distance from the center of the subset to the point (x_i, y_j) in DIC analysis

Lowercase Greek Letters

α_1	Exponent in the formulation for the evaluation of the strength of confined masonry, in CNR-DT 200/2013 and Balsamo et al. (2018)
α_2 and α_3	Coefficients in the formula of CNR-DT 200/2013 and Balsamo et al. (2018) for the evaluation of k_1
α_4	Coefficient in the formula of Balsamo et al. (2018) for the evaluation k_{mat}
β	Strain-hardening ratio in the model of Campione and Miraglia (2003)
γ_f	Partial safety factor of FRP according to CNR-DT 200/2013
$\partial u/\partial x$, $\partial u/\partial y$	First-order displacement gradients of the reference subset in DIC analysis
$\partial v/\partial x$, $\partial v/\partial y$	First-order displacement gradients of the reference subset in DIC analysis
ε_I	Strain at peak stress at the end of Stage I in FRCM characteristic curve
ε_{II}	Strain at peak stress at the end of Stage II in FRCM characteristic curve
ε_{III}	Strain at peak stress at the end of Stage III in FRCM characteristic curve
ε_a	Axial strain of masonry column or cylinder
ε_{cr}	Crack strain of the matrix of FRCM system
$\varepsilon_{fd,rid}$	Reduced maximum strain in the composite according to CNR-DT 200/2013

ε_{fk}	Characteristic value of the ultimate tensile strain of FRP according to CNR-DT 200/2013
ε_{fu}	Ultimate tensile strain of the fibre
ε_{h}	Hoop strain of masonry column or cylinder
ε_{m0}	Axial strain at peak stress of unconfined masonry column or cylinder
ε_{m0}'	Axial strain at peak stress of unconfined masonry cylinder, obtained by using DIC
ε_{m0h}	Hoop strain at peak stress of unconfined masonry cylinder, obtained by using DIC
ε_{m0u}	Ultimate axial strain of unconfined masonry cylinder
ε_{mc}	Axial strain at peak stress of confined masonry column or cylinder
ε_{mc}'	Axial strain at peak stress of confined masonry cylinder, obtained by using DIC
$\varepsilon_{mc,exp}$	Experimental value of the axial strain at peak stress of confined masonry cylinder
ε_{mch}	Hoop strain at peak load of confined masonry cylinder, obtained by using DIC
$\varepsilon_{mc,th}$	Theoretical prediction of the axial strain at peak stress of confined masonry cylinder
ε_{mcu}	Ultimate axial strain of confined masonry cylinder
ε_{v}	Volumetric strain of masonry cylinder
η	Efficiency factor defined as the ratio between the tensile strength of FRCM system and the tensile strength of dry basalt textile
η_a	Environmental conversion factor according to CNR-DT 200/2013
ν_{m0}	Poisson's coefficient of unconfined column

ν_{mc}	Poisson's coefficient of confined column
ρ_f	Geometrical ratio of external wrap
σ_I	Peak stress at the end of Stage I in FRCM characteristic curve
σ_{II}	Peak stress at the end of Stage II in FRCM characteristic curve
σ_{III}	Peak stress at the end of Stage III in FRCM characteristic curve
$\phi(x_i, y_j)$	Displacement mapping function in the y direction in DIC analysis
$\psi(x_i, y_j)$	Displacement mapping function in the x direction in DIC analysis

1. INTRODUCTION

1.1 Background

Recent earthquakes occurred in the Mediterranean area pointed out the high vulnerability of the masonry building heritage, especially when structural details and quality of materials are not adequate. Masonry constitutes the main construction material of a wide part of the world building historical heritage and several of these structures need to be preserved for their cultural, historical and architectural value.

Particularly vulnerable structural members are columns or piers, which usually sustain mainly axial loads. When a structure is subjected to lateral loads, great variations of the compressive force can occur in these members and, consequently, brittle crushing failure can arise if the member was not designed for seismic actions. As a consequence, the need to repair and upgrade masonry columns constitutes an ongoing demand.

In this context, the use of external wraps made by composite materials represents one of the most popular techniques proven to be effective in upgrading the performance of weak masonry. The goal of this method is to increase the axial capacity and the local ductility of the material, producing a passive confinement action. The effectiveness of the technique is related to the great tensile strength achievable by the composite, which ensures high values of confinement pressure.

The most common types of composite materials are Fibre Reinforced Polymers (FRPs), which are made by the combination of organic matrixes – i.e. resin - and fibres. During the last decades, a huge amount of research work was carried out on the application of FRPs for repairing masonry structures, mainly concerning composites made by synthetic materials such as carbon or glass fibres, while limited work was performed on the application of natural materials such as basalt fibres. Several studies pointed out that considerable enhancements in terms of axial bearing capacity and ductility can be achieved by FRP

wrapping, ensuring adequate safety levels and structural performances. Despite these important results, some limitations on the use of FRPs on masonry structures arise due to the synthetic nature of the composite. In fact, these systems present some drawbacks due to the low compatibility of epoxy resins or synthetic materials in general when applied to the masonry substrate. As an example, frequently natural masonry blocks are subjected to moisture entrapment from the ground, released through the external surface during their service life. For this reason, it is not always recommendable to apply continuous epoxy-bonded jacketing, which inhibits the material transpiration. Moreover, the FRP strengthening has further limitations, such as: - poor behaviour of epoxy resins at temperatures above the glass transition temperature; - inability to apply FRP on wet surfaces or at low temperatures; - poor fire resistance; - no reversibility.

In the effort to alleviate these drawbacks due to the organic nature of polymer-based composites, in the last years growing attention has been paid to Textile Reinforced Mortar (TRM) composites, which constitute a new generation of high strength composite materials, where the epoxy matrix is replaced by an inorganic matrix, e.g. mortar. The inorganic matrix makes the composite more compatible to the masonry substrate, ensuring durability also in aggressive environmental conditions, vapour permeability and good resistance to high temperatures. Inorganic-matrix fibre reinforced composite materials account for a multitude of systems depending on the type of grid and matrix used, resulting in the derivation of many different acronyms: Textile Reinforced Concrete (TRC), Fabric Reinforced Cementitious Matrix (FRCM), Cementitious Matrix Grid (CMG), Inorganic Matrix Grid (IMG), Mineral Based Composite (MBC), Steel Reinforced Grout (SRG).

Fewer studies were carried out in the literature on the use of FRCMs for masonry confinement in comparison to similar works on FRPs, but the existing results pointed out that the efficiency of these systems can be affected by the limited tensile strength of the mortar and the consequent formation of cracks. In fact, the compatibility between mortar and fibres is lost after cracking and relative sliding between fibre and matrix can occur, with a consequent non-uniform distribution of stresses in the composite.

Despite some efforts were made on the development of mortar-based materials compatible with the masonry substrate, few studies were carried out on the application of natural fibres in composites for structural retrofit. In this field,

basalt fibres proved to be a promising alternative to the most common synthetic fabrics. The simplicity of the manufacturing process of basalt fibres reduces the costs and requires a lower amount of energy, with several benefits in terms of environmental impact. Moreover, the nature of basalt and its production process make it particularly suitable for applications on masonry structures, allowing the achievement of a sustainable and reversible intervention.

1.2 Research significance

Despite several works were developed on the application of composites for the confinement of masonry members, a few of studies addressed the use of basalt to be employed as fibre for composites. The adoption of this material could allow overcoming the main drawbacks arising with the use of synthetic fibres, such as carbon or glass fibres, and therefore its development can be useful for the optimization of a retrofit intervention, allowing a reduction of costs with a sustainable and reversible solution.

Additionally, the literature review reveals that a small number of studies are currently available on the use of FRCMs for the confinement of masonry members and they are limited to state general conclusions on the efficiency of this system in enhancing the mechanical properties of the strengthened members. In fact, few indications are available on the modelling of the compressive behaviour of FRCM-confined masonry and only few expressions are provided for the strength prediction.

Finally, a reasonable comparison between the performance of Basalt Fibre Reinforced Polymer (BFRP) and Basalt Fibre Reinforced Cementitious Matrix (BFRCM) systems is still missing in the literature, which could allow evaluating the reliability of composites with inorganic matrix in enhancing the compressive strength of masonry.

1.3 Thesis objectives and methodology

The aim of this study is the comparative evaluation of the effectiveness of BFRP and BFRCM systems in increasing the load carrying capacity and the ductility of confined masonry columns. This target concerns two matters: one is the evaluation of performance of basalt textile as new material for strengthening applications; the other issue is to understand if cement-based composites,

involving the use of basalt fibres, can be considered a valid alternative to FRP systems for strengthening columns, with several advantages when applied on masonry substrates.

With this aim, clay brick masonry cylinders are reinforced with continuous BFRP or BFRCM wraps and subjected to uniaxial compressive tests. In particular, the masonry specimens are manufactured considering two different assembling schemes and reinforced by using either one or two layers of basalt FRP/FRCM. The results of these experimental tests are analyzed and compared to each other and to those obtained by testing reference specimens in order to evaluate the retrofitting potential of the used strengthening systems.

The study is supported by a preliminary investigation on the mechanical properties of constituent materials of the masonry and the composites and by a detailed experimental characterization of the tensile behaviour of the BFRCM.

The whole experimental investigation is supported by the use of Digital Image Correlation (DIC), with several advantages respect to traditional monitoring techniques.

Finally, the experimental data obtained from compressive tests on masonry cylinders are employed to evaluate the reliability of theoretical formulations available in literature.

1.4 Thesis organization

The issues introduced above will be accurately addressed hereafter.

Including the present chapter, the thesis is composed of six chapters, briefly described in the following:

Chapter 2 starts with a brief description on the behaviour of masonry when the latter is subjected to axial loads. Then, the chapter introduces the main physical and mechanical characteristics of composite materials and provides a description on basalt fibres, pointing out the suitability of this material to be used for retrofit applications.

In a second part, the chapter contains an overview of the most relevant studies available in the literature with regard to FRP and FRCM-confined masonry columns. Firstly, the state of the art is discussed by addressing the main existing

experimental investigations, with particular attention to the studies involving the use of basalt fibres. In a second step, the attention focuses on the main theoretical formulations available in the literature for the definition of the compressive stress-strain law of confined masonry and the evaluation of the strength enhancement due to FRP and FRCM confinement.

Finally, a deep discussion on the tensile characterization of FRCM composites is presented, with reference to the main studies available in the literature.

Chapter 3 presents the experimental campaign carried out at Queen's University of Belfast (UK). The study focuses on the compressive behaviour of clay brick masonry cylinders manufactured using two different assembling schemes, in order to investigate on the influence of vertical mortar joints, and wrapped through either BFRP or BFRCM jackets, using one or two basalt textile layers.

A preliminary investigation is carried out on the mechanical properties of constituent materials of the masonry and the external wrap. In particular, an extensive study is performed on the basalt textile used for wrapping the cylinders, taking into account different gripping systems, test rates and geometries.

Moreover, an in-depth analysis on the behaviour of the BFRCM composite under tensile load is carried out. Three series of composite specimens are reinforced respectively with one, two or three basalt textile plies, with the aim of evaluating the influence of the volume fraction of fibres on the tensile response of the composite.

Used materials, manufacturing procedure and test setups are widely described and discussed. Particular attention is given to the use of the DIC technique, which is employed during all the performed tests. The basic principles and advantages of the technique are presented and its utility is underlined relating to the performed experimental tests.

Chapter 4 is dedicated to the discussion of the experimental outcomes. First, the results of the mechanical characterization of constituent materials of the masonry and the external wrap are presented. Particular attention is paid to the results obtained from the tensile characterization of the basalt grid, which are discussed with reference to the used clamping systems, the dimensions of the specimens and the test rate.

The outcomes of tensile tests on the BFRCM composite specimens are presented and discussed in terms of load-elongation or stress-elongation curves, allowing the study of the effect of the reinforcing fabric ratio on the overall tensile response of the composite system. The use of the DIC allows analyzing the strain/displacement full-field, giving significant information about the strain distributions on the surface of the specimens and about the crack development during tests.

The results from compressive tests on unconfined and basalt FRP/FRCM-confined cylinders are finally presented in terms of stress-strain curves and failure modes of the cylinders tested up to failure. It is shown that the strengthening by BFRP and BFRCM significantly increases the performance of the brick masonry cylinders, with different gains in terms of strength and ductility depending on the number of vertical mortar joints and on the number of layers used for wrapping the specimens. The readings obtained by traditional measuring instruments are integrated with those obtained by the DIC technique, which allows exploring the hoop strain of the cylinders.

Chapter 5 is focused on the validation of the available theoretical formulations on FRP and FCRM-confined masonry columns and on the proposal of possible approaches for the evaluation of the stress-strain curve in compression of these members.

First, a comprehensive comparative study of the available analytical models on FRP-confined masonry is presented in order to evaluate their reliability in reproducing, in terms of strength increase, experimental results of a large database borrowed from the literature. Moreover, the combination of the expressions from different models is adopted for predicting the overall constitutive law in compression of FRP-confined masonry columns and quantitative comparisons are made with a wide range of experimental data.

Then, the analytical formulas presented and discussed in Chapter 2 are applied for the evaluation of the strength increase due to confinement by BFRP and BFRCM, and comparisons are made with the experimental data obtained in the framework of this thesis. A revised version of the CNR-DT 200/2013 is also proposed, which seems to give reliable results. The evaluation of the strain at peak stress is addressed, evaluating the reliability of available formulas. Finally,

the compressive law of BFRP and BFRCM-confined cylinders is defined by proposing new possible approaches.

The comparison between theoretical predictions and experimental curves points out a good correlation in terms of average compressive response, peak stress, corresponding strain and slope of ascending and softening branches.

Finally, **Chapter 6** presents the most relevant conclusions regarding the use of basalt-fibre strengthening systems for confining masonry elements, by summarizing the main results obtained experimentally and their predictions discussed by proposed theoretical expressions. The chapter also recommends further researches which need to be followed as extension of the present research work.

2. CONFINEMENT OF MASONRY MEMBERS BY COMPOSITE MATERIALS: STATE OF THE ART

2.1 Introduction

The use of composite materials for structural upgrading has become common in practical applications to retrofit existing columns with poor structural features. The target of this method is to improve the axial capacity and local ductility of the material by inducing a passive confinement action. This retrofit method has shown noticeable capabilities since its origin, due to the great tensile strength of composites and the high values of confinement pressure achievable. Additionally, the increase of weight due to the intervention can be considered negligible and therefore the confinement using FRP or FRCM systems can be a suitable solution to retrofit masonry columns in buildings vulnerable to seismic actions.

In this chapter a brief description on the behaviour of masonry when subjected to axial loads is presented.

Then, composite materials are introduced with reference to their main characteristics and a description on basalt fibre is provided.

An overview of the most important research studies on the confinement of masonry by composite materials is presented, with reference to FRP and FRCM wrapping. After a review of the main experimental studies, with particular interest in works involving the use of basalt fibres, the analytical formulations available in the literature are analyzed by presenting the existing predictive models for calculating the strength or the stress-strain law of confined masonry in compression.

Finally, the main aspects regarding the tensile characterization of FRCM composites are discussed on the base of the available literature studies.

2.2 Basics of masonry behaviour under axial loads

Several authors investigated on the behaviour of masonry under axial loads, stating that different parameters are involved on its structural behaviour. Among these last, the physical and mechanical properties of brick units and mortar, the arrangement of units and the geometrical features of the units represent some of the most important key variables.

Independently from the different characteristics of masonry, the experimental evidence proved the masonry columns show an intermediate compressive behaviour, in terms of elastic modulus and strength, between that of its components, namely brick and mortar.

In fact, the collapse of axially-loaded masonry members in compression is characterized by the progressive formation of subvertical cracks in the bricks (Figure 2.1a), which propagate along the column widening their opening. This mechanism is due to the different deformability of the two components. In particular, the mortar in the joints is usually more deformable and it tends to a greater expansion than the units. In the case of compression, the mortar experiences a triaxial stress state between the units (Figure 2.1b). By contrast, the contact surface of brick units is subjected to a biaxial state of tensile stress and consequently, bricks are subjected to progressive cracking, which lead to the failure of the column.

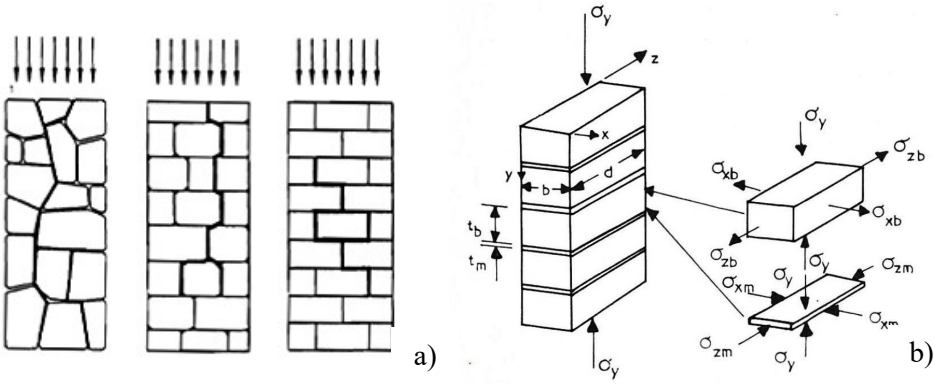

Figure 2.1 Masonry under compression: a) crack pattern of masonry columns in compression; b) stress state in the components (Francis et al., 1971)

Masonry in compression typically exhibits nonlinear stress-strain relations. Most of the nonlinear deformation occurs in the mortar joints with the brick often exhibiting linear stress-strain characteristics. Because of the influence of the bed joints and the possible anisotropic properties of the bricks, the deformation characteristics of the masonry will not necessarily be isotropic and can vary markedly with loading direction. For this reason several researches focused on the interaction between bricks and mortar, proposing expressions for the biaxial strength of the bricks (Hilsdorf 1969, Khoo and Hendry 1973, Atkinson et al. 1985), not here resumed for the sake of conciseness. The effect of joint thickness on the compressive strength of brick masonry was also studied by Hendry (1998), Francis et al. (1971), Shrive and Jessop (1982) and others.

From a theoretical point of view, it is not straightforward to define a unique constitutive law for the "homogenized" masonry material due to the great number of parameters which characterize masonry members. Nevertheless, some past studies tried to propose some formulation for its prediction.

Among the numerous expressions presented in the literature, as an example, Hendry (1998) proposed a non-linear stress-strain law, defined in the following non-dimensional form:

$$\frac{\sigma}{f_{wc}} = 2 \cdot \left(\frac{\varepsilon}{\varepsilon_u} \right) - \left(\frac{\varepsilon}{\varepsilon_u} \right)^2 \tag{2.1}$$

where f_{wc} is the uniaxial compressive strength of masonry and $\varepsilon_u = 2.5 \div 3.5‰$ is the ultimate strain.

Concerning the value of the elastic modulus in compression, experimental data deduced by Hendry et al. (1998) allowed correlating this parameter to the compressive strength, finding linear relationships between the two parameters in the form $E=k \cdot f_{k,}$ being f_k the characteristic value of the compressive strength and k a coefficient which depends on the nature of the bricks (k=1000/400).

It should be considered that the trend of the softening branch depends substantially by the size of the member and by the loading rate, and it is also affected by the kind of masonry, but in all the cases it is characterized by a marked brittle behaviour. This fact highlights the need of retrofit interventions and for this reason over the years several works were dedicated to study possible

confinement methods for improving the compressive behaviour of masonry members.

In this context, during the last decades ever growing attention has been paid to the use of composite materials, which have shown to constitute a valid alternative to tradition systems thanks to the many advantages they can offer. In the following, the main characteristics of composite materials are addressed.

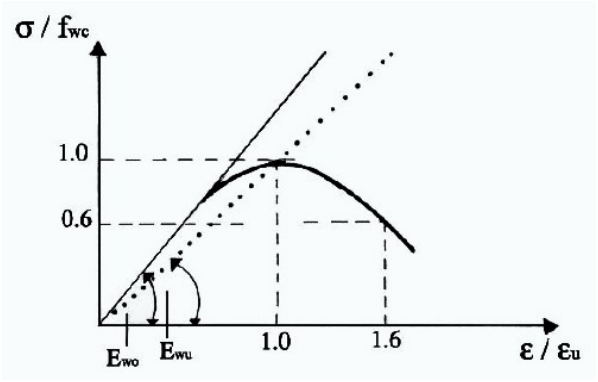

Figure 2.2 Dimensionless stress-strain curve of masonry under axial loads (Hendry 1998)

2.3 Composite materials

In the field of civil engineering, the advancement of alternative materials and methods for structural rehabilitation is of critical importance to the safety and preservation of the world habitable heritage. Over the last decades, there has been a growing awareness among structural engineers of the importance to investigate and develop new composite materials.

In this section a brief discussion is presented with regard to the general characteristics of composite materials. The strengthening systems involved in the experimental study presented herein are introduced and their main aspects are discussed. Finally the attention focuses on basalt fibres as new material for strengthening applications.

2.3.1 General aspects

Composite materials are heterogeneous materials made from two or more different phases combined and working together, whose mechanical performances and properties are designed to be superior to those of the constituent materials (Arboleda 2014). Modern well designed and manufactured composites, compared to traditional materials such as metals, offer high mass-specific stiffness and strength, as well as better resistance to fatigue and environmental degradation.

One of the phases of composite materials is continuous and constitutes the matrix. The matrix performs several functions, including maintaining the inclusions in proper orientation providing form and rigidity. Additionally, the matrix guarantees the distribution of the applied load within the composite and protects the dispersed phase from environmental factors causing its degradation (Talreja 2005).

The other phase is the reinforcement, which is embedded in the matrix and it is usually stronger, providing the strength and stiffness of the composite. The type and form of reinforcement is chosen on the base of the design requirements of the composite. However, there are some desirable qualities the materials must have in order to be employed as reinforcement, such as high strength, high modulus, low weight, environmental resistance and ease of manufacture (Koutsomitopoulou 2013).

The mechanical behaviour of fibre reinforced composites is governed by a complex relationship between the properties of the constituent materials, their volume fraction, the bond interface between them and their orientation with respect to the applied load.

Classification of composites is at two levels: by matrix type and by reinforcement type. The main composite categories with fibrous reinforcement include Metal Matrix Composites (MMC), Polymer Matrix Composites (PMC) and Brittle Matrix Composites (BMC) (Montesi 2015). The following overview is limited to polymer and brittle matrix composites, in particular FRPs and FRCMs respectively, being these materials included in the present thesis.

2.3.2 Fibre Reinforced Polymer (FRP) composites

Fibre Reinforced Polymer (FRP) materials are strengthening materials comprised of fibres embedded into a polymeric resin matrix. During the last decades, FRPs have been proven to be a suitable alternative to traditional repair methods for reinforced concrete and masonry structures.

FRP composites exhibit excellent tensile strength in the longitudinal direction of the fibres and relatively low strength in the transversal direction, which underlines an isotropic behaviour of the system. These systems have a very strong interfacial bond, with a fibre reinforcement strain limit generally lower than that of the epoxy matrix ($\varepsilon_{fib}<\varepsilon_{mt}$).

The composite shows a pure brittle linear elastic behaviour up to failure. Initially, matrix and fibres deform elastically; eventually, the matrix yields and deforms plastically but the fibres continue to stretch elastically (Callister and Rethwisch 2012). This relationship gives raise to the nearly elastic characteristic stress-strain curve shown in Figure 2.3.

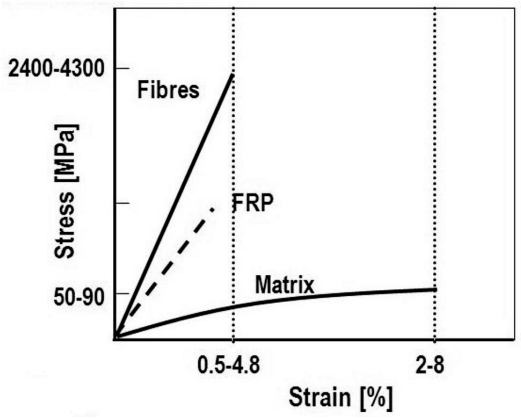

Figure 2.3 Typical stress-strain curves for FRP composites (Montesi 2015)

Despite numerous advantages associated with the use of FRP for strengthening concrete and masonry structures, there are some possible shortcomings attributed to the organic nature of the resin used to bind and impregnate the fibre reinforcement, such as:

- poor performance above the glass transition temperature of the polymer resin;
- low resistance to high temperature and no resistance to fire;
- impossibility to apply FRP on wet surfaces or at low temperatures;
- lack of vapor permeability;
- toxic health hazards for installers;
- relevance for application on historical buildings;
- incompatibility with some substrate materials.

2.3.3 Fibre Reinforced Cementitious Matrix (FRCM) composites

Fibre Reinforced Cementitious Matrix (FRCM) composites are currently receiving great attention as alternative strengthening materials to FRPs, especially for masonry elements and when specific preservation criteria need to be fulfilled. In FRCM composites the organic matrix is replaced with an inorganic one, which makes the composite more compatible to masonry substrate and highly resistant to high temperature.

This system consist of a "dry" fabric in a cementitious matrix. The definition "dry" fabric is generally used in literature in order to differentiate from fabrics impregnated by resin (Pino and Nanni 2015). Indeed, the cementitious matrix in FRCM does not fully impregnate the fibres and this is a significant factor affecting the mechanical behaviour and performance of these composites.

The cement based matrix of FRCMs exhibits high compressive strength but low tensile strength. The mechanical behaviour of these systems is very different from FRPs because the interfacial bond between fibre and matrix is weaker and more complex and the strain limit of the matrix is much lower than that of the fibres ($\varepsilon_{mt}<\varepsilon_{fib}$). When subjected to tensile stresses, the matrix starts to crack at its strain limit; on the other hand, fibre debonding and slipping are the mechanisms that mitigate crack localization. This behaviour leads to a kind of pseudo-ductility for these composites, which is a benefit in structural applications.

The mechanical effectiveness of FRCM system is strongly affected by the ability of the cementitious matrix to saturate dry fibre rovings, the bond between

the matrix and the fibres and the bond between the matrix and the substrate. Typically, FRCM composite mechanical behaviour is characterized by a linear-elastic trend up to the tensile strength of the matrix (Nanni 2012). Then, as the load increase, multiple cracks develop in the matrix and the stress is redistributed through the fibres, which allow the composite to endure additional strains. At this point, a strain-hardening behaviour develops, which depends on the amount of fibres and the quality of the fibres-matrix interfacial bond (Arboleda 2014).

2.3.4 The use of basalt fibres

Recently researchers have turned their attention towards the development of materials able to guarantee a certain degree of sustainability, without renouncing to adequate mechanical properties. In this context, basalt appears to be a material which could offer interesting opportunities in the future, in particular as alternative to glass fibres. Recent studies have included basalt as reinforcement in FRP composites, even if it was in the FRCM field where its structural application started.

In the following, the main characteristics of basalt fibres are briefly presented, with reference to the chemical composition, the manufacturing process and the properties of the material.

Chemical composition

Basalt is a natural volcanic rock originating at a depth of hundreds of kilometres beneath the earth and reaching the surface as molten magma. Analyzing the chemical composition of the material, it is evident that SiO_2 and Al_2O_3 are the main constituents (Fiore et al. 2015).

In Table 2.1 a comparison of the chemical composition of basalt fibres and E-glass fibres is reported.

Table 2.1: Chemical composition of basalt and E-glass fibres (Branston 2015)

Fibre Type	Weight % of compound							
	SiO_2	Al_2O_3	CaO	MgO	B_2O_3	Na_2O	K_2O	Fe_2O_3
Basalt	52-58	17-18	5-8	1-4	-	3-6	1-5	4-10
E-glass	52-56	12-16	16-25	0-5	5-10	0.8	0.2-0.8	>0.3

Manufacturing process

Basalt fibres are produced with a manufacturing process which is similar to that adopted for the production of glass fibres. As first step, the basalt rock is crushed, positioned into a furnace and melted at 1450-1500 °C. Then, basalt filaments are created by using a platinum-rhodium bushing. This technology is named continuous spinning and it can offer the reinforcement material in the form of chopped fibres or continuous fibres (Figure 2.4), which can be employed in the textile manufacturing process and have great potential application in composite materials. Short fibres are produced by blowing melt technologies, while continuous fibres are made by spinneret method (Figure 2.5), similarly to glass fibres (Fiore et al. 2015).

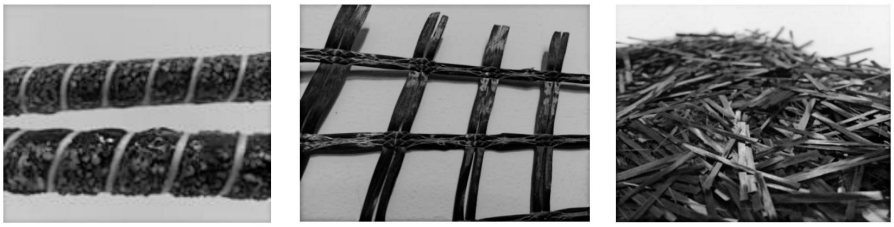

(a) Rebar (c) Mesh (c) Chopped fibre

Figure 2.4 Basalt fibre product (Branston 2015)

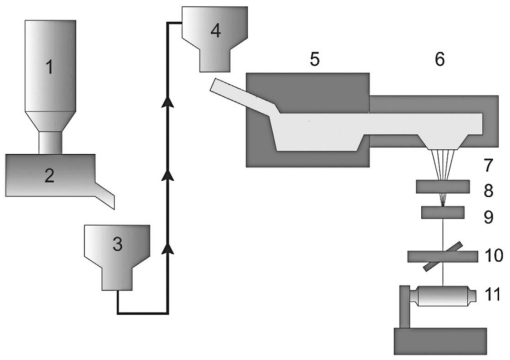

Figure 2.5 Scheme of basalt fibreization processing line: 1) crushed stone silo; 2) loading station; 3) transport system; 4) batch charging station; 5) initial melt zone; 6) secondary heat zone with precise temperature control; 7) filament forming bushings; 8) sizing applicator; 9) strand formation station; 10) fibre tensioning station; 11) automated winding station (Fiore et al. 2015)

Advantages and properties of basalt fibre

Basalt fibres show several advantages, which make them a good alternative to glass fibres as reinforcing material in composites used in several fields. Basalt fibres are produced directly from the raw material, by melting basalt rock with no other additives, differently from glass fibres that are made from a complex batch of materials. The simplicity of the manufacturing process reduces the production costs (Sim and Park 2005) and the fabrication process requires a lower amount of energy, with several benefits in terms of environmental impact. Moreover, basalt is a natural material, which makes it particularly suitable for applications on masonry structures and guarantees no toxic reaction with air or water.

From another hand, the quality and the chemical composition of the raw material have a major effect on cost and properties of basalt fibres and it can lead to a broad range of fibres with different mechanical properties (Fiore et al. 2015). As a result, elastic modulus and strength of basalt composites should be evaluated carefully.

Basalt is known for its excellent mechanical and physical properties such as high elastic modulus and high strength. In Table 2.2 some physical and mechanical characteristics of basalt and E-glass are compared.

Table 2.2: Comparison of basalt and E-glass fibres (Branston 2015)

Fibre Type	Density (g/cm^3)	Elastic Modulus (GPa)	Tensile Strength (GPa)	Elongation at Break (%)
Basalt	2.8	89	2.8	3.15
E-glass	2.56	76	1.4-2.5	1.8-3.2

Moreover, basalt fibres are not combustible, they have a high chemical stability and a good resistance to weather, alkaline and acid exposure. Additionally, these fibres can be used from very low temperatures (i.e. about -200 °C) up to the comparative high temperature (i.e. in the range 600-800 °C) (Deàk and Czigàny 2009).

2.4 Confinement with composite materials: overview

In general, the compressive strength and the deformation capacity of confined masonry can be evaluated depending on the mechanical properties of the unconfined material, the type of strengthening system and the shape of the transverse cross-section.

The mechanical behaviour of the masonry subjected to confining pressure provided by composite materials depends on the failure conditions of the jacket, the latter not always easy to be predicted accurately. The different tensile behaviour of FRP and FRCM composites has an unavoidable effect on the compressive behaviour of columns confined by using these systems. In the case of FRP, the high performance of the polymeric matrix and the perfect fibres-matrix bond ensure that the confining action strongly depends on the quality of the fibres (Cascardi et al. 2017a). On the other hand, the mechanical behaviour of FRCM systems proved to be affected by the brittle behaviour of the inorganic matrix, since the cracking development within the mortar may significantly reduce the stress transfer from the column substrate to the fibre of the jacket, with a consequent reduction of the confining pressure and the final compressive strength (Bournas et al. 2007). Anyway, when a high bond level between fibres and matrix is ensured, the FRCM confining behaviour tends to be close to that of FRP, because the effective stress transfer from the column to the grid is guaranteed (Valdés et al. 2014).

An important aspect for the characterization of the compressive behaviour of confined columns is the evaluation of the lateral confinement pressure f_l provided by the composite jacket, generally expressed through the forces equilibrium of the masonry core subjected to axial and, consequently, lateral expansion and the reaction of the composite confining device.

Considering the general case of circular section (Figure 2.6), the stress in the fibres can be assumed to be uniform along the perimeter of the circumference and the forces equilibrium in the ultimate conditions can be obtained as follows:

$$f_l = \frac{2 \cdot E_f \cdot \varepsilon_{fu} \cdot t_f}{D} \tag{2.2}$$

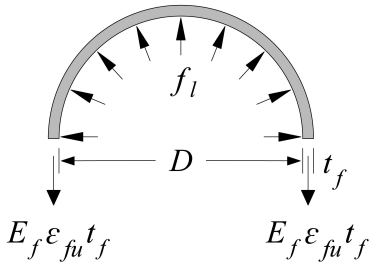

Figure 2.6 Confinement action on circular masonry section

In Eq. (2.2) E_f and t_f represent the elastic modulus and the thickness of the confining device respectively, ε_{fu} is the ultimate tensile strain of the composite and D is the diameter of the circumference.

Failure of the column is due to the rupture of the fibres subjected to tensile stresses in the circumferential direction.

In the case of square/rectangular section (Figure 2.7), the confinement lateral pressure f_l can be obtained from the following balance forces:

$$f_l = \frac{f_{l,b} + f_{l,d}}{2} = \frac{(b+d)}{b \cdot d} \cdot f_r \cdot t_f \tag{2.3}$$

where b and d are the lengths of sectional sides, while the terms $f_{l,b}$ and $f_{l,d}$ refer to confining stresses along the two cross-section sides. The term f_r indicates the effective stress in the wrap at failure. In a square cross-section the stress is not uniform along the perimeter because of stress concentration near the corners of the section. In an approximate way, this can be taken into account by considering a constant reduced uniform stress along the perimeter equal to f_r, as shown in the following.

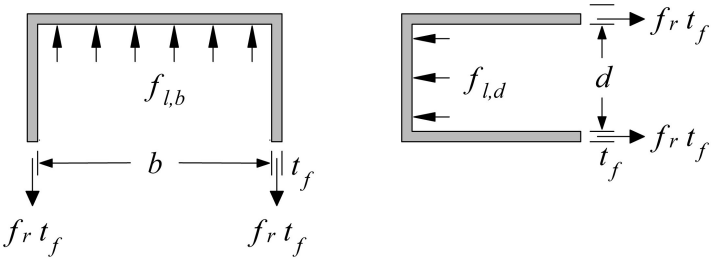

Figure 2.7 Confinement action on rectangular masonry section

The effective confinement pressure f'_l is calculated by considering the in-plane efficiency coefficient k_e:

$$f_l^{'} = k_e \cdot f_l \tag{2.4}$$

$$k_e = 1 - \frac{(b^{'2} + d^{'2})}{3 \cdot A_m} \tag{2.5}$$

where $b'=b-2\cdot r_c$ and $d'=d-2\cdot r_c$ are the straight sides of the section, r_c is the corner radius (Figure 2.8a), while $A_m=b\cdot d$ is the gross area.

Eq. (2.5) derives from the ratio between the area of effectively confined masonry and the gross area. In the case of circular section k_e is equal to 1, while for a polygonal section with rounded corners it can be calculated assuming that the effectively confined masonry is enclosed between parabolic curves starting from the end of the corner radius with slope equal to 45° (Figure 2.8b).

In general, besides the in-plane efficiency coefficient, the effective confinement pressure f'_l is dependent from another parameter, namely the vertical efficiency coefficient. However, for the analyses carried out in the context of this thesis, this factor is always assumed equal to 1, since only continuously wrapped columns are analyzed here.

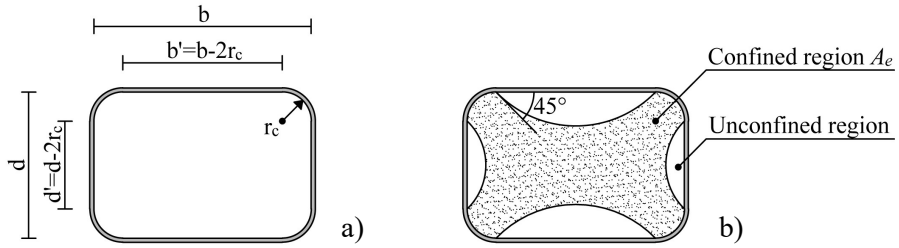

Figure 2.8 Cross-section: a) indication of symbols of the cross-section; b) effectively confined area

2.5 Compressive behaviour of FRP-confined masonry columns

The use of FRPs for structural upgrading of weak piers and columns has been widely studied and adopted in reinforced concrete members for about twenty years, while its suitability to masonry elements has been investigated during the last decade.

Despite the large number of advantages derived from the use of FRP materials, several critical issues are involved in this technique, such as stress concentration in sharp-cornered sections, brittle behaviour of FRP and evaluation of in-plane and in-elevation efficiency coefficients. Furthermore, the wide variability of kinds of masonry and the different mechanics of the latter compared to concrete lead to difficulties in expressing the strength and ductility increase as a function of the amount of reinforcing FRP wraps.

For these reasons, several researches have been carried out in the recent past with the aim of investigating the compressive behaviour of FRP-confined masonry columns. In the following, the most relevant experimental and theoretical studies are presented and discussed.

2.5.1 Experimental investigations

Several experimental studies were addressed in the past to study the effect of FRP confinement on the compressive behaviour of masonry members and the majority of the works involves the use of carbon and glass fibres. Among the most important scientific contributions there are those of Micelli et al. (2004), Krevaikas and Triantafillou (2005), Corradi et al. (2007), Aiello et al. (2007), Di Ludovico et al. (2008), Aiello et al, (2009), Alecci et a. (2009), Faella et al. (2011a), Borri et al. (2011), Galal et al. (2012), Micelli et al. (2014a), Witzany et al. (2014), Witzany et Zigler (2016), Rao and Pavan (2014), Fossetti et al. (2016), Incerti et al. (2015), Fossetti and Minafò (2017), Alotaibi and Galal (2017), Sandoli et al. (2019).

As general findings, most of the experimental studies have pointed out that: - the strength increase is generally higher in the case of weak masonry columns and for stiffer wrapping layers, confirming the influence of the basic parameters on the behaviour of confined members; - stress concentration at the corners induces brittle failure, and does not make it possible to reach the maximum confining stress; - the bond between masonry and FRP depends on the kind of resin and tissue adopted.

More recently, Basalt Fibre Reinforced Polymer (BFRP) materials have gained increasing attention as system for strengthening applications, especially as alternative to glass fibres. However, despite of numerous studies on columns wrapped with carbon and glass FRP, there are very limited experimental data on

columns wrapped by BFRP and the most of studies investigate on concrete members (Campione et al. 2015, Ouyang et al. 2017, Sadeghian and Fillmore 2018).

Among the available studies on BFRP-confined masonry members, Di Ludovico et al. (2010) presented the results of an experimental investigation on the compressive behaviour of square cross-section tuff and clay-brick masonry columns confined with carbon, glass and basalt FRP, in order to evaluate and compare the effectiveness of these strengthening systems. The main experimental results were presented in terms of axial stress-axial strain relationships and effective strains at failure on the composite system. With reference to clay brick masonry columns, researchers found that GFRP and BFRP confining systems led to similar compressive strength gain (about 57%), but BFRP wrapping was more effective in terms of ultimate axial strain gain (413% for BFRP confinement against 259% for GFRP one) even if its mechanical external reinforcement ratio was lower than GRFP. Indeed, by comparing the transverse strain registered at failure on the external wrap of the columns with the ultimate FRP axial strain provided by flat coupon tests, higher values were recorded on BFRP laminates compared to GFRP.

Micelli et al (2014b) investigated on the mechanical behaviour of circular masonry columns confined by using glass and basalt FRP systems and subjected to axial compressive tests. Moreover, active confinement was studied by using a new technique that utilizes Shape Memory Alloys (SMA). Experimental outcomes highlighted the effectiveness of the FRP confinement. In particular, the presence of full wrapping with unidirectional glass and basalt sheets produced the highest values of strength, with gains of 224% and 132% respectively compared to unconfined columns. The use of discontinuous wraps allowed also a considerable enhancements of the mechanical characteristics of confined columns, with an increment of 82% and 33% for glass and basalt wrapping respectively. Significant increments of the ductility were observed for both the strengthening systems. The model of the Italian CNR-DT 200/2013 Guidelines was adopted by the authors for obtaining a prediction of the compressive strength and for comparing experimental results and design approach, also for new types of fibre like basalt which were not included in the technical codes.

In relation to the number of parameters governing the failure mechanism such as kind of brick element and mortar layer, dimension of columns and so on, the

experimental studies carried out on strengthening masonry columns by using BFRP wraps are not enough to formulate more general conclusions about the use of BFRP confinement as alternative strengthening method to the application of carbon or glass fibres. Therefore, further investigations are needed in order to widen the knowledge of this new material and to assess his ability of enhancing the carrying capacity of masonry columns.

2.5.2 Analytical models

The evaluation of the lateral confinement pressure and the ultimate compressive strength and corresponding strain, along with the definition of the overall trend of the stress-strain curve, represent a key aspect to the definition of the compressive behaviour of FRP-confined masonry. For this reason, many research works are aimed at defining design expressions for the evaluation of these parameters.

One of the first studies on the effect of external FRP wrapping on masonry columns was carried out by Krevaikas and Triantafillou (2005), who tested forty-two clay brick masonry columns and formulated some expressions for calculating the strength and ultimate strain increase. Similarly, Corradi et al. (2007) performed compressive tests on FRP-confined clay brick columns and provided a model for the calculation of confinement pressure, efficiency coefficients and strength increase. They also adapted the stress-strain law proposed by Campione and Miraglia (2003) to model the compressive behaviour of FRP-confined masonry.

On the base of the experimental investigation presented in the previous section, Di Ludovico et al. (2010) proposed new expressions for evaluating the strength enhancement in masonry columns strengthened by FRP systems.

Faella et al. (2011b) presented an analytical formulation for obtaining the strength of FRP-confined concrete members, analyzing their effectiveness when applied to confined masonry elements. Furthermore, the researchers demonstrated that analogous models available for masonry members provided inaccurate estimations, due to the fact that often they were calibrated on experimental results carried out on specific types of masonry. Finally, the authors proposed a general expression for a design formula with reference to the

experimental database obtained by blending the test results presented by the same authors with other data available in the literature.

More recently, Lignola et al. (2014) summarized previous literature studies and proposed a theoretical approach based on the Mohr-Coulomb strength criterion for determining the strength increase due to FRP confinement.

Additionally, it worth to cite the CNR-DT 200/2013 Guidelines, which represents the Italian reference document for the design and implementation of upgrading interventions on concrete and masonry structure through the use of FRP composite materials.

It is evident from the literature review that a unified approach for the definition of the stress-strain law of FRP-confined masonry in compression is still missing. In fact, most of the works have focused on the evaluation of strength enhancement and confinement efficiency (Krevaikas and Triantafillou 2005, Corradi et al. 2007, Aiello et al. 2009, Di Ludovico et al 2010, Lignola et al. 2014) by relating the increase of axial capacity with the confinement pressure, while a few studies have particularized the calculation of ultimate strain and the definition of an analytical stress-strain relationship (Krevaikas and Triantafillou 2005, Corradi et al. 2007).

In the following, the formulations of some mentioned analytical studies are presented in detail, focusing the attention on the models that will be considered for the theoretical investigations carried out in Chapter 5.

Campione and Miraglia (2003)

Despite it was originally defined for concrete members, the model of Campione and Miraglia (2005) is here presented since it is used for the analytical investigations involved in this thesis, being the only model able to consider a reduced stress in the external wrap by means of an analytical expression.

The analytical compressive behaviour of concrete members reinforced by FRP was investigated by the authors, with particular attention to the variation of the shape of the transverse cross-section.

According to this model, the compressive strength of FRP-confined concrete, here indicated as f_{mc} for consistency, is defined as:

$$f_{mc} = f_{m0} + k_1 \cdot f_l^{'} \tag{2.6}$$

being f_{m0} the compressive strength of unconfined concrete, f'_l the effective lateral confinement pressure and k_1 an experimental coefficient assumed equal to 2.

The effective confinement pressure is evaluated through Eqs. (2.2)-(2.5), on the base of the shape of the transverse cross-section.

In the case of square or rectangular columns, the effective stress in the wrap is calculated as:

$$f_r = f_{fu}\left[\left(1-\frac{\sqrt{2}}{2}\cdot k_i\right)\cdot\frac{2r_c}{b}+k_i\cdot\frac{\sqrt{2}}{2}\right] \tag{2.7}$$

where r_c is the corner radius of the cross-section, k_i = 0.2121 is a coefficient defined by the authors by means of regression analysis on the experimental data and f_{fu} is the tensile strength of the FRP defined as:

$$f_{fu} = E_f \cdot \varepsilon_{fu} \tag{2.8}$$

Being E_f and ε_{fu} respectively the elastic modulus and the ultimate tensile strain of the FRP laminates.

The ultimate strain ε_{mc} is assumed as:

$$\frac{\varepsilon_{mc}}{\varepsilon_{m0}} = 1 + \rho_f \cdot \frac{1}{\varepsilon_{m0}} \cdot \frac{f_r^2}{E_f} \cdot \frac{1}{f_{m0} + k_e \cdot f_l} \tag{2.9}$$

where ε_{m0} is the ultimate strain of unconfined masonry, f_l is the confinement lateral pressure, k_e is the in-plane efficiency factor and ρ_f is the geometrical ratio of the external wrap, defined as:

$$\rho_f = \frac{2\cdot\left[2\cdot\left(b-2r_c\right)+\pi r_c\right]\cdot t_f}{b^2-4\cdot\left[r_c^2-\left(\pi r_c^2/4\right)\right]} \tag{2.10}$$

For the analytical modelling of the complete compressive stress-strain response of FRP-confined members the following relationship is provided:

$$\frac{\sigma(\varepsilon)}{f_{m0}} = \beta\frac{\varepsilon}{\varepsilon_{m0}} + \left[\frac{(1-\beta)\cdot\varepsilon}{\varepsilon_{m0}}\right] \Bigg/ \left[1+\left(\frac{\varepsilon}{\varepsilon_{m0}}\right)^{R}\right]^{1/R} \tag{2.11}$$

Eq. (2.11) represents a curved transition from a straight-line asymptote with slope E_0, E_0 being the initial modulus of the FRP-confined masonry, to another asymptote with slope equal to the hardening modulus E_h, the latter being equal to:

$$E_h = \frac{f_{mc} - f_{m0}}{\varepsilon_{mc} - \varepsilon_{m0}} \tag{2.12}$$

The β parameter is the strain hardening ratio defined as:

$$\beta = \frac{E_h}{E_0} \tag{2.13}$$

The term R is a shape parameter, proposed equal to 3. The hardening part is governed by the strength and by the maximum strain characteristics of the confined and unconfined masonry. The stress-strain curve stops when the maximum stress f_{mc} and maximum strain ε_{mc} are reached and FRP fails in tension because its ultimate strain is achieved.

Krevaikas and Triantafillou (2005)

According to the model proposed by Krevaikas and Triantafillou (2005), the strength of FRP-confined masonry columns under axial load is evaluated considering the experimental evidence, which shows that for very low values of the confining stress the confined compressive strength does not exceed the unconfined value. Then, the following formulation is proposed:

$$\begin{cases} f_{mc} = f_{m0} & \text{if } \dfrac{f_l'}{f_{m0}} \le 0.24 \\ f_{mc} = f_{md}\cdot\left(0.6 + 1.65\cdot\dfrac{f_l'}{f_{md}}\right) & \text{if } \dfrac{f_l'}{f_{m0}} \ge 0.24 \end{cases} \tag{2.14}$$

where the terms f_{mc}, f_{m0} and f'_l have the meaning introduced above.

The effective confinement pressure is calculated with Eqs. (2.2)-(2.5), by assuming $f_r=f_{fu}$.

In this model the ultimate strain ε_{mc} is deduced by the following expression:

$$\frac{\varepsilon_{mc}}{\varepsilon_{m0}} = 1 + \frac{k_2}{\varepsilon_{m0}} \cdot \frac{f_l^{'}}{f_{m0}} \tag{2.15}$$

where ε_{m0} is the ultimate strain of unconfined masonry and k_2 is a coefficient equal to 0.034.

Corradi et al. (2007)

In the model of Corradi et al. (2007) the compressive strength of masonry confined by FRP is calculated through Eq. (2.6), where the coefficient k_1 is evaluated as:

$$k_1 = 2.4 \cdot \left(\frac{f_l^{'}}{f_{m0}} \right)^{-0.17} \tag{2.16}$$

The effective confinement pressure is evaluated using Eqs. (2.2)-(2.5). In particular, the evaluation of the effective stress in the external wrap is made through the following expression:

$$f_r = f_{fu} \cdot k_g \tag{2.17}$$

where f_{fu} is the tensile strength of the FRP and k_g is a reduction coefficient, defined by authors as the ratio between the actual confinement pressure f_l and that on a circular section having a diameter equal to the significant dimension for which f_l is calculated. This coefficient depends on the shape ratio of the section (b/d) and on the corner radius adopted. It is equal to 0.82 for square sections and between 0.38 and 0.43 for rectangular sections.

Di Ludovico et al. (2010)

On the base of the main existing models in literature and considering a wide database of experimental data, Di Ludovico et al. (2010) proposed a refined equation for the evaluation of the strength of FRP-confined masonry. The

formulation assumes the form of Eq. (2.6), where the coefficient k_1 is evaluated as:

$$k_1 = 1.53 \cdot \left(\frac{f_l^{'}}{f_{m0}} \right)^{-0.10} \tag{2.18}$$

The effective confinement pressure is calculated through Eqs. (2.2)-(2.5). The model considers the effective confinement pressure calculated by assuming the external wrap at maximum tensile stress, which means $f_r = f_{fu}$.

CNR-DT 200 (2013)

The Italian CNR-DT 200/2013 code provides an expression for the definition of the strength of FRP-confined masonry columns. The axial strength f_{mc} is defined depending on the compressive strength of unconfined masonry f_{m0} and the effective confinement pressure f'_l:

$$f_{mc} = f_{m0} + k_1 \cdot \left(\frac{f_l^{'}}{f_{m0}} \right)^{\alpha_1} \tag{2.19}$$

being k_1 a dimensionless coefficient and α_1 an exponent assumed equal to 0.5. The value of k_1 depends on the mass density g_m (expressed in kg/m^3) of unconfined masonry:

$$k_1 = \alpha_2 \left(\frac{g_m}{1000} \right)^{\alpha^3} \tag{2.20}$$

where α_2 and α_3 are coefficients that can be assumed equal to 1 when experimental data are not available.

The effective confinement pressure is determined on the base of Eqs. (2.2)-(2.5), assuming the stress in the external FRP wrap equal to:

$$f_r = \varepsilon_{fd,rid} \cdot E_f \tag{2.21}$$

where E_f is the elastic modulus of the FRP and $\varepsilon_{fd,rid}$ is the reduced maximum strain in the wrap, expressed as:

$$\varepsilon_{fd,rid} = \min\left\{\eta_a \cdot \varepsilon_{fk} / \gamma_f ; 0.004\right\} \tag{2.22}$$

η_a being the environmental conversion factor, equal to 0.75 and 0.65 for an external or internal exposure condition, ε_{fk} the characteristic value of the ultimate tensile strain of the FRP and γ_f the partial safety factor equal to 1.1.

The Italian CNR-DT 200/2013 Guidelines proposes a constitutive law of FRP-confined concrete members, here presented since it will be employed in Chapter 5 for the evaluation of the compressive behaviour of FRP-confined masonry. The compressive stress-strain response is defined by means of the following expressions

$$\begin{cases} \dfrac{\sigma(\varepsilon)}{f_{m0}} = a \cdot \bar{\varepsilon} - \bar{\varepsilon}^2 & for\ 0 \le \bar{\varepsilon} \le 1 \\ \dfrac{\sigma(\varepsilon)}{f_{m0}} = 1 + b \cdot \bar{\varepsilon} & for\ 1 \le \bar{\varepsilon} \le \dfrac{\varepsilon_{mc}}{\varepsilon_{m0}} \end{cases} \tag{2.23}$$

where ε_{mc} and ε_{m0} are the ultimate strain of FRP-confined and unconfined masonry respectively, $\bar{\varepsilon} = \varepsilon / \varepsilon_{m0}$ is the normalized strain, while the other parameters setting the shape of the curve are defined as follows:

$$a = 1 + \gamma \tag{2.24}$$

$$b = \gamma - 1 \tag{2.25}$$

$$\gamma = \frac{f_{m0} + E_t \cdot \varepsilon_{m0}}{f_{m0}} \tag{2.26}$$

$$E_t = \frac{f_{mc} - f_{m0}}{\varepsilon_{mc}} \tag{2.27}$$

2.6 Compressive behaviour of FRCM-confined masonry columns

Fibre Reinforced Cementitious Matrix (FRCM) composite materials are currently receiving great attention as alternative strengthening technique to FRP materials, especially for masonry elements and when specific preservation criteria need to be fulfilled.

In the recent years, several experimental studies confirmed the effectiveness of the confinement by FRCM for masonry columns. The use of such technique increases the compressive strength of the members and lead to a more ductile failure, with a softer descending behaviour in the post-peak range with respect to unreinforced members. However, the number of studies on this subject is not sufficient to understand the behaviour of the masonry strengthened by FRCM or to derive general results, due to the variety of masonry materials and differences in loading states.

Here, the experimental studies carried out on FRCM-confined masonry columns are addressed, with particular attention to those involving the use of basalt fibres. Moreover, the available theoretical formulations to predict the strength increase due strengthening by means FRCM are presented and discussed.

2.6.1 Experimental investigations

A quite number of experimental campaigns have been carried out with the aim of investigating on different parameters involved in the compressive behaviour of masonry columns confined by FRCM systems. The state of the art points out as the compressive performance of elements strengthened by FRCMs depends on different parameters, the latter related to the adopted fibres, but also to the type of matrix employed to apply the textile to the column.

The experimental evidence regarding FRCM confinement of masonry columns is dated back to 2008, when Di Ludovico et al. tested square cross-section tuff masonry columns strengthened by glass-grid bonded with a cement based mortar and subjected to uniaxial compression.

Actually, the number of experimental tests on masonry columns confined by using FRCM systems is very limited, even if during the last years the experimental investigations have been increased. Significant contributions derive from research of Yilmaz et al. (2013), Micelli et al. (2014b), Carloni et al. (2014), Incerti et al. (2015), Ombres (2015), Krevaikas (2015), Mazrea et al. (2016), Witzany and Zigler (2016), Fossetti and Minafò (2017), Maddaloni et al. (2017), Santandrea et al. (2017), Sneed et al. (2017), Cascardi et al. (2018), Minafò and La Mendola (2018), Ombres and Verre (2018a), Murgo and Mazzotti (2019). Different types of textile have been employed, among these it can be

found glass, PBO, carbon, steel, basalt. In the same way, different type of mortar have been investigated. Here, the experimental studies involving the use of basalt fibres are discussed.

Yilmaz et al. (2013) investigated on the efficiency of historical masonry columns externally confined by using open-grid basalt fibre reinforced mortar. With this aim, square cross-section masonry columns were produced employing solid bricks collected from historical buildings and local mortar with characteristics able to simulate those of existing historical mortar. Reference and FRCM-confined columns were tested under concentric compressive load. The basalt reinforced specimens showed quite small compressive strength enhancement (25%) compared to unconfined ones; on the other hand, a significant energy dissipation improvement was attained (86%). The rupture of the basalt fibres at the corners of the columns was observed.

As part of the experimental study discussed in the section about FRP, Micelli et al. (2014b) tested circular masonry columns confined by using continuous and discontinuous basalt FRCM wraps. The outcomes pointed out a considerable enhancement of the BFRCM strengthened columns compared to unconfined specimens. When columns were confined with discontinuous basalt grid, unexpected results were found, namely the strength increase, equal to 73%, was higher than that obtained in the case of full-wrapped columns (47%). The authors related this outcome to the double layer of the FRCM jacket and to the scattering typical of masonry material. The failure mode was by tensile rupture of the fibres, accompanied by a diffusive cracking along the height of the column. The buckling of the cement-based composite jacket was observed.

More recently, Mazrea et al. (2016) presented an experimental investigation on BFRCM-confined brick masonry piers. Eighteen specimens with square/rectangular cross-section were assembled and tested under compressive loads. The use of FRCM jacketing guaranteed significant increments in terms of axial strain, while the compressive strength gains were not so pronounced. Moreover, the confinement system showed more effective behaviour on the square masonry piers than on rectangular ones. The traditional monitoring systems were supported by the use of a digital image correlation system, which made possible to obtain information about the progression of cracks subjected to increasing incremental loading. In particular, the digital system is suggested for monitoring of the confinement layer behaviour of the FRCM-confined columns,

while the LVDTs system can be used to describe the overall behaviour of specimens.

The results of an experimental study on the compressive behaviour of clay brick masonry columns strengthened with basalt FRCM wraps was presented by Fossetti and Minafò (2017). Two masonry strength were considered by varying the mortar grade in order to investigate on the effects of a different binding mortar composition. The outcomes, discussed in terms of axial stress-strain curves and failure mode of tested columns, pointed out the capability of this system in increasing the structural efficiency of strengthened members. It was found that the efficiency of the strengthening system depends on the mortar grade of the masonry. In particular, BFRCM jacketing proved to be effective in terms of strength gain for low-grade mortar masonry, with an average increments of about 75%, while negligible effects were observed in the case of normal strength masonry columns.

Santandrea et al. (2017) presented the results of an experimental study on square cross-section masonry columns, confined by using basalt FRCM jackets and subjected to monotonic concentric compressive load. The effectiveness of the confinement was investigated in terms of load-bearing capacity, comparing results from strengthened columns to those obtained from unconfined specimens. Particular attention was addressed to the influence of corner radius. The basalt FRCM jackets provided an average compressive strength enhancement of 14-16% with respect to control specimens. The relatively low increase of the average compressive strength was mainly caused by the brittle failure of basalt fibres at the corners of the square cross-section columns. Specimens with sharp and rounded corners showed the same failure mode.

An experimental study on real scale masonry columns was performed by Maddaloni et al. (2017). The researchers investigated on the behaviour of full-scale columns made of limestone masonry blocks and strengthened using different FRCM systems, among them basalt FRCM jackets. The results pointed out the effectiveness of the basalt FRCM confinement system, with enhancements in terms of both load bearing capacity and ultimate axial strain. In particular, the axial strength of reinforced columns increased of about 67% in comparison to unconfined specimens. The post-peak branch of the stress-strain curves showed a softening trend due to the cracking and expulsion of the mortar layers and the axial displacement of confined specimens was three times the one

of reference columns. The spalling of the jacket started at the corners of the columns, with the formation of vertical cracks, followed by the buckling of mortar reinforcement in different areas of the specimens.

The studies discussed above allow underlining some common conclusions that were reached by different authors about BFRCM system. In general, the use of basalt fibres embedded in mortar matrix for strengthening masonry columns can guarantee a significant enhancement of the load-carrying capacity of the confined element, ensuring also considerable improvements of ductility. The efficiency of BFRCM jacketing changes in relation to the basic properties of plain masonry, with higher strength gains in the case of weaker masonry. The cross-section shape (square or rectangular) of the confined columns seems to affect the performance of the strengthening system and stress concentrations at the corners were always observed. The failure mode is characterized by the propagation of longitudinal cracks, usually near the corners of polygonal cross-section columns, and by the consequent rupture of fibres in correspondence of the cracks. Sometimes, failure occurred at the overlap region.

For an overall view, the key aspects of the above-mentioned experimental works are summarized in Table 2.3. Information related to specimens and strengthening system are provided for each study. In particular, Table 2.3 reports: the authors (*Authors*); the label of each specimen (*Label*); the number of tested specimens with the same characteristics (*n*); the type of masonry (*M*); the cross-section shape of the specimen (*CS*); the used corner radius (r_c); the type of fibre used as reinforcement (*F*); the number of layers of fibre textile (*L*); the type of mortar used as matrix of the FRCM system (*MT*); the thickness used for applying the FRCM jacket (*t*). Some other labels used in Table 2.3 are reported in the explanation below the table.

Except from Micelli et al. (2014b), who tested two FRCM-reinforced circular columns, the totality of the works focuses on square/rectangular cross-section shaped columns. Moreover, among the discussed studies, only Krevaikas (2015) and Ombres and Verre (2018a) investigates on the effect of the number of reinforcing layers on the stress-strain response of FRCM-confined columns. Other works consider only specimens reinforced with one or two grid plies.

Table 2.3: Tested FRCM-confined specimens

Authors	Specimen	Masonry			Reinforcement				
	Label	n	M	CS	r_c (mm)	F	L	MT	t (mm)
Di Ludovico et al. (2008)	GRM	3	Tuff	Sq	20	Glass	1	CM	8
Yilmaz et al. (2013)	S-2B-L	2	Brick	Sq	12	Basalt	2	CM	15
Micelli et al. (2014)	$C\_B_{GRID}C\_T$ $C\_B_{GRID}C\_D$	1 1	Calcareous stone	Circ	/	Basalt	2	CM	10
Carloni et al. (2014)	W C SQ C RECT 1 C RECT 2 C	3 3 3 3	Brick	Rect Sq Rect Rect	10	PBO	1	CM	8
Incerti et al. (2015)	CP_RC170 CP_RV320 CP_GV160	2 2 2	Brick	Sq	20	Carbon Glass Carbon	2	LM	10
Ombres (2015)	C-1-0	1	Brick	Sq	20	Carbon	2	CM	6
Krevaikas (2015)	C1_1_R20 C1_1_R10 C2_1_R10 C3_1_R10	3 3 3 3	Brick	Sq	20 10	Carbon	1 2 3	CM	-*
Mazrea et al. (2016)	S-2B-L S-2B-F R-2B-L R-2B-F	2 2 2 2	Brick	Sq Rect	12	Basalt	2	LM	18
Witzany and Zigler (2016)	CB_CFRCM_W CB_CFRCM_S	1 1	Brick	Sq	20	Carbon	1	CM	10
Fossetti and Minafò (2017)	M1_BF M3_BF	2 2	Brick	Sq	20	Basalt	1	CM	10
Santandrea et al. (2017)	C-B-S C-S-S C-B-R	5 5 5	Brick	Sq	0 20	Basalt Steel Basalt	1	LM	10
Maddaloni et al. (2017)	S_Ggrid S_Bgrid	1 1	Limestone	Sq	20	Glass Basalt	1	LM	15
Sneed et al. (2017)	C-1-6-0 C-1-6-9 C-1-6-38 C-1-12-9	4 3 4 4	Brick	Sq	0 9.5 38.1 9.5	Steel	1	LM	8
Cascardi et al. (2018)	FRCM_M4 FRCM_M7 FRCM_M23	3 3 3	Limestone	Sq	30	Glass	1	LM CM	10
Minafò and La Mendola (2017)	CM8 CM13 CC25	3 3 3	Calcarenite stone	Sq	20	Glass	1	LM CM	10
Ombres and Verre (2018a)	C-12-1-1-0 C-12-2-1-0 C-12-3-1-0	1 1 1	Brick	Sq	20	Steel	1 2 3	LM	-*
Murgo and Mazzotti (2019)	CP_RC170 CP_RV320	2 2	Brick	Sq	20	Carbon Glass	1	LM	7

* Data not available in the reference paper

CM: cement-based mortar; **LM**: lime-based mortar; **Rect**: rectangular; **Sq**: square; **Circ**: circular

Because of the novelty of the strengthening technique and the wide spectrum of FRCM materials (both grouts and grids) available on the market, further studies are needed to better understand the compressive behaviour of columns strengthened by FRCM.

2.6.2 Analytical models

The evaluation of the effectiveness of FRCM-materials in confining masonry columns, through the use of validated theoretical formulations for the prediction of the strength increase and the stress-strain law in compression constitutes a key factor.

Relationships used for FRP-confined columns are not always adequate to predict the compressive strength when the confinement is achieved by FRCM systems. As a matter of fact, the confining action due to FRPs strongly depends on the quality of the fibres, while the mechanical parameters of the polymer matrix are not influential. On the other hand, the efficiency of FRCM systems proved to be affected by the characteristics of the inorganic matrix, since the cracking development within the matrix may significantly reduce the stress transfer from the column substrate to the fibre of the jacket, with a consequent reduction of the confining pressure. Then, the mechanical properties of the adopted inorganic matrix significantly affect the effectiveness of the whole FRCM system. For this reason, the analytical study of the FRCM confinement of masonry column requires specific design equations, with attention to the influence of both the type of fibre and matrix (Cascardi et al 2017b).

A review of the state of the art pointed out that no design indications are now available for such strengthening technique, for both concrete and masonry elements. However, some authors made the effort to define analytical formulations in order to evaluate the strength increase due to confinement of columns by FRCM systems and to characterize the behaviour in compression of these elements.

Cascardi et al. (2017a)

Cascardi et al (2017a) proposed an Analysis-Oriented Model (AOM) for the definition of the axial stress-strain law of axially loaded FRCM-confined

columns made of concrete or masonry and having circular or square cross-section. The model is based on a step-by-step iteration of the axial strain, with the hypothesis that within the single step the column behaves elastically and the FRCM jacket remains uncracked. The non-linear behaviour of the column is taken into account by introducing a damage index able to consider the decay of mechanical properties of the column. Moreover, a damage index is also adopted for the FRCM jacketing to model the damage evolution of the strengthening system with the increase of the axial load. The formulations adopted in the proposed model are those commonly used for classical FRP modelling, but they are applied following an iterative procedure.

The analysis begins with an input phase (k=0) including the definition of the properties of unconfined column and FRCM system. Initial information about the column includes the definition of the geometrical parameter D_0, the elastic modulus E_{m0}, the Poisson coefficient v_0 and the values of the compressive strength f_{m0} and corresponding strain ε_{m0}. Regarding the FRCM, the jacket thickness t_f as geometrical parameter is required; moreover, it is needed to define the whole stress-strain response of FRCM under tension, in terms of tangent modulus and ultimate strain relative to each stage of the constitutive law (E_I and ε_I, E_{II} and ε_{II} for stage I and II respectively).

The calculation starts by imposing a longitudinal deformation ε_a to the FRCM reinforced column, with a consequent lateral dilatation ε_h.

The evaluation of the Poisson's ratio v_{mc} of the confined column depending on the lateral pressure is defined through the expression:

$$\frac{\upsilon_{mc,k}}{\upsilon_{m0}} = 1 + \frac{\varepsilon_{a,k}}{\varepsilon_{mc,k}} \left(0.719 + 1.914 \frac{f_{l,k}}{f_{m0}} \right) \tag{2.28}$$

being v_{m0} the Poisson's coefficient of the unconfined column, ε_{mc} the compressive strain related to the compressive strength of the FRCM-confined column, f_l the confinement pressure provided by the FRCM system. At step k=0 the lateral pressure is considered null and the value ν_0 equal to 0.2 is adopted.

Once the Poisson's ratio defined, the lateral strain and the confinement pressure can be evaluated as:

$$\left| \varepsilon_{h,k} \right| = \left| \upsilon_{mc,k} \cdot \varepsilon_{a,k} \right| \tag{2.29}$$

$$f_{l,k} = \frac{2 \cdot E_{f,k} \cdot \varepsilon_{h,k} \cdot t_f}{D_k} \tag{2.30}$$

being E_f the longitudinal elastic modulus of the FRCM system and D the diameter or the diagonal of the column for circular and square cross-section respectively.

The compressive strength increase and the corresponding strain are calculated using the expressions:

$$f_{mc,k} = f_{m0} + 6.7 \cdot f_{l,k}^{0.587} \tag{2.31}$$

$$\varepsilon_{mc,k} = \varepsilon_{m0} \left[1 + \left(\frac{f_{l,k}}{f_{m0}} \right)^{0.5} \right] \tag{2.32}$$

The constitutive law in compression of FRCM-confined column is defined by adopting the Popovics's curve:

$$\frac{f_{m,k}}{f_{mc,k}} = \frac{x \cdot r}{r - 1 + x^r} \tag{2.33}$$

$$\text{where} \quad x = \frac{\varepsilon_{a,k}}{\varepsilon_{mc,k}}; \quad r = \frac{E_{m0}}{E_{m0} - E_{mcs,k}}; \quad E_{ccs,k} = \frac{f_{cc,k}}{\varepsilon_{cc,k}} \tag{2.34}$$

being f_{mc} the compressive strength of the FRCM-confined column, E_{m0} the Young's modulus of the unconfined column, E_{mcs} the secant modulus of the confined column.

The calculation phase finishes with the check of the failure criterion, which can stop the procedure or conduct to the upgrading phase and to a new iteration (k+1). In particular, the failure criterion is defined as the attainment of the 85% of the ultimate strain of FRCM system. The cross-section expansion is taken into account by the following expression:

$$D_k = D_0 \sqrt{\frac{1}{1 - \varepsilon_{a,k}}} \tag{2.35}$$

Cascardi et al. (2017b)

A new Design-Oriented-Model (DOM) aimed at evaluating the strength increase due to masonry confinement by using FRCM system was presented by Cascardi et al. (2017b). The authors performed a multiple linear regression analysis in order to evaluate the influence of the fibres-matrix properties interaction on the effectiveness of the confining pressure. It was shown that the properties of the matrix play a key role in the FRCM-confining of masonry columns. Hence the need to take into account the characteristics of the mortar besides those of the fibres in the definition analytical formulations.

The following expressions are proposed for the evaluation of the strength of masonry columns reinforced with FRCM systems, through the definition of the lateral confinement pressure:

$$f_{mc} = f_{m0}\left[1 + k_1\left(\frac{f_l}{f_{m0}}\right)^{0.5}\right] \tag{2.36}$$

$$f_l = \frac{n \cdot t_f \cdot E_f \cdot \varepsilon_{fu}}{D}; \quad k_1 = 6\rho_{mat}\frac{f_{c,mat}}{f_{m0}}; \quad \rho_{mat} = \frac{4 \cdot t_{mat}}{D} \tag{2.37}$$

where f_{mc} and f_{m0} are respectively the strength of confined and unconfined masonry, f_l is the lateral pressure. The terms t_f, E_f and ε_{fu} represent the thickness, Young's modulus and ultimate strain of the textile respectively, while n is the number of reinforcing layers. The characteristics of the matrix are taken into account through $f_{c,mat}$ and t_{mat}, which represent respectively the compressive strength and the thickness of the adopted mortar. The term D refers to the diameter of the circular cross-section or the diagonal of the square/rectangular cross-section of the column.

Balsamo et al. (2018)

An analytical study for calibrating design formulations about masonry columns confined by FRCM was carried out by Balsamo et al. (2018), taking into account experimental compressive tests available in the literature.

The proposed design-oriented-model (DOM) is based on the proposal of the Italian CNR-DT 200/2013 code for the FRP confinement of masonry columns.

The axial strength of the FRCM-confined column f_{mc} is defined depending on the compressive strength of unconfined masonry f_{m0} and the effective confinement pressure f'_l:

$$f_{mc} = f_{m0}\left[1 + k_1\left(\frac{f'_l}{f_{m0}}\right)^{\alpha_1}\right] \tag{2.38}$$

The term k_1 is a dimensionless coefficient and α_1 is an exponent assumed equal to 0.5. The value of k_1 depends on the mass density g_m (expressed in kg/m^3) of unconfined masonry:

$$k_1 = \alpha_2\left(\frac{g_m}{1000}\right)^{\alpha^3} \tag{2.39}$$

where α_2 and α_3 are coefficients that can be assumed equal to 1 when experimental data are not available.

The effective confinement pressure is determined on the base of the geometrical and mechanical characteristics of the unconfined column and those of the FRCM system, including fibres and mortar:

$$f'_l = k_e \cdot k_{mat} \cdot f_l \tag{2.40}$$

$$f_l = \frac{2 \cdot n \cdot t_f \cdot E_f \cdot \varepsilon_{fu}}{D} \tag{2.41}$$

$$k_{mat} = \alpha_4\left(\rho_{mat}\frac{f_{c,mat}}{f_{m0}}\right)^2 \tag{2.42}$$

$$\rho_{mat} = \frac{4 \cdot t_{mat}}{D} \tag{2.43}$$

where k_{mat} is the "*matrix effectiveness coefficient*", a dimensionless coefficient introduced in order to evaluate the effectiveness of the FRCM confinement based on the performance of the mortar matrix, and k_e is the "*horizontal effectiveness coefficient*", namely the cross-section shape factor (CNR-DT 200/2013). The other terms have the meaning introduced above, while the value of 1.81 can be assigned to the parameter α_4.

The accuracy of the proposed equations in predicting the compressive axial strength of FRCM-confined masonry columns was evaluated by experimental results comparison. The study underlined the validity of the proposed formulations, confirming the importance of taking into account the matrix contribute for the definition of proper design formula.

2.7 FRCM tensile characterization

Materials need to be tested in order to find parameters able to describe their behaviour under different load conditions. Tensile tests on composite materials have the aim to understand the response of these strengthening systems in tension and to find the values necessary for design.

There are some structural applications in which the tensile behaviour of the externally bonded strengthening systems plays a particularly important role and the maximum attainable stress can be fully exploited. The identification of the ultimate tensile strength may be decisive for those applications in which the tensile failure of the textile may occur, such as the confinement of masonry columns.

In FRPs, the matrix offers a more ductile behaviour than fibres and, due to this reason, the organic composites follow the fibres behaviour with an elastic trend up to the point of failure. The tensile behaviour of cement-based composites is different from that of polymeric matrices due to the brittleness of the inorganic matrix, which presents an ultimate strain in tension considerably smaller than that of the fibres. Because of the more complex and variable mechanical behaviour than the one observed for the FRP systems, FRCM composites require appropriate tensile characterization. Here the main aspects concerning the tensile characterization of FRCM composites are discussed.

The behaviour of FRCM strengthening systems depends on several parameters and nowadays, with the only exception of the US documents AC434 (2013) and ACI 549.4R-13 (2013), there are no normalized testing methods and design procedures regarding these systems. In Europe, international scientific committees, such as the RILEM TC 250-CSM, and standardization boards have been activated to achieve a better knowledge and develop guidelines (Ascione et al. 2015, De Santis et al. 2017a).

In order to characterize FRCMs, tensile tests play a key role and in the last decades many experimental studies have been carried out with the aim of better investigate on the tensile behaviour of this system (Bilotta et al. 2017a, Caggegi et al. 2017b, D'Antino and Papanicolaou 2017, Donnini and Corinaldesi 2017, Lignola et al. 2017, De Santis et al. 2017b). Cement-reinforced composites show a complex mechanical behaviour in tension, which is affected not only by the properties of the fabric and the matrix but also by the bond strength at the interface between these two components. The grid-matrix interaction has a fundamental role in the performance of this strengthening technique and represents the central issue of many investigations (Dalalbashi et al. 2018a, Dalalbashi et al. 2018b, Donnini et al. 2018, Bellini et al. 2019). Furthermore, the effectiveness of FRCM systems is strongly related to the bond developed at the interface between the inorganic matrix and the substrate; for this reason recently researchers have analyzed in deep the bond behaviour of different mortar-based systems along the substrate (De Felice et al. 2014, Alecci et al. 2015, Roscini et al. 2016, Olivito et al 2016, Carozzi et al. 2017, Ceroni and Salzano 2018, De Felice et al. 2018, Ombres et al. 2018b).

The large number of available textiles and mortars result in a wide variability in terms of mechanical behaviour, tensile strength capacity, bond performance with the substrate and expected failure modes (Ascione et al. 2015). Composite materials made with different types of fibres, especially glass fibres (Carozzi and Poggi 2015, Codispoti et al. 2015, De Santis and De Felice 2015b, Bilotta et al. 2017a, Leone et al. 2017a, Leone et al. 2017b, Donnini et al. 2019), carbon fibres (De Felice et al. 2014, Carozzi et al. 2017, Ombres et al. 2018b, Garbin et al. 2018) and aramid fibres (De Santis and De Felice 2015b, Caggegi et al. 2017b) have been investigated. In order to reduce the cost of carbon and glass fibres, the use of new types of fibres, such as high strength steel cords, has been explored (Ghiassi et al. 2016b, De Santis et al. 2017b, Santandrea et al. 2019). Moreover, the growing concern regarding the sustainability increased the interest towards products based on materials with low environmental impact. In the field of civil structures, some efforts have been done to replace the most common composites by materials less harmful to the environment, as natural fibres (Cevallos and Olivito 2015, Ghiassi et al. 2016a, Mercedes et al. 2018) or basalt fibres (Larrinaga et al. 2014, De Felice et al. 2014, Bilotta et al. 2017b, D'Antino and Papanicolaou 2017, Caggegi et al. 2017a, Tekieli et al. 2017, D'Antino and Papanicolaou 2018, Iorfida et al. 2017).

Literature shows as the most common failure of FRCM system under loading is by slippage of fibres inside the matrix (Carozzi and Poggi 2015). This failure mode is different compared to the cohesive failure frequently recorded in FRP strengthening systems. Since the inorganic matrix is not able to fully impregnate the yarns, the adhesion between mortar and textile is not as strong as in FRPs. The fibre yarns can be modeled as having a sleeve and a core and it is important to investigate on both the adhesive bond between external fibres of the yarn and mortar and the frictional bond among the internal fibres within the yarn (Arboleda et al. 2015). Slippage at the matrix-fibre interface is due to incomplete impregnation of texture, debonding or chemical incompatibility, while slippage among fibres in the yarn is caused by the so called *telescopic failure.* The external fibres in yarn are in direct contact with the matrix and are then closely bonded, while the internal fibres in the core of the yarn can slip more easily because of the low friction between the fibres (Larrinaga et al. 2014). During debonding failure at the matrix-fibre interface, the external filaments fracture while the internal ones, not in direct contact with the matrix, slip without any apparent damage (Arboleda et al. 2015, Carozzi and Poggi 2015). The telescopic failure mode is influenced by different factors, such us the cement penetrability, the textile geometry, the friction level among the fibres in each yarn and the presence of coating. Experimental studies pointed out as a polymer coating treatment on the textile roving can improve the adhesion strength between textile and mortar (D'Antino and Papanicolaou 2017, Mercedes et al 2018), with resulting increase of ultimate strength of the FRCM system.

The mechanical properties derived from separate tests on fibres and matrix cannot be directly employed to obtain the mechanical properties of the composite material, due to the fundamental role played by the interaction between the two materials. Nevertheless, usually tensile and bond tests on FRCM composites are accompanied by tests carried out on composite components, i.e. mortar (Carozzi and Poggi 2015, De Santis and De Felice 2015a, Codispoti et al. 2015) and textiles (De Felice et al. 2014, Larrinaga et al. 2014, Carozzi and Poggi 2015, Alecci et al. 2015, Roscini et al. 2016, Codispoti et al. 2015), in order to investigate the contribution provided by the two components.

Different setups for tensile testing of composite materials comprising fibre textiles and inorganic matrices have been proposed in the literature (De Santis and de Felice 2015a, Carozzi and Poggi 2015, Arboleda et al. 2015, De Santis et

al. 2018, D'Antino and Papanicolaou 2018). The tensile behaviour of FRCM materials is influenced by several factors, including the specimen geometry and fabrication, the strain measurement technique and the load transfer mechanism (grip method). In particular, the clamping method plays a fundamental role in achieving a uniform load distribution and may significantly influence the stress-strain response of composite specimens (De Santis and De Felice 2015a, Carozzi and Poggi 2015, D'Antino and Papanicolaou 2017, Arboleda et al. 2015). The US standard (AC434, 2013) suggests to use the *clevis-type* gripping mechanism, in which the load is transferred from the testing machine to the mortar by shear adhesion, using two metal plates glued at each end of the specimen and connected with a transversal pin outside of the length of the sample. This system is connected with a clevis joint to the testing frame. This clamping solution reduces parasitic bending moments and failure is expected to occur by textile slipping within the matrix. An alternative type of gripping mechanism is the *clamping grip* method, which uses friction for the load application realized by applying a compressive force normal to the plane of the specimen at his ends. This solution improves the stress-transfer mechanism between fibres and matrix, preventing fibres slippage (Arboleda et al. 2015, D'Antino and Papanicolaou 2017).

Depending on the type of gripping mechanism adopted, but also on the characteristics of the composite material, there are two constitutive laws that can describe the idealized behaviour of FRCM composites in tension (Arboleda et al. 2015). If a good bond between fibres and matrix can be assumed, the material behaves following a trilinear stress-strain response (Figure 2.9) characterized by a first elastic uncracked branch, a second branch characterized by several jumps associated to cracking of the cementitious matrix and a last linear branch up to failure of the textile reinforcement (Figure 2.9a). This behaviour is typical of a specimen tested employing the clamping grip method. On the other hand, the presence of a certain grade of slippage between fabric and mortar makes it impossible to reach the textile rupture and the stress-strain FRCM response can be idealized by a bilinear behaviour (Figure 2.9b). This response is typical of composite materials tested by using the clevis-type gripping mechanism. The two models are not in contradiction, but are strictly related to the grip method adopted to test the material.

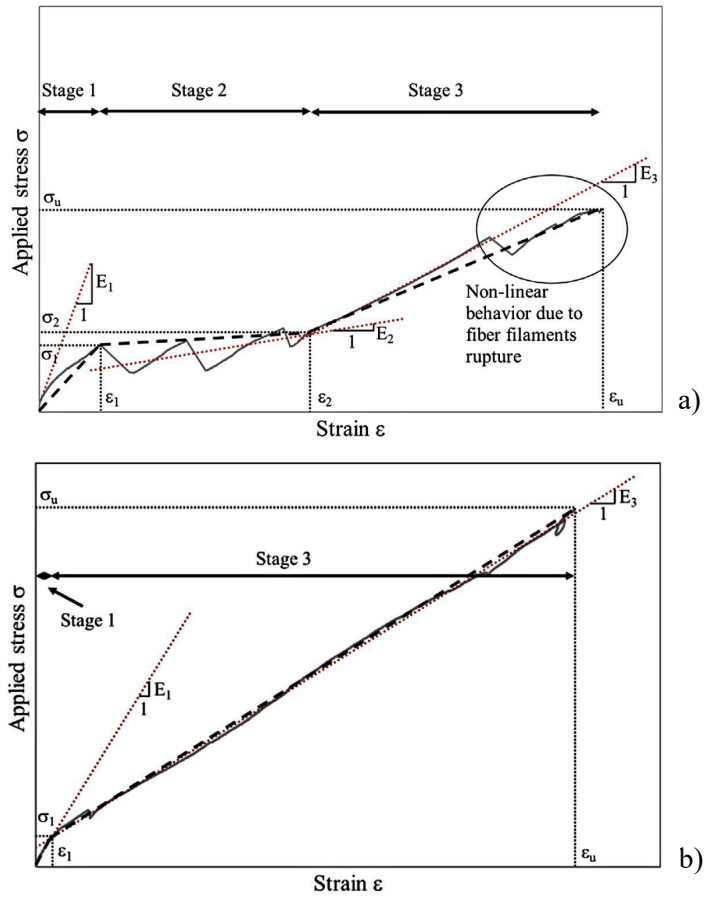

Figure 2.9 Tensile behaviour of FRCM composite (D'Antino and Papanicolaou 2017): a) trilinear stress-strain response; b) bilinear stress-strain response

The behaviour of such heterogeneous systems like FRCM material needs to be investigated with adequate monitoring techniques. In most experimental tests available in the literature, traditional systems, i.e. displacement transducers and strain gauges, allowed acquiring experimental data in terms of displacement and local strains. However, it is worth to note as the traditional monitoring systems showed to be not always adequate for FRCM materials: the strain gauges are able to measure only local values, while the reliability of displacement measures obtained from the use of transducers is strongly related to the choice of their position that depends on the cracking pattern, unknown before the test (De Santis et al. 2017a). For these reasons, in some cases traditional acquirement systems

were complemented or substituted by innovative monitoring techniques such as Digital Image Correlation (DIC), useful to investigate the mechanical behaviour of the FRCM systems, both in the case of tensile and bond tests (Bilotta et al. 2017a, Bilotta et al. 2017b Caggegi et al. 2017a, Tekieli et al. 2017, D'Antino and Papanicolaou 2018, Donnini et al. 2019).

The volume fraction of fibres represents a significant parameter and affects the tensile behaviour of FRCM composite materials. The effect of reinforcement ratio was analyzed in some studies (Larrinaga et al. 2014, Cevallos and Olivito 2015, Arboleda et al. 2015, Caggegi et al. 2017a). All the works showed that the increase of the reinforcement ratio affects many factors, such as strength, Young's modulus, failure more and crack pattern of tested FRCM specimens. In particular, it was shown that the number of cracks is larger for composite specimens with more multiple layers and, in this case, the crack development stage of the composite constitutive law is concentrated in a shorter interval of strain.

On the base of the discussion presented above, it is clear that a large number of parameters can affect the tensile behaviour of inorganic-matrix composites. Despite the outcomes achieved so far allow a better understanding of the role of different parameters on the tensile response of these systems, further investigations are needed in order to define an appropriate qualification procedure.

3. EXPERIMENTAL PROGRAMME

3.1 Introduction

The literature review presented in the previous chapter highlights that few research works were developed on the use of basalt fibres for confinement applications on masonry members. Then, it is not possible to formulate general conclusions about the employment of basalt fabric composites as an alternative to the application of carbon or glass fibres for the confinement of masonry. Additionally, literature studies reveal that the use of FRCM materials can be considered a real alternative to the use of FRPs, but the experimental comparative studies adopting the same fibre fabric are very limited in number and a direct comparison between BFRP and BFRCM performance is still missing.

In this context, this chapter presents an experimental programme, which aims to compare the structural performance of composite materials based on basalt fibre fabric for the confinement of masonry members. The same basalt textile is adopted combined with organic (BFRP) or inorganic (BFRCM) matrix, in order to evaluate the performance of both types of composite as confinement system of clay brick masonry cylinders.

The details of the performed investigation in terms of employed materials, manufacturing procedures and test methods are here discussed in deep, while the experimental results will be presented in the next chapter. In particular, the chapter addresses the mechanical characterization of constituent materials of the masonry and the used strengthening systems, with great attention to the tensile characterization of the basalt textile grid used as reinforcement. Given the more complex mechanical response compared to that exhibited by FRPs, an in-depth investigation on the tensile behaviour of BFRCM system is presented, involving the analysis of the influence of different reinforcement ratios. The procedures followed for making up and for testing the masonry cylinders are also discussed.

Additionally, the chapter involves a wide discussion on the Digital Image Correlation (DIC) technique that is here employed as innovative measuring method.

All the tests were carried out at the Heavy Structure Laboratory of the Queen's University of Belfast (UK).

3.2 Experimental programme

Aiming to evaluate the efficiency of composite materials with basalt fabric for confinement applications on masonry members, a total of twenty-six clay brick masonry cylinders were assembled and tested under uniaxial monotonic compression. The specimens included unconfined cylinders, adopted as control samples, and cylinders confined by BFRP or by BFRCM.

The specimens were arranged considering two different assembly schemes (Figure 3.1) in order to investigate on the effects of the number of vertical mortar joints.

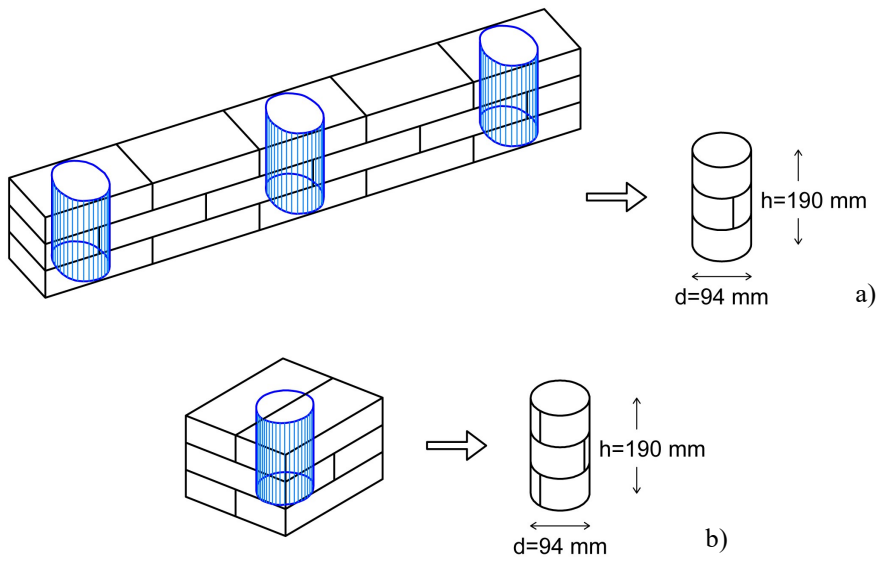

Figure 3.1 Brick assembly schemes for preparing cylinders: a) Scheme I (wall); b) Scheme II (column)

Fifteen cylinders were assembled with one vertical mortar joint (Scheme I, Figure 3.1a), including: - four unconfined specimens, - four BFRP-reinforced cylinders, of which two wrapped using one BFRP layer and two confined with two layers; - seven BFRCM-reinforced cylinders, of which four wrapped with one layer and three with two layers. The other scheme (Scheme II, Figure 3.1b) included eleven specimens with three vertical joints, subdivided in: - two unconfined cylinders; - four FRP-confined cylinders, of which two wrapped employing one basalt grid layer and two using two layers; - five BFRCM-strengthened cylinders, three reinforced by using one layer of fabric, two using two layers.

The identification of unreinforced and reinforced specimens is presented in Table 3.1.

Specimens were named following the designation CNX_YZL, where C means "cylinder", N is used to number specimens of the same typology, X indicates the matrix used for wrapping the cylinders (R for resin, M for mortar), Y is used to designate the assembly scheme (W for cylinders obtained from walls, Scheme I; C for cylinders obtained from columns, Scheme II), Z indicates the number of layers used for confining the cylinder (1 for one-layer wrapped cylinders, 2 for two-layer wrapped cylinders), L means "layer". In the case of unconfined cylinders, the last two letters are replaced by the designation "Un" (unconfined).

3.3 Investigated variables and assumptions

It is reminded that several parameters can influence the compressive behaviour of confined masonry. In the framework of the current investigation, focus was made on the role of the following key variables: kind of matrix adopted in the external wrap (i.e. organic or inorganic matrix), number of fibre fabric layers, number of vertical mortar joints in the masonry (i.e. grade of unconfined masonry). As a consequence, the number of performed tests was calibrated to cover the investigated variables. In this context, it should be also considered that six specimens were planned to be tested for each investigated typology (Table 3.1), but some cylinders were damaged during the coring or the preparation operations. For this reason, the number of tested specimens was limited to twenty-six.

Table 3.1: Test specimens

	Specimen designation	Brick layup scheme	Number of vertical joints	Number of specimens	Number of basalt grid layers
Unconfined	C1_WUn	Scheme I	1	4	None
	C2_WUn				
	C3_WUn				
	C4_WUn				
	C1_CUn	Scheme II	3	2	
	C2_CUn				
FRP	C1R_W1L	Scheme I	1	2	1
	C2R_W1L				
	C1R_W2L			2	2
	C2R_W2L				
	C1R_C1L	Scheme II	3	2	1
	C2R_C1L				
	C1R_C2L			2	2
	C2R_C2L				
FRCM	C1M_W1L	Scheme I	1	4	1
	C2M_W1L				
	C3M_W1L				
	C4M_W1L				
	C1M_W2L			3	2
	C2M_W2L				
	C3M_W2L				
	C1M_C1L	Scheme II	3	3	1
	C2M_C1L				
	C3M_C1L				
	C1M_C2L			2	2
	C2M_C2L				

In addition, some assumptions were made on the shape and on the scale of tested samples, and their role on the obtained results need to be clarified.

In particular, it should be noted that the circular section of masonry specimens was chosen in the current investigation in order to study the effect of pure confinement. In fact, the absence of corners in the section allows avoiding stress concentration in the external wrap and, consequently, the strengthening system

can reach theoretically its maximum stress in a uniform manner. Additionally, the confinement pressure in circular sections is not affected by the geometric efficiency coefficient (see Chapter 2, Section 2.4). In this way, the obtained experimental data can be compared with theoretical predictions avoiding to make assumptions on the calculation of the effectively confined area of the transverse cross-section. By contrast, the obtained strength increase can be considered as an upper bound of the confinement effect for real case studies, and consequently, further research works need to be addressed on the evaluation of BFRP and BFRCM confinement on masonry columns with polygonal sections.

It is also reminded that the adoption of small scale specimens was due to the fact that the coring of masonry was the more precise and practical way for obtaining cylindrical specimens. Additionally, the reduced bearing capacity of the testing machine did not allow making up bigger specimens and, consequently, obtained results could be affected by scale effect. Future efforts should be made for extending the current investigation to full-scale masonry columns.

3.4 Materials

In this section, the materials adopted in the current investigation are presented, making difference between the components of the assembled masonry and those of the adopted composite materials. The main features are presented, including the main physical and mechanical properties.

3.4.1 Masonry components

Brick units

Pressed bricks with nominal dimensions 50x100x210 mm were used for assembling walls and columns from which the cylinders were cored.

Mortar for masonry

The mortar used for assembling walls and columns was composed of cement and sand with a weight ratio of 1/5. Water was added until the minimum workability was achieved.

3.4.2 Components of composite materials

Basalt textile grid

The textile used as internal reinforcement of the composite consisted of a primed alkali-resistant basalt fibre bidirectional grid. The longitudinal and transversal rovings of the mesh were woven and fixed at their intersection with nylon fibres. According to the technical sheet, the textile had a nominal cell size of 6x6 mm (Figure 3.2), unit weight equal to 250 g/m^2 and the density of the fibre was 2.75 g/cm^3. The equivalent thickness was 0.039 mm and the nominal values of tensile strength, ultimate strain and Young's modulus provided by the manufacturer were f_{fu} = 60 kN/m, ε_u = 1.8%, E_f = 89 GPa respectively. The mechanical properties of the grid provided by the manufacturer are summarized in Table 3.2.

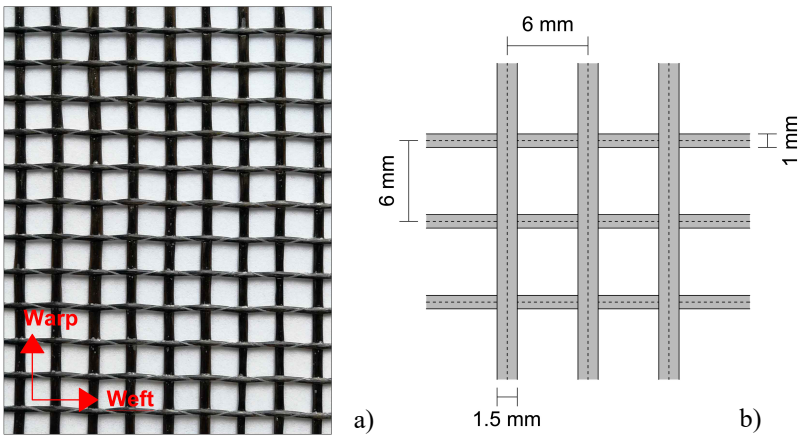

Figure 3.2 Basalt textile: a) representation of basalt grid; b) geometry of basalt grid

Table 3.2: Mechanical properties of basalt grid (manufacturer data)

Material	Unit weight	Mesh size	Density	Tensile strength	Elastic modulus	Equivalent thickness	Elongation at failure
BFRP grid	250 g/m^2	6 x 6 mm	2.75 g/cm^3	60 kN/m	89 GPa	0.039 mm	1.8%

Mortar for BFRCM jacket

A two-component premixed cement-based mortar, made of hydraulic natural lime, sand, special additives, polymers and short glass fibres spread in the matrix, was used as matrix for the BFRCM material. According to the mechanical characteristics provided by the manufacturer, the mortar had flexural strength equal to 8 MPa, compressive strength of 25 MPa and Young's modulus equal to 10 GPa.

Epoxy resin for BFRP jacket

A two-component epoxy resin based product with selected fine graded aggregates and special additives was employed as matrix for the BFRP system. In accordance with the datasheet provided by the manufacturer, the product had a tensile strength of 40 MPa and Young's modulus equal to 2.6 GPa.

3.5 The Digital Image Correlation (DIC)

The Digital Image Correlation (DIC) is an innovative non-contact optical technique that has become widely accepted and commonly used as a powerful and flexible tool for the full-field surface deformation measurement of any type of object. Due to its several advantages with respect to traditional measurement systems, it was employed in the current experimental investigation.

In this section, the basic principles of DIC technique and advantages offered by this method are presented. Moreover, the software employed for the elaboration of the data acquired during tests is presented.

3.5.1 Basic principles of Digital Image Correlation (DIC)

Developed by a group of researchers at the University of South Carolina in the 1980s, during the past few years the DIC method has been largely investigated and improved in order to achieve high accuracy deformation measurement and reduce the computational complexity (Yoneyama and Murasawa 2009). Nowadays, many applications of this method to various fields can be found, thanks to the ability of DIC to provide a "box-seat" to the events that occur during deformation.

The DIC technique is based on recording digital images of a specimen surface before and after deformation caused by an applied load. The DIC estimates the displacement of each image point by comparing the images of the object surface in different states.

The DIC can be applied indifferently to classical 2D or volumetric (3D) images, but in the context of the experimental study presented in this thesis, only two-dimensional DIC (2D DIC) is used. Being an efficient method for quantitative in-plane deformation measurement of a planar object surface, 2D-DIC is widely accepted and commonly used within the field of experimental mechanics (Pan et al. 2009).

In general, the application of the DIC method involves three main steps (Pan et al. 2009): specimen preparation; recording a series of images of the specimen surface before and after the load application; elaboration of the acquired images in order to obtain displacement and strain information.

Specimen preparation consists in painting the specimen surface with a random speckle pattern with the aim of guaranteeing a random grey intensity distribution that deforms along with the surface of the sample. The presence of random speckle pattern is a basic requirement for DIC analyses in order to obtain a unique solution in the correlation process (Caporossi et al. 2018). This can be achieved by spraying the object with white and black paints or using other techniques; sometimes, the speckle pattern can be the natural texture of the specimen surface.

In two-dimensional DIC, displacements are directly detected from digital images of the surface of an object. Images can be obtained from a wide variety of sources including conventional CCD or consumer digital cameras, high-speed video, macroscopes and microscopes, including scanning electron and atomic force microscopes (McCormick and Lord 2010). Figure 3.3 shows a typical example of an experimental setup for two-dimensional DIC.

The images of the surface of the object, one before and others after deformation, are recorded, digitized and stored in a computer as digital images. Later, these images are compared to detect displacements by searching a matched point from one image to another.

The input data of the analysis are positive integers, called grey levels, of the image at the first configuration, called "reference image", and those of the second

configuration, named “deformed image”. These two images can be extracted from a temporal sequence comprising a large number of images, of which any image can be selected as the reference image or the deformed image (Grédiac and Hild 2012).

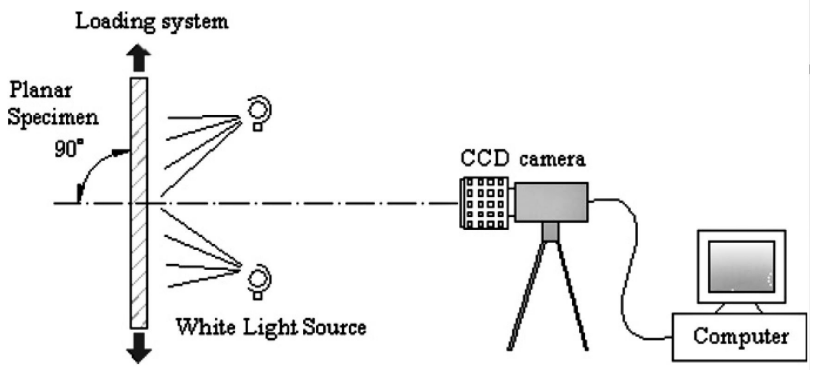

Figure 3.3 Setup for displacement measurement using DIC (Pan et al. 2009)

In the classic DIC method, the elaboration of the acquired images starts with the detection of the Region Of Interest “ROI”. The ROI represents an area of the picture selected by the operator and it covers only the part of the object to be correlated. Therefore, the ROI constitutes the analysis area, on the surface of the object, in which the correlation algorithm operates (Caparossi et al. 2018)

This domain is then divided into subsets (Zones Of Interest “ZOI”) and a mathematical correlation is performed between a pair of images that were taken before and after a given deformation of the object, to track the centre point of each subset and estimate his displacement vector (Xavier et al. 2012). A schematic illustration is given in Figure 3.4.

In order to evaluate the displacements of point $P(x_0, y_0)$, a square reference subset of $(2M+1)\cdot(2M+1)$ pixels centered at point P in the reference image is identified and used to track its corresponding location in the deformed image (Pan et al. 2009). M indicates the number of whole pixels from the center to edge of the subset.

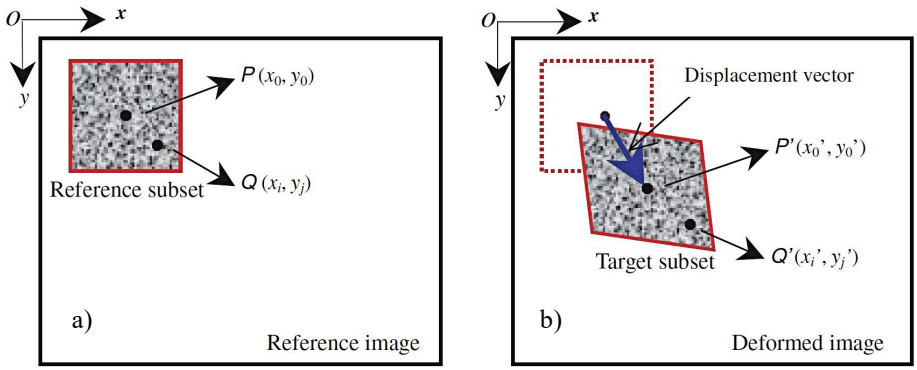

Figure 3.4 Schematic illustration of subset matching: a) square reference subset; b) deformed subset after deformation (Pan et al. 2009)

The position of point P in the deformed image, namely $P'(x_0', y_0')$, is impossible to determine by comparing single pixels, as many pixels of the deformed image may have the same grey level pixel value. Therefore, the consistency between the points P and P' is accomplished by considering a pixel and its neighbourhood in the reference image and searching for the same subset in the deformed image (Figure 3.4b) (Caporossi et al. 2018). Selecting a square subset instead of an individual pixel guarantees a wider variation in grey levels and allows the subset to be distinguished from other subsets, resulting uniquely identified in the deformed image. The identification of the subset comes from the assumption that the grey levels distribution does not change during deformation (Yoneyama and Murasawa 2009).

Therefore, the choice of the subset size is of fundamental importance. The optimum subset size should not be too small and it is influenced by the granularity of the speckle pattern. On the other hand, a too large subset is not suitable to describe large heterogeneous deformations and could affect the DIC accuracy (Lava et al. 2010). In general, the size of the subset should be at least equal to the dimension of the largest spot of the speckle pattern.

Another important parameter that needs to be selected attentively is the step size, which is defined as the shift of the subset during the correlation process (Caporossi et al. 2018). Setting the step size, the measurement point density within the surface is influenced. In particular, the smaller the step size the larger

the measurement point density. For a higher spatial resolution, the subset shift should be decreased (GOM Testing 2016).

The DIC algorithm looks for the deformed subset that best matches the undeformed one. The equivalence degree between the reference subset (undeformed image) and the deformed subset (deformed image) is evaluated through a correlation criterion that, in general, can be a Cross-Correlation criterion (CC) (Eq. 3.1) or a Sum-Squared Difference criterion (SSD) (Eq. 3.2) (Pan et al. 2009):

$$C_{CC} = \sum_{i=M}^{M} \sum_{j=-M}^{M} \left[f(x_i, y_j) g(x_i', y_j') \right] \tag{3.1}$$

$$C_{SSD} = \sum_{i=M}^{M} \sum_{j=-M}^{M} \left[f(x_i, y_j) - g(x_i', y_j') \right]^2 \tag{3.2}$$

where $f(x_i, y_j)$ and $g(x_i', y_j')$ represent the grey levels within the subset of undeformed and deformed images respectively, while (x_i, y_j) and (x_i', y_j') are the coordinates of a subset point, before and after deformation. The symbol of the summation indicates the sum of the values within the subset.

The calculation of the correlation between the undeformed subset and all possible deformed subsets generates a discrete correlation surface (Figure 3.5): the maximum point of the correlation surface gives the position of the center of the deformed subset in the deformed image that best matches the undeformed subset. The difference in the position between the reference subset center and the target subset center defines the in-plane displacement vector at point *P* (Figure 3.4) (Chakinala 2013).

Because of the assumption of deformation continuity of a deformed solid object, neighbouring points in a reference subset remain as neighbouring points in the target subset (Chu et al. 1985, Pan et al. 2009). However, a square patch on the surface of the reference image may no longer be square once the object is deformed. Therefore, the neighbouring points in the reference subset can move by a different amount than the subset center. The coordinates of point $Q(x_i, y_j)$ located around the subset center $P(x_0, y_0)$ in the reference image will be represented by point $Q'(x_i', y_j')$ in the target subset (Figure 3.4) according to the "shape function" or "displacement mapping function" (Lu and Cary 2000):

$$\begin{aligned} x_i^{'} &= x_i + \psi(x_i, y_j) \\ y_j^{'} &= y_i + \phi(x_i, y_j) \end{aligned} \qquad (i, j = -M : M) \tag{3.3}$$

In Eq. (3.3), $\psi(x_i, y_j)$ and $\phi(x_i, y_j)$ refer to the displacement mapping functions in the x and y directions respectively. The displacement mapping functions are used to calculate the displacement of a neighbouring surface point, based on the distance of the point from the center in the reference surface.

The method through which the subset can deform during the correlation process depends on different number of parameters (Caporossi et al. 2018). In the case of a rigid translation of the reference subset, namely when each point of the subset undergoes the same displacement and the relative displacement between points in the target subset is zero (Figure 3.6), then a zero-order displacement mapping function can be used:

$$\begin{aligned} \psi(x_i, y_j) &= u \\ \phi(x_i, y_j) &= v \end{aligned} \tag{3.4}$$

where u and v are the x- and y-directional displacement components of the reference subset center $P(x_0, y_0)$.

It is clear that these functions cannot be used if the subset is subjected to a deformation. When not only translation, but rotation, shear, normal strain and their combination (Pan et al. 2009) are involved in the displacement from the reference subset to the target subset, then the first-order displacement mapping function need to be used. In this case, the general form of an affine transformation is obtained (Caporossi et al. 2018) (Figure 3.6):

$$\begin{aligned} \psi(x_i, y_j) &= u + \frac{\partial u}{\partial x}\Delta x + \frac{\partial u}{\partial y}\Delta y \\ \phi(x_i, y_j) &= v + \frac{\partial v}{\partial x}\Delta x + \frac{\partial v}{\partial y}\Delta y \end{aligned} \tag{3.5}$$

where Δx and Δy are the x- and y-directional components of the distance from the center of the subset to the point (x_i, y_j) respectively, while $\partial u/\partial x$, $\partial u/\partial y$, $\partial v/\partial x$, $\partial v/\partial y$ are the first-order displacement gradients of the reference subset.

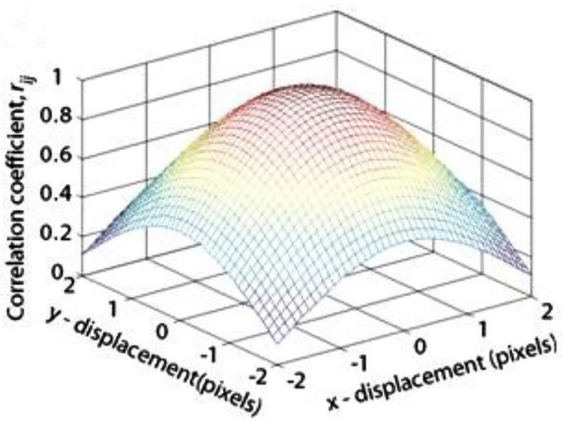

Figure 3.5 Correlation surface (Zucchini 2011)

Higher order shape functions can be used to express more complicated deformation states of the subset. Second-order terms can be included in the shape function to take into account the effects of full bending of the subset (Caporossi et al. 2018) (Figure 3.6).

A surface point that lies at the center of a pixel in the undeformed image may not be exactly in the center of a pixel in the deformed image, but between pixels. In a digital image, grey values exist on discrete pixel points. In order to calculate the correlation on the position among pixel points, the values of grey level among pixel points are required. In this case, before evaluating the match between undeformed and deformed subset employing a correlation criterion (Eqs. 3.1, 3.2), it is essential to know the intensity (value of grey level) of these points having sub-pixel location. Therefore, a sub-pixel interpolation scheme should be used. In literature many sub-pixel interpolation schemes are available, such as bilinear interpolation, bicubic interpolation, bicubic B-spline interpolation (Pan et al. 2009), to mention some of them.

To enhance the accuracy of the DIC method, improving the displacement measurement precision, a more sophisticated algorithm able to compute displacements with resolution better that a pixel is necessary: this is called subpixel DIC algorithm. The sub-pixel algorithm allows overcoming drawbacks related with the spatial resolution, namely the smallest distance between two statically independent measuring points. This issue can be a problem in

applications with discontinuous displacement fields or when high strain gradients are present (Xavier et al. 2012).

In general, to achieve sub-pixel accuracy the implementation of DIC is based on the so called "coarse-fine approach", which involves two steps: pixel-level (coarse) estimation and subpixel-level (fine) estimation of displacement fields (Pan et al. 2009, Xavier et al. 2012). There are some techniques regarding the initial guess of the deformation vector and also, in literature, it is possible to find various sub-pixel registration algorithms.

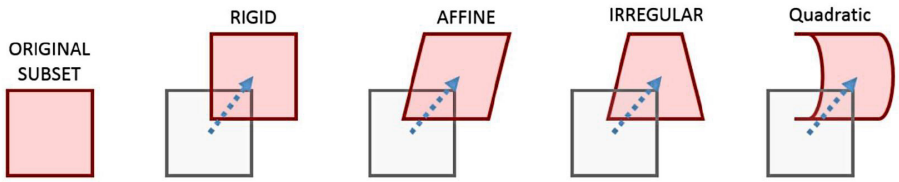

Figure 3.6 Subset transformation typologies (Caporossi et al. 2018)

3.5.2 Advantages of the DIC technique

The DIC technique is simple to use and cost effective compared to other full-field optical techniques for displacement and strain measurements, leading to a huge range of potential applications (Xavier et al. 2012). The main advantages offered by the employing of DIC are reported in the following:

- simplicity of experimental setup: the application of the method only needs the use of a digital camera able to record the images of the surface of the specimen before and after deformation;
- ease of specimen preparation: in some cases the natural surface of the component has sufficient image texture for DIC to work without the need of any special surface preparation. When the surface of the specimen is not adequate to guarantee a correct application of DIC, paint is applied that results in a random speckle pattern;
- low requirements in measurement environment: the use of DIC requires only a white light source to light up the object during testing. Sometimes, the natural light is suitable and additional light sources are not needed;

- full-field deformation analysis: the technique allows obtaining the full displacement and strain field, as the full surface of interest covered by the chromatic texture can be analyzed. This is of high importance in those cases the zone of damage localization is not known a priori and the local measurement devices (i.e. strain gauges, extensometers and so on) are difficult to be poisoned;
- low cost: the application of DIC requires only the availability of a high-resolution camera;
- use at different scales: DIC can be used at different scales of space and time to the extent that it relies on principles applicable to pictures obtained by very different imaging systems.

In the frame of this work, it is believed that the performances of DIC technique are appropriate to analyze the two-dimensional displacement of BFRCM and BFRP-wrapped cylinders subjected to uniaxial compressive tests and the displacement/strain field of BFRCM composite specimens subjected to tensile tests.

3.5.3 Employed software: GOM Correlate

The software GOM Correlate was employed to compute the displacement and strain field upon the surface of the tested samples. GOM Correlate is a DIC evaluation software program used for materials research and component testing. The software works according to the principle of parametric inspection. Each single element keeps its creation sequence within the software structure and the dependency of the elements regarding each other is stored. Therefore, it is possible modifying single elements and, due to the parametric inspection, tracing them back to its creation (GOM Testing 2016).

In GOM Correlate, parameters need to be initialized. In the correlation process, the digital photographs obtained by the camera are matched. The software allows obtaining the displacement/strain field at each loading step by defining square-shaped subzones, called “facets” (ZOIs defined in the previous section), in the initial image and tracking these subzones in subsequent images. The vertical and horizontal displacements related to each facet are evaluated by the algorithm, assuming they are applied at the centre of each square subzone. The definition of these facets is allowed by the presence of a random speckle

pattern on the sample surface, which facilitates the definition of a grey level distribution sufficient to differentiate the subzones. The benefit is the possibility of choosing whatever position and size of the facet within the field of view of the image; moreover, the facet can be tracked in any direction within the plane of the image. This allows, by settling couples of facets, the evaluation of in plane strains over any chosen gauge length and in any direction.

In their original state, facets are square areas in the image. It is possible to adjust the size to each facet in the software. Depending on the measuring tasks and the stochastic pattern, it is possible to increase the accuracy or reduce the computational time by using a different size. It is suitable choosing the facet size as small as possible, but large enough so that the computation of the facet is still possible. A pattern structure with three to four contrast points in one facet has proven to be ideal (GOM Testing 2016).

Besides the evaluation of strains over defined gauge lengths, the software makes it possible to define a "surface component", which is an area of the image representing the specimen surface. The surface component is defined by the operator and constitutes the part of the object to be correlate (ROI defined in the previous section). The definition of the surface component allows the analysis of the full displacement/strain fields of the surface of the specimen.

During the creation of the surface component, the software finds square-shaped facets in the collected images. The software identifies the facets by the stochastic pattern structure, in all the stages. From each valid computed facet, a measurement point is obtained after the computation of the surface component. The software combines all computed measurement points to a surface component and can trace the surface component in every stage.

When a surface component is analyzed, besides the facet size, the distance between the individual facets has to be properly set. The point distance describes the distance between the center points of the adjacent square facets. This setting influences the measurement point density within the surface component. In particular, the measurement point density increases as the point distance decreases (GOM Testing 2016).

In GOM Correlate, the DIC analyses are performed by using adaptive approaches providing the image correlation through the iterative least squares

algorithm (GOM Testing 2016). The main assumption is that a causal connection exists between the original state and the deformed state:

$$f(x,y) \leftrightarrow g(x',y') \tag{3.6}$$

The correlation function provides a rate for the similarity of two signals *f* and *g*:

$$c(u,v) = \frac{\langle f(x,y), g(x+u,y+v) \rangle}{|f(x,y)| \cdot |g(x,y)|} \tag{3.7}$$

where *u* and *v* are the x- and y-directional components of the displacement. Then, the software can determine the correspondence of two subsets of pixels at different examined locations and with different displacements. Different subpixel interpolations, such as bilinear interpolation, bicubic interpolation or spline interpolation provide the corresponding maximum of similarity in the subpixel area.

3.6 Test programme

In addition to tests on masonry cylinders, the experimental programme included the mechanical characterization of the BFRCM system, as well as the characterization of constituent materials of the masonry and the external wrap. Overall, the test schedule was organized as it follows:

- Characterization tests on components
  - Tests on masonry components
    - Three point bending tests on mortar prisms;
    - Compressive tests on clay bricks;
  - Tests on the components of composite materials
    - Tensile tests on basalt fabric strips;
    - Three point bending tests on mortar matrix prisms;
- Tensile tests on BFRCM composite coupons
- Tests on masonry cylinders
  - Compressive tests on unconfined cylinders;
  - Compressive tests on BFRP-confined cylinders;

- Compressive tests on BFRCM-confined cylinders.

3.7 Characterization tests on components: specimens and methods

In the following, the stages for making up the specimens, the test setups and the instrumentations are presented and discussed for the characterization tests on components of the masonry and components of the external strengthening systems.

3.7.1 Compressive tests on brick units

With the aim of characterizing the mechanical behaviour of the clay brick units, six cubes with side equal to 50 mm were cut from bricks and tested under uniaxial compression (Figure 3.7) according to EN 772-1. Before testing, the cubes were capped at both ends to ensure levelled top and bottom faces for uniform load application.

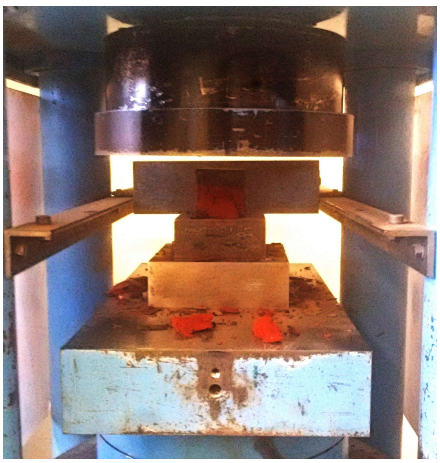

Figure 3.7 Compressive tests on brick cubes

3.7.2 Three point bending tests on mortar prisms

In order to characterize the mechanical properties of the mortar of the masonry, three-point bending tests were carried out on six standard 40x40x160 mm prisms (Figure 3.8a) and uniaxial compressive tests were performed on twelve standard 40 mm cubes (Figure 3.8b), according to EN 1015-11.

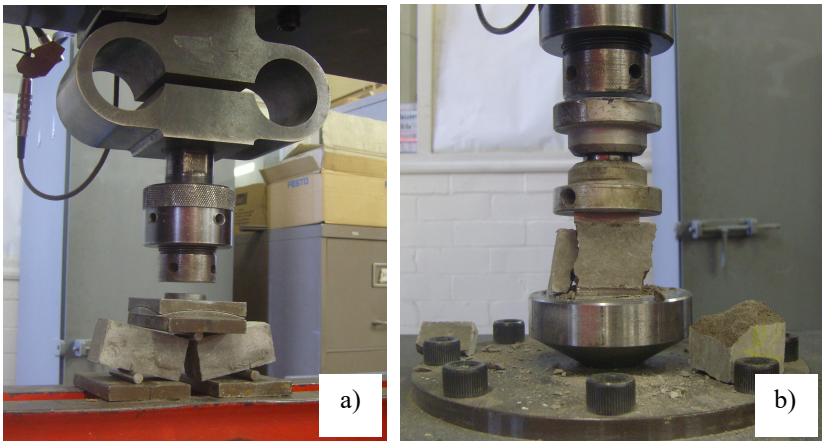

Figure 3.8 Tests on mortar samples: a) three-point bending test; b) compressive test

3.7.3 Tensile tests on basalt fabric strips

A series of monotonic tensile tests on basalt grid strips were carried out in accordance with ISO 13934-1:2013, in order to define the mechanical characteristics of the dry textile.

Among other advice, the code gives some suggestions concerning the clamping device, which is one of the most important aspects for the success of the test, since it influences substantially the results. For this reason, the tests on the basalt fabric were divided into two parts:

- preliminary investigation on the effect of the clamping devices on the tensile behaviour of basalt fabric;
- tensile characterization tests on basalt fabric strips.

Preliminary investigation on the effect of the clamping devices on the tensile behaviour of basalt fabric

The target of the first test stage was to find the most suitable configuration for the characterization tests, aiming to prevent slippage of the specimens at the gripping area. The standard suggests the use of some auxiliary materials in order to improve the gripping of the specimens inside the machine. According to that, twenty-nine tests were performed on basalt fabric strips using different clamping

methods, namely employing rough paper, leather or aluminium tabs in the gripping area. Moreover, specimens were made with different geometry and tested using different elongation rates, in order to find the most suitable configuration among those provided by the standard.

Tests were carried out under displacement control using a 100 kN universal testing machine, obtaining the displacements by the global displacement of the machine cross-head.

Table 3.3 summarises the geometrical characteristics of the specimens, the used auxiliary material and the test speed. Specimens were named following the designation NML-WXSY, where N is used to number samples of the same type, M refers to the used auxiliary material, L indicates the specimen gauge length, W means "width", X indicates the width measure (1, 3 and 4 are used for 13.5, 33.5 and 47.5 thick specimens), S means "speed", Y is used to refer to the test speed (1, 2, 3 or 4 mm/min).

Clamping by rough paper

First the specimens were tested using pieces of rough paper, cut with a length of 50 mm and a width depending on the specimen width. Without any additional glue, the paper pieces were positioned at the extremities of the basalt fabric strip so to enclose the grid and the sample was positioned inside the machine jaws, gripping the extremities over a length of 50 mm. High care was used in order to ensure a good alignment between the longitudinal axis of the sample and the centre of the front edge of each jaws.

Clamping by leather

In a second step, fabric strips were tested employing leather pieces, with the same size used for the paper pieces. The leather was positioned at the strip extremities, between the grid and the machine clamps over a length of 50 mm, with the same aim to prevent possible slippage of the samples during the test.

Clamping by aluminum tabs

An alternative solution generally used in the literature, aimed at guaranteeing a uniform load distribution during tensile tests, is to provide the textile strips with

aluminium/steel tabs at the ends. Then, this solution was also explored, employing aluminium tabs with dimensions 80x30x2 mm. Aluminium was preferred to steel because of its higher deformability, allowing for better stress transfer.

Three samples with free length of 100 mm and width of 13.5 mm were prepared and equipped with two couples of aluminium tabs at the ends. The preparation procedure was very accurate and involved the following steps:

- cutting and preparation of basalt grid strips: the strips were cut along the principal direction, with dimension 13.5x260 mm, in order to have a 100 mm free gauge length;

- cutting and deburring of aluminium tabs: the tabs were cut with dimension 80x30 mm and deburred to avoid any shape defect and to ensure an adequate contact with the textile;

- preparation of glass plates: four glass plates were used as support to glue the couples of aluminium tabs, in order to have a perfectly smooth surfaces that could guarantee a very good distribution of the glue and parallelism between the couples of tabs;

- marking of aluminium tabs: the tabs were marked with a central longitudinal line in order to allow the alignment between their axis and the longitudinal axis of the basalt grid to be positioned;

- positioning of aluminium tabs on the glass plates: two of the glass plates were positioned at the right distance in accordance with the textile strip length and fixed on the working base to avoid any movement during the preparation process. Then, two aluminium tabs were fixed to the glass by using double-sided tape;

- mixing and application of glue: a strong bi-component epoxy with fast setting was used. The two components of the glue were mixed and quickly applied on the tabs surface, guarantying a uniform distribution;

- positioning of the grid: masking tape was used to protect the zones of the grid close to the tabs, in order to avoid possible glue impregnation during the application of pressure. The basalt grid was then placed following the marks on the two already in place tabs;

Table 3.3: Preliminary tests on basalt fabric strips

Clamping method	Sample	Length [mm]	Width [mm]	Test rate [mm/min]
PAPER	1P200-W1S1	200	13.5	1
	1P200-W1S2			2
	1P200-W1S3			3
	1P200-W3S1		33.5	1
	1P200-W3S2			2
	1P200-W3S3			3
	1P200-W4S1		47.5	1
	1P200-W4S2			2
	1P200-W4S3			3
LEATHER	1L200-W1S1	200	13.5	1
	2L200-W1S1			1
	3L200-W1S1			1
	1L200-W1S2			2
	2L200-W1S2			2
	1L200-W1S4			4
	1L200-W3S1		33.5	1
	1L200-W3S2			2
	2L200-W3S2			2
	3L200-W3S2			2
	1L200-W3S4			4
	1L200-W5S1		47.5	1
	1L200-W5S2			2
	1L200-W5S4			4
	1L150-W1S1	150	13.5	1
	1L150-W1S2			2
	2L150-W1S2			2
ALL. TABS	1A100-W1S1	100	13.5	1
	1A100-W1S2			2
	2A100-W1S2			2

- placing of the other two aluminium tabs: to end the process, the other two tabs, already provided of a uniform glue layer on one face, were positioned on the previous ones, ensuring a perfect correspondence between the couples of tabs;

- placing of glass plates and curing of glue: prescriptions about glue suggested to apply a pressure for about twenty minutes; two hours were needed to attain full

strength before handling. Then, other two glass plates were applied on both the ends of the sample and they were pressed applying a heavy and uniform weight.

Figure 3.9 shows one grid sample at the last step of the process, while Figure 3.10 reproduces some specimens already equipped with aluminium tabs.

Before to be positioned inside the machine clamps, all the external surfaces of the aluminium tabs were marked with central longitudinal lines to ease a centred positioning of the samples inside the machine jaws. Additional transversal marks helped to grip the strips over a length of 50 mm, leaving 30 mm out of the machine grips to avoid any possible stress concentration because of a localized variation of the axial stiffness (Figure 3.11).

Tensile characterization tests on basalt fabric strips

For the characterization tests, twenty-one basalt fabric strips, twelve along the warp and nine along the weft direction, were prepared following the procedure described above. The samples had dimensions of 13.5x260 mm (100 mm free length) and were provided of 80 mm long aluminium tabs.

Measuring instrumentation: the videoextensometer

Tensile characterization tests were performed using a videoextensometer, taking advantage from the DIC technique. This system was adopted in order to achieve a more reliable evaluation of the stress-strain response of the specimens, avoiding to have measurements of strain affected by the rigidity of the testing system.

The videoextensometer is a contact-free measurement system for high-resolution tensile and bending strain test for nearly all different types of materials. This device is able to measure strains or displacements by running the distance measurement between two or more assigned markers. The apparatus works linked to a computer for managing and storing data through a suitable software. The images taken from the videoextensometer are processed directly during testing, thanks to the processing software provided with the instrument. However, it is also possible to collect the series of photos to be worked out by using another software (GOM Correlate for example).

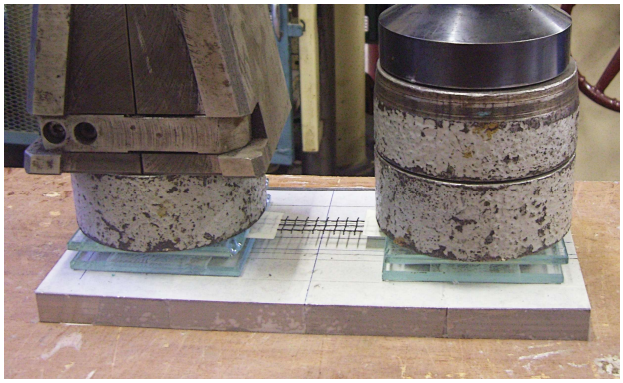

Figure 3.9 Preparation of basalt fabric strips

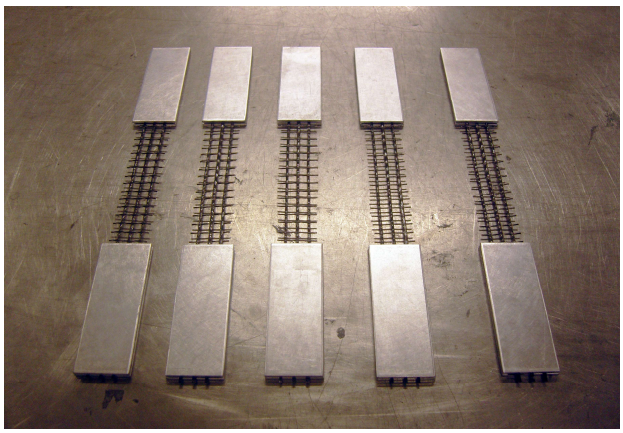

Figure 3.10 Basalt samples equipped with aluminium tabs

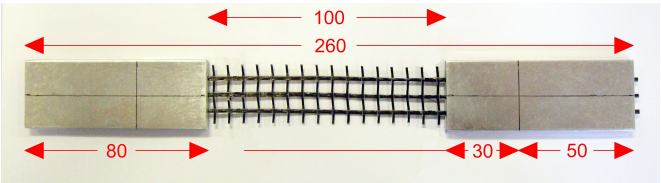

Figure 3.11 Basalt textile sample before testing

As opposed to conventional extensometers, which are extension measuring devices about a set gauge length, the videoextensometer is inherently an absolute measuring device and does not require scaling for determination of strain. At the onset of a test, the distance between the targets is recorded as L_0 (initial gauge

length) and as the test progresses the distance between the targets is re-measured and recorded. However, sometimes it is desirable to have a record of the actual test extensions and, to achieve this, the displayed field of view must be scaled (VideoXtens Manual, 2015). The easiest way to scale the field of view is to place a specimen with targets at known distances, ensuring that the scaling device surface is set at the same distance from the camera as the intended specimen surface. Regarding the tests herein presented, the scaling procedure was always applied before testing the basalt textile specimens, by using a scaling device provided with the extensometer by the supplier.

The use of the videoextensometer must be supported by an illumination source, which can be a front light or a backlight, and by markers to be placed on the specimen surface.

Concerning the lighting, the specimen illumination through the use of a rear light is preferred to the front light for transverse strain measurement, while both methods are suitable for the axial strain recording.

Different methods for marking samples are possible: markers can be put on the specimen with manual or automatic lines, dots or pattern or the specimen material itself has textured surface for pattern recognition. The goal is to use markers with intense light-dark-contrast to achieve highest possible accuracy and less signal noise. In general, the greater the contrast the more consistent the results obtained.

In the framework of this study, with reference to markers, some methods were investigated in order to obtain the most suitable solution allowing the achievement of the best results. Dots or linear targets supported by a front light (Figure 3.12) or linear markers with support of a retro light (Figure 3.13) were used.

In the case of linear markers, particular attention should be paid to the positioning of the strips on the specimen: as suggested by the manual (VideoXtens Manual, 2015), the best measurement results are obtained when the targets are applied slightly inclined to the measured axis (approximately 2-5°) (Figure 3.12b).

In the context of this work, the most reliable records were obtained by adopting linear markers supported by rear illumination, as shown in Figure 3.13. Then, a retro light was assembled behind the specimens (Figure 3.13a), mounted

opposite the videoextensometer, to get a high-contrast transition at the sample edge.

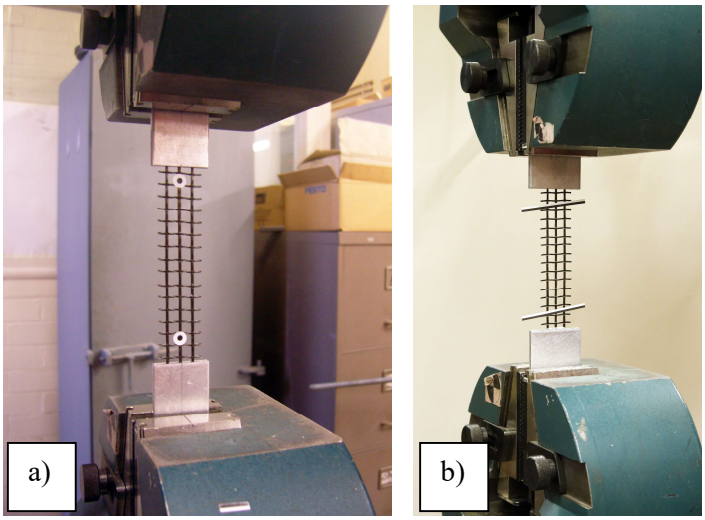

Figure 3.12 Markers for strain tracking: a) dot markers; b) line markers

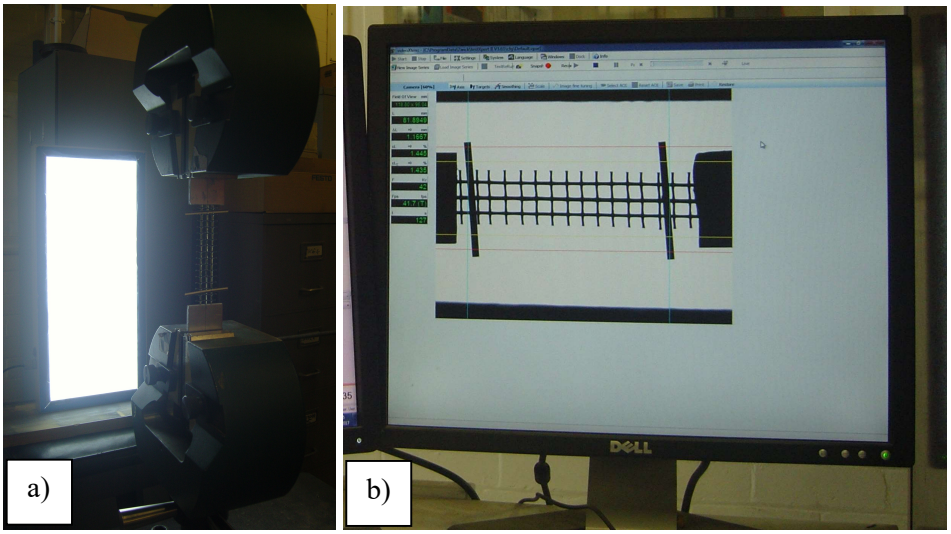

Figure 3.13 Test of basalt grid sample using backlight: a) specimen during testing; b) software screen view during testing

Target strips were placed on the specimen, providing overhanging projections, which could be selected as axial targets through the use of the backlight. The overlapping ends of the targets were visible together with backlight as black lines and so the positon could be detected with the videoextensometer (Figure 3.13b). This was made on the left and the right side of the specimen in order to achieve a better signal quality. In order to obtain best results, attention was paid so that the contrast between light and dark could be as great as possible, resulting in a grey level diagram having very steep target edges (VideoXtens Manual, 2015).

Test setup of characterization tests on the basalt fabric

Tests were performed under displacement control by a 100 kN universal testing machine, using a rate equal to 2 mm/min.

Before to be positioned inside the clamps, the specimens were equipped with linear targets in order to allow the recording of displacements. During testing, the samples were lighted up with a retrolight, as described above, and displacements were recorded using the videoextensometer able to track the linear targets attached to the fabric strips over a gauge length of 80 mm. The sequence of images was acquired with a frequency of three photos per second. The overall test setup is shown in Figure 3.14.

3.7.4 Three point bending tests on mortar matrix prisms

In order to characterize the mechanical properties of the mortar used as matrix of the BFRCM composite, three-point bending tests were carried out on six standard 40x40x160 mm prisms, according to EN 1015-11. Tests were conducted in displacement control, using a rate of 0.2 mm/min, in order to explore the full experimental curve, including the softening branch.

Before testing, the surface of the specimens was painted with a high-contrast texturing effect, using white paint with black speckle pattern, in order to allow the strain field analysis through the use of the DIC. The sequence of images was acquired through the use of the videoextensometer (Figure 3.15) connected to the testing machine, with a frequency of three photos per second. Figure 3.16 shows a mortar specimen during testing.

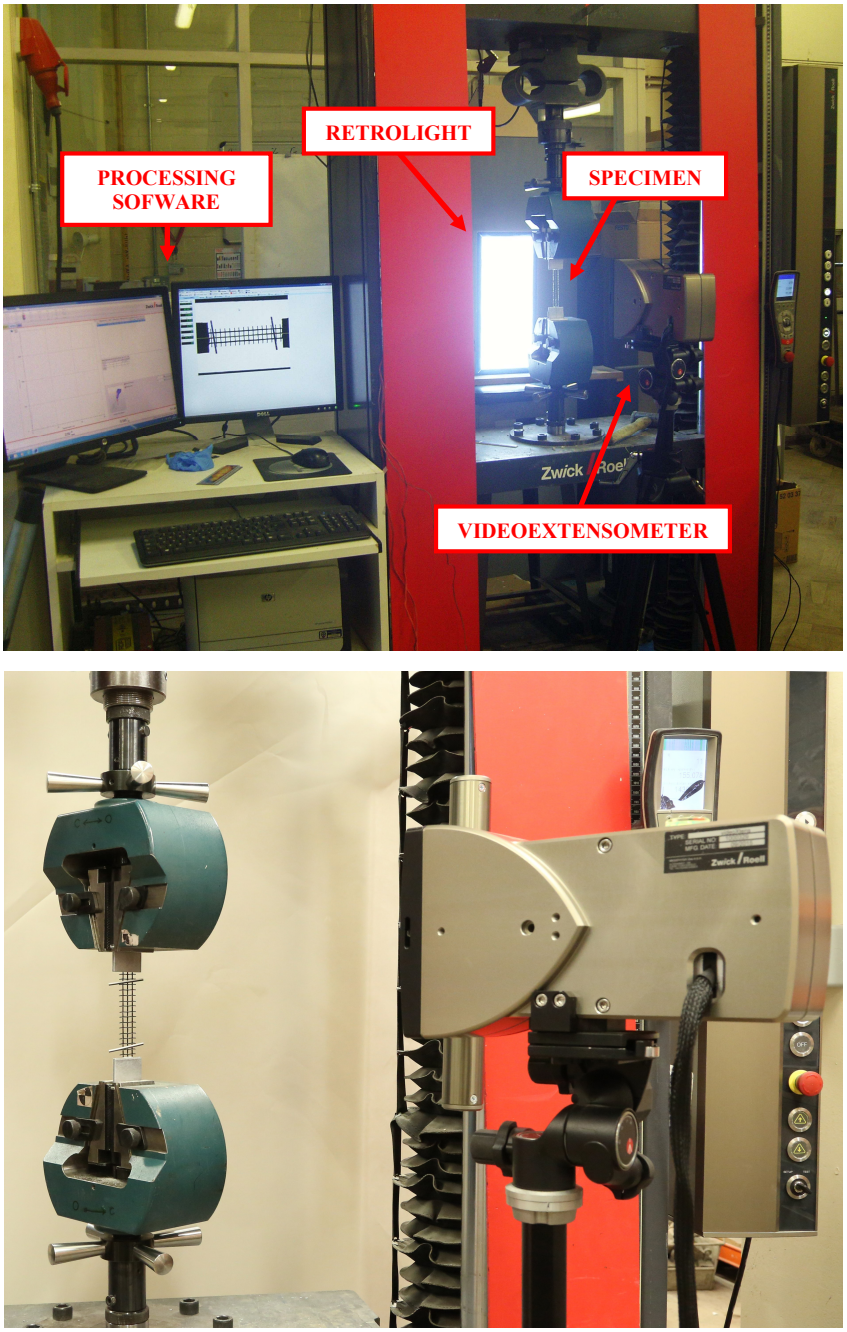

Figure 3.14 Test setup for tensile tests on basalt fabric

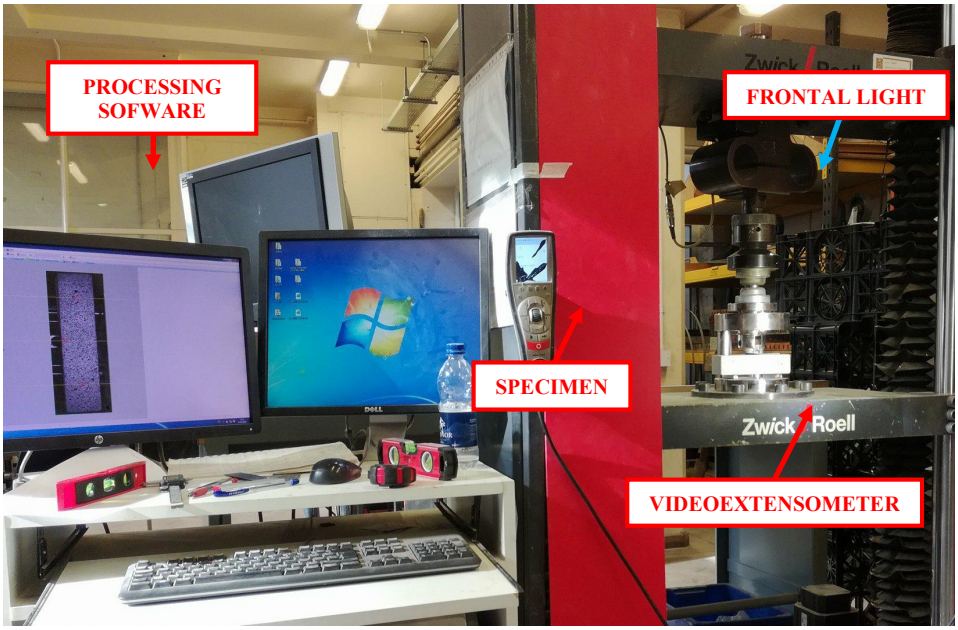

Figure 3.15 Three point bending tests: test setup

Figure 3.16 Three point bending tests: specimen during testing

3.8 Tensile tests on BFRCM composite coupons: specimens and methods

The experimental program involved tests on a total of fourteen BFRCM composite specimens, manufactured using different reinforcement ratios. In

particular, the first series comprised eight specimens reinforced with one grid layer, the second series involved five specimens strengthened with two layers; additionally, one specimen was prepared employing three basalt textile layers. All the specimens were produced using the same mortar type.

The identification of the three series of specimens is presented in the first column of Table 3.4. Specimens were named following the designation SPX_YL, where SP means "specimen", X indicates the specimen number, Y is used to designate the number of reinforcing layers (1, 2 or 3), L means "layer".

Table 3.4: Tensile tests on BFRCM composite coupons

Series designation	Number of specimens	Number of reinforcing layers
SP_1L	8	1
SP_2L	5	2
SP_3L	1	3

BFRCM specimens geometry and preparation

The dimensions of the specimens were selected based on published research and existing regulations (AC434 2013, RILEM TC 232-TDT 2016, Lignola et al. 2017). All composite coupons had 40x8 mm cross sectional area and length of 400 mm. Samples were cut from a large 500x500 mm slabs prepared in wood formworks (Figure 3.17a), in agreement with AC434 American Standard (2013).

The molds for the preparation of the slabs were made using a wood board and installing wood edges (8 mm thick) in order to control the thickness of the panel (Figure 3.17a). The BFRCM slabs were manufactured using the manual impregnation technique. In particular, after wetting the mould with a special product to minimize the adhesion of the mortar, a first layer of mortar was applied on the base using a flat trowel (Figure 3.17b), while monitoring to have a constant thickness using a marked instrumentation. The basalt textile layers, pre-cut with the panel size, were placed uniformly over the panel thickness and pressed, taking care to include a constant mortar thickness between grid layers in the case of multilayer reinforced specimens (Figure 3.17c). A top layer of matrix was then applied as flat as possible, using a finishing trowel (Figure 3.17d to

Figure 3.17f). In order to ensure the flatness of the top surface, a steel bar was run leaning on the wood edges of the mould (Figure 3.17g). Figure 3.17h shows the slab at the end of the manufacturing process.

After casting, the large slabs were cured in a saturated atmosphere (20°C and 70% relative humidity) for more than one month. In order to avoid differential shrinkage which could cause a curvature of the panel and bending problems during testing, the slabs were covered with wet drenched gunny cloths and plastic sheets.

After the curing period, the panels were demolded and the composite strips were cut from the slabs using a circular wet saw with a rigid fixture to ensure consistent specimen width (Figure 3.18). The specimens were then stored in laboratory conditions till the test day.

In the case of one-layer reinforced specimens, one basalt ply was positioned between two 4 mm thick mortar layers (Figure 3.19a). For the specimens reinforced with two or three layers, the textile pieces were placed uniformly, e.g. two layers placed every 2.7 mm in the case of two-layer reinforced samples and three textile plies placed every 2 mm for the three-layer reinforced specimen (Figure 3.19b and Figure 3.19c).

Moreover, for specimens reinforced with one basalt grid layer, the ends of the coupons were over-reinforced each one with two additional layers of 150x40 mm textile, in order to promote the failure of the samples in their 100 mm middle portion (Figure 3.20). The additional textile pieces were positioned during the slab preparation and were involved inside the mortar thickness (Figure 3.17e and Figure 3.17f). Additional reinforcements at the extremity were not used for specimens reinforced with two and three layers because of the difficulty of placing many layers inside such a small thickness.

Before testing, the BFRCM coupons were equipped with aluminum tabs at the edges, in order to reduce local concentration of stresses near the clamping wedges of the testing machine and to avoid the premature damage of the specimens.

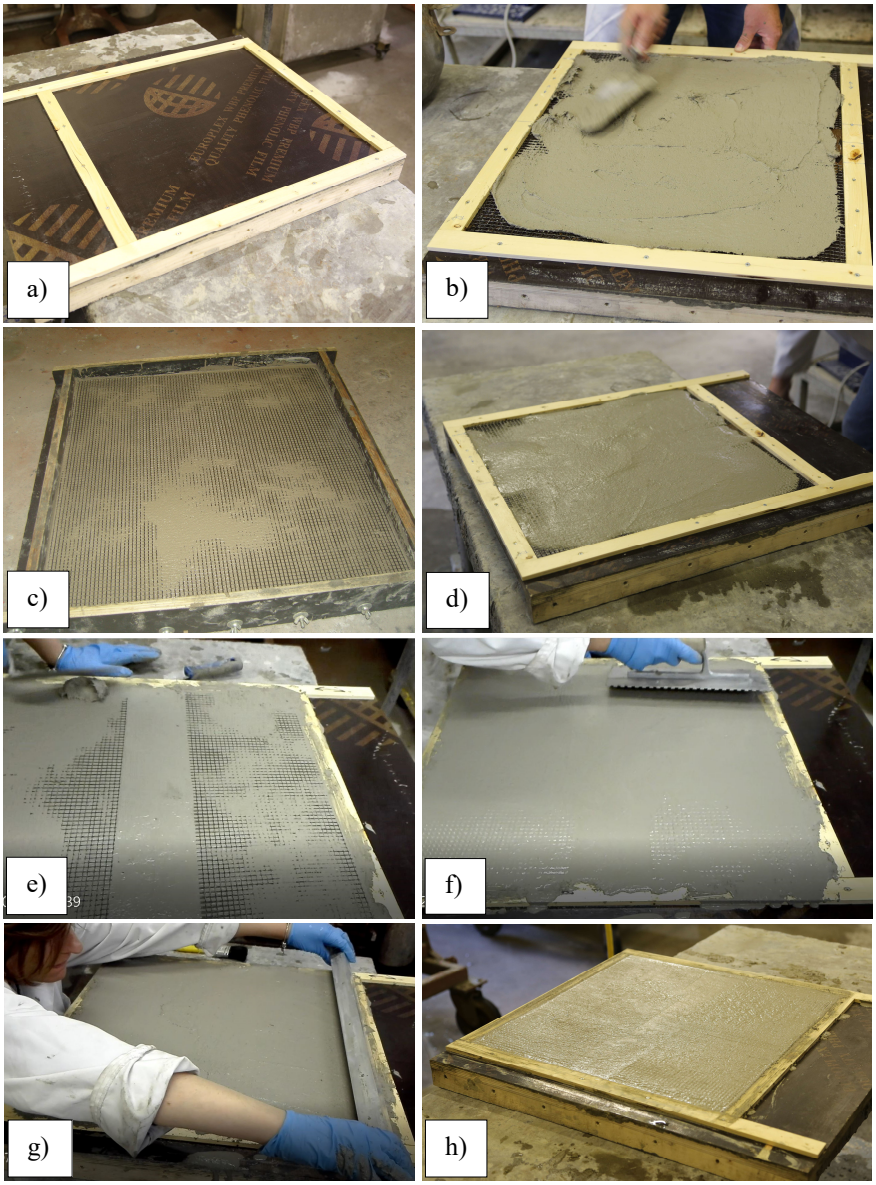

Figure 3.17 Specimens manufacturing: a) wood framework; b) application of first mortar layer; c) positioning of basalt textile layers; d) application of top mortar layer; e) positioning of additional textile pieces; f) flattening of top mortar surface using a finishing trowel; g) checking of flatness using a steel bar; h) slab at the end of the manufacturing process

Figure 3.18 Cutting of the BFRCM slab

The aluminum tabs were cut using a width equal to that of the composite coupons and length of 80 mm and deburred in order to avoid shape defects and guarantee a perfect adherence to the surface of the specimens. As mentioned about the preparation of bare basalt strips, even in this case glass plates were employed as support to glue the tabs to the composite coupons, in order to work on a perfectly smooth surfaces. The same type of epoxy was used and the tabs were kept in place during a curing period of 2 hours, fundamental to reach the full strength of the epoxy.

In order to ensure an easier and centered placing of the specimens inside the machine clamps, the external surfaces of the aluminium tabs were marked with central longitudinal lines. Transversal lines were also highlighted in order to identify the length to be gripped (70 mm) over the total tabs length (80 mm).

Finally, the front side and the thickness side of the specimens were painted with a high-contrast texturing effect using white paint with black speckle pattern in order to enable for contactless measurement readings during testing with the use of the DIC (Figure 3.21), as discussed in the following section.

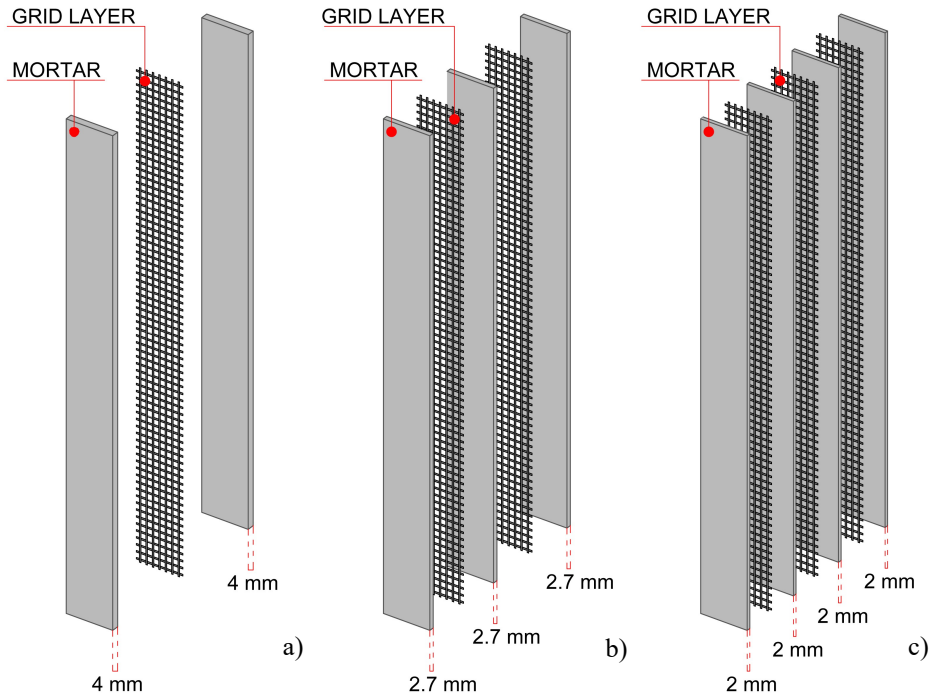

Figure 3.19 Geometry of BFRCM composite specimens: a) one layer; b) two layers; c) three layers

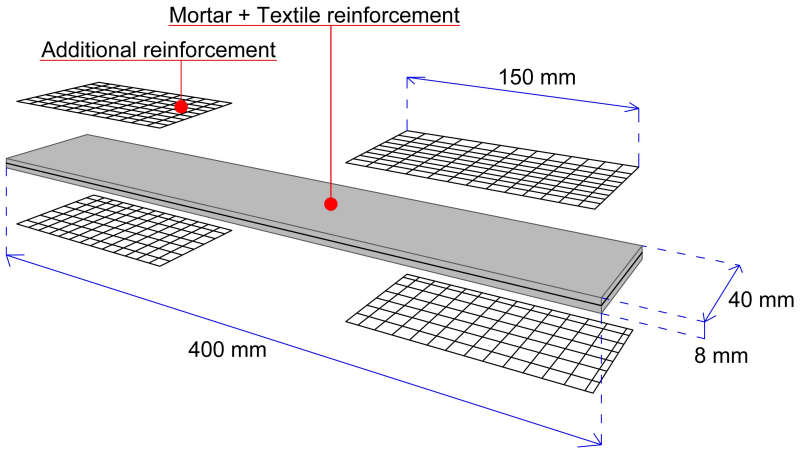

Figure 3.20 Additional reinforcement in composite specimen strengthened with one basalt grid layer

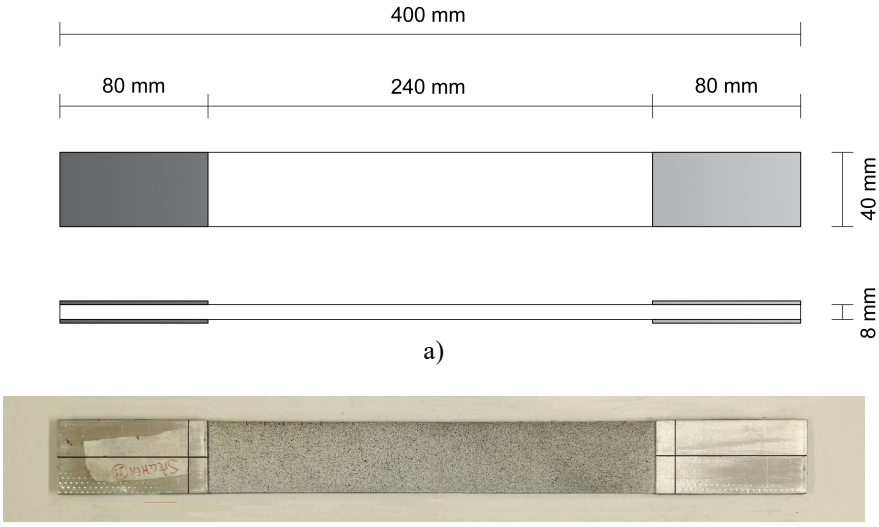

a)

b)

Figure 3.21 BFRCM sample equipped with aluminium tabs: a) schematization of sample; b) painted sample, with marked aluminium tabs

Test setup of tensile tests on BFRCM coupons

The tensile monotonic tests were carried out using a 100 kN universal testing machine (Figure 3.22), in displacement control mode with a loading rate of 0.2 mm/min. The test setup, as mentioned about the geometrical characteristics of the specimens, was selected based on published studies and existing codes (AC434 2013, RILEM TC 232-TDT 2016, Lignola et al. 2017).

The applied tensile load was measured through a load cell and recorded by a data acquisition system.

The strain field over the surface of the specimens was obtained using DIC measurements. Figure 3.22 provides a view of the test setup. The instrumentation for the data acquisition involved the use of a high-resolution camera placed in front of the testing machine, with the lens directed towards the centre of the composite coupon and in perpendicular position respect to the specimen surface (Figure 3.22a). The camera was fixed at a distance from the specimen surface able to allow the acquisition of photos involving the entire length of the coupon. This choice allowed, afterwards, taking into account all the cracks developed

along the specimen surface, also those developed close to the testing machine grips, obtaining the measure of global displacements/strains.

The accuracy of DIC technique is influenced by many factors, one of the most important is the uniformity of light distribution. The lightness should be constant and homogeneous for the entire duration of the test and for this reason the specimens were lighted up using a white light to provide uniform light intensity across their surface.

In addition, a videoextensometer was used in order to monitor the thickness of the specimens (Figure 3.22b). Many aspects can influence the results of tensile tests and most of them relate with the fabrication of the samples that, as far as accurate, can involve unavoidable imperfections. One problem could be the non-symmetric distribution of reinforcement in the thickness causing, during tensile test, a warping of the sample with consequent different opening of cracks on the front and back surface. Another issue could be the non-perfect planarity of the sample, producing a parasitic bending moment and a different crack development on the convex and concave specimen surface. The will of investigating on these possible issues led to include the use of the videoextensometer during tensile tests. It was not possible to position the videoextensometer in front of the other specimen surface because this required the use of an auxiliary light that would have affected the results of the camera, being in front of his lens. Then, the solution was to place the apparatus in front of the thickness of the sample, following the same procedure already described about the camera.

The camera, monitored through a remote trigger during testing, captured images of the specimens every two seconds, while the extensometer took images with a frequency of one photo per second.

Regarding the choice of the gripping system, in general it depends on the final objective of the experimental investigation and, for the current study, it was made on the base of the suggestions provided from existing studies (Arboleda et al. 2015). In particular, if the goal is the characterization of the FRCM system and the determination of the maximum strength of the composite, the clamping grips can provide a full evaluation of the mechanical properties and allow the determination of all the parameters that characterize the trilinear stress-strain curves. On the other hand, if the objective is the investigation of the maximum load-bearing capacity of the system for the reinforcing application, then the

clevis-type grips are preferred (Arboleda et al. 2015). Nevertheless, as already mentioned, there are some applications in which the load is applied to the textile (confinement of columns and pillars) and the maximum strength of the composite can be the design parameter. In this case, the complete behaviour of the composite need to be captured, up to the textile failure. In other applications where load is transferred from the substrate to the matrix by means of shear bond stresses and then to the textile through mortar-to-textile bond, the use of the clevis system allowing failure by slippage permits to capture the real composite behaviour. For these reasons, the tensile tests here presented were carried out by employing the clevis-type grips method (Figure 3.22).

Measuring instrumentation: the Digital Image Correlation (DIC)

The use of Digital Image Correlation (DIC) enabled the analysis of the strains of the FRCM composite specimens. The DIC technique constitutes an adequate monitoring system for investigating on such a heterogeneous system like FRCM composite material. Indeed, it is clear as traditional monitoring systems (strain gauges, transducers) are not always adequate for FRCM materials, because they can offer only local information and the reliability of their readings is strongly affected by the device position (De Santis and De Felice 2015a).

During tensile tests on BFRCM coupons, the DIC measurement system was adopted for recording the strain values on the surface of the samples. After testing, the recorded images of each specimen were post-processed using the software GOM Correlation, which allowed carrying out different analyses by measuring the strains along defined gauge lengths or in the form of continuous field on the surface of the specimen.

In the first case, the evaluation of strain values along defined gauge lengths required the assignment of couples of facets onto the surface of the composite coupons, which defined the virtual extensometers. In the current study, the analysis was performed with reference to six subsets chosen on the surface of each coupon, i.e. facets 1 to 6 (F1-F6) in Figure 3.23, considering three virtual extensometers: two positioned at the extremities of the specimen surface and one placed at the middle axis of the sample. The choice to use three virtual extensometers equally distributed on the specimen width allowed investigating on the possible presence, during the test, of in plane bending effects caused from: - dissymmetric reinforcement distribution in the width of the specimen; - not

perfect alignment of the specimen inside the gripping area causing a non-uniform load application; - non-uniform slipping of the specimen inside the clamps of the testing machine.

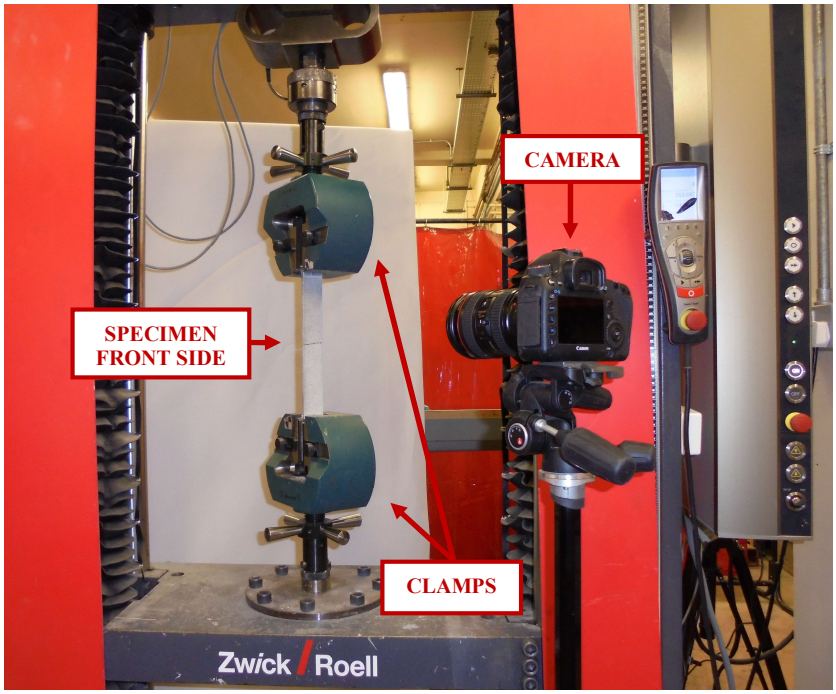

a)

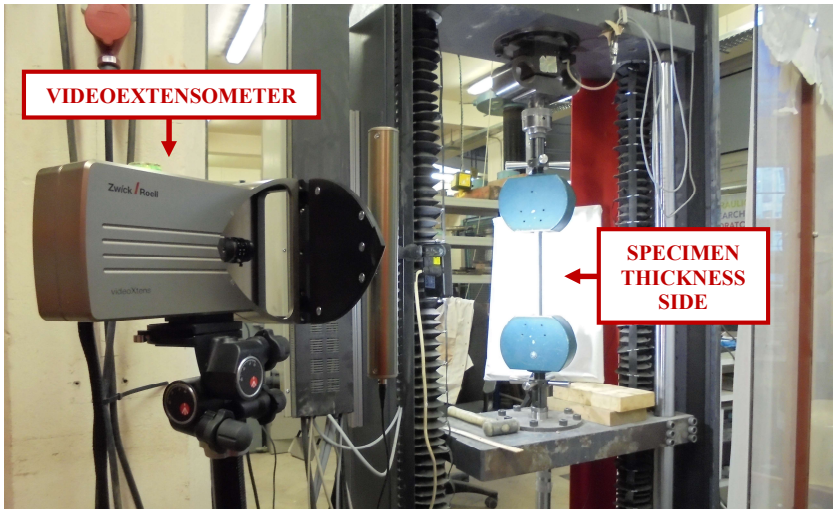

b)

Figure 3.22 Setup for tensile test on composite coupon: a) hight-resolution camera; b) videoextensometer

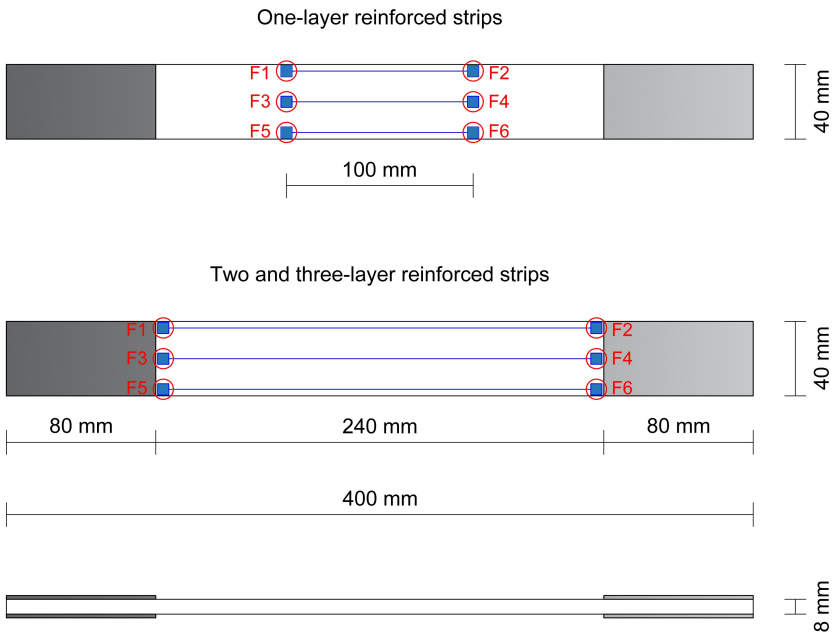

Figure 3.23 Position of virtual extensometers on the front surface

Each couple of facets involved a gauge length of 240 mm in the case of two and three-layer strengthened specimens, while in the case of one-layer reinforced specimens three virtual extensometers 100 mm long were selected in the middle length of the samples, in accordance with the expected failure in the middle part of the coupons.

It should be noted that the chosen values of gauge length are in accordance with available standards and with literature studies. In fact, RILEM TC 232-TDT (2016) suggests a measurement length during tensile tests equal to at least 200 mm and this choice was adopted by several authors during their experimental works (Larrinaga et al. 2014, De Santis and De Felice 2015a, Lignola et al. 2017). Nevertheless, some authors, particularly if supported by contactless monitoring instrumentations during testing, decided to analyze the full length of the specimens, obtaining information on the whole specimen elongation (Bilotta et al. 2017b, Caggegi et al. 2017a).

Additional analyses were carried out referring to the thickness of the specimens, in order to investigate on possible issues related to fabrication

defects. In this case, two couples of facets were chosen on the thickness of the BFRCM coupons, forming two virtual extensometers positioned at the extremities of the thickness surface. As already done in the previous case, the gauge length of the virtual extensometers was equal to 240 mm for two and three-layer reinforced samples and 100 mm in the case of specimens strengthened with one basalt textile layer. Figure 3.24 presents the chosen position of the facets on the thickness surface of the specimens.

The relative displacement between the extremities of each virtual extensometer was assessed during the correlation process tracking the subzones in subsequent images and assuming that the displacement was applied at the centre of each facet. At the end of the analysis, the results in terms of strain were combined with the load obtained from the load cell during tensile tests. The load corresponding to each image was known from the load versus time curve.

For the strain/displacement continuous field analysis, it was required the definition of an area to be monitored. In this case, the DIC algorithm worked by defining the strain/displacement fields of several subzones (facets in Figure 3.25) into a defined surface component. The facets were placed homogeneously over the surface component and they had the same square size. The displacements related to each subzone were evaluated by the algorithm assuming, as already mentioned, that they were applied at the centre of each facet. The correlation was referred to a surface component equal to the global surface of the specimen for two and three-layer strengthened coupons. In the case of specimens reinforced with one layer, a 150 mm long surface component was selected, in order to monitor the middle 100 mm of the samples, where cracks were expected to develop.

As discussed above, the software adopted for processing the data was GOM Correlate. The parameters used in GOM Correlate for analyzing the experimental tests are reported in Table 3.5. The size of the facets was chosen on the base of the suggestion provided by the manual of the software, which recommended to choose the facet size as small as possible, but large enough so that the computation of the facet is still possible.

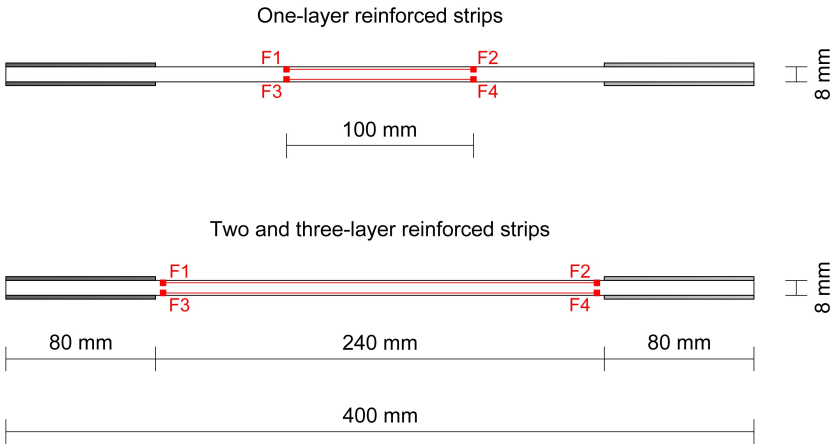

Figure 3.24 Position of virtual extensometers on the thickness surface

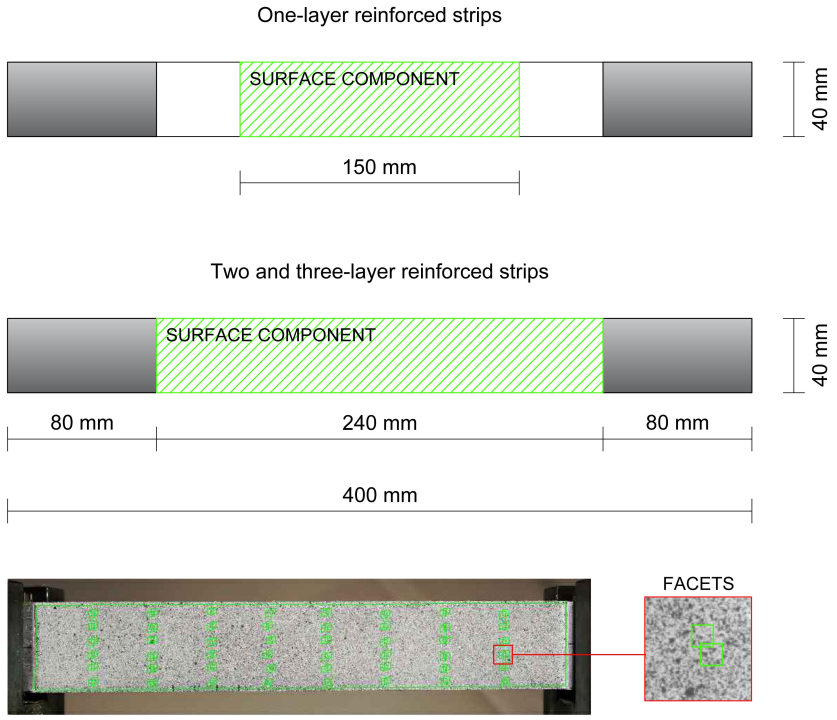

Figure 3.25 Full-field analysis: surface components and distribution of facets

Additionally, it was decided to match the facets on the stochastic pattern with respect to the initial stage. More in detail, the stochastic pattern painted on the specimen surface was computed and compared, at each stage, with the stage in which the facets were created. This option was adopted by other authors (Bilotta et al. 2017b) and it is also suggested from the manual (GOM Testing 2016), in order to avoid an accumulation of errors arising when the stochastic pattern of each stage is compared with the respective previous during the computation.

In the case of full field analysis of the surface of the specimens, the software required to set the point distance, which was chosen equal to 18 pixels.

Table 3.5: GOM Correlate parameters

Facet size	20 (pixels)
Computation	Standard
Facet matching	Against definition stage
Point distance	18 (pixels)

3.9 Compressive tests on masonry cylinders: specimens and methods

Geometry and manufacturing of specimens

As discussed in section 3.2, cylindrical specimens, made using pressed bricks, were extracted by two different assembly schemes, here named Scheme I and Scheme II, in order to investigate on the effects of the number of vertical mortar joints.

With this aim, masonry walls (Figure 3.26a) and columns (Figure 3.26b) were assembled using three rows of 50x100x210 mm pressed bricks divided by about 8 mm thick mortar joints. In the case of walls, the depth of the members was equal to the depth of a single brick and the brick units were arranged ensuring that the mortar joints were not aligned along the member. With the same aim, bricks were placed in columns in order to have the longer side in orthogonal direction to the longer side of upper and lower rows. The members were cured for a period of 30 days, after which a laboratory-coring machine was used to extract cylindrical specimens.

All specimens had three layers of bricks, but cylinders cored from the masonry walls (Scheme I) had only one vertical joint in the middle third, while those from the columns (Scheme II) had three staggered vertical joints, one for each level. All of specimens, with circular cross-section shape 94 mm in diameter, were about 190 mm height

Application of the FRP jacket

The installation of FRP laminates was carried out by means of some operational steps (Figure 3.27). The first phase consisted in the preparation of the primer by mixing the two components until a homogeneous fluid resin was obtained. An even coat of primer was applied on the clean and dry surface of the masonry specimens with a brush (Figure 3.27a). The next step involved the preparation of the epoxy resin mixing the two components until a uniform, grey blend was obtained and the application of a first coat of approximately 2 mm tick with a notched trowel over the still fresh primer (Figure 3.27b).

Figure 3.26 Brick assembly schemes for preparing cylinders: a) Scheme I (wall); b) Scheme II (column)

Then the epoxy was smoothed using a flat trowel to remove any surface defects (Figure 3.27c). Instantaneously the BFRP grid was placed over the still fresh resin, ensuring there were no creases (Figure 3.27d). After having flattened, a second 2 mm thick coat of resin was placed over the mesh so that it was completely covered. A ribbed roller was used to pass over the surface of the impregnated fabric in order to eliminate any air bubbles trapped in the system during the previous phases (Figure 3.27e). The BFRP grid was overlapped by 1/3 of the circumference to ensure that there was sufficient bond. The specimens were left to cure for one month (Figure 3.27f).

Application of BFCRM jacket

The application of FRCM jacket involved some sequential steps. In order to ensure good adhesion of the system particular care was taken in the preparation of the substrates, which needed to be perfectly clean and free of crumbling areas or dust. Before applying the products, the specimens were wet in order to have a saturated substrate with a dry surface.

The bi-component mortar was prepared by mixing the two components until they were thoroughly blended. Then, an even layer of product of approximately 2 mm was applied on the surface of the specimens by using a flat metal smoothing trowel. While the mortar was still wet, the basalt mesh was placed on the surface and pressed down so that it adhered to the mortar. A second 2 mm thick layer of the same mortar was applied, so that the basalt grid was completely covered. The surface was then smoothed with a smoothing trowel.

With the aim to ensure a sufficient bond, even in this case the basalt mesh was overlapped for a length equal to 1/3 of the circumference.

The specimens were left to cure for more than one month. During this period, the cylinders were daily wet and covered using drenched gunny clothes covered by plastic sheet in order to ensure an adequate humidity level for the curing of the BFRCM jacket.

Capping and painting of specimens

All the cylinders, wrapped and unwrapped, were capped at both ends to ensure levelled top and bottom faces for uniform application of the axial load.

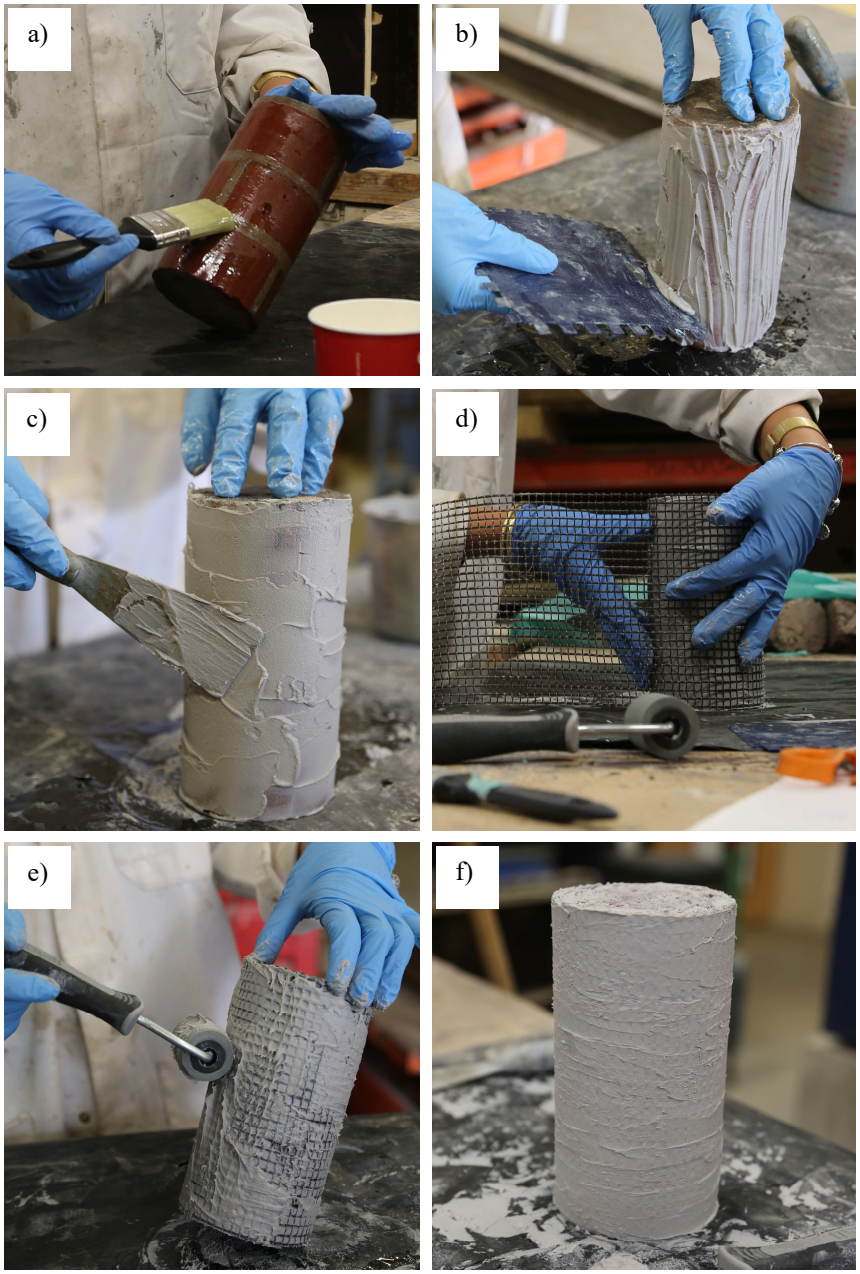

Figure 3.27 Preparation of BFRP-reinforced masonry specimens: a) application of primer; b) c) application of first coat of resin; d) installation of basalt grid; e) application of second coat of resin; f) specimen after wrapping

The mortar cap was prepared using a 1:2 sand to cement ratio mix, employing high strength rapid hardening cement and sand that was sieved through a 0.6 mm wire mesh. Water was added up to a good workability was achieved.

Before the application of the cap, the top and bottom surfaces of the specimens were wet in order to have a saturated substrate and to avoid the possible development of cracks during the curing of the cap.

The top and bottom of the cylinders were prepared, in two different steps, placing a steel metal wrap overhanging the specimen surface by 3 mm (Figure 3.28a), which was the mortar cap thickness. The role of the metal wrap was to hold the mortar in place, ensuring a levelled surface (Figure 3.28b).

The mortar was then placed and compacted (Figure 3.28c) and a glass capping plate was pressed against the edge of the steel metal wrap using a rotatory hand motion to eliminate any surfacing air bubbles, until a horizontal surface was achieved and checked with a spirit level. Note that the glass capping plate was sprayed with a layer of grease oil to ensure that the adhesion of the mortar was minimized.

The specimen was then turned in order to leave the glass plate in position under the weight of the cylinder (Figure 3.28d) for 24 hours, until the steel mould could be removed (Figure 3.28e). A drenched gunny cloth was used to keep the specimens in a humid condition. The procedure was repeated for the second base surface.

The last step before testing was the painting of the unconfined and confined cylinders in order to allow the displacement/strain measurement through the use of the DIC technique. All the specimens needed a smooth surface for the use of DIC, then the surface preparation of wrapped cylinders involved a slight sandpaper smoothing. Unconfined specimens had already a well smoothed surface from the coring process.

Finally, wrapped cylinders and two unwrapped cylinders were painted with a high-contrast texturing effect using white paint with black speckle pattern in order to enable DIC measurements of strain (Figure 3.28f).

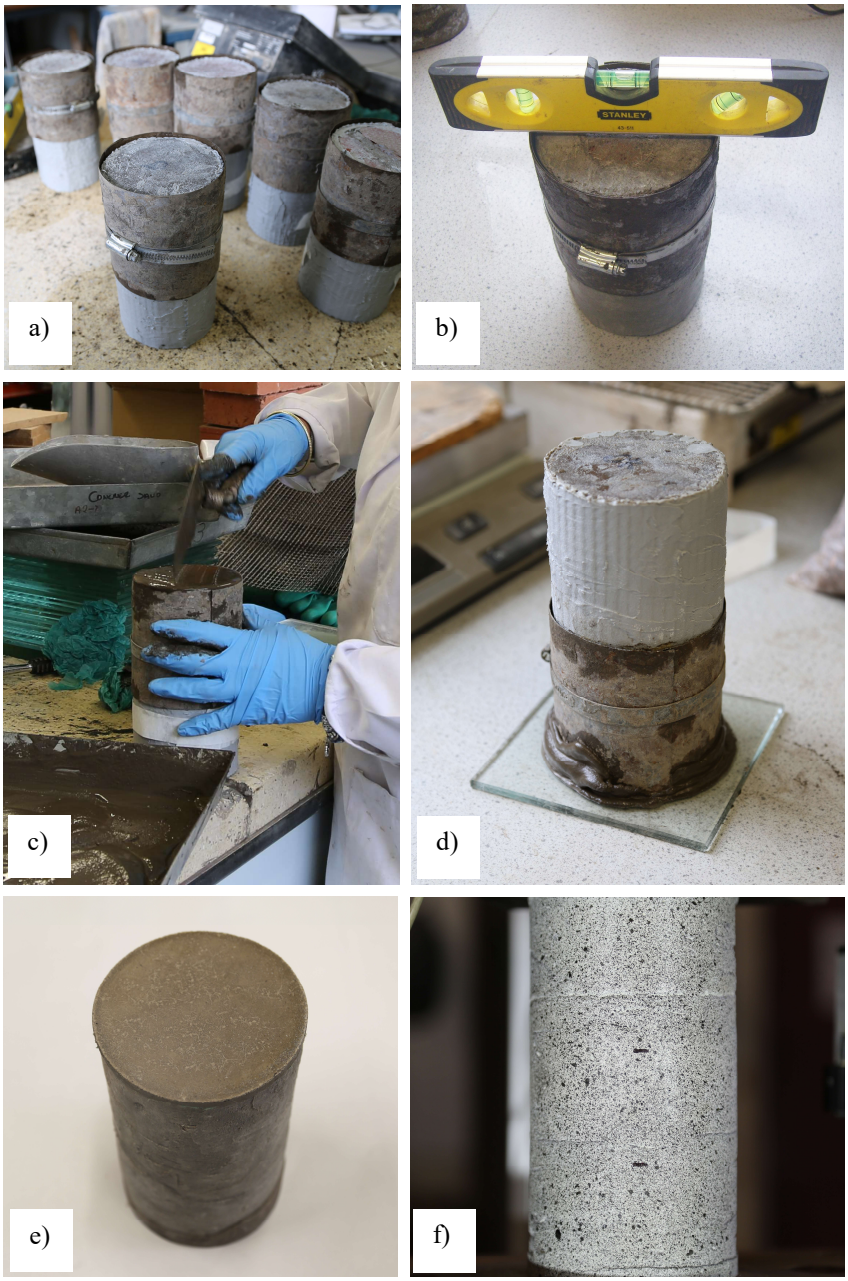

Figure 3.28 Capping and painting of masonry cylinders: a) placing of steel metal wrap; b) checking of horizontality; c) placing of mortar; d) application of glass plate; e) capped cylinder; f) painted cylinder

Test setup of compressive tests on masonry cylinders

The monotonic compressive tests on the cylinders were carried out using a 600 kN electro-hydraulic loading frame (Figure 3.29). Three loading/unloading cycles were applied under load control up to 40-50 kN for each specimen, followed by test to failure under displacement control at a loading rate of 0.005 mm/sec. A hydraulic jack connected to a manually controlled motor pump was used to apply the axial compression force on the tested cylinders. The applied compression load was measured by a load cell attached to the loading cylinder and recorded by a data acquisition system. A steel spherical head was placed above the upper bearing plate and centered with the specimen to maintain uniform distribution of stress and avoid any eccentricity.

Six Linear Voltage Differential Transducers (LVDTs) were installed, four to monitor the displacement of the upper loading platen and two at the lower platen (Figure 3.29). Three extensometers connected to two steel rings placed around the specimens were also used to measure the local deformation in the middle half of the specimens.

Additionally, the strain field on the surface of the specimens was obtained from DIC measurements. For this purpose, a high-resolution digital camera was used to capture images of the cylinders every four seconds using a remote trigger during testing. The camera was positioned in front of the testing machine, perpendicular to the cylinder surface, with the lens directed towards the centre of the sample (Figure 3.29). In the case of confined cylinders, it was ensured that the specimens were positioned in order to have the camera opposite to the FRP/FRCM overlap (Figure 3.30).

Similarly to tensile tests on FRCM coupons, the specimens were lighted up using two symmetrical white lights, able to provide a uniform light intensity on the front side of the samples (Figure 3.29).

Measuring instrumentation: the Digital Image Correlation (DIC)

Besides the use of LVDTs, the DIC technique was also adopted to measure the strain values on the surface of the cylinders during compressive tests, as similarly done in previous literature studies on FRP-confined cylinders (Bisby and Take 2009, Bisby and Stratford 2011, Bisby et al. 2011).

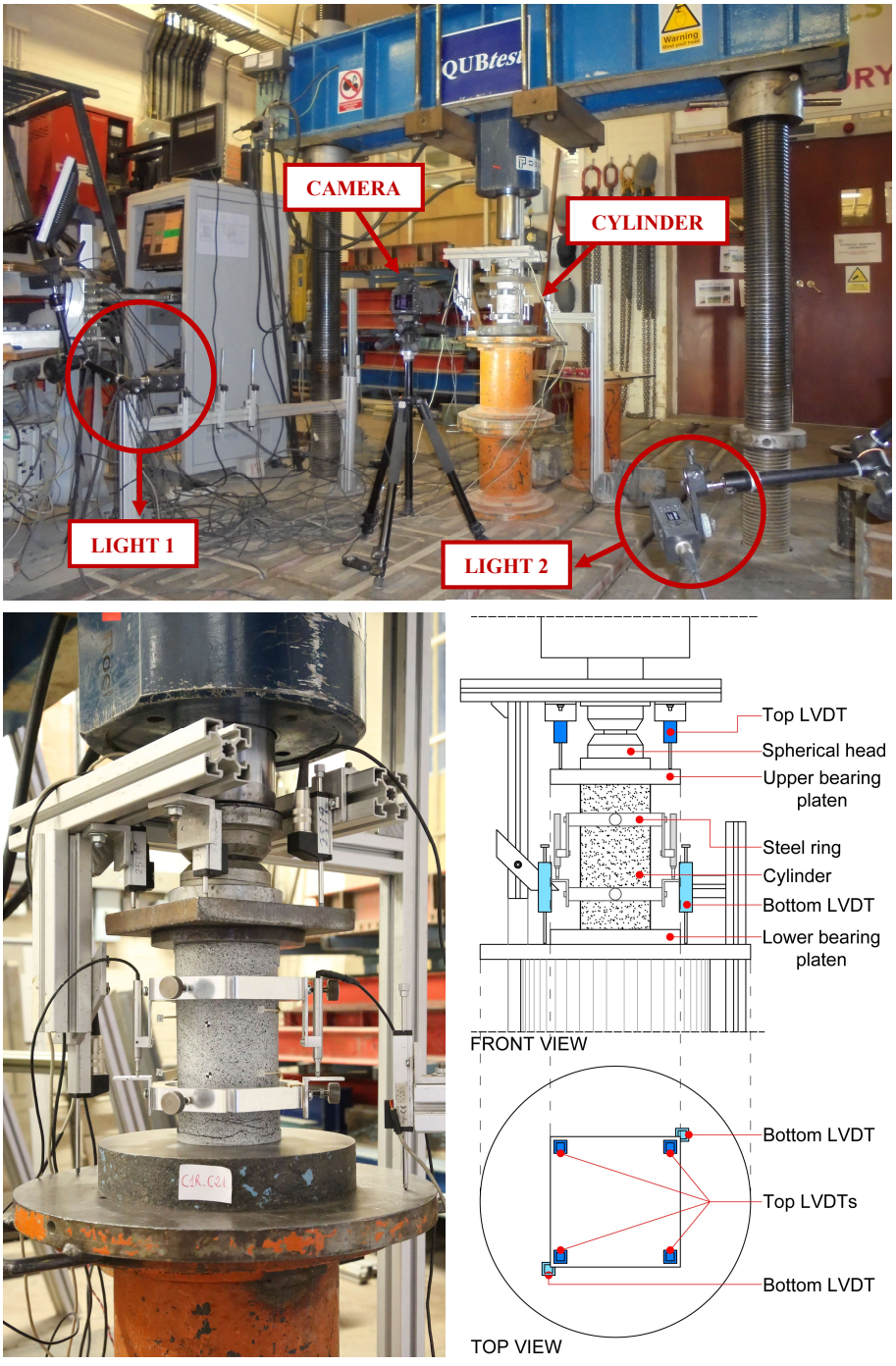

Figure 3.29 Test setup for compressive tests on masonry cylinders

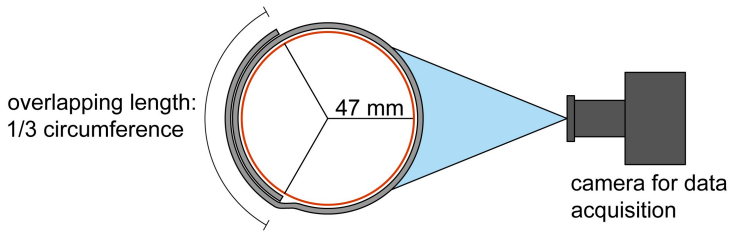

Figure 3.30 Camera positioning respect to the overlapping region in confined cylinders

Previous works showed that the DIC technique is valid for measuring axial and hoop strain in circular cylinders reinforced by FRP. In particular, Bisby and Take (2009) tested FRP-wrapped concrete cylinders and compared results from bonded foil strain gauges with those from DIC in order to evaluate axial and hoop strains, gaining good results. Moreover, Take and Kemp (2006) validated this technique for measuring hoop strains in cylindrical samples, even if the hoop displacements are slightly out of plane.

Bisby and Stratford (2011) used the DIC technique to quantify the variation of axial and hoop strain over the surface of concrete cylinders confined by FRP. The authors showed as strains in FRP-wrapped cylinders are affected by a considerable variability. For this reason, average strains should be calculated and the optical strain technique (DIC) is a useful solution since it allows the investigation of many individual virtual gauges, while this would not be possible by using bonded foil strain gauge.

As done about data acquired during tensile tests on FCRM specimens, even in this case the software GOM Correlate was adopted to process the images acquired during compression tests on the masonry cylinders. Referring to a previous work (Bisby et al. 2011), the analyses presented in this study were carried out considering a strain rectangle for measuring of axial and hoop strains on the surface of the cylinders (Figure 3.31). Axial strains were computed as the average of 20 virtual strain gauges placed over the width of the middle 50 mm of the diameter of the specimens; strain gauges had a length of 90 mm. In the same way, hoop strains were measured as the average of 45 virtual strain gauges placed over the height of the middle 90 mm of the length of the specimens, using a gauge length of 50 mm.

The analyses in GOM Correlate were carried out adopting the same settings described in the previous section about tensile tests on BFRCM coupons (Table 3.5).

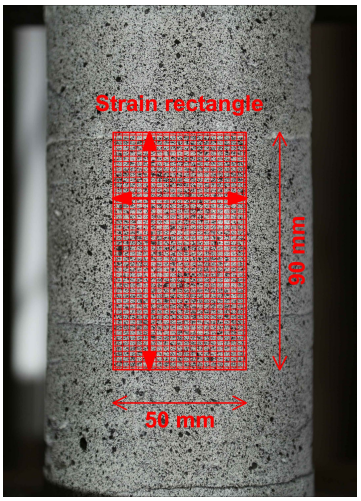

Figure 3.31 Strain rectangle used to calculate hoop and axial strains

4. EXPERIMENTAL RESULTS

4.1 Introduction

This chapter presents the results of the performed experimental investigation. The first part concerns the results of the mechanical characterization of constituent materials of the masonry and the external strengthening systems. In particular, the outcomes of tensile tests on the basalt textile grid are discussed in deep, with reference to the aspects concerning the clamping devices, the dimensions of the samples and the test rate.

Afterward, the results of tensile tests on the BFRCM coupons are presented in terms of stress-strain or load-strain curves, defining the characteristic points of the idealized tensile behaviour for the three series of samples strengthened by using different reinforcement ratios. Strain/displacement distributions on the surface of the samples and crack patterns are analyzed by means of the measurements made by the DIC technique and failure modes are also discussed.

Finally, attention is paid to the outcomes obtained from compressive tests on the masonry cylinders, presenting the trend of the axial stress as a function of the axial or hoop strain. The efficiency of BFRP or BFRCM confinement is highlighted in terms of strength and ductility enhancements. Finally, the failure modes are discussed on the base of analyzed key variables, such as the number of reinforcing layers and the realization scheme.

4.2 Characterization tests on components

In this section, the results obtained from characterization tests on the components are presented. First the outcomes of the mechanical characterization of the components of masonry, namely bricks and mortar, are discussed. Thus, the results obtained from tests on constituent materials of the external wrap are examined, with particular attention to the tensile characterization of the basalt textile grid.

4.2.1 Compressive tests on brick units

Results of compressive tests on bricks are presented in Table 4.1 along with their average value (42.53 MPa) and their coefficient of variation (COV). Figure 4.1 depicts the samples after the test.

Table 4.1: Mechanical characteristics of bricks

Sample	Compressive strength [MPa]	Average compressive strength [MPa]	COV
1	40.80	42.53	8.75 %
2	46.36		
3	45.72		
4	39.76		
5	37.36		
6	45.20		

Figure 4.1 Brick cubes after compressive tests

4.2.2 Three point bending tests on mortar prisms

With reference to the mortar used for the masonry, the mechanical characteristics of the mortar samples, i.e. the flexural strength and the compressive strength, obtained through three point bending tests are summarized in Table 4.2, along with the average values (average flexural strength equal to

5.33 MPa; average compressive strength equal to 20.93 MPa) and the coefficients of variation (COV). Note that the average compressive strength was calculated considering only six values, because the other six values were excluded according to the code prescription (EN 1015-11).

Table 4.2: Mechanical characteristics of mortar

Sample	Flexural strength [MPa]	Av. flexural strength [MPa] and COV	Sample	Compressive strength [MPa]	Av. compressive strength[MPa] and COV
1	5.32	5.33 (5.13 %)	1a	22.47	20.93 (5.52 %)
			1b	22.57*	
2	5.35		2a	15.09*	
			2b	20.82	
3	5.82		3a	20.64	
			3b	21.35	
4	5.21		4a	23.14*	
			4b	21.33	
5	5.32		5a	18.96	
			5b	15.76*	
6	4.98		6a	24.37*	
			6b	18.17*	

* Values excluded from the calculation of the average strength

4.2.3 Tensile tests on basalt fabric strips

This section presents the results of tensile tests on basalt fabric strips in terms of stress-strain curves. It should be reminded that, as discussed in Chapter 3, the investigation was subdivided in two parts. As a consequence, the results are here presented making distinction between:

- preliminary investigation on the effect of the clamping devices on the tensile behaviour of basalt fabric;
- tensile characterization tests on basalt fabric strips.

For all the tests, because of the discrete distribution of fibres along the width of the strips, the stress values were evaluated considering a cross sectional area of the textile calculated as its design thickness multiplied by its fictitious width, being this last the product of the number of yarns by their spacing (Ascione et al. 2015).

In the case of preliminary investigations, the strain values were obtained by dividing the global displacement of the machine cross-head to the gauge length, which coincided with the specimen length, excluding the gripping areas. Differently, during tensile characterization tests of basalt fabric strips, the strains were derived on the base of the distance between the linear targets tracked by the videoextensometer during testing.

Results of the preliminary investigation on the effect of the clamping devices on the tensile behaviour of basalt fabric

Clamping by rough paper

Figure 4.2a to Figure 4.2c show the stress-strain results of 13.5 mm, 33.5 mm, 47.5 mm wide fabric strips respectively, tested at different speed rates (1, 2, 3 mm/min), while Figure 4.2d to Figure 4.2f present the same results plotted by setting the test speed rate and varying the width of the specimens. The results in terms of tensile strength, tensile strain at peak stress and failure modes are reported in Table 4.3

The outcomes point out that, for fixed width, the speed of 1 mm/min gives lower values in terms of peak stress, while better fully comparable results are achieved with speeds of 2 mm/min and 3 mm/min respectively. This outcome is less evident in the case of 13.5 mm wide samples, which show comparable results independently from the used test speed.

By setting the test speed rate and making a comparison between samples with variable widths, it is clear as greater values of peak stress are achieved when a width equal to 33.5 mm is used, regardless to the test speed. It is worth to note that for a speed rate of 1 mm/min, the 13.5 mm and 33.5 mm curves are not so scattered.

All the curves present the same trend up to the peak stress. Apart from an apparent stiffness increase in the very first part of the curves, which is due to the progressive load transfer to the whole specimen, a linear elastic trend can be clearly detected up to the brittle failure. The post-peak branches are characterized by different load drops due to the progressive failure of wires. One of the samples with width equal to 47.5 (1P200-W4S3) shows a smooth post-peak branch, which indicates that the sample undergoes slipping.

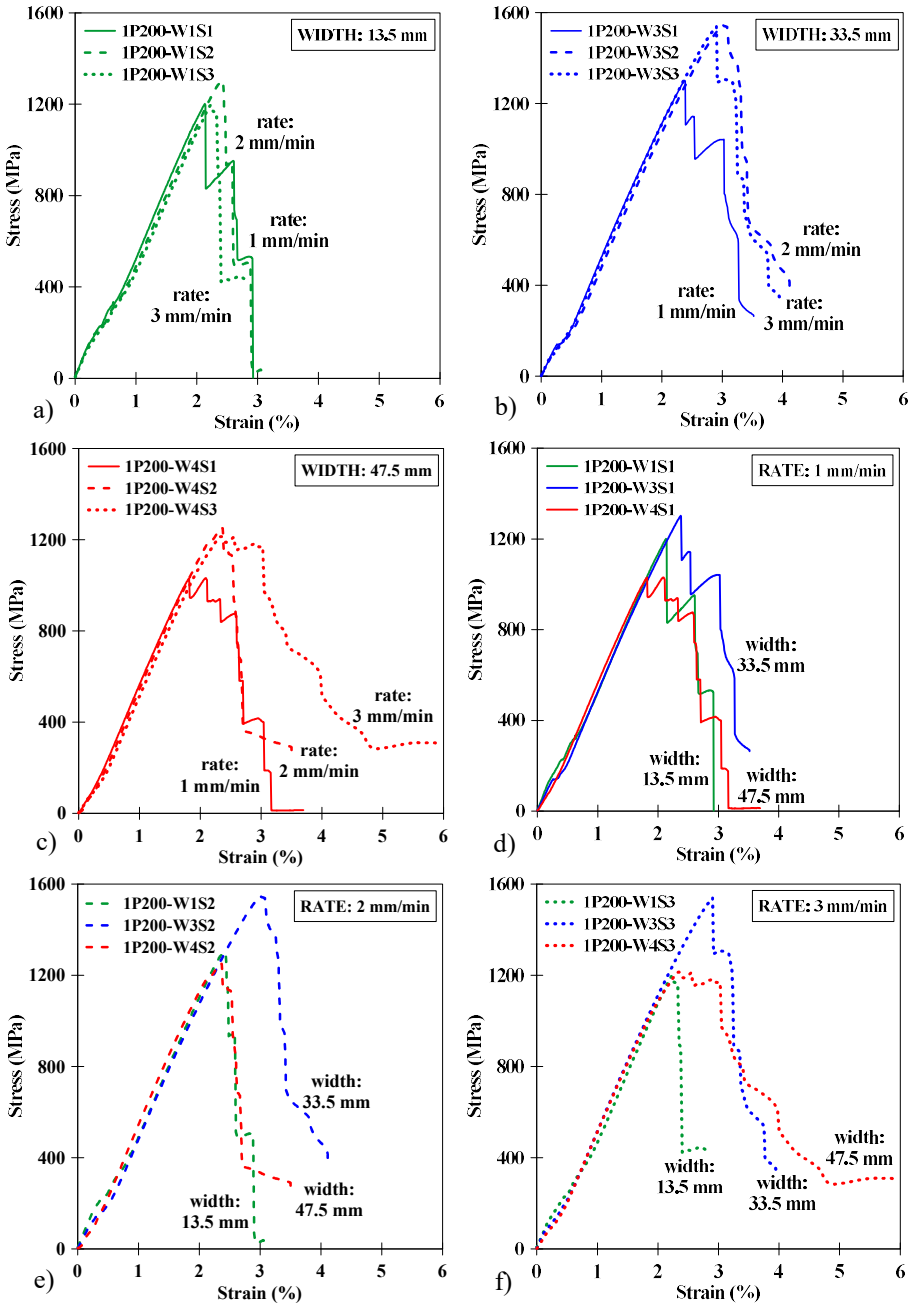

Figure 4.2 Stress-strain results of 200 mm long specimens, clamped using rough paper: a) b) c) set width and variable speed rate; d) e) f) set speed rate and variable width

Figure 4.3 shows the failure modes of the basalt textile strips tested by using rough paper as clamping device. Specimens with width equal to 13.5 mm were always characterized by the tensile failure of the grid close to the gripping area (Figure 4.3a). On the other hand, 33.5 mm wide specimens showed a rupture characterized by the slippage of the transversal yarns respect to the longitudinal ones at the gripping area, with consequent failure in this zone (Figure 4.3b). The same type of rupture interested one of the 47.5 wide specimens (1P200-W4S3) (Figure 4.3c), while the other two samples failed close to the gripping area, without undergoing slippage (Figure 4.3d).

Clamping by leather

Figure 4.4 presents the outcomes in terms of stress-strain for specimens clamped by leather. In particular, Figure 4.4a to Figure 4.4c show the results obtained setting the width of the specimens (13.5, 33.5 or 47.5 mm) and varying the speed rate (1, 2, 4 mm/min), while Figure 4.4d to Figure 4.4f present the same results plotted by setting the test speed and changing the width of the fabric strips. Table 4.3 presents the values of tensile strength and tensile strain at peak stress obtained for each tested specimen, along with the failure modes.

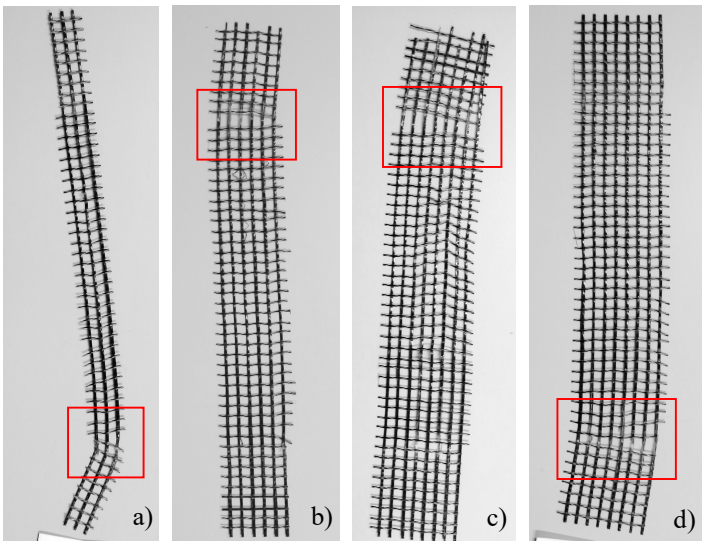

Figure 4.3 Failure modes of basalt textile strips tested by using rough paper in the gripping area: a) 13.5 mm wide specimen; b) 33.5 mm wide specimen; c) d) 47.5 mm wide specimens

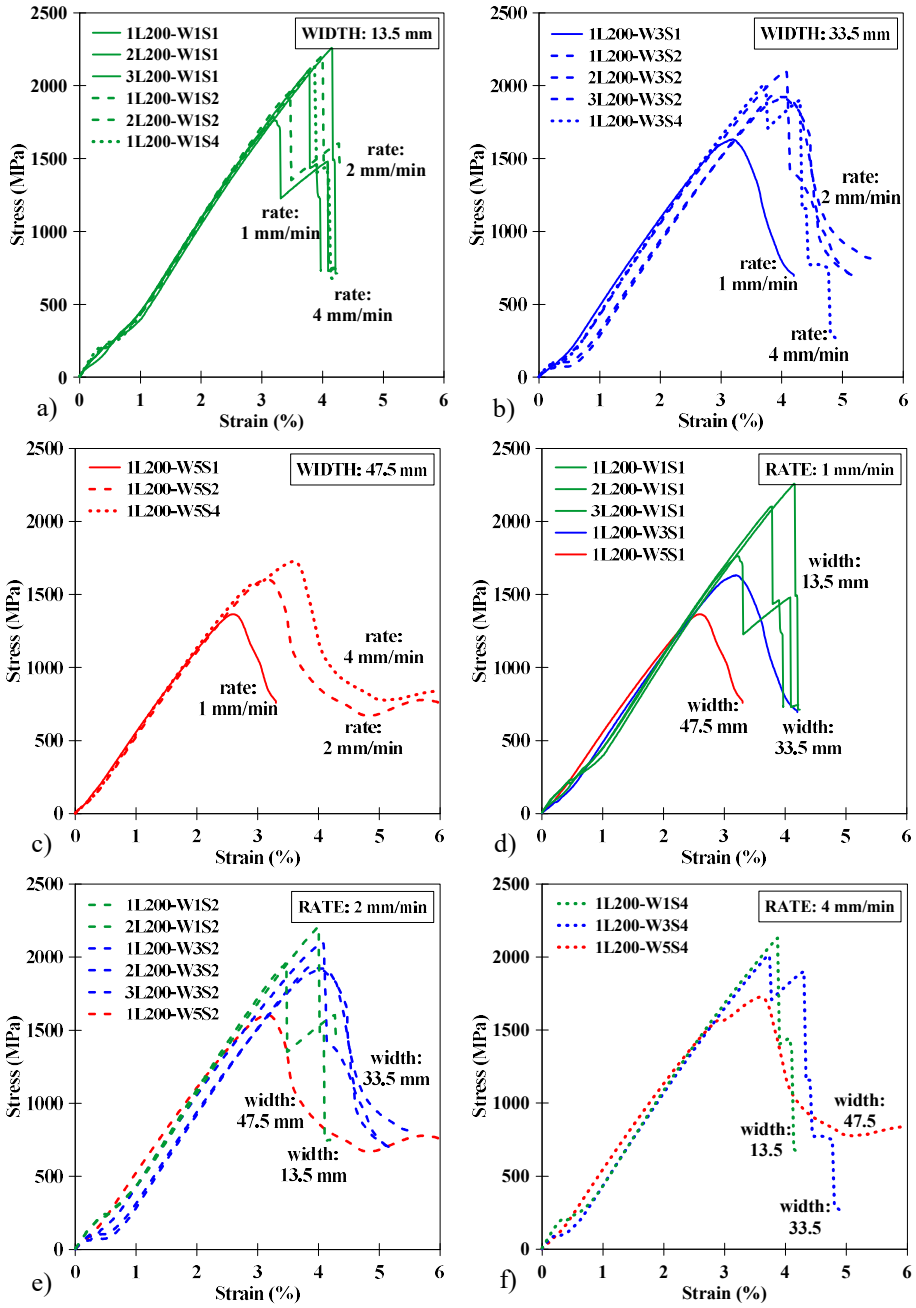

Figure 4.4 Stress-strain results of 200 mm long specimens, clamped using leather: a) b) c) set width and variable speed rate; d) e) f) set speed rate and variable width

The first aspect to be underlined is that, in general, all the curves show higher values of strength compared to those of specimens tested by using rough paper as clamping device. Thus, clamping by leather allowed better exploring the mechanical properties of basalt grid.

As already shown for samples tested using paper, even in this case the test speed of 1 mm/min gave lower results, apart from samples having width of 13.5 mm, which presented uniform results regardless of the speed rate. The obtained strength values for the speed rates of 2 mm/min and 4 mm/min were quite similar for 33.5 mm and 47.5 mm wide specimens respectively.

The comparison between the curves by fixing the test speed and changing the samples width, points out that the greatest values of strength are achieved when a width equal to 13.5 mm is employed and this is much more evident for the speed rate of 1 mm/min. On the other hand, very good results are also obtained for a width equal to 33.5 mm in the case of speed rates of 2 mm/min and 4 mm/min respectively.

As shown for the tests carried out using rough paper, even in this case all the curves are characterized by a change in stiffness in their first part due to the settlement of the test apparatus. After this limited stage, a linear trend develops up to failure, which generally is brittle.

Most of 33.5 and 47.5 mm wide samples presented problems of slipping during testing: this can be clearly detected from a very smooth post-peak branch of the stress-strain curves and it is also obvious by observing Figure 4.5a and Figure 4.5b. The latter show clearly the slipping of the transversal yarns along the longitudinal ones. In particular, for specimens with width of 33.5 mm, the slipping was followed by the rupture of the grid for some of the tested strips (Figure 4.5a), while 47.5 mm wide strips were characterized by slipping without tensile failure of the basalt cords (Figure 4.5b).

The failure mode of 13.5 mm wide specimens was by tensile rupture of the grid in the middle of the strips or close to the gripping zone (Figure 4.5c).

Three more samples were tested considering a gauge length of 150 mm instead of 200 mm. Figure 4.6a presents the curves of the three 13.5 mm wide samples, one tested at 1 mm/min rate, two tested at 2 mm/min. The results confirm that the lowest test speed gives the lowest values of strength. Moreover, in Figure 5.3b the outcomes are compared to those obtained from specimens

having the same width, but 200 mm long, with the aim of evaluating the influence of the length of the samples on the trend of the curves. It is clear that the reduced length of the specimens allows obtaining a more marked linear trend, avoiding the uncertainty in stiffness of the first part of the curves, thanks to a faster load transfer to the whole specimen. Figure 4.5d shows the failure mode of one of the samples after test.

Figure 4.7 compares the results obtained from 200 mm long samples equipped with paper and leather pieces respectively. Independently from the width of the specimens and despite the above-mentioned slipping phenomena, the use of leather allowed reaching higher values of stress for all the used test speeds, leading to better explore the basalt grid properties. The curves are very similar in their pre-peak trend.

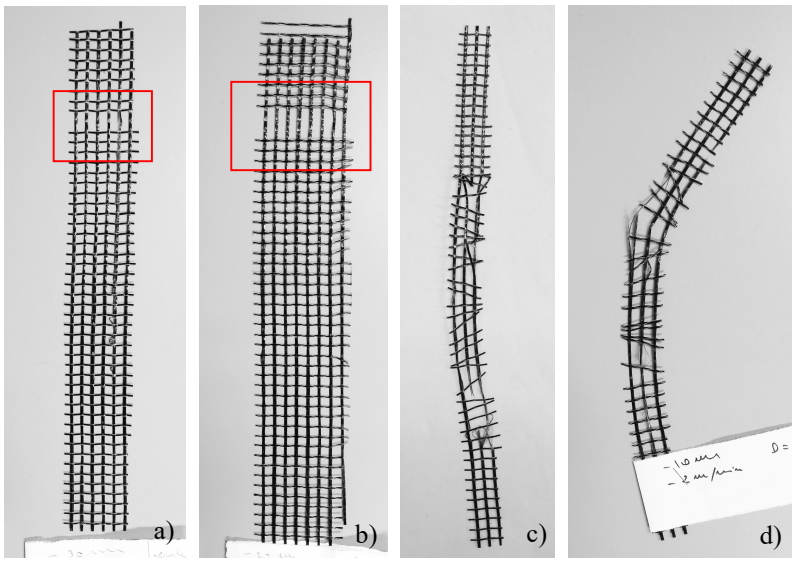

Figure 4.5 Failure modes of basalt textile strips tested by using leather in the gripping area: a) specimen with dimensions 33.5x200 mm; b) specimen with dimensions 47.5x200 mm; c) specimen with dimensions 13.5x200 mm; d) specimen with dimensions 13.5x150 mm

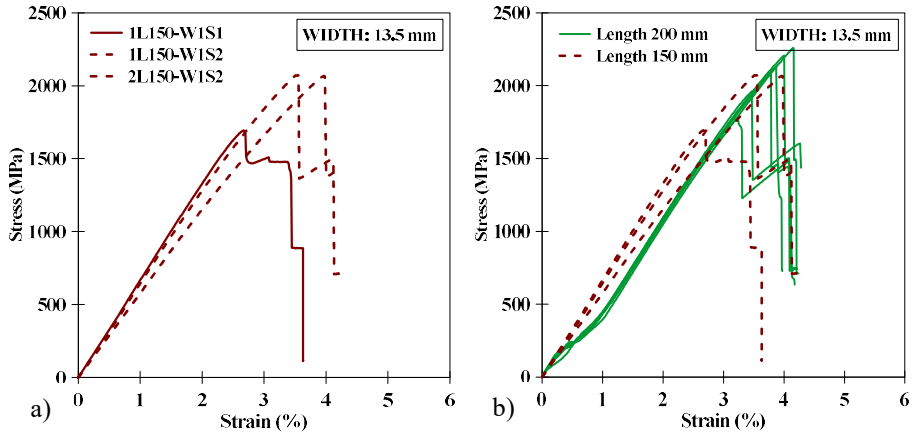

Figure 4.6 Stress-strain results of 150 mm long specimens, clamped using leather: a) set width and variable speed rate; b) comparison between the trend of 200 mm and 150 mm long specimens

Clamping by aluminium tabs

Figure 4.8a shows the stress-strain curves of the three tested basalt grid samples and the results in terms of tensile strength and tensile strain at peak stress are reported in Table 4.3, which presents also the failure mode of each tested specimen.

One of the samples was tested at 1 mm/min speed rate, the other two using a test speed of 2 mm/min, which gave better results as already observed for the previous tests.

In Figure 4.8b the outcomes are compared with those obtained from the fabric strips tested using leather pieces. Except of one curve, which shows a slightly lower Young's modulus, the results are coincident in terms of initial trend. Strength values obtained using aluminium tabs are slightly higher than those obtained from specimens equipped with leather at clamps.

The failure of the samples was characterized by progressive tensile rupture of the basalt yarns in the middle of the strips, while slipping phenomena were not observed.

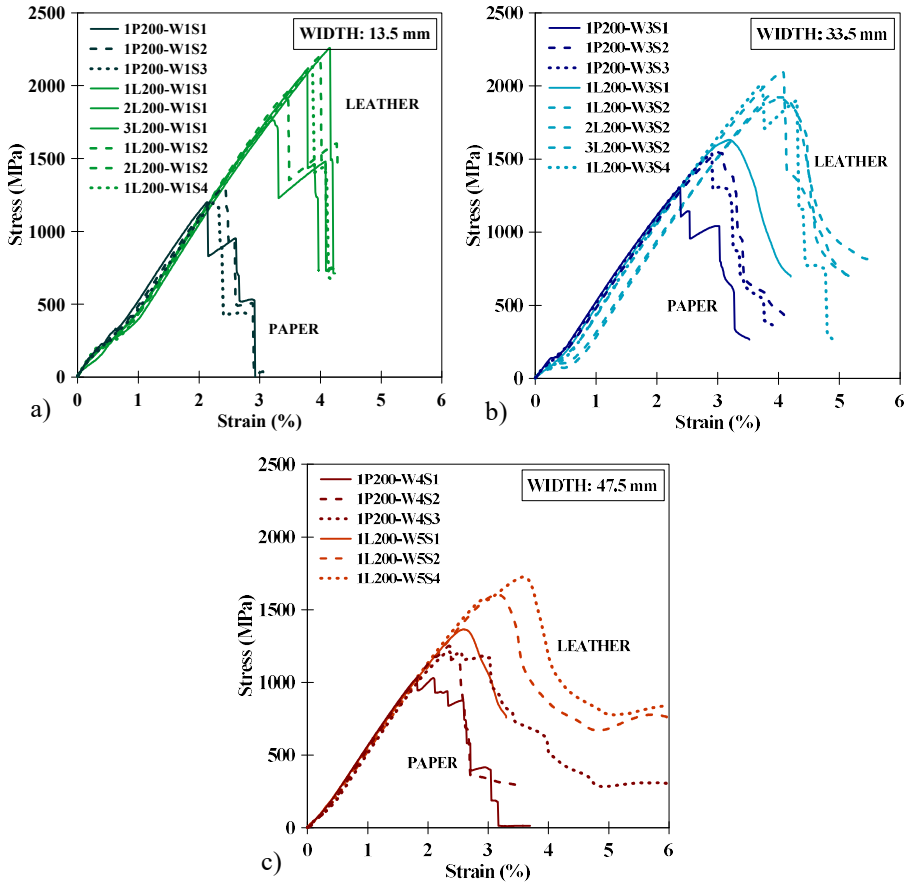

Figure 4.7 Comparison of stress-strain results obtained from 200 mm long specimens clamped using rough paper and leather respectively, setting the width

Considering the results of this preliminary investigation, it is possible to conclude that, in reference to the clamping method and the test speed, the most appropriate test setup in order to characterize the basalt textile was the one involving the use of aluminium tabs and a speed rate of 2 mm/min. Additionally, a width equal to 13.5 mm was chosen to carry out the tests presented in the next section. Indeed, considering the results obtained from tensile tests on samples clamped employing leather (which are much better than those obtained using paper), 13.5 wide specimens gave the best outcomes in terms of strength, independently from the used speed rate (1 mm/min, 2 mm/min, 4 mm/min) and the textile failure was always reached.

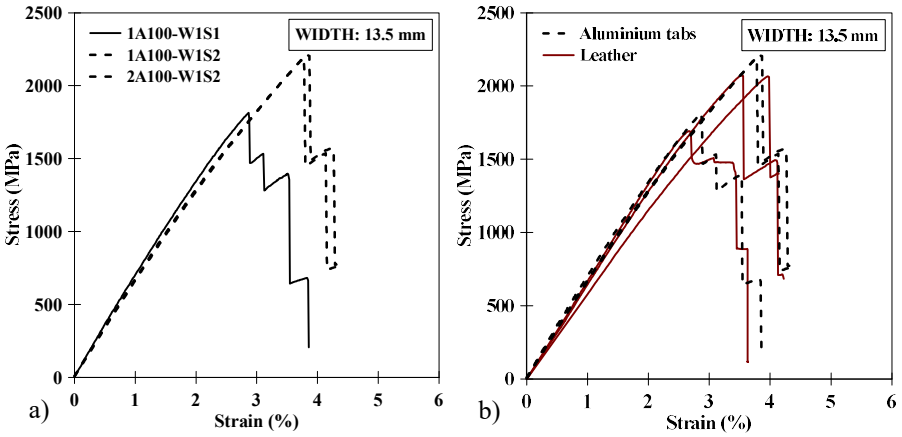

Figure 4.8 Stress-strain results of specimens equipped with aluminium tabs at the ends: a) set width and variable speed rate; b) comparison between results of strips equipped with aluminium tabs and leather pieces

On the other hand, 33.5 and 47.5 mm wide strips, showed a pre-peak loss of linearity, as well as a post-peak softening behaviour, underlining the presence of slipping phenomena, probably due to the greater difficulty to guarantee a uniform load distribution among a larger number of cords.

Results of tensile characterization tests on basalt fabric strips

As mentioned above, the results in terms of strain presented so far were obtained by the global displacement of the machine cross-head. However, this displacement hardly corresponds to the displacement applied to the specimen because of the lack of rigidity of the system. Then, these outcomes were useful to study the basalt grid behaviour in relation to the clamping system, the testing speed rate and the geometry of the samples. Nevertheless, the need to have more reliable displacement/strain information led to introduce the use of the videoextensometer, taking advantage from the DIC technique, as discussed in Chapter 3.

To confirm the advantage of introducing the use of the videoextensometer, Figure 4.9 presents the stress-strain result of tensile test on a basalt textile strip tested with the support of the videoextensometer. In particular, this result is compared to the outcomes presented above (Figure 4.8a) and obtained from

samples having the same characteristics, but tested obtaining the strains from the global displacement of the machine cross-head.

Table 4.3: Preliminary test results of basalt grid strips

Clamping method	Sample	Tensile strength [MPa]	Tensile strain [mm/mm]	Failure mode
PAPER	1P200-W1S1	1201.87	2.13	A
	1P200-W1S2	1300.81	2.44	A
	1P200-W1S3	1195.92	2.23	A
	1P200-W3S1	1302.31	2.38	C
	1P200-W3S2	1539.38	2.90	C
	1P200-W3S3	1546.69	3.0	C
	1P200-W4S1	1030.76	2.08	A
	1P200-W4S2	1253.00	2.35	A
	1P200-W4S3	1213.33	2.35	C
LEATHER	1L200-W1S1	2103.38	3.78	A
	2L200-W1S1	1765.94	3.21	A
	3L200-W1S1	2214.50	4.05	B
	1L200-W1S2	1961.39	3.47	B
	2L200-W1S2	2206.78	4.0	A
	1L200-W1S4	2129.43	3.87	A
	1L200-W3S1	1631.88	3.18	D
	1L200-W3S2	2101.72	4.07	C
	2L200-W3S2	1916.20	4.03	D
	3L200-W3S2	1934.43	3.87	D
	1L200-W3S4	2009.21	3.74	C
	1L200-W5S1	1365.02	2.59	D
	1L200-W5S2	1601.61	3.17	D
	1L200-W5S4	1725.31	3.57	D
	1L150-W1S1	1813.45	2.87	A
	1L150-W1S2	2191.78	3.78	B
	2L150-W1S2	2215.46	3.82	B
ALL TABS	1A100-W1S1	1693.75	2.67	B
	1A100-W1S2	2066.60	3.96	B
	2A100-W1S2	2072.38	3.65	B

A: tensile failure near the gripping area; B: tensile failure in the middle of the specimen; C: textile slippage in the gripping area with tensile rupture; D: textile slippage in the gripping area without tensile rupture

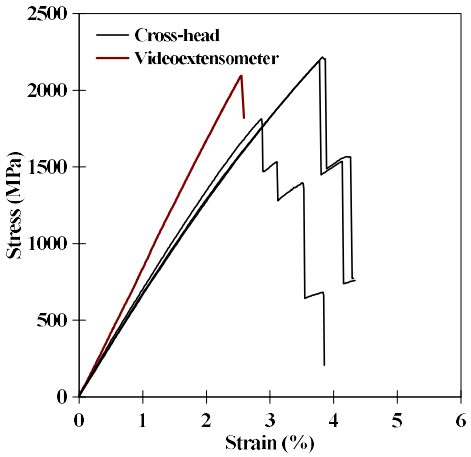

Figure 4.9 Comparison between stress-strain curves of basalt textile obtained from the videoextensometer and the testing machine cross-head

The comparison shows clearly that the curve obtained through the use of the videoextensometer is stiffer than those plotted referring to the testing machine cross-head displacement, being latter affected by the rigidity of the system. This result justifies the employment of the videoextensometer for all the characterization tests on basalt textile samples presented in the following.

In Figure 4.10 the experimental stress-strain curves deduced from characterization tests on basalt grid specimens are shown. The tests results are presented in Table 4.4 in terms of tensile strength, tensile strain and elastic modulus; the corresponding average values are also reported along with the COV. The basalt fabric strips were tested along the warp direction, which coincided with the circumferential direction when wrapped around the cylinders, and the weft direction. The tensile curves of the specimens tested along the longitudinal (Figure 4.10a) and the transversal direction (Figure 4.10b) show a linear trend characterized by the brittle failure of some or all rovings in the strips width. Figure 4.11 shows some of the basalt specimens after failure. Slipping phenomena inside the gripping area were not observed.

The average peak stress and strain, averaged from twelve samples tested along the warp direction, were 2045 MPa and 2.6 % respectively, both higher than the values provided by the manufacturer. It should be noted that the value provided by the manufacturer (1542 MPa) and reported in Table 4.4 was obtained considering the load-resistant area per unit of width (38.91 mm^2/m). The

experimental average elastic modulus was 82 GPa, slightly lower than the value provided by the manufacturer (Table 4.4). The values obtained from the specimens tested along the weft direction were 1983 MPa, 2.4 % and 82 GPa respectively for the average strength, average strain and average Young's modulus.

Table 4.4: Results of basalt grid tests

Sample	Tensile strength [MPa]	Av. Tensile strength [MPa] and COV	Tensile strain [%]	Av. Tensile strain [%] and COV	Elastic modulus [GPa]	Av. Elastic modulus [GPa] and COV
S_1	2162	2045 (10.55 %)	2.50	2.55 (8.21 %)	84.02	81.91 (3.48 %)
S_2	2431		2.92		87.96	
S_3	2289		2.87		81.08	
S_4	2221		2.70		84.18	
S_5	2096		2.55		88.73	
S_6	1976		2.60		80.64	
S_7	1941		2.44		79.35	
S_8	1779		2.56		81.32	
S_9	2037		2.39		81.03	
S_10	2083		2.58		83.07	
S_11	1703		2.20		77.26	
S_12	1819		2.31		79.24	
S_1	2170	1983 (7.80 %)	2.75	2.40 (12.05 %)	79.01	81.88 (4.60 %)
S_2	2078		2.51		82.84	
S_3	2130		2.49		85.72	
S_4	2073		2.43		85.44	
S_5	1942		2.31		84.10	
S_6	1874		2.40		78.01	
S_7	2053		2.72		75.37	
S_8	1790		2.21		80.98	
S_9	1736		1.78		85.46	
Manufacturer values	**1542***		**1.80**		**89.00**	

* The tensile strength value provided from manufacturer was 60 kN/m. The value 1542 MPa was obtained considering the load-resistant area per unit of width (38.91 mm^2/m)

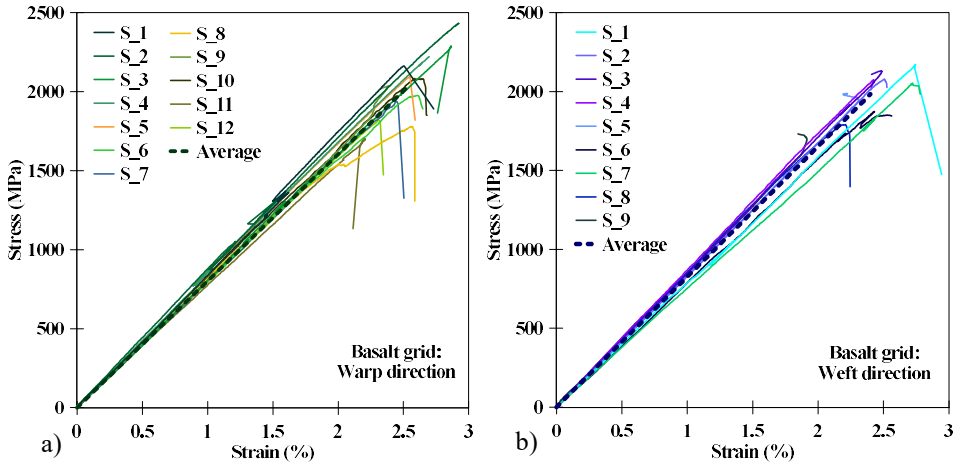

Figure 4.10 Stress-strain curves for basalt fibre: a) warp direction; b) weft direction

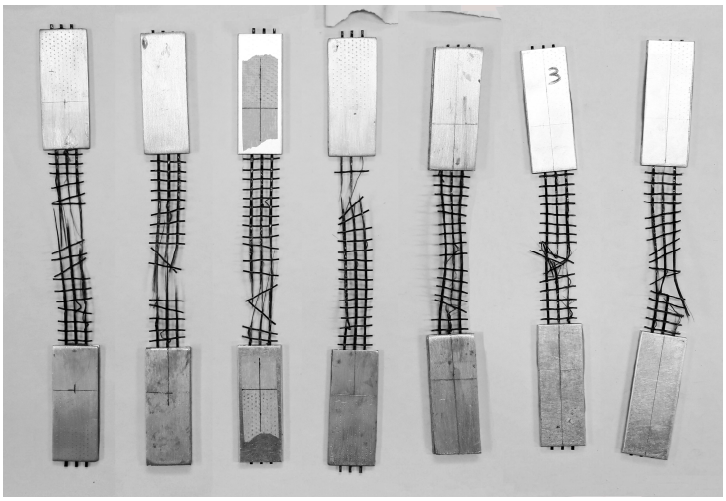

Figure 4.11 Basalt textile strips after failure

4.2.4 Three point bending tests on mortar matrix prisms

With reference to the mortar adopted as matrix of the BFRCM system, the load-deflection curves of six mortar prisms are shown together in Figure 4.12, while the main test results are presented in Table 4.5, along with the average value and the COV.

Table 4.5: Results of three point bending tests on mortar prisms

Sample	Flexural strength [MPa]	Av. flexural strength [MPa] and COV
1	5.84*	7.18 (2.8 %)
2	7.34	
3	7.18	
4	7.03	
5	7.42	
6	6.95	

* Value excluded from the average value calculation

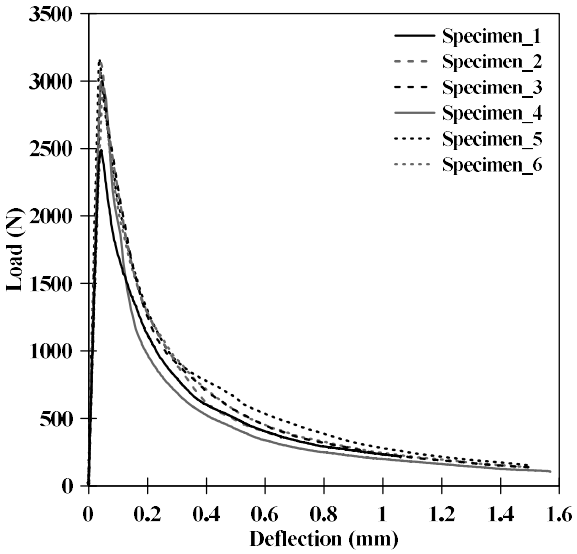

Figure 4.12 Load-deflection curves from three-point bending tests on mortar matrix samples

4.3 Tensile tests on BFRCM composite coupons

The results obtained from tensile tests on BFRCM coupons are here presented. First, the outcomes of the analysis performed through the use of DIC by varying the position of the virtual extensometers on the front surface and the thickness of the specimens are discussed.

Then, the results of the tests are analyzed in terms of load-strain and stress-strain curves, exploring the role of the number of fabric layers on the tensile behaviour of the three series of specimens.

Finally, the strain/displacement full-field analyses carried out by the DIC technique on the surface of the composite specimens are used to discuss the crack pattern evolution and the strain distribution for coupons strengthened with different reinforcement ratios. The failure mode are also commented.

4.3.1 Results of analysis with virtual extensometers (DIC)

For clarification of the results that will be presented in the following, the outcomes of the analysis carried out by varying the position of the facets on the surface of the coupons are here discussed.

At a first step, the front side of the specimens was analyzed and the results achieved by the three virtual extensometers placed as discussed in the previous chapter were evaluated. The comparison between the outcomes of these measurements allowed checking the uniformity of response of the tested specimens and the absence of load eccentricities or manufacturing defects. Figure 4.13 presents the tensile stress-strain curves for three specimens reinforced with one layer of basalt grid. For each specimen the records of the three virtual extensometers placed on the front side (Figure 4.13a) are shown.

The curves point out as the results of the correlation for the three virtual extensometers, for one-layer strengthened specimens, are not scattered. Considering the readings of the three extensometers for each specimen, the scatter between the strains at peak stress ranges from 0.16% and 4% and this result confirms the absence of important unexpected bending effects in the plane of the specimens.

Similarly, Figure 4.14 shows the position of the virtual extensometers (Figure 4.14a) and the stress-strain curves of three specimens reinforced with two or three basalt textile layers. Results of specimen SP2_2L (Figure 4.14b) show a scatter between readings from the three virtual extensometers equal to 2.3%, which underlines, once again, the absence of considerable bending effects in the plane of the specimen.

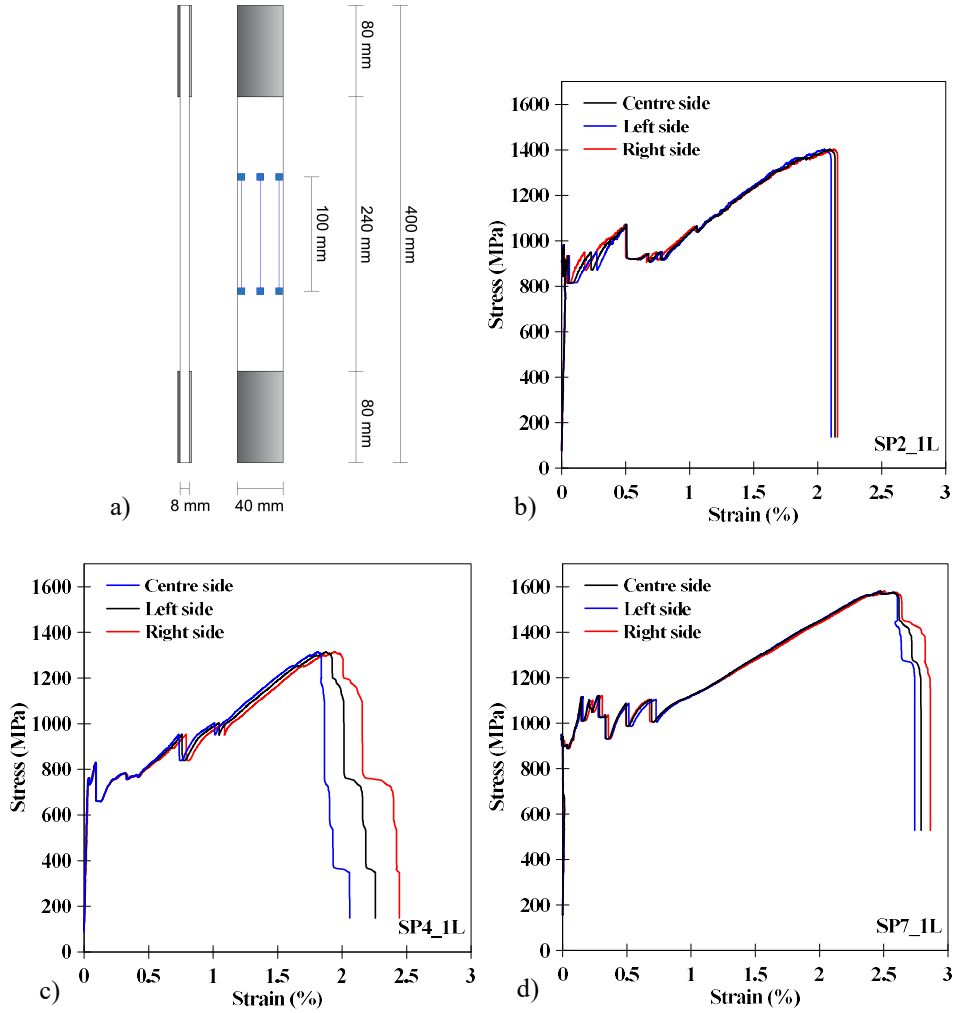

Figure 4.13 Variability of stress-strain results obtained changing the position of the facets on the front side of one-layer reinforced specimens: a) chosed position of facets; b) c) d) stress-strain curves obtained from three virtual extensometers

Similar results were found for sample SP1_3L (Figure 4.14d), with a low value of scatter equal to 3%. On the other hand, Figure 4.14c points out a certain difference in the results of the three extensometers, with a scatter of about 14% relating to strains at peak stress. This result evidences a not really uniform load distribution over the cross-section of specimen SP4_2L. This is due to the fact that, during testing, starting from the end of the second stage, this specimen was

affected by slight slipping inside the clamping area with a consequent non-uniform load distribution over his cross-section. Similar outcomes were obtained from specimens SP3_2L and SP5_2L. It is worth to note that these three samples showed lower results in terms of peak stress compared to the other two-layer reinforced specimens, as it will be discussed in the following.

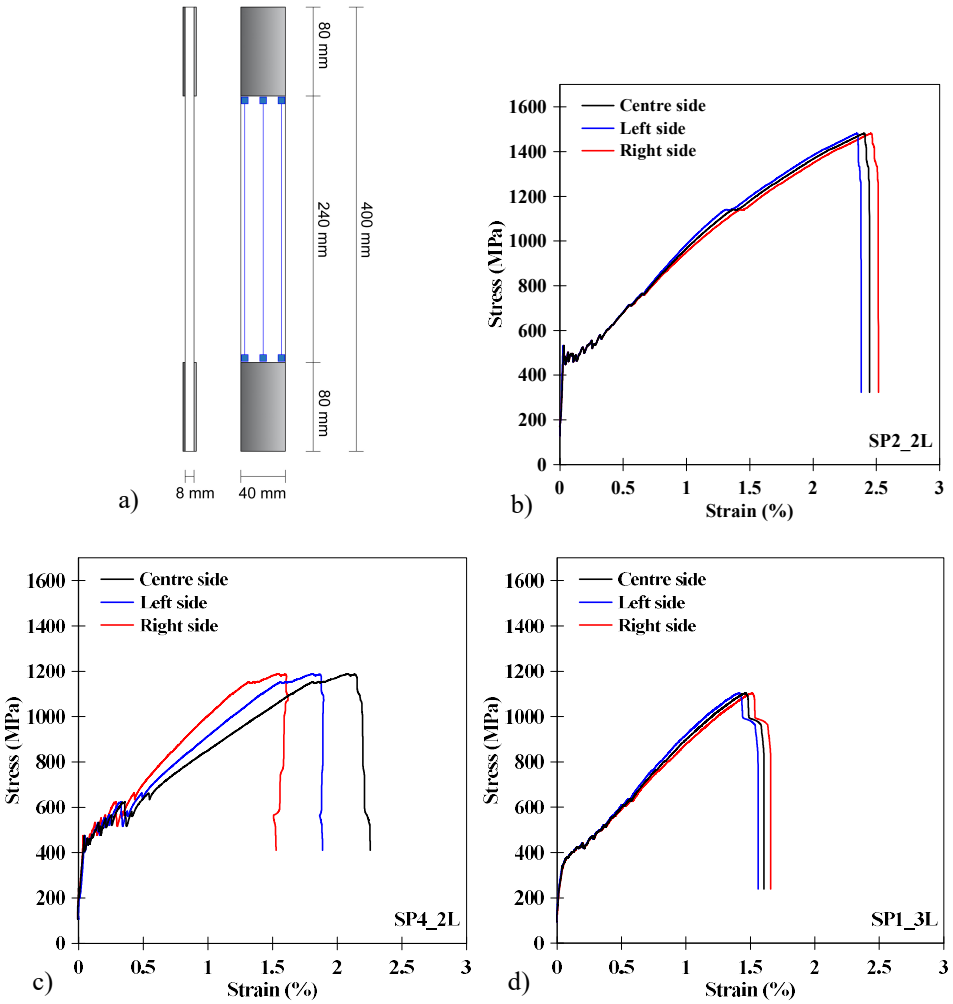

Figure 4.14 Variability of stress-strain results obtained changing the position of the facets on the front side of two and three-layer reinforced specimens: a) chosed position of facets; b) c) d) stress-strain curves obtained from three virtual extensometers

In a second step, data acquired by the videoextensometer and related to the thickness of the specimens were processed with the aim of investigating on possible out-of-plane bending effects. Then, two vertical virtual extensometers were tracked along the thickness surface of the samples (Figure 4.15a).

Figure 4.15b and Figure 4.15c report the outcomes of two tested specimens. In this case, the results obtained from the readings of the two extensometers for each sample are very consistent, underlining a uniform cracks development along the front and back surface of the specimens and the absence of important defects causing out-of-plane curvature of the samples.

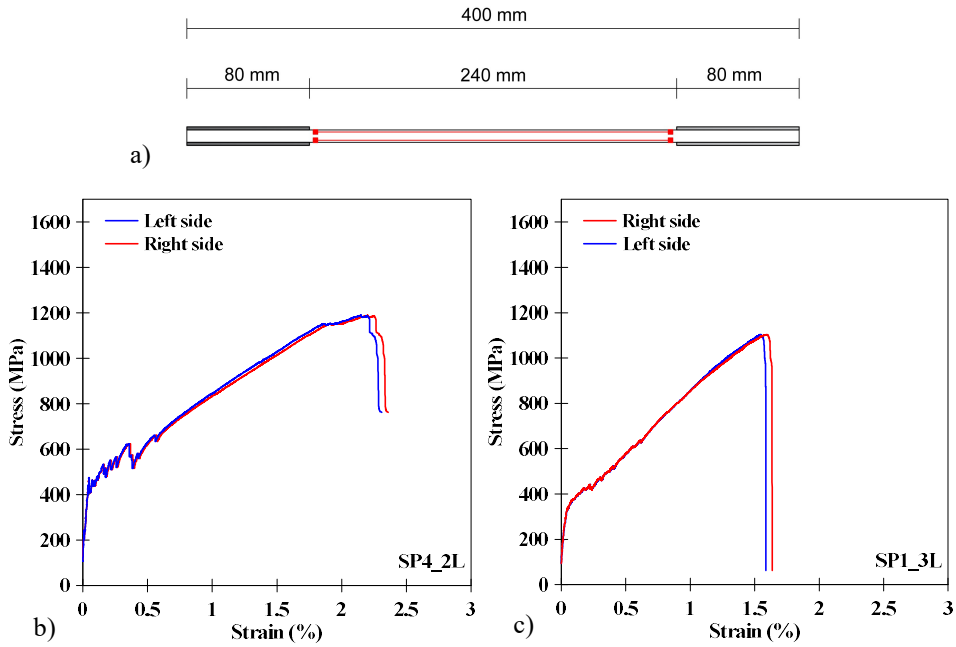

Figure 4.15 Variability of stress-strain results obtained changing the position of the facets on the thickness surface of the specimens: a) chosed position of factes; b) c) stress-strain curves obtained from two virtual extensometers

4.3.2 Load-strain curves

As it was shown in the previous section, the readings from different virtual extensometers positioned on the front side or on the thickness surface of the samples were found to be very close, highlighting the absence of significant

defects in the specimens or in the test setup. For this reason, in the following the load-strain curves are analyzed with reference to the measurement recorded by the central virtual extensometer on the front side of each specimen.

In order to discuss the characteristic behaviour of the employed mortar-based system under tension, Figure 4.16a shows the experimental result of one of tested specimens (SP1_2L), with the indication of different stages and characteristic points. Moreover, for a more immediate visualization of the tensile behaviour, the evolution of the crack pattern obtained through the use of the DIC is shown in Figure 4.16b, where each image corresponds to a specific point of the load-strain curve (Figure 4.16a).

As already well known in the literature, the curve shows a trilinear trend in which three stages can be clearly detected, such as un-cracked (I), crack development (II) and crack widening (III).

Stage I is characterized by a linear response of the undamaged specimen and the mortar provides a considerable contribution to both load bearing capacity and stiffness. This branch ends when the stress exceeds the tensile strength of the matrix and the first crack appears in the mortar.

The second branch (Stage II), characterized by several jumps and reduced stiffness, is due to the formation of several cracks in the matrix. First, cracks generally formed in the middle of the specimen and close to its ends (stages a and b of Figure 4.16b). Then, subsequent cracks occurred between existing ones until the matrix crack saturation was achieved (stages c and d of Figure 4.16b). This stage ends when crack number stabilizes.

In the last stage (Stage III) additional imposed strain causes the widening of existing cracks, while new ones are not developed generally (stages e, f, g of Figure 4.16b). A stiffness increase occurs and the curve regains a more regular, smooth trend, but with a lower slope than that shown in the first stage. The load bearing capacity and the tensile modulus mainly depend on the textile, although the uncracked matrix between cracks may still provide transversal load redistribution. This phase ends when the tensile rupture of the reinforcement is reached (stage h of Figure 4.16b).

The sensitivity of the tensile behaviour of FRCM coupons to the reinforcing textile ratio can be deduced by observing the tensile load-strain curves obtained from all the tested specimens, reported in Figure 4.17.

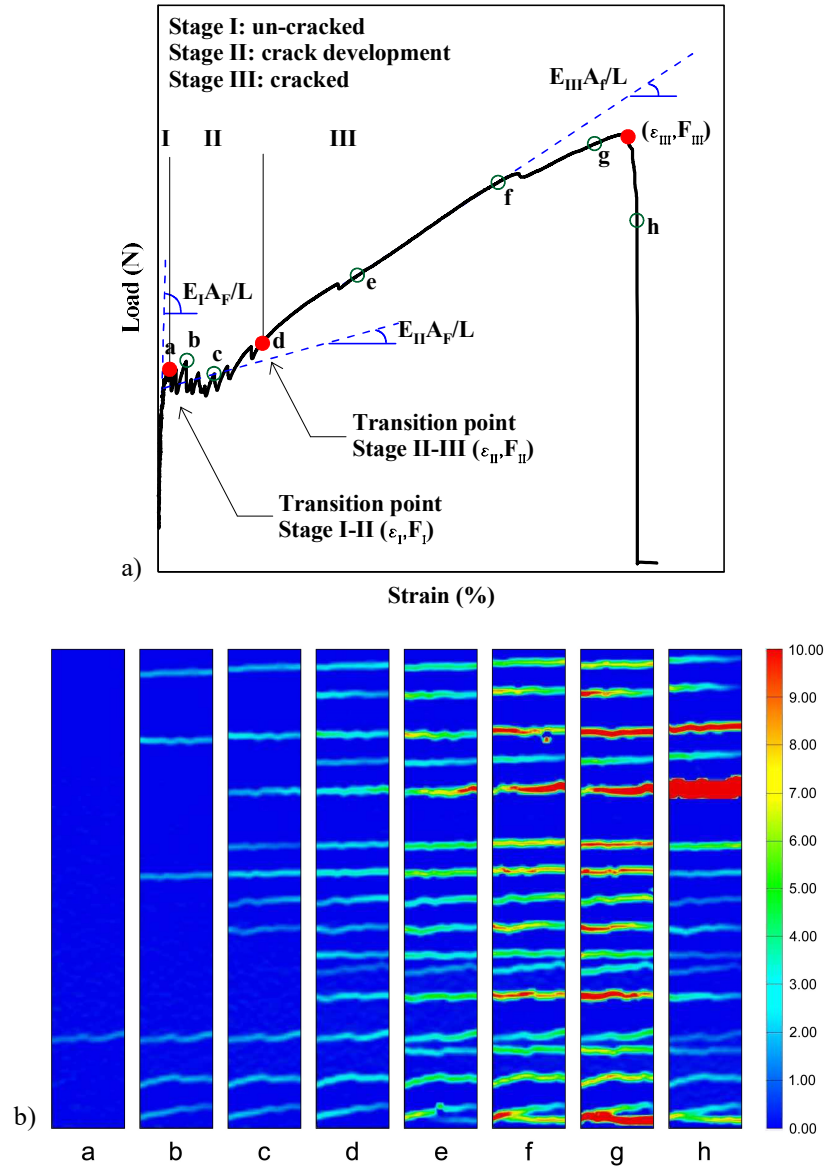

Figure 4.16 Characteristic response of composite specimens: a) load-strain curve of specimen SP1_2L, representing characteristic stages and points; b) crack pattern evolution for specimen SP1_2L

As expected, the initial slope of the curves is similar for all the tested specimens. The transition from Stage I to Stage II for one-layer reinforced

specimens is characterized by a more drastic drop of the stress after the formation of the first crack in the matrix, due to the low fabric volume fraction, insufficient to absorb the energy released at the first crack. The same happens during the formation of following cracks. The use of multiple layers of textile made the system more efficient when passing from the uncracked to the cracked stage and jumps due to the formation of cracks involve a lower stress reduction.

After the formation of the first crack, specimens with two and three grid layers appear to give raise to a larger number of progressively closely spaced cracks compared to one-layer series. The length and the slope of Stage II are influenced by the volume proportion of the fibres activated for the load transfer. In particular, the slope of the second branch increases with the number of grid layers. On the other hand, specimens reinforced with one layer show a greater extension of the second branch, compared to two and three-layer strengthened samples (Figure 4.17).

The post-treatment of the experimental data allowed the definition of the peak loads F_I, F_{II}, F_{III} (Figure 4.16a) related to the end of the three stages which characterize the tensile behaviour of BFRCM specimens. In Table 4.6 these values are presented for each specimen, except for specimen SP1_1L for which only the value of F_{III} is reported because of a discrepancy of the outcomes referred to Sage I and Stage II compared to those of the other specimens. Moreover, the average values referred to specimens of the same series and the corresponding COV are reported (Table 4.6).

In general, BFRCM coupons with higher reinforcement ratio carried higher maximum load, but the load increase was not proportional to the reinforcement ratio: +17% and +16% increments for Stage I, for SP_2L and SP_3L series respectively compared to SP_1L series; +33% and +30% for Stage II; +72% and +125% for Stage III.

These outcomes show that the average force F_I recorded at the end of the first stage for the three series of specimens is not subjected to large variations and this is due to the mechanical properties of the mortar. On the other hand, Stage II and III are more related to the reinforcement ratio and the bearing capacity (F_{III}) increases for higher reinforcing fabric ratios.

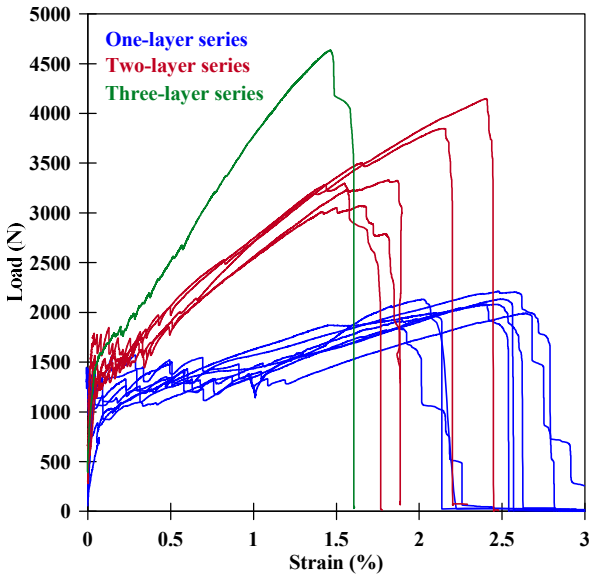

Figure 4.17 Load-strain curves of BFRCM composite coupons

4.3.3 Stress-strain curves

Figure 4.18a to Figure 4.18c present the stress-strain curves of the sets of BFRCM coupons, reinforced with one, two and three layers respectively. For two and three-layer series respectively, the trilinear curve passing through the average characteristic points obtained from specimens of the same series is reported in the corresponding graph; the trilinear curve is also depicted for specimen SP1_3L (Figure 4.18c). Moreover, the outcomes of the three sets of samples are shown together in Figure 4.19a, for a more convenient comparison between the series. In Figure 4.19b the trilinear curves of one, two and three-layer reinforced specimens are plotted with the average stress-strain curve obtained from tensile tests on dry basalt textile.

It is worth to note that the tensile stresses σ of the specimens, represented in the ordinate of the graphs, refer to the ratio between the applied load and the cross sectional area of plain textile (F/A_f), as suggested by the code AC434 (2013) and already done in many studies in the literature (De Santis and De Felice 2015a, Ascione et al. 2015). The area of the internal reinforcement A_f was calculated, for consistency with the procedure used for the textile, considering

the number of yarns in each textile layer and the number of textile layers used as reinforcement of the composite specimen. Additionally, the secondary y-axis shows the tensile stresses evaluated by dividing the load by the full area of the FRCM system, A_{FRCM}, according to the recent RILEM recommendations about test methods for FRCM materials (RILEM TC 232-TDT 2016).

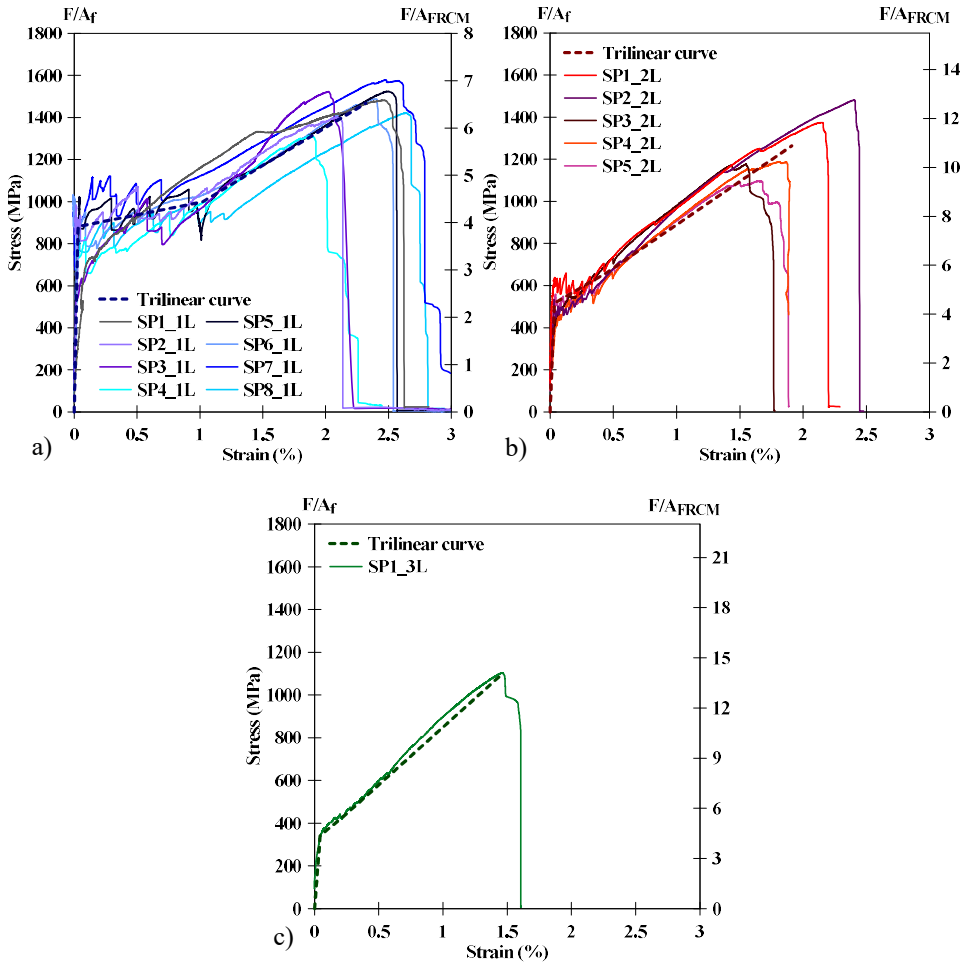

Figure 4.18 Stress-strain curves of BFRCM composite coupons: a) one-layer reinforced samples; b) two-layer reinforced samples; c) three-layer reinforced sample

Table 4.6 presents the experimental results in terms of peak stresses (σ_I, $\sigma_{II,}$ σ_{III}) and corresponding strains (ε_I, $\varepsilon_{II,}$ ε_{III}), evaluated at the end of each stage of the tensile stress-strain curves of FRCM specimens. Additionally, the values of the moduli were calculated as the slope of the curve in the three branches. In particular, the slope of Stage II was evaluated by fitting the stress-strain curve between points (σ_I, ε_I) and (σ_{II}, ε_{II}), which in general produces a slope different from the one obtained by connecting points (σ_I, ε_I) and (σ_{II}, ε_{II}) (D'Antino and Papanicolaou 2017). These values are reported for each specimen of the three series, along with the average values and the COV. As mentioned before, for SP1_1L only the values related to Stage III are indicated.

Comparing the three sets of composite samples represented in Figure 4.19, the stress-strain curves show that the peak stress of the coupons at the end of each stage decreases when the reinforcement ratio increases. This occurs for the first and second branch and in a less marked way for the third branch (stress at failure).

Two-layer reinforced series compared to one-layer series showed an average decrease of 41%, 34%, 14% respectively for Stage I, II and III, while the same decreases for specimens reinforced with three layers were equal to 61%, 57% and 25% respectively. It is evident that the stress reductions are more marked in the case of higher reinforcement ratio, and this may be due to the reduced thickness of mortar between textile layers in over-reinforced specimens. The small thickness of mortar did not allow an adequate redistribution of the stresses between the cords of the grid and made the performance of the strengthening system very sensitive to misalignment.

Considering the values of F_I at the end of Stage I for each specimen, the mean stress in the mortar was evaluated for each series at the transition point between Stage I and Stage II (first crack in the mortar), dividing the load by the homogenized cross-section of the composite specimens, in which the area of the textile was amplified by the ratio between the tensile Young's modulus of the two materials (fibre and matrix). The obtained stress values at the transition point (σ_I) were always lower compared to the tensile strength of the mortar: the average values 3.60 MPa, 4.15 MPa and 3.87 MPa were found for specimens reinforced with one, two and three layers respectively, with reductions of 49%, 42% and 46% with respect to the tensile strength of the mortar (7.18 MPa). Indeed, it is

well known that three point bending tests may produce an overestimation of the actual tensile strength of the mortar.

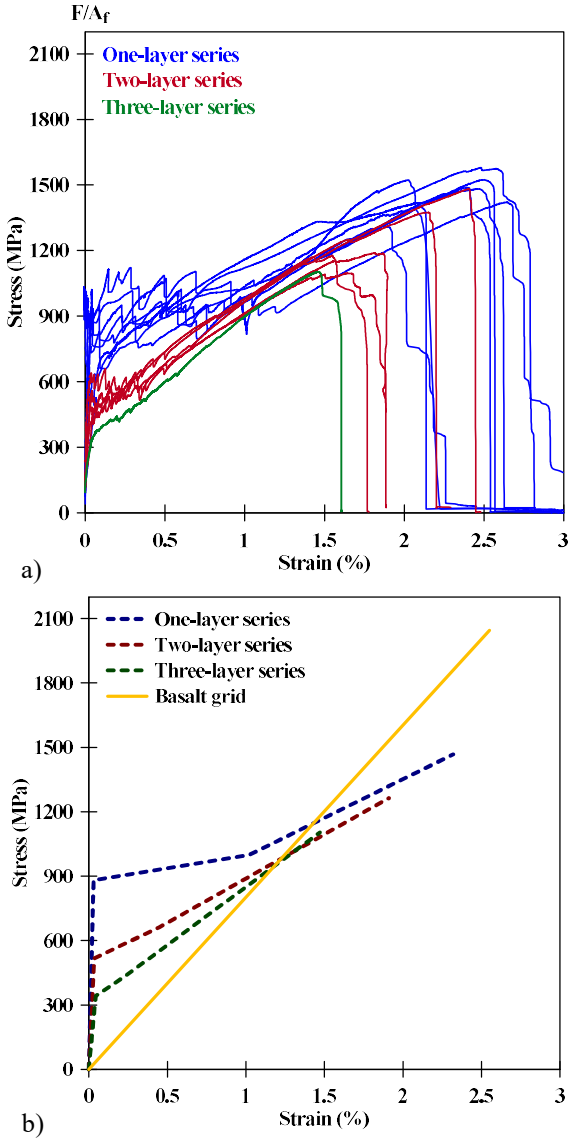

Figure 4.19 Stress-strain curves of BFRCM composite coupons: a) comparison between series strengthened using different reinforcement ratios; b) relation between trilinear curves of BFRCM series and basalt grid

Table 4.6: Results of BFRCM coupons in Stage I, II and III

	Samples	Peak load [kN]	Peak stress [MPa]	Strain [%]	Tangent modulus [GPa]
Stage I		F_I	σ_I	ε_I	E_I
	SP1_1L	-	-	-	-
	SP2_1L	1306.85	933.46	0.048	1947.14
	SP3_1L	756.24	540.17	0.015	3684.67
	SP4_1L	1067.87	762.76	0.034	2233.56
	SP5_1L	1427.38	1019.56	0.042	2432.16
	SP6_1L	1446.39	1033.13	0.018	5739.64
	SP7_1L	1315.78	939.84	0.021	4475.45
	SP8_1L	1318.24	941.60	0.035	2653.89
	Average (COV %)	**1234.11 (19.8 %)**	**881.50 (19.8 %)**	**0.030 (41.8 %)**	**3309.50 (42 %)**
	SP1_2L	1788.57	638.77	0.038	1690.90
	SP2_2L	1491.68	532.74	0.031	1722.97
	SP3_2L	1063.47	379.81	0.015	2566.29
	SP4_2L	1331.08	475.39	0.048	987.92
	SP5_2L	1566.32	559.40	0.041	1353.67
	Average (COV %)	**1448.22 (18.7 %)**	**517.22 (18.7 %)**	**0.035 (36.7 %)**	**1664.35 (35.2 %)**
	SP1_3L	1437.38	342.23	0.044	786.74
Stage II		F_{II}	σ_{II}	ε_{II}	E_{II}
	SP1_1L	-	-	-	-
	SP2_1L	1318.42	941.73	0.826	9.33
	SP3_1L	1264.24	903.03	0.862	38.57
	SP4_1L	1426.55	1018.96	1.145	26.33
	SP5_1L	1517.34	1083.82	1.202	6.05
	SP6_1L	1430.40	1021.71	0.979	18.55
	SP7_1L	1523.73	1088.38	0.874	11.53
	SP8_1L	1305.57	932.55	1.242	8.70
	Average (COV %)	**1398.03 (7.4 %)**	**998.60 (7.4 %)**	**1.019 (17.2 %)**	**17.01 (69.2%)**
	SP1_2L	1973.63	704.87	0.458	18.66
	SP2_2L	1693.58	604.85	0.383	31.07
	SP3_2L	1896.52	677.33	0.411	65.45
	SP4_2L	1885.00	673.21	0.531	40.87
	SP5_2L	1827.60	652.71	0.460	26.48
	Average (COV %)	**1855.26 (5.6 %)**	**662.59 (5.6 %)**	**0.448 (12.5 %)**	**36.51 (49.5%)**
	SP1_3L	1821.68	433.73	0.229	43.78
Stage III		F_{III}	σ_{III}	ε_{III}	E_{III}
	SP1_1L	2080.92	1482.14	2.463	-
	SP2_1L	1964.19	1402.99	2.096	36.31
	SP3_1L	2132.64	1523.32	2.028	53.22

SP4_1L	1841.98	1315.70	1.876	40.61
SP5_1L	2134.09	1524.35	2.503	33.86
SP6_1L	2083.79	1488.42	2.392	33.01
SP7_1L	2211.45	1579.61	2.577	28.84
SP8_1L	1990.37	1421.69	2.643	34.93
Average (COV %)	**2054.93 (5.7 %)**	**1467.28 (5.7 %)**	**2.322 (12.2 %)**	**37.25 (21.2 %)**
SP1_2L	3847.49	1374.10	2.151	39.53
SP2_2L	4149.43	1481.94	2.405	43.38
SP3_2L	3295.68	1177.03	1.549	43.89
SP4_2L	3328.44	1188.73	1.815	40.14
SP5_2L	3069.95	1096.41	1.641	37.56
Average (COV %)	**3538.20 (12.6 %)**	**1263.64 (12.6 %)**	**1.912 (18.8 %)**	**40.90 (6.6 %)**
SP1_3L	4633.19	1103.14	1.466	54.13

The response curves of some two-layer reinforced specimens (SP3_2L, SP4_2L, SP5_2L) present a loss of linearity and instantaneous stress reductions before the achievement of the maximum stress (Figure 4.18b), caused by the failure of one or few lateral cords. In particular, for these specimens slight slipping occurred at the gripped ends during testing (Stage III), leading to a premature failure because of the misalignment of the cords and the consequent non-uniform load distribution over the cross-section of the textile, with higher stresses on the prematurely failed cords. The irregular load application caused strain/stress concentrations particularly in correspondence of the cracks because of the lack of matrix redistribution effects. Beyond the physiological scatter of experimental results, the slightly lower peak stress of these samples respect to the other two specimens of the same series may be due to the occurrence of the described phenomenon, which was observed from other authors (De Santis and De Felice 2015a).

In regard to strain values, the averages of the three series were quite close for Stage I (0.030%, 0.035%, 0.044%). For Stage II there was a marked reduction of the average maximum strain between one-layer specimens and two and three-layer reinforced specimens, with a drop of 56% and 78% respectively. Finally, the curves of coupons strengthened with two and three basalt textile layers showed an average strain reduction in Stage III equal to 18% and 37% respectively compared to specimens involving one reinforcement layer. The length of the crack development stage can be represented by the ratio $\varepsilon_{II}/\varepsilon_{III}$

(where ε_{III} is the strain at peak stress). In specimens reinforced with one basalt layer, ε_{II} was on average 45% of the ultimate strain (values ranging between 34% and 61%), pointing out that the crack development stage was quite extended. On the other hand, ε_{II} was on average equal to 24% (values ranging between 16% and 29%) and 16% of the ultimate strain for two and three-layer reinforced series respectively, showing the predominance of Stage III because, in this case, the contribution of the reinforcing fabric was prevalent to that of the matrix.

Considering the average values, the tangent modulus in Stage III increased with the number of grid layers, but all the series presented a considerable reduction of stiffness if compared with the average value obtained from basalt grid strips (55%, 50%, 34% for one, two and three layers respectively). Stiffness reductions were mainly due to slipping phenomena occurred between the basalt mesh and the matrix, as observed by other authors (Carozzi and Poggi 2015, De Santis and De Felice 2015a, Caggegi et al. 2017a, Bilotta et al. 2017a, Bilotta et al. 2017b); the occurrence of this phenomenon was evidenced by DIC analysis of the specimens presented in the following.

Also the values of tensile strength in Stage III (σ_{III}) were quite lower compared to the tensile strength of the basalt grid (Figure 4.19b). Aiming to compare the strength of the BFRCM specimens with that of the bare basalt fibre, Table 4.7 shows the efficiency factor η, which is defined as the ratio between the tensile strength in composite coupons, σ_{III}, and the average experimental strength of dry fibres, f_{fu}.

The efficiency factor η varied from 0.64 to 0.77 for one-layer reinforced specimens, from 0.54 to 0.72 for two-layer reinforced specimens, while for the three-layer strengthened sample the efficiency factor was equal to 0.54 (Table 4.7). These results underline as the BFRCM coupons did not fully exploit the nominal capacity of the fibres, as confirmed by previous studies in the literature (Carozzi and Poggi 2015, De Santis and De Felice 2015a, Caggegi et al. 2017a, Bilotta et al. 2017a, Bilotta et al. 2017b). The strength decrease of composite specimens compared to dry fibres may be due to stress concentrations because of geometric defects of the grid, which could cause unavoidable imperfect alignment of rovings inside the mortar thickness during manufacturing procedure, and possible damage of the fibres near to cracks edges. Moreover, strength reductions increasing with the increase of the number of layers could be related to a non-uniform load distribution in the cross-section of the textile of

over-reinforced FRCM specimens, because of the small mortar thickness unable to guarantee a uniform loading of the cords. It is likely that the overlapping of fabric layers may cause a modified interaction between basalt textile and mortar, with a reduction of the adhesion between the two components.

4.3.4 Crack patterns and displacement fields

As mentioned in the previous chapter, in the framework of this thesis the DIC technique was used not only to obtain the strains needed to plot the stress-strain curves of composite specimens, but also for analyzing the crack development and the strain distribution through the definition of a full-field analysis on the surface of the BFRCM coupons.

Figure 4.20 presents the strain contours at failure for three specimens reinforced with one, two and three layers respectively. The figures show that the cracks are well widespread along the surface of the specimens and this points out the significant ability of the basalt grid in transferring load to the matrix.

Table 4.7: Evaluation of efficiency factor η

Samples	Peak stress [MPa]	Efficiency factor	Range of variation
	σ_{III}	η	
SP1_1L	1482.14	0.72	0.64-0.77
SP2_1L	1402.99	0.69	
SP3_1L	1523.32	0.74	
SP4_1L	1315.70	0.64	
SP5_1L	1524.35	0.75	
SP6_1L	1488.42	0.73	
SP7_1L	1579.61	0.77	
SP8_1L	1421.69	0.70	
SP1_2L	1374.10	0.67	0.54-0.72
SP2_2L	1481.94	0.72	
SP3_2L	1177.03	0.58	
SP4_2L	1188.73	0.58	
SP5_2L	1096.41	0.54	
SP1_3L	1103.14	0.54	-

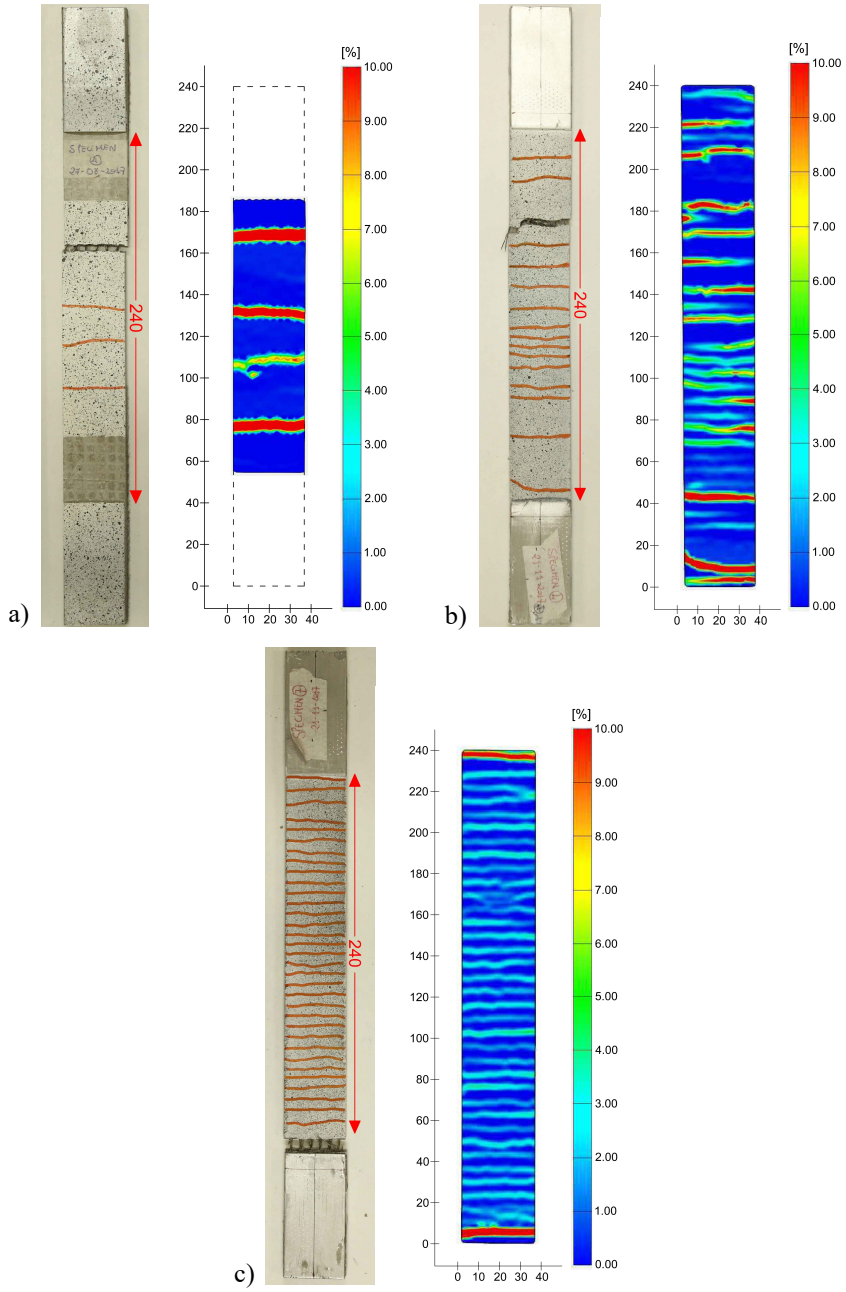

Figure 4.20 Strain pattern at failure load: a) one-layer reinforced specimen (SP8_1L); b) two-layer reinforced specimen (SP2_2L); c) three-layer reinforced specimen (SP1_3L)

In particular, the increase of textile layers gave rise to a larger number of cracks, progressively closely spaced. Then, less cracks at larger distance developed for one-layer reinforced specimen, while the better interlocking between reinforcement and matrix, linked to the higher reinforcement ratio, caused the development of tighter and more distributed cracks, with a short saturation crack spacing (distance between cracks).

This was due to the fact that a higher volume fraction of fibres was able to absorb the energy released during the formation of cracks and to transfer stresses to areas where the mortar was un-cracked.

The full-field analysis allowed underlining another important condition: in correspondence of cracks, the maximum recorded strain values (10%) were sensibly higher than the maximum tensile strain obtained from tensile tests on dry basalt strips (2.7%) and this demonstrated the presence of slipping phenomena between the basalt grid and the matrix at cracks.

The use of DIC allowed the analysis of the displacement fields on the external surface of the samples, giving information about the localization of the crack openings and their evolution during tensile tests.

The DIC analysis outcomes are here presented in terms of *P*-*y* curves, being "*P*" the displacement along the longitudinal direction (*y*) of the samples, and displacement fields.

In Figure 4.21 the load-displacement curves of specimens SP8_1L, SP4_2L and SP1_3L reinforced with one, two and three basalt textile layers respectively, are presented and each curve reports some points corresponding to the load steps where DIC measurements were carried out.

The DIC measurements related to the identified load steps are presented in Figure 4.22, which shows the displacement values (*P*) along the longitudinal direction of the samples (*y*), at determined load steps. In the curves, each drop is representative of a crack opening and the difference between values of *P* before and after drop (*dP*) measures the crack opening. The distance between the drops (*L*) corresponds to the distance between subsequent cracks.

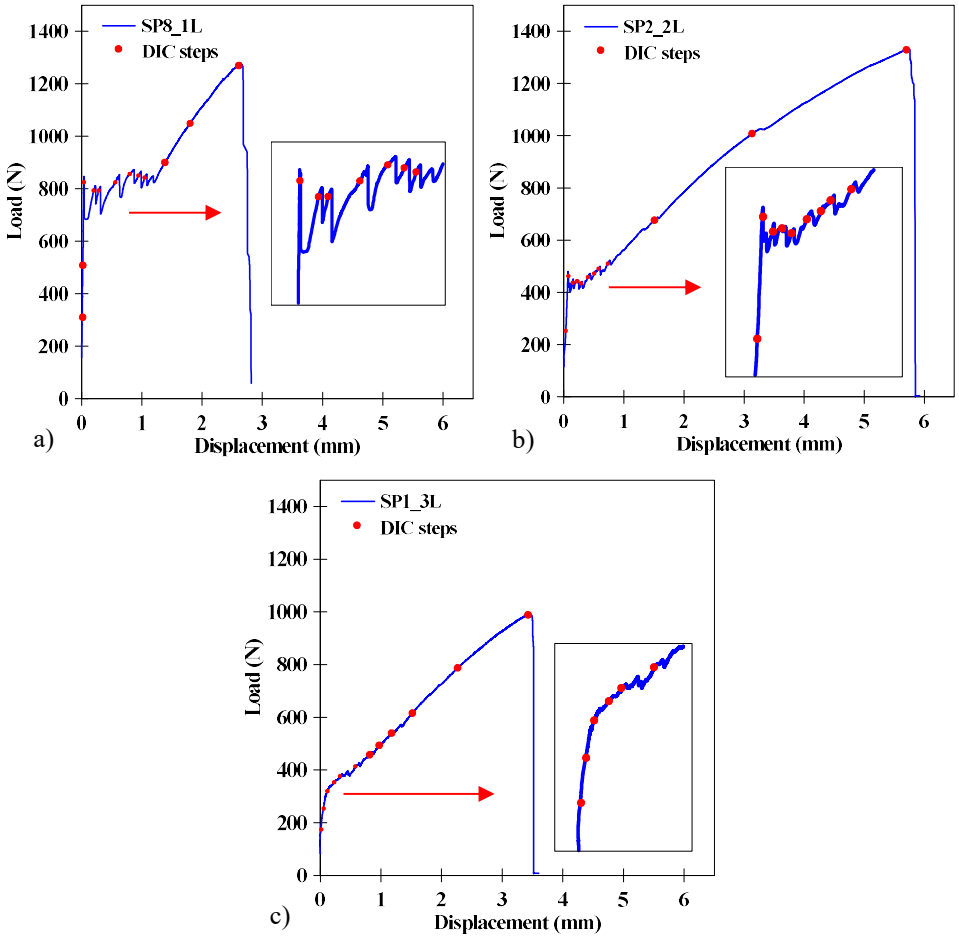

Figure 4.21 Load-displacement curves: a) one-layer reinforced specimen (SP8_1L); b) two-layer reinforced specimen (SP2_2L); c) three-layer reinforced specimen (SP1_3L)

The outcomes show that the distance *L* ranges between 25 and 40 mm for one-layer reinforced specimen; the distance between cracks spaces from 6 to 34 mm for two-layer reinforced specimen, with a mean values of 14 mm. In the case of three-layer reinforced sample, *L* ranges between 5 and 10 mm, with an average value of 7 mm, which is approximately the distance between the transversal yarns of the basalt mesh. Indeed, the yarns perpendicular to the load direction caused a local reduction of the mortar section, which became a preferential weak location for the development of cracks, as already observed in the literature (De

Santis and De Felice 2015a, Caggegi et al. 2017a). This was even truer for the specimen SP1_3L because of the presence of more basalt textile layers and a lower thickness of mortar between textile plies compared to one and two-layer reinforced samples.

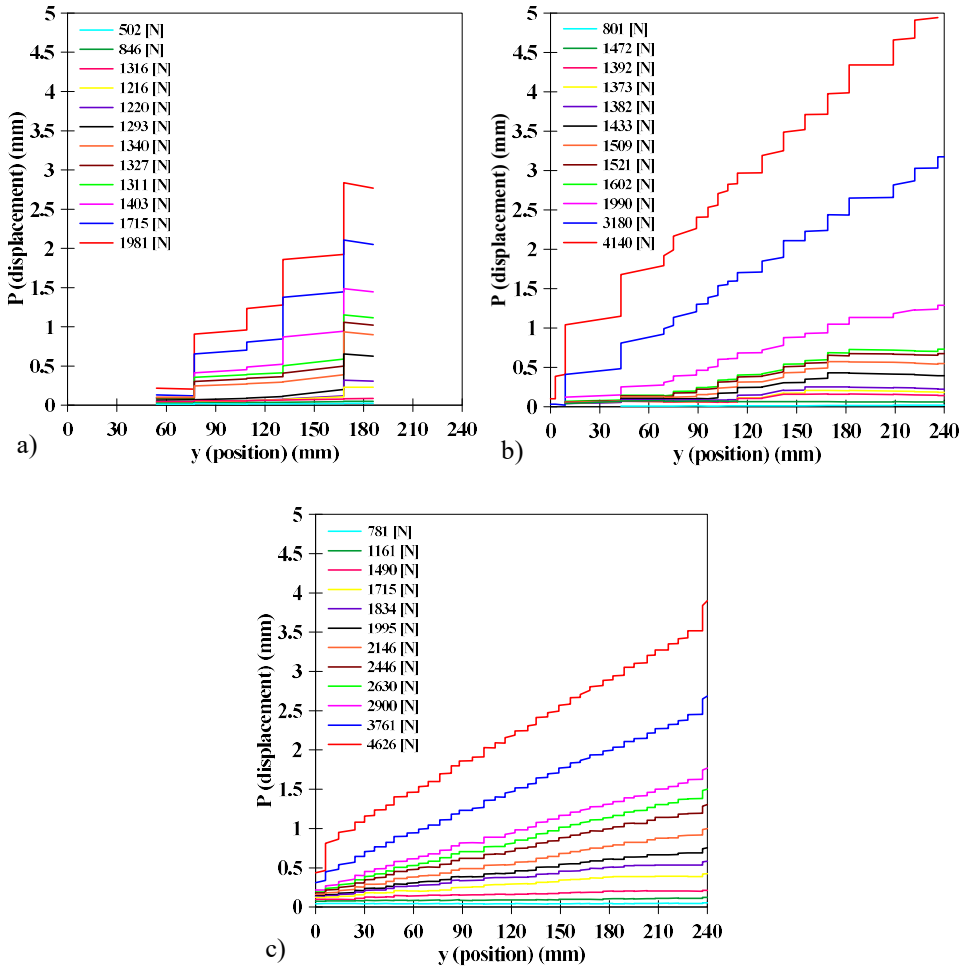

Figure 4.22 Displacement values (P) along the longitudinal direction (y) of the specimens and related to twelve loading steps: a) specimen SP8_1L; b) specimen SP2_2L; c) specimen SP1_3L

Figure 4.23 to Figure 4.25 present the continuous displacement contours related to three specimens (SP8_1L, SP2_2L, SP1_3L) reinforced with one, two and three layers respectively, in correspondence of some of the identified load steps of Figure 4.21. In the images, the reported iso-lines represent points with equal displacement. The evolution of the crack pattern is clearly detectable and it is characterized by the progressive development of cracks transversal to the direction of the applied load. At the ultimate load step, iso-lines tend to be close each other, highlighting the development of cracks.

The evolution of the crack opening *dP* was also analyzed as a function of the sustained external load F, as shown by the curves presented in Figure 4.26 for specimens SP8_1L, SP2_2L and SP1_3L respectively. In the graphs, each curve corresponds to one crack and the label of the curve refers to the distance, along the specimen length, where the crack is placed. Observing the graphs it is clear that, once a crack develops, its opening *dP* recorded by the use of DIC increases proportionally to the applied load. For values of *F* corresponding to the first two stages of the tensile behaviour of FRCM specimens (un-cracked stage and crack development stage in Figure 4.21), the curves *dP-F* (Figure 4.26) show an inhomogeneous development, because of the different opening endured by different cracks. Conversely, once the crack development ability of mortar is saturated and the third stage (cracks evolution) starts, the *dP-F* curves begin to be almost perfectly parallel.

Moreover, the graphs in Figure 4.26 depict the ratio $E_f A_f/L$, where E_f and A_f are the Young's modulus and the cross sectional area of the grid respectively, while *L* indicates the distance between cracks. In particular, the three curves $E_f A_f/L$ reported in graphs of Figure 4.26 were obtained considering a distance *L* equal to 40, 15 and 9 respectively for specimens SP8_1L, SP2_2L and SP1_3L, values that were close or equal to the average spacing between cracks actually observed for the examined specimens. It was obtained that the ratio $E_f A_f/L$ was closely equal to the ratio F/dP during the third stage of the BFRCM tensile behaviour.

The graphs point out that the maximum crack opening in one-layer reinforced specimen (SP8_1L) was greater compared to that measured in samples reinforced with two layers. The same decrease of crack opening was observed when the specimen was strengthened with three basalt layers, compared to the sample reinforced with two textile plies. Moreover, this opening increase was inversely

proportional to the number of cracks developed along the surface of the composite coupons: the greater the number of cracks, the lower the maximum crack opening recorded.

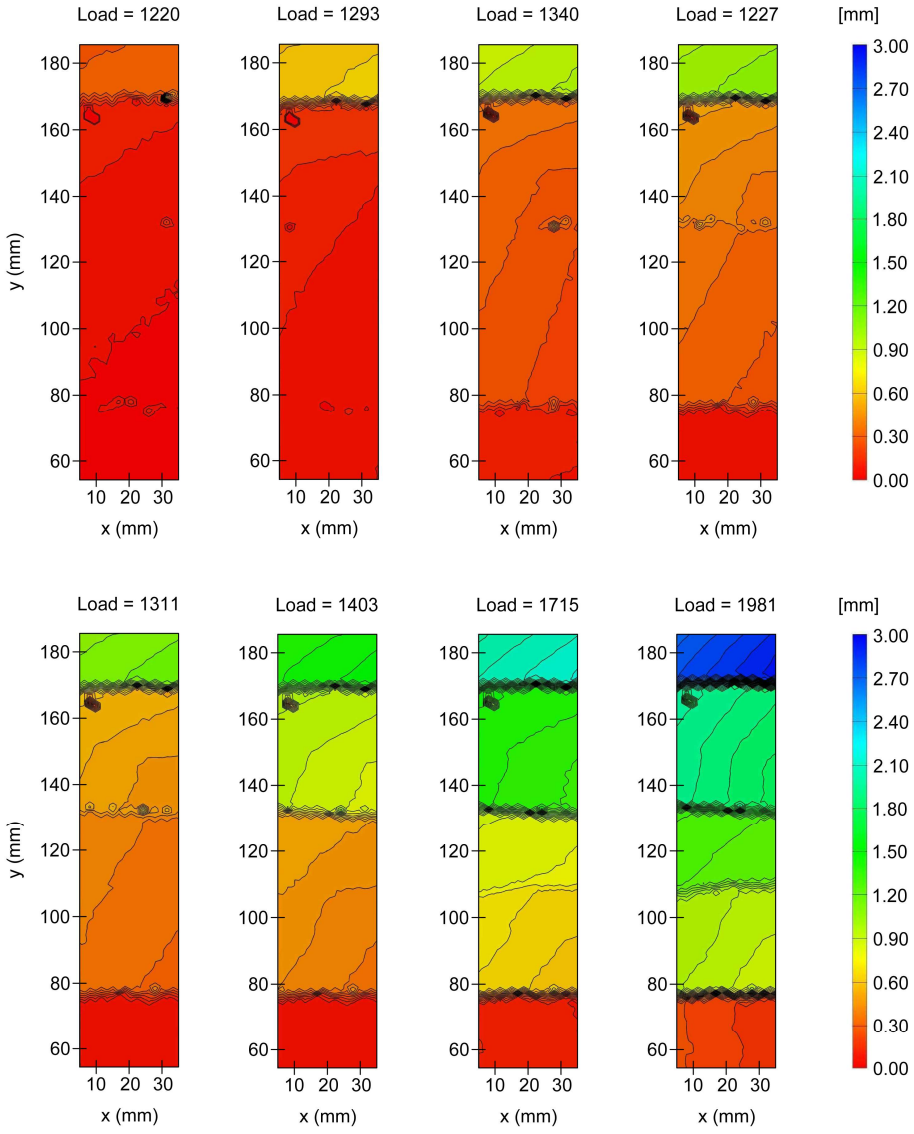

Figure 4.23 Displacement field of specimen SP8_1L, related to eight load steps

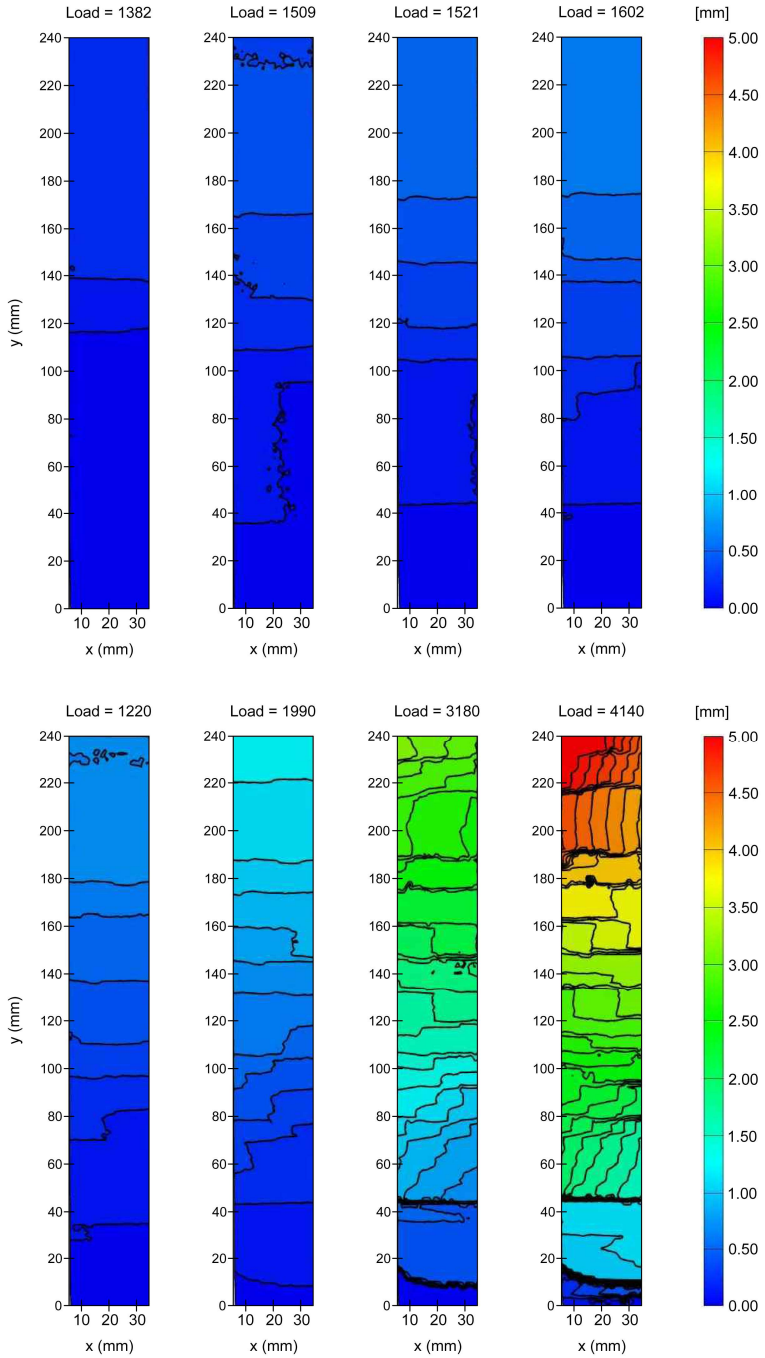

Figure 4.24 Displacement field of specimen SP2_2L, related to eight load steps

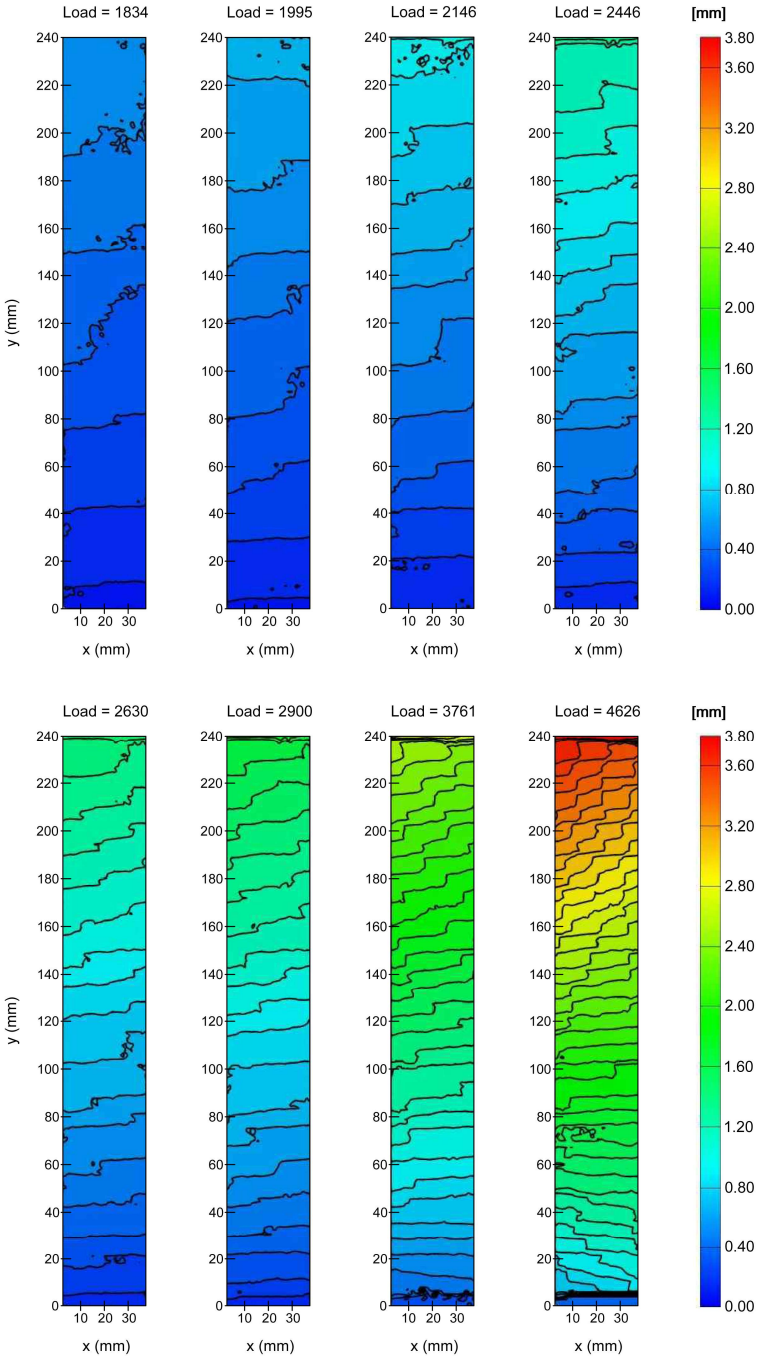

Figure 4.25 Displacement field of specimen SP1_3L, related to eight load steps

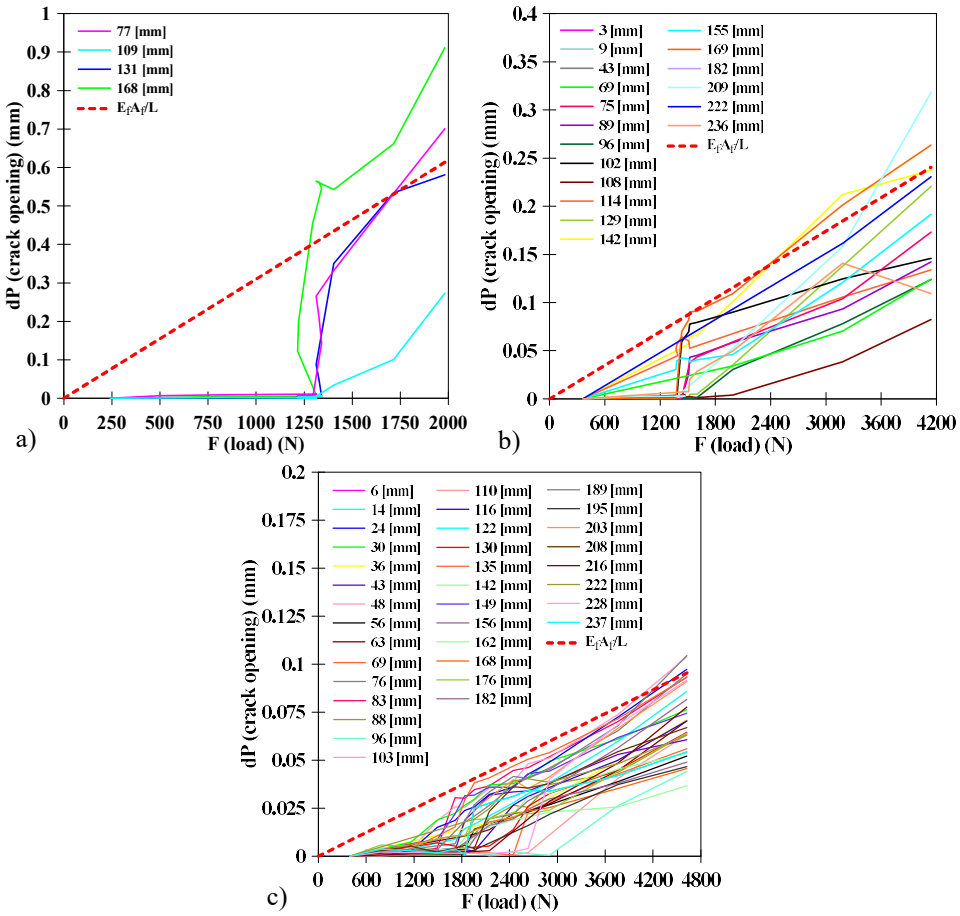

Figure 4.26 Evolution of crack opening dP as a function of the applied load F: a) specimen SP8_1L; b) specimen SP2_2L; c) specimen SP1_3L

4.3.5 Failure modes

Figure 4.27 and Figure 4.28 show respectively the BFRCM specimens with one and two fabric layers after testing. After a homogeneous cracking along the length of the samples, fibre tensile failure was observed for all the tested specimens, including rupture near the gripping area or in the middle of the sample, while slippage of the textile within the matrix at the gripping area was never recorded. This was mainly due to the use of the clamping grip method

ensuring a sufficient compressive stress applied while gripping the specimen ends inside the wedges of the testing machine.

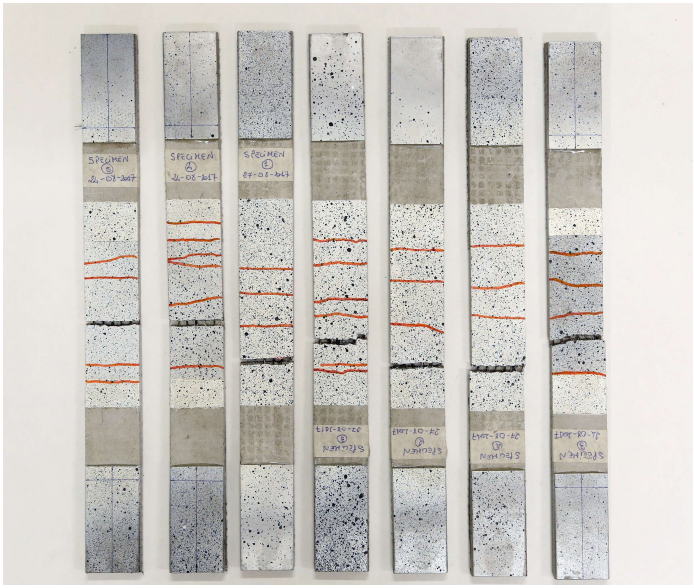

Figure 4.27 One-layer reinforced BFRCM specimens after testing

Figure 4.28 Two-layer reinforced BFRCM specimens after testing

The development of cracks close to the gripping area did not affect the final results of tensile tests and also other authors (Lignola et al. 2017) showed that the peak loads associated to this failure mode are comparable to those attained when the main crack develops in the middle of the specimen. Moreover, even when ruptures formed near to the clamping areas, reliable strain values were obtained thanks to the use of DIC, which allowed a full length measurement of strains.

Most of the time failure was recorded in a cross-section comprising a transversal yarn of the mesh (Figure 4.29a and Figure 4.29b): the presence of rovings in the transversal direction implied a local reduction of the mortar cross-section with unavoidable consequent reduction of its resistance.

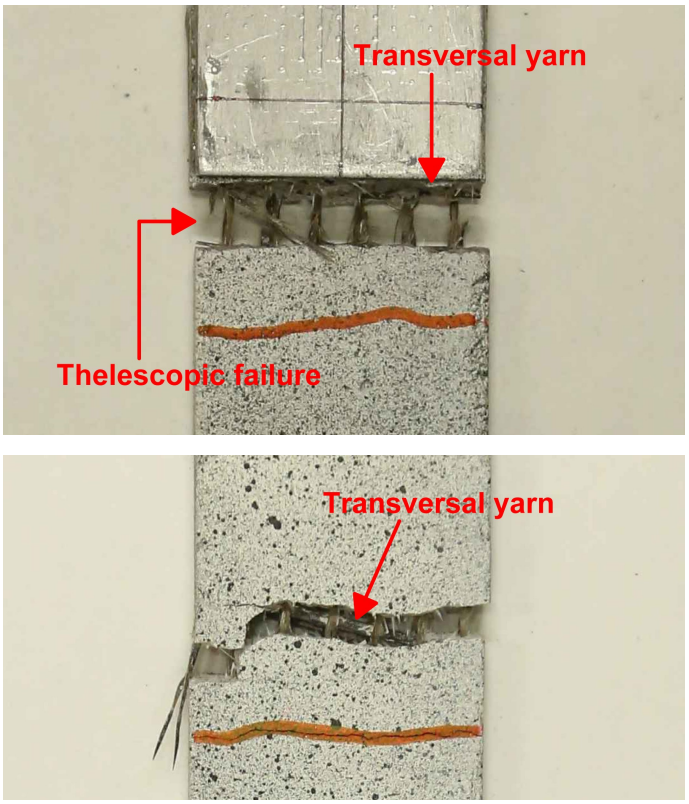

Figure 4.29 Failure mode of BFRCM specimens: a) thelescopic failure of textile longitudinal yarns and crack at the transversal yarn b) critical crack at the transversal yarn

The analysis of the specimens after failure showed sliding between external and internal wires of the yarns, namely a telescopic failure (Figure 4.29a). This type of failure in basalt coated textile was already observed by other authors (Lignola et al. 2017) and it is due to the fact that in coated textile the load is transferred from the mortar matrix to the coating eternal layer by chemical adhesion and, later, from the external layer to the inner core by friction, because of the impossibility of the mortar to impregnate the inner wires. Being the matrix-to-wire transfer capacity higher than that between wires, the telescopic pull-out failure may occur (Banholzer et al. 2006). The failure mechanism of the yarns started with the fracture of the outer filaments, followed by the rupture of adjacent fibres, until reaching the core filaments, which were not in direct contact with the mortar (Figure 4.29a).

For some specimens failure occurred involving all the yarns simultaneously; in other cases, the failure was characterized by progressive damage of one or few lateral cords. This is confirmed by the dentate post-peak behaviour of some load-strain curves evidencing the close progressive rupture of the basalt yarns, which started from a side of the sample and propagated to the other side.

4.4 Compressive tests on masonry cylinders

In this section the results of compressive tests on unconfined and BFRP or BFRCM-confined cylinders are discussed.

First, the axial stress-strain results obtained by using traditional measurement devices are presented and commented. Then, these results are compared with those provided by DIC analysis.

The use of DIC technique allowed also the study of the hoop behaviour of the cylinders, here analyzed in terms of stress-hoop strain curves and correlated to the axial strain in order to investigate on the volumetric strain.

Finally the failure modes are discussed for unconfined and BFRP/BFRCM-confined cylinders respectively.

4.4.1 Stress-strain curves

The outcomes of monotonic compressive tests are presented in terms of axial stress-strain curves for unconfined and BFRP/BRCM confined cylinders. The

data here reported were obtained by using external LVDTs (placed at top and bottom of the cylinders) and local transducers (supported by the steel ring) for all the cylinders from Scheme I and Scheme II respectively.

The axial stress was calculated dividing the axial load measured by the load cell by the cross sectional area of the specimens. The axial strain was obtained considering the readings of the transducers supported by the steel ring up to the peak load, using a gauge length of 100 mm. After the peak, the strains obtained through these transducers were affected by local deformations. For this reason, the readings from LVDTs placed at top and bottom platens were used to calculate the post-peak axial strain, using a gauge length equal to the height of cylinders.

Unconfined cylinders

Figure 4.30 shows the compressive stress-strain results obtained using readings of LVDTs for Scheme I and Scheme II unconfined cylinders respectively. The experimental outcomes along with the average values and COV are reported in Table 4.8 for all the tested cylinders. In Table 4.8, f_{m0} is the compressive strength of unconfined masonry, ε_{m0} is the axial strain at peak stress and ε_{m0u} is the ultimate axial strain. The latter was calculated as the axial strain at 15% strength degradation.

The curves show a brittle behaviour, characterized by a non-linear ascending branch and a steep drop in strength after reaching the peak load.

The average peak stress for the control specimens was 25.19 MPa and 19.85 MPa respectively for Scheme I and II cylinders (Table 4.8), showing a significant detrimental effect of the vertical joints.

For cylinders C2_WUn and C3_WUn the axial strain was fully obtained using the readings from the LVDTs placed at top and bottom platens, because data from the transducers supported by the steel ring were lost during testing of both these specimens. Note that the stiffness obtained in this way is likely lower than the actual stiffness of the specimens, so it may be used as reference only. For this reason the strain values of these cylinders were excluded for the calculation of the average strain of unconfined specimens. For two of the unconfined cylinders (C1_WUn, C4_WUn), the ultimate axial strain coincides with the last detected value (Table 4.8) because of the brittle behaviour which do not allow reaching a strength degradation of 15% after the peak load.

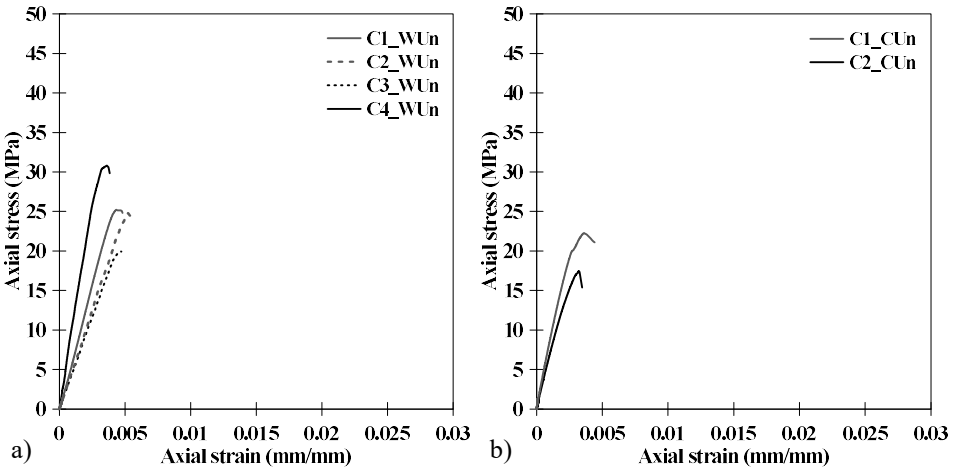

Figure 4.30 Axial stress-strain curves of unconfined cylinders plotted by using readings of LVDTs: a) Scheme I specimens; b) Scheme II specimens

Table 4.8: Test results of unconfined masonry cylinders by using LVDTs

Specimen designation	f_{m0} (MPa)	Average and COV	ε_{m0} [mm/mm]	Average and COV	ε_{m0u} [mm/mm]	Average and COV
C1_WUn	25.24	25.19 17.60%	0.0043	0.0040 12.41%	0.0048**	0.0043 15.91%
C2_WUn	24.78		0.0052*		0.0054*	
C3_WUn	19.95		0.0049*		0.0049*	
C4_WUn	30.79		0.0036		0.0038**	
C1_CUn	22.25	19.85 17.14%	0.0036	0.0034 8.88%	0.0042	0.0038 13.56%
C2_CUn	17.44		0.0032		0.0035	

*Results neglected for the calculation of the average peak and ultimate strain
** Last detected deformation

BFRP-confined cylinders

For cylinders confined by BFRP wraps, the axial stress-strain results are plotted in Figure 4.31 for both the schemes, along with the results from unconfined specimens for a more convenient comparison. The experimental outcomes are presented in Table 4.9 for all the BFRP-confined cylinders, along with the average values and the COV. In Table 4.9 f_{mc} is the peak stress of confined masonry, ε_{mc} is the axial strain at peak stress and ε_{mcu} is the ultimate axial strain, the latter evaluated at 15% degradation of the peak stress.

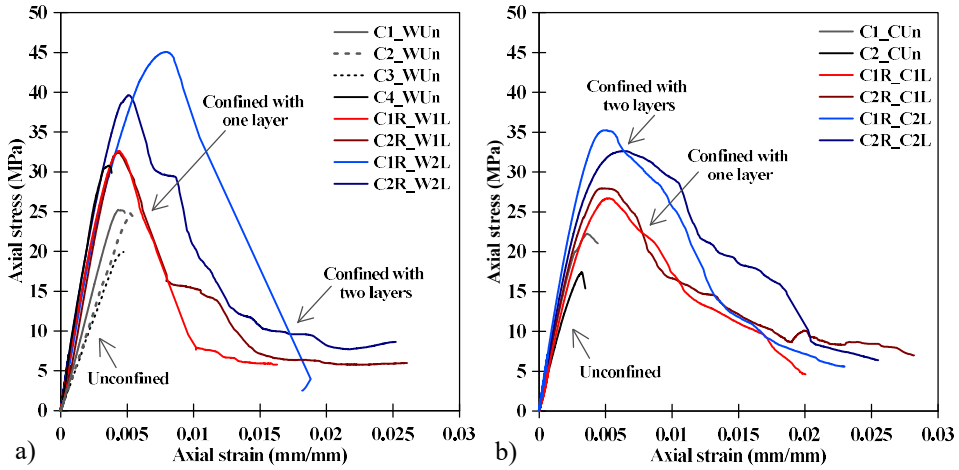

Figure 4.31 Axial stress-strain curves of BFRP-confined cylinders plotted by using readings of LVDTs: a) Scheme I specimens; b) Scheme II specimens

Table 4.9: Test results of BFRP-confined masonry cylinders by using LVDTs

Specimen designation	f_{mc} (MPa)	Average and COV	ε_{mc} [mm/mm]	Average and COV	ε_{mcu} [mm/mm]	Average and COV
C1R_W1L	32.64	32.56 0.35%	0.0044	0.0042 7.08%	0.0057	0.0056 1.23%
C2R_W1L	32.47		0.0040		0.0056	
C1R_W2L	45.08	42.36 9.08%	0.0080	0.0065 31.47%	0.0092	0.0078 24.73%
C2R_W2L	39.64		0.0051		0.0065	
C1R_C1L	26.71	27.33 3.21%	0.0053	0.0051 4.54%	0.0075	0.0074 1.58%
C2R_C1L	27.95		0.0049		0.0073	
C1R_C2L	35.26	33.95 5.45%	0.0051	0.0058 17.90%	0.008	0.0094 21.80%
C2R_C2L	32.64		0.0065		0.011	

All stress-strain curves of tested cylinders show a non-linear ascending branch, followed by a descending portion in the case of reinforced specimens. The confined cylinders exhibited a more ductile behaviour as evidenced by a clear softening branch, which was hardly seen for the unconfined reference specimens. Comparing one-layer and two-layer wrapped cylinders, for both Scheme I and Scheme II, it can be observed a considerable increase in terms of strength, while the descending branch of the stress-strain curves shows a similar

slope. Moreover, it can be seen that Scheme II specimens are more ductile, with a less steep softening branch than Scheme I specimens. This behaviour underlines the influence of the number of mortar vertical joints, which was higher for Scheme II specimens.

In order to evaluate the effect due to the use of BFRP jackets, Table 4.10 provides the average strength increase and average strain increase due to BFRP confinement. As it can be seen, compared to unconfined specimens, one layer of BFRP enhanced the average strength of cylinders by 29% and 38% respectively for Scheme I and II. For cylinders confined by two layers of BFRP the average strength gain was 68% for Scheme I and 71% for Scheme II. These results underline that the effectiveness of BFRP wrapping was higher for Scheme II cylinders, namely in the case of weaker masonry involving three vertical joints.

The average strength increased by 30% and 24% respectively for Scheme I and Scheme II cylinders with two layers compared to one-layer specimens. This points out as adding a second layer of reinforcement provided a considerable gain of axial strength.

In general, all the cylinders showed a significant enhancement in terms of strength if compared to unconfined specimens, highlighting the effectiveness of BFRP jacketing as method for confining masonry cylinders. Moreover, from Table 4.9 it can be noted that results in terms of strength relative to confined specimens are characterized by a lower scatter, i.e. a lower value of the COV compared to control specimens.

The use of BFRP wraps was also effective in terms of ultimate strain gain. In particular, Scheme I cylinders exhibited an average ultimate axial strain increase of 30% and 81% for specimens confined by one and two layers respectively. For cylinders from Scheme II, the average increases of ultimate axial strain were 93% and 146% for specimens wrapped using one and two layers respectively, compared to unconfined samples. It is clear as, even in terms of strain, BFRP jacketing was much more effective for cylinders involving three vertical joints (Scheme II). Moreover, increasing the jacket thickness by adding a second layer enhanced considerably the strain ductility of the cylinders.

The enhancement of the strain corresponding to the peak stress was also pronounced. Scheme I cylinders wrapped with two layers exhibited an average increase of 65% compared to control specimens; on the other hand, there was

almost not gain for specimens from Scheme I reinforced with one layer. Concerning cylinders from Scheme II confined with one and two layers of BFRP, the strains at peak stress were on average 49% and 69% higher than those of unreinforced specimens. Comparing one and two-layer wrapped cylinders, for Scheme I and Scheme II respectively, the average gain of strain at peak stress was 56% and 14%.

It can be concluded that BFRP jacketing was more effective in the case of weaker masonry (Scheme II) and this is evident considering strength and strain gains of wrapped cylinders compared to control specimens.

In particular, using one layer of BFRP led to greater enhancements of strength and strain for Scheme II cylinders, while adding a second layer led to very similar increases for both Scheme I and Scheme II in comparison to unconfined specimens. This means that the addition of a second layer of BFRP was more effective in the case of Scheme I in terms of axial strength and strain at peak stress.

BFRCM-confined cylinders

Figure 4.32 shows the results in terms of stress-strain curves for Scheme I and Scheme II cylinders, wrapped with one and two basalt grid layers.

Table 4.10: Strength and strain increments for BFRP-confined masonry cylinders, evaluated using LVDT

Specimen designation	f_{mc}/f_{m0}	Average	$\varepsilon_{mc}/\varepsilon_{m0}$	Average	$\varepsilon_{mcu}/\varepsilon_{m0u}$	Average
C1R_W1L	1.30	1.29	1.11	1.06	1.31	1.30
C2R_W1L	1.29		1.00		1.29	
C1R_W2L	1.79	1.68	2.02	1.65	2.13	1.81
C2R_W2L	1.57		1.28		1.49	
C1R_C1L	1.35	1.38	1.53	1.49	1.96	1.93
C2R_C1L	1.41		1.44		1.91	
C1R_C2L	1.78	1.71	1.48	1.69	2.08	2.46
C2R_C2L	1.64		1.90		2.83	

In Table 4.11 the experimental outcomes from compressive tests on BFRCM-confined cylinders are presented, along with their average values and COV. As in the case of BFRP-confined cylinders, the symbol f_{mc} is used to refer to the peak stress, while ε_{mc} and ε_{mcu} are respectively the axial strain at peak stress and the ultimate axial strain corresponding to 0.85 f_{mc} along the descending branch of the stress-strain curve. Note that the full stress-strain curve of the cylinder C3M_W2L is not available because of an issue with the testing machine during the test of the specimen. In particular, in Table 4.11 the compressive strength value is reported, but the corresponding strain is missing.

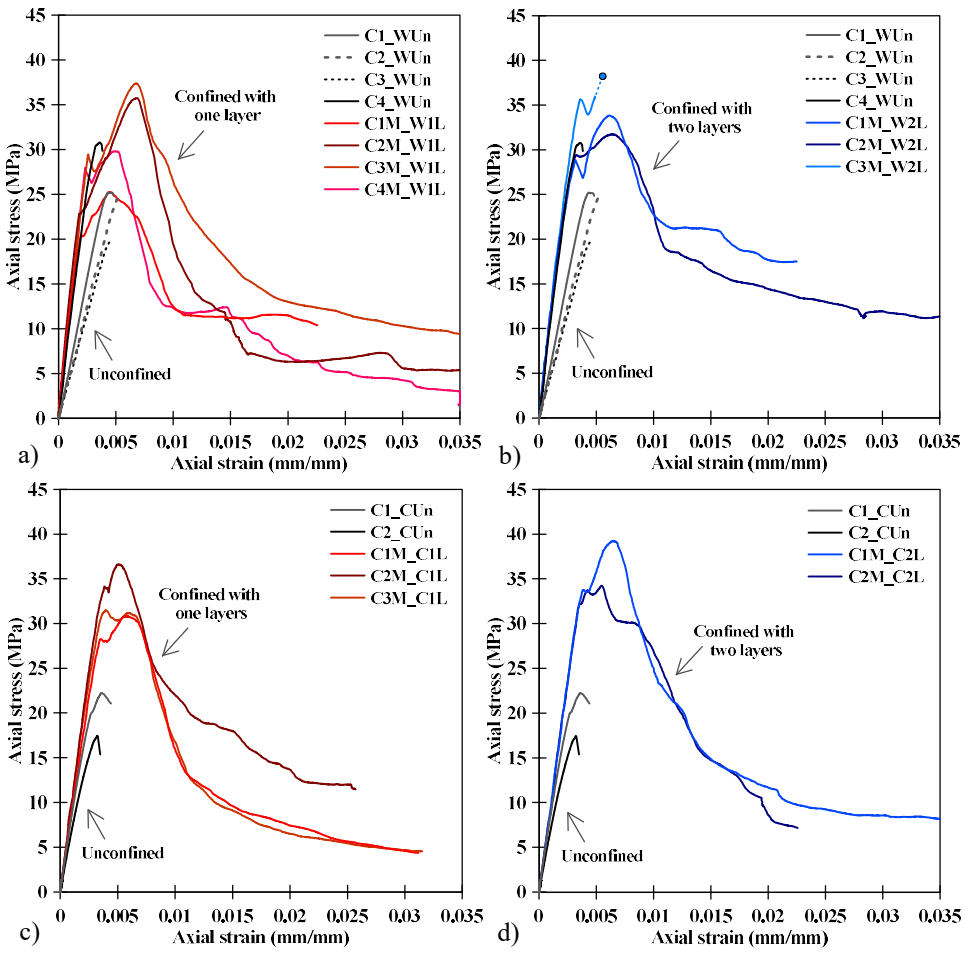

Figure 4.32 Axial stress-strain curves of BFRCM-confined cylinders plotted by using readings of LVDTs: a) Scheme I specimens; b) Scheme II specimens

Table 4.11: Test results of BFRCM-confined masonry cylinders by using LVDTs

Specimen designation	f_{mc} (MPa)	Average and COV	ε_{mc} [mm/mm]	Average and COV	ε_{mcu} [mm/mm]	Average and COV
C1M_W1L	25.25	32.04 (17.40 %)	0.0045	0.0058 (21.27 %)	0.0072	0.0074 (13.37 %)
C2M_W1L	35.73		0.0068		0.0083	
C3M_W1L	37.38		0.0068		0.0081	
C4M_W1L	29.80		0.0050		0.0061	
C1M_W2L	33.84	34.78 (10.35 %)	0.0061	0.0062 (2.75 %)	0.0081	0.0085 (6.76 %)
C2M_W2L	31.75		0.0064		0.0089	
C3M_W2L	38.76		/		/	
C1M_C1L	30.81	32.98 (9.60 %)	0.0058	0.0050 (18.78 %)	0.0078	0.0075 (7.07 %)
C2M_C1L	36.61		0.0051		0.0069	
C3M_C1L	31.52		0.0040		0.0079	
C1M_C2L	39.22	36.73 (9.58 %)	0.0065	0.0060 (12.16 %)	0.0079	0.0085 (8.90 %)
C2M_C2L	34.24		0.0055		0.0090	

The stress-strain curves of BFRCM-confined cylinders present a linear behaviour up to the development of the first crack in the mortar of the jacket. The beginning of cracks on the external wrap of the cylinders coincided with the failure of the internal masonry core and it can be easily detected from the curves, which experience a reduced drop in strength. Afterwards, the curves present a new stress increase due to the activation of the jacket because of the lateral expansion of the crushed masonry core. This new stress enhancement develops up to the peak value, with a less stiff trend than the initial one. After the maximum stress is reached, a quite steep descending branch can be detected, with a sudden drop in strength due to the basalt grid damage. Afterwards, the stress decrease starts to show a smoother trend: at this point the mesh was already broken in some parts, but the jacket could still guarantee a certain degree of ductility.

The post-peak drop is quite pronounced for both Scheme I and Scheme II cylinders. All the specimens show an almost bilinear softening branch characterized by a steep strength decrease followed by a plateau region, with considerable values of residual strength, particularly in the case of two-layer

wrapped specimens from Scheme I. On the other hand, there are not considerable differences in the softening behaviour of Scheme II cylinders wrapped with one or two basalt grid layers.

With the aim of evaluating the beneficial effect due to BFRCM confinement, strength and strain increases are presented in Table 4.12.

For cylinders confined employing one layer of BFRCM, the average strength increases were equal to 27% and 66% for Scheme I and Scheme II specimens respectively, compared to unconfined cylinders. Two layers of BFRCM produced an average strength enhancement of 38% for Scheme I and 85% for Scheme II cylinders. Comparing specimens reinforced with one and two layers, the strength gain was of 9% and 11% for Scheme I and Scheme II respectively.

It is clear that the effectiveness of confinement by BFRCM in increasing the bearing capacity of wrapped cylinders was higher for weaker masonry, namely in the case of Scheme II cylinders involving three vertical joints, as already found for BFRP-confined cylinders.

As general finding, the confinement by BFRCM showed to be effective to enhance the ultimate axial strain values. In particular, cylinders from Scheme I showed an average ultimate strain enhancement of 72% and 97% for one and two-layer confined specimens respectively, in comparison to unconfined ones. For cylinders from Scheme II, the average ultimate strain gains were 96% and 121% for specimens wrapped with one and two layers respectively.

The results showed an increase of the strain at peak stress of BFRCM-confined specimens. One-layer reinforced cylinders from Scheme I and Scheme II exhibited the same increase of average strain at peak stress, equal to 45% compared to control samples. Regarding cylinders confined with two layers, Scheme I reinforced cylinders showed an average increase of 57% compared to unconfined cylinders, while specimens from Scheme II presented an average strain gain of 75%.

In conclusion, the overall findings have underlined considerable strength and strain increases for BFRCM-confined cylinders compared to unconfined specimens, pointing out that this strengthening system can be considered an effective solution for enhancing the bearing capacity and the ductility of masonry columns.

Table 4.12: Strength and strain increments for BFRCM-confined masonry

Specimen designation	f_{mc}/f_{m0}	Average	$\varepsilon_{mc}/\varepsilon_{m0}$	Average	$\varepsilon_{mcu}/\varepsilon_{m0u}$	Average
C1M_W1L	1.00	1.27	1.13	1.45	1.67	1.72
C2M_W1L	1.42		1.72		1.93	
C3M_W1L	1.48		1.71		1.87	
C4M_W1L	1.18		1.25		1.42	
C1M_W2L	1.34	1.38	1.54	1.57	1.88	1.97
C2M_W2L	1.26		1.60		2.07	
C3M_W2L	1.54		/		/	
C1M_C1L	1.55	1.66	1.69	1.45	2.04	1.96
C2M_C1L	1.84		1.50		1.80	
C3M_C1L	1.59		1.15		2.05	
C1M_C2L	1.98	1.85	1.90	1.75	2.07	2.21
C2M_C2L	1.73		1.60		2.34	

4.4.2 Digital Image Correlation (DIC) measurements: axial stress-axial/hoop strain

In this section, the axial stress-axial strain results obtained referring to the readings from LVDTs and presented above are compared with the outcomes achieved by using the DIC technique. Moreover, thanks to the use of DIC system, hoop strains were recorded and axial stress-hoop strain curves are here introduced for unconfined and confined cylinders.

The strains measured through DIC were obtained considering the average reading of virtual extensometers inside the strain rectangle, as commented in the previous chapter. It should be noted that DIC results are reliable up to the peak (FRP) or first cracking (FRCM) load. After that point, local cracks started to appear and develop, and it could happen that the recorded strain values were not anymore representative of the global behaviour of the cylinders.

Unconfined cylinders

In Figure 4.33 the results of unconfined cylinders are presented in terms of axial stress-axial strain and axial stress-hoop strain curves. In particular, the outcomes in the axial direction from DIC analysis are compared with those obtained through the use of traditional measurement systems (LVDTs). The DIC technique was used only for specimens C2_WUn and C3_WUn and, as a consequence, for the remaining cylinders only results in the axial direction presented in the previous section are available.

Table 4.13 shows the results obtained using DIC in terms of axial and hoop strains at peak load for unconfined cylinders. ε_{m0}' and ε_{m0h} are respectively the axial and hoop strain at peak load and they are reported for each cylinder, along with the average value and the COV. Moreover, the ratio $\varepsilon_{m0}'/\varepsilon_{m0}$ is reported.

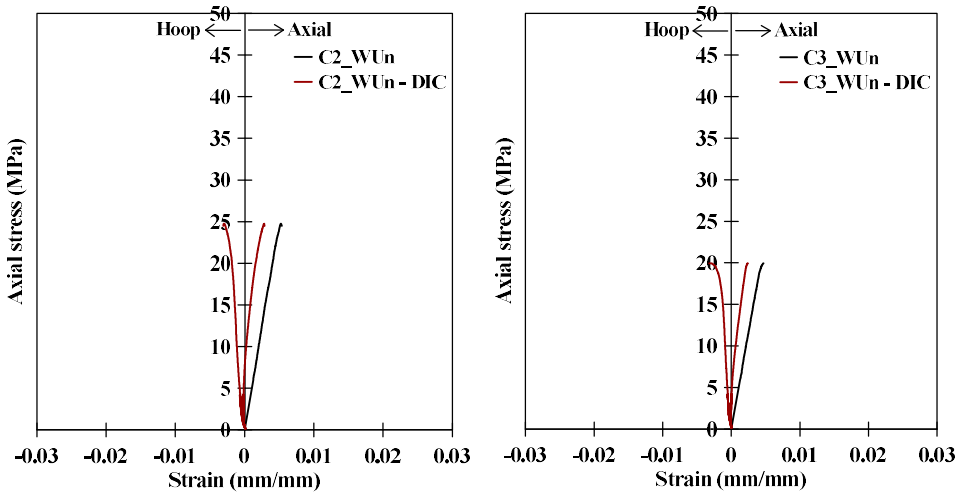

Figure 4.33 Stress-strain curves in the axial and hoop direction for Scheme I unconfined cylinders, plotted by using DIC and LVDTs

Table 4.13: Test results of unconfined masonry cylinders by using DIC

Specimen designation	f_{m0} (MPa)	ε_{m0}' [mm/mm]	Av. and COV	ε_{m0h} [mm/mm]	Av. and COV	$\varepsilon_{m0}'/\varepsilon_{m0}$	Av. and COV
C2_WUn	25.19	0.0028	0.0026 11.71%	0.0030	0.003 2.23%	0.54	0.52 (6.43%)
C3_WUn	19.85	0.0024		0.0029		0.49	

Figure 4.33 shows that the stress-axial strain results obtained by using DIC are close to those obtained from LVDTs and in general stiffer.

The strain at peak load from DIC analysis resulted smaller of 46% and 51% for C2_WUn and C3_WUn specimens respectively, compared to the values obtained from LVDTs. It is worth to note that these percentages were evaluated making a comparison with values fully obtained from the readings of the external LVDTs (placed at top and bottom of the cylinders). Most likely the percentages are higher than those that would have been obtained if reading from internal transducers had been available.

BFRP-confined cylinders

Figure 4.34 and Figure 4.35 show the results for each BFRP-confined cylinder, from Scheme I and Scheme II respectively. In the graphs, the axial stress-axial strain data obtained through the use of DIC are compared with results from LVDTs. Moreover the axial stress-hoop strain outcomes from DIC are presented for each specimen.

As mentioned, DIC measurements can be considered reliable up to the peak load, since after that point strain readings were affected by local deformations and they could be not representative of the global behaviour of the cylinders.

The curves plotted in Figure 4.34 and Figure 4.35 point out a good correspondence between results of DIC and LVDTs in terms of axial stress-axial strain. In some cases the DIC curves are slightly stiffer, while for many cylinders the curves are pretty much coincident.

The main results obtained by DIC are presented in Table 4.14, where ε_{mc}' and ε_{mch} are respectively the axial and the hoop strain at peak load of confined specimens. The ratio $\varepsilon_{mc}'/\varepsilon_{mc}$ is reported in order to compare values recorded by DIC and LVDTs. These values are reported for each cylinder, along with the average values and COV for specimens of the same type.

The outcomes underline that the axial strain values evaluated at peak stress using DIC were lower of about 32% and 13% respectively for one-layer and two-layer confined cylinders from Scheme I, compared to results obtained by LVDTs. For cylinders from Scheme II, the strain at peak stress decreased of 12% and

29% respectively for one-layer and two-layer wrapped specimens, in comparison with measurements of transducers.

The axial and hoop stress-strain curves obtained using DIC for cylinders unconfined (when available) and confined by one and two layers are shown all together in Figure 4.36, for Scheme I and Scheme II cylinders respectively, for a more convenient visualisation. Curves show as DIC results are quite consistent. As a matter of fact, all the stress-axial strain curves of each scheme present the same slope and the difference in axial stiffness related to the readings of LVDTs for cylinders C2_WUn and C3_WUn is no longer noticeable, being all results referred to the middle half of the cylinders.

The increases of axial strain at peak stress evaluated by using DIC for Scheme I BFRP-confined cylinders respect to unconfined specimens, are presented in Table 4.15.

Cylinders strengthened with one basalt textile layer exhibited an average increase of the axial strain at peak stress of 6% compared to control samples, while two-layer reinforced cylinders showed an average gain of 1.18%. The strain enhancement could not be evaluated for confined cylinders from Scheme II because DIC was not used for corresponding unconfined specimens.

Table 4.14: Test results of BFRP-confined masonry cylinders by using DIC

Specimen designation	f_{mc} (MPa)	ε_{mc}' [mm/mm]	Average and COV	ε_{mch} [mm/mm]	Average and COV	$\varepsilon_{mc}'/\varepsilon_{mc}$	Average and COV
C1R_W1L	32.64	0.0019	0.0028 45.22%	0.002	0.0030 50.36%	0.43	0.68 51.48%
C2R_W1L	32.47	0.0037		0.0041		0.92	
C1R_W2L	45.08	0.0069	0.0057 30.32%	0.0064	0.0049 43.37%	0.87	0.87 1.20%
C2R_W2L	39.64	0.0045		0.0034		0.88	
C1R_C1L	26.71	0.0036	0.0045 27.63%	0.0044	0.0046 3.86%	0.68	0.88 31.97%
C2R_C1L	27.95	0.0053		0.0047		1.08	
C1R_C2L	35.26	0.0031	0.0042 37.38%	0.0032	0.0036 15.83%	0.60	0.70 20.16%
C2R_C2L	32.64	0.0052		0.004		0.81	

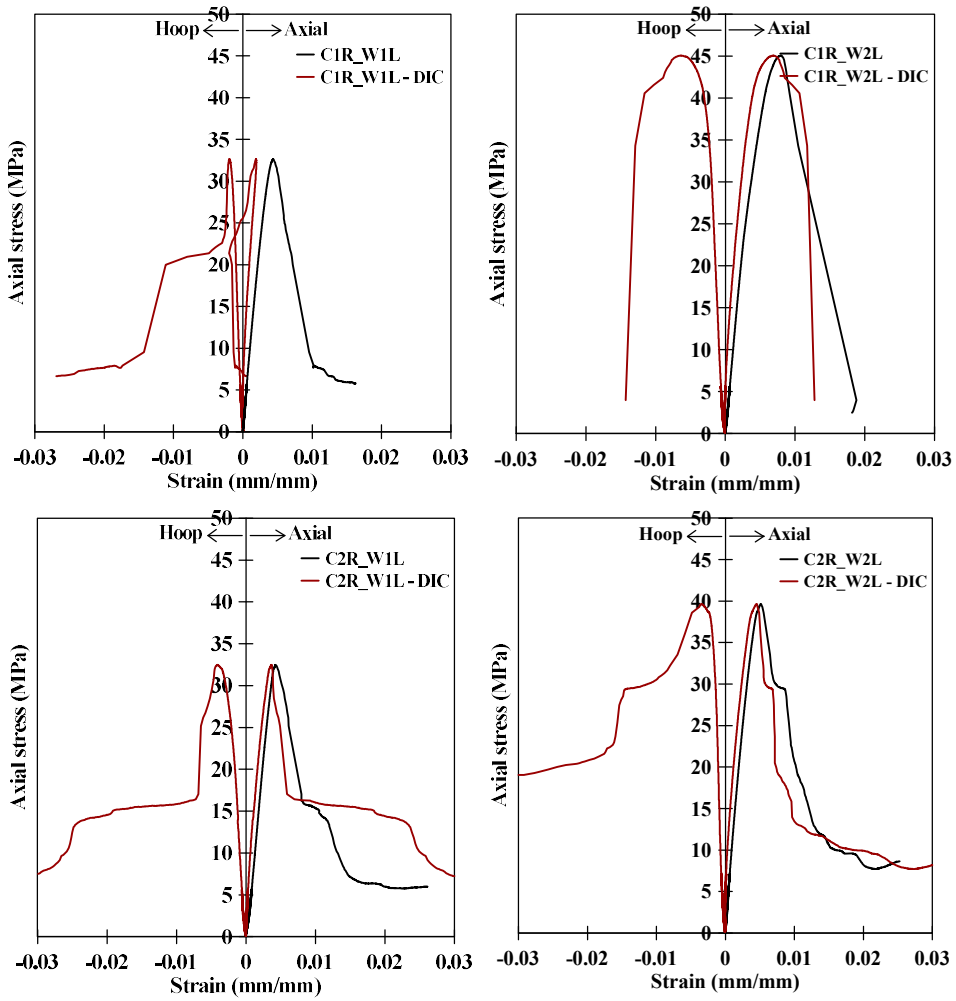

Figure 4.34 Stress-strain curves in the axial and hoop direction for Scheme I BFRP-confined cylinders, plotted by using DIC and LVDTs

Also in the hoop direction the results are consistent (Figure 4.36). Unconfined and confined specimens show the same slope of the non-linear ascending branch.

In order to evaluate the effect due to the use of BFRP jackets on the hoop strain of wrapped cylinders, Table 4.15 provides the enhancement of hoop strain at peak stress for confined cylinders in comparison to unconfined ones ($\varepsilon_{mch}/\varepsilon_{m0h}$).

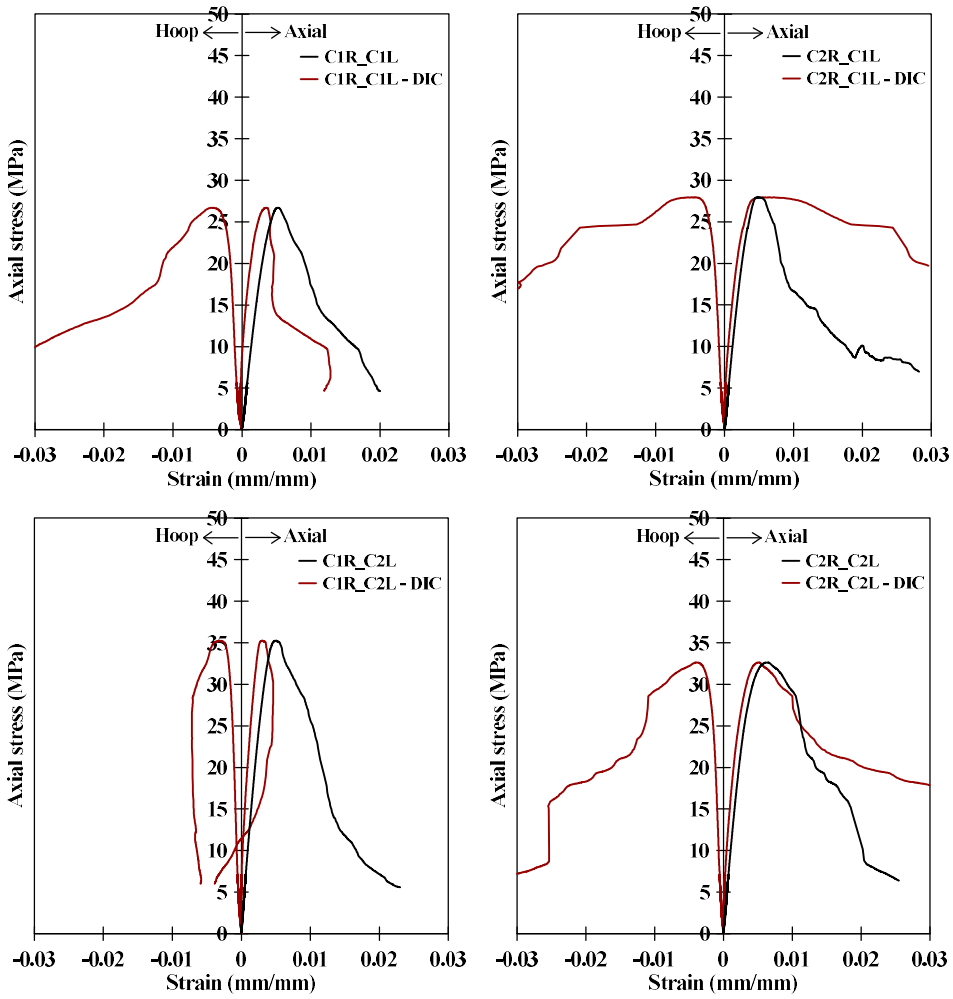

Figure 4.35 Stress-strain curves in the axial and hoop direction for Scheme II BFRP-confined cylinders, plotted by using DIC and LVDTs

Cylinders from Scheme I wrapped with two layers gave an average increase of hoop strain at peak stress of 67% with respect to control specimens. Cylinders strengthened by one layer of BFRP showed a negligible increase. For cylinders from Scheme II, it was not possible evaluating the gains of hoop strain at peak stress because of the lack of data on unconfined cylinders. Nevertheless, for this scheme, it was observed that the increase of one layer in external jacket caused a decrease of the average hoop strain at peak stress from 0.0046 to 0.0036.

Table 4.15: Strain increments for Scheme I BFRP-confined masonry cylinders, evaluated by using DIC

Specimen designation	$\varepsilon_{mc}'/\varepsilon_{m0}'$	Average And COV	$\varepsilon_{mch}/\varepsilon_{m0h}$	Average and COV
C1M_W1L	0.72	1.06 45.22%	0.66	1.03 50.36%
C2M_W1L	1.40		1.39	
C1M_W2L	2.65	2.18 30.33%	2.18	1.67 43.38%
C2M_W2L	1.71		1.16	

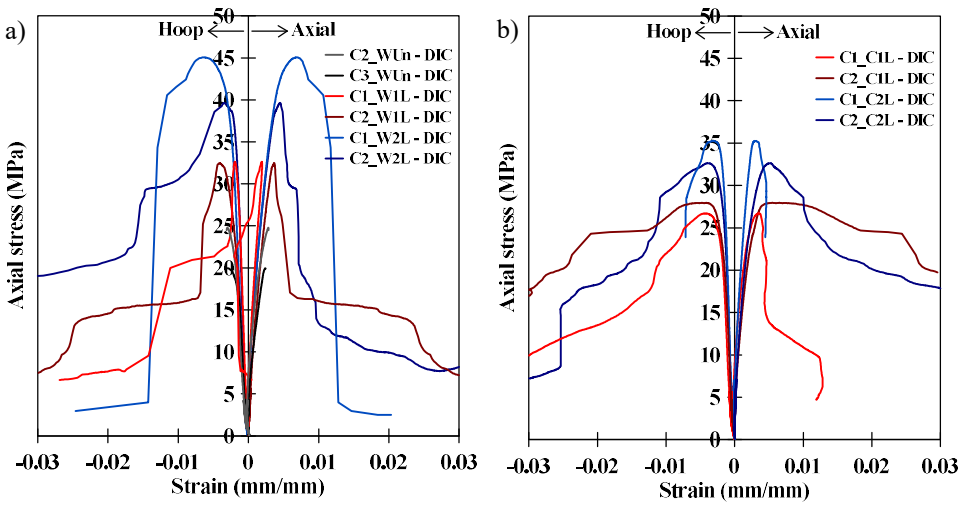

Figure 4.36 Comparison of stress-strain curves in the axial and hoop direction for unconfined and BFRP-confined cylinders, using DIC: a) Scheme I specimens; b) Scheme II specimens

BFRCM-confined cylinders

Figure 4.37 and Figure 4.38 depict the axial stress in BFRCM-confined specimens as a function of the axial and hoop strain respectively. In particular, Figure 4.37 shows results of Scheme I cylinders confined using two basalt layers, while data of cylinders reinforced with one layer are not available because DIC was not used. Outcomes of Scheme II cylinders are presented in Figure 4.38.

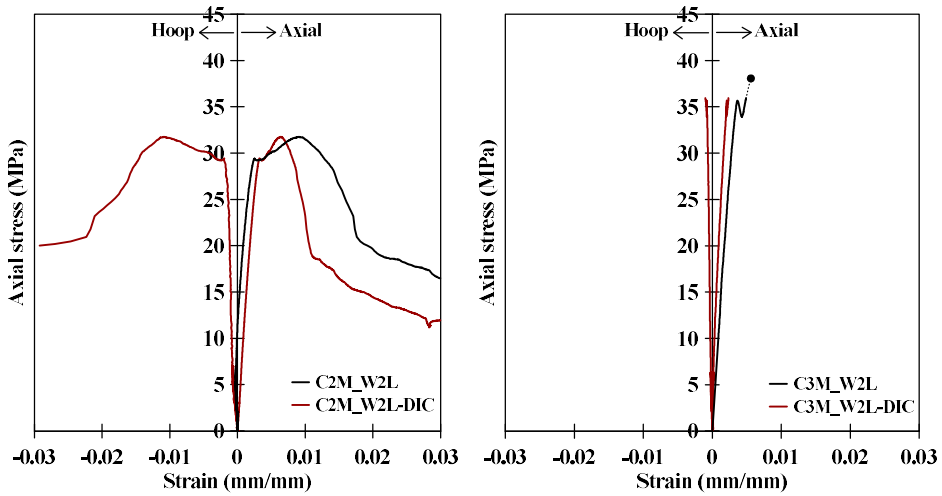

Figure 4.37 Stress-strain curves in the axial and hoop direction for Scheme I BFRCM-confined cylinders, plotted by using DIC and LVDTs

In the same figures, the results achieved by the DIC technique are compared with those recorded by LVDTs. The comparison points out as readings of DIC are in some cases stiffer with respect to those of LVDTs, while for some specimens the curves are very close along the first branch.

In particular, the stress-axial strain curves for each specimen match each other pretty well up to the first load drop, which coincides with the starting point of the development of cracks over the FRCM jacket. After this point, the strain measurements of the two systems (LVDTs and DIC) are comparable and show an accurate matching for some of the tested specimens, namely C1M-C1L, C2M_C1L, C2M_C2L (Figure 4.38). On the other hand, in some other cases (specimen C1M_C2L) there are inconsistencies in the readings of the two acquisition systems. This result can be explained considering that the digital system acquired measurements over a limited zone of the surface of the cylinders (90x50 mm). In this way, the vertical deformations that occurred on the wrapped surface of the specimens (i.e. on the confinement layer) could be gauged directly. On the other hand, the system formed by LVDTs placed at top and bottom of the cylinders measured global vertical displacements with a gauge equal to the cylinder length and without contact with the confinement device. Moreover, during the development of the test, the confinement jacket started to crack and the external layer of mortar started to separate from the core in certain areas.

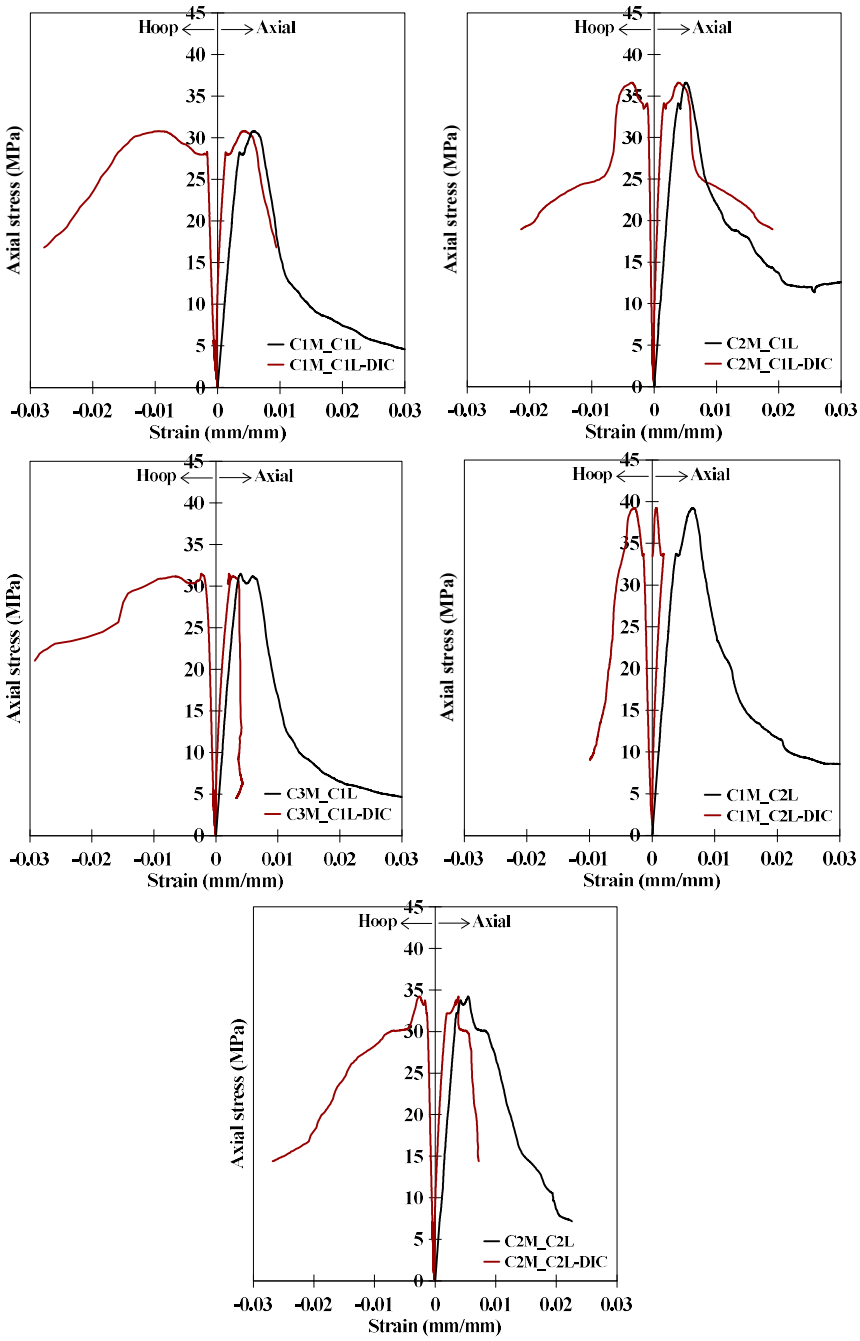

Figure 4.38 Stress-strain curves in the axial and hoop direction for Scheme II BFRCM-confined cylinders, plotted by using DIC and LVDTs

Then, it is possible to assert that whereas the readings of DIC indicate the behaviour of the external wrap, the measurements of the LVDTs represent the overall behaviour of the specimen. As result, because of the differences in gauge length, the measuring location (on the jacket for DIC and between loading plates for the LVDTs) and the detachment of the jacket from the core, differences between the two measurements could not be avoided.

These problems did not arise in the case of FRP-confined cylinders because of the different behaviour of the FRP jacket, which remained undamaged and strongly attached to the masonry core until the maximum stress was reached.

4.4.3 Comparison between the performance of BFRP and BFRCM confinement

Figure 4.39 shows the comparison between the axial stress-strain curves of BFRP and BFRCM-confined cylinders belonging to the same scheme and strengthened with the same amount of reinforcing fabric layers.

In general, as shown in the previous sections, it is clear that the two strengthening systems offered substantial gains of axial strength, showing the ability of both systems in enhancing the bearing capacity of masonry. The strength increased on average of about 29% for cylinders of Scheme I confined by one layer of BFRP (Figure 4.39a), while specimens of the same scheme wrapped by one layer of BFRCM exhibited an average strength gain of 27% with respect to control samples.

Concerning two-layer reinforced specimens of the same scheme (Figure 4.39b), the strength increase due to confinement was equal to 68% for BFRP-confined cylinders and 38% for BFRCM-strengthened cylinders. However, it should be reminded that three specimens were tested by using BFRCM; differently, two cylinders were confined by BFRP and, consequently, differences observed in the strength increases should be revised by testing the same number of specimens. Despite the different strength enhancement, it is evident that BFRP confinement induced a more brittle behaviour with respect to BFRCM wraps. In fact, the stress-strain curves of BFRP-confined specimens of Scheme I are characterized by a steep post-peak branch, which reflects the failure mode of the cylinders. Differently, BFRCM-wrapped specimens exhibited a more ductile softening branch, with a greater value of residual strain.

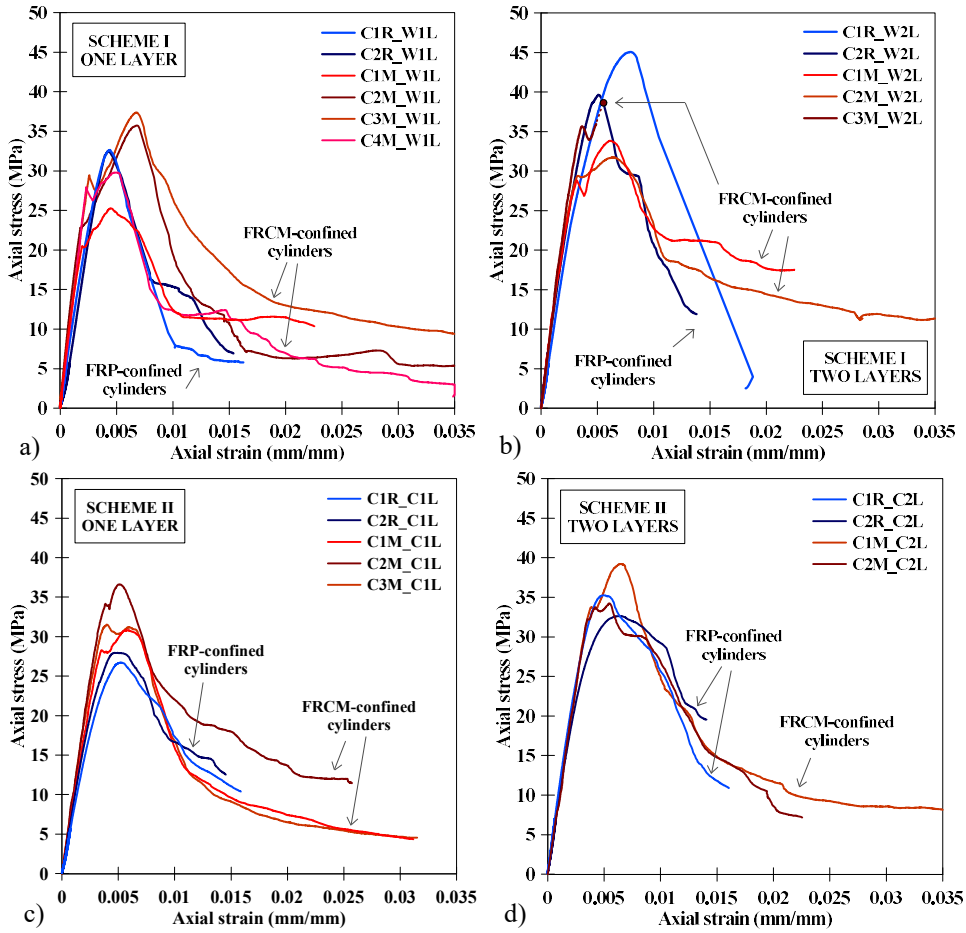

Figure 4.39 Axial stress-strain curves of confined cylinders: a) one-layer reinforced specimens of Scheme I; b) two-layer reinforced specimens of Scheme I; c) one-layer reinforced specimens of Scheme II; d) two-layer reinforced specimens of Scheme II

Analogously, BFRP and BFRCM-confined cylinders of Scheme II showed a different behaviour in terms of strength enhancement. In fact, specimens wrapped with one BFRP layer (Figure 4.39c) obtained an average strength increase equal to 38%, while the compressive strength enhanced of 66% in the case of BFRCM-confined cylinders. The strength gains for specimens reinforced with two layers of fabric (Figure 4.39d) were equal to 71% and 85% for BFRP and BFRCM confinement respectively.

The commented outcomes prove the capability of composites with inorganic matrix to enhance the performance of masonry members, being able to guarantee great gains in terms of axial strength and inducing a more ductile behaviour.

4.4.4 Failure modes and crack patterns

Unconfined cylinders

Figure 4.40 shows the failure modes of unwrapped cylinders at the end of compressive tests. The unconfined masonry specimens exhibited, as expected, a brittle behaviour and specimens failed due the formation of large and almost vertical cracks through their entire height.

There were not considerable differences in the failure mode of Scheme I (Figure 4.40a) and Scheme II (Figure 4.40b) cylinders. In general, vertical joints created preferential routes for the development of cracks, which propagated at the interface between bricks and mortar joints. This was more evident for Scheme II specimens involving three vertical joints (Figure 4.40b) and less for Scheme I (Figure 4.40a), in which there were cracks at interface between mortar and bricks, besides other random cracks.

The failure of unconfined cylinders involved crushing of masonry with spalling of material for whole the height of the cylinders. In particular, the loss of material regarded bricks between the vertical joints, while the latter were less damaged: dashed rectangles in Figure 4.40 highlight this behaviour. Even in this case, this was clearer for Scheme II specimens, because of the larger number of vertical joints.

BFRP-confined cylinders

The failure of BFRP-wrapped cylinders was always by tensile rupture of the BFRP jacket. The damage of confined specimens at the end of the tests can be seen in Figure 4.41. As a general rule, specimens were characterized by two or more almost vertical cracks which propagated for the entire length and turned horizontal, linking each other, near to the horizontal mortar joints. Due to the cracks, the jacket bulged in some areas. The ultimate condition of BFRP-confined specimens was reached due to the failure of the basalt textile at the cracks.

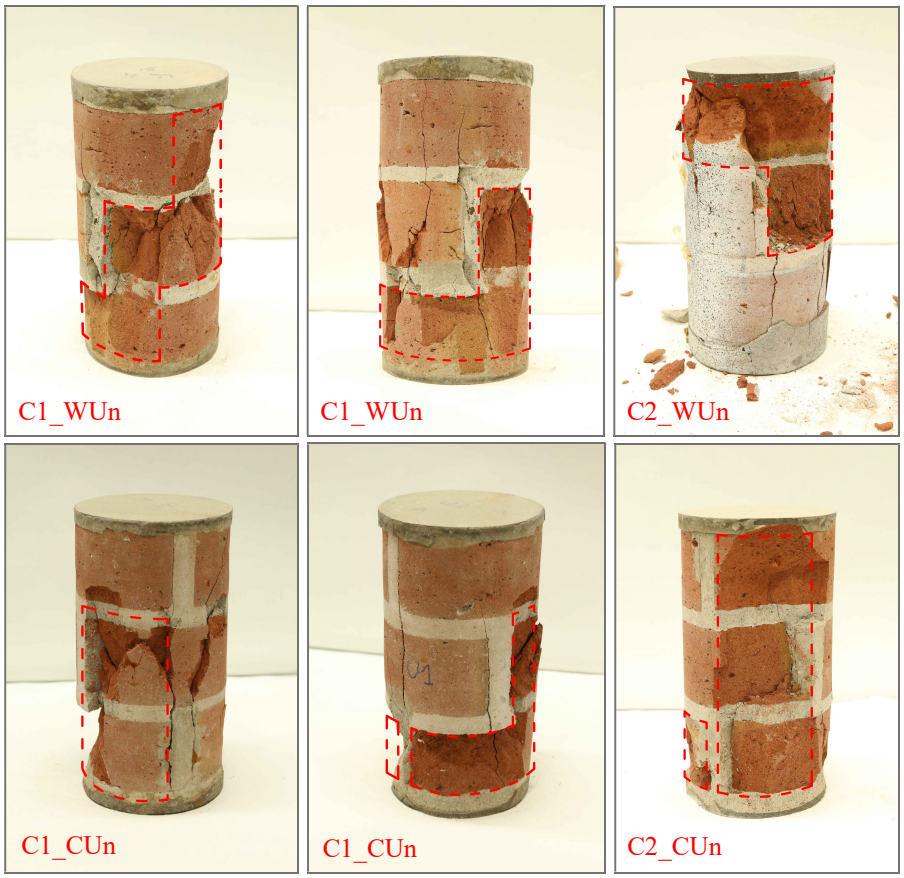

Figure 4.40 Failure modes of unconfined cylinders: a) Scheme I; b) Scheme II

Giving a look to the inner masonry core through the cracks, it was possible to observe the crushing of the material.

There were not considerable differences in the failure mode of cylinders wrapped with one or two BFRP layers, both for Scheme I and Scheme II. As an example, it is worth to observe the damage of cylinders C2_W2L and C1_C1L after testing, in Figure 4.42. Specimens presented the same crack pattern even if one cylinder (C2R_W2L) belonged to Scheme I and was wrapped with two layers, the second one (C1R_C1L) was obtained from Scheme II and was wrapped by using one layer. There were two large vertical cracks, covering two thirds of the height, from the middle to the bottom. One crack turned horizontally, apparently near the upper horizontal joint.

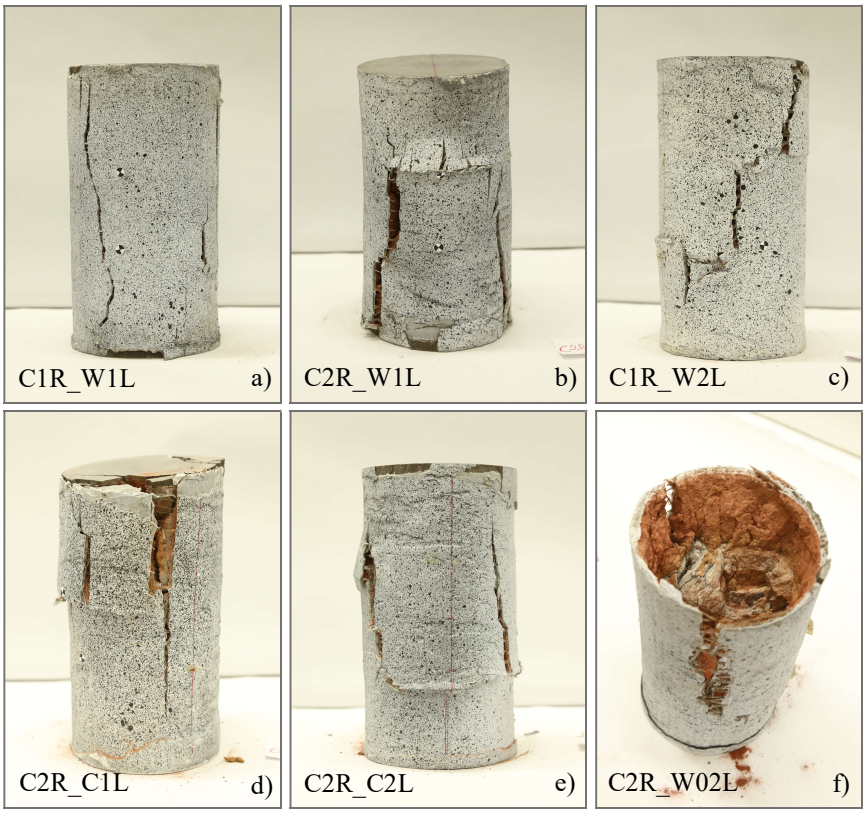

Figure 4.41 Failure modes of BFRP-confined cylinders: a) b) Scheme I–1 layer; c) Scheme I–2 layer; d) Scheme II-1 layer; e) Scheme II-2 layers; i) BFRP-masonry strong bond and severely crushed core

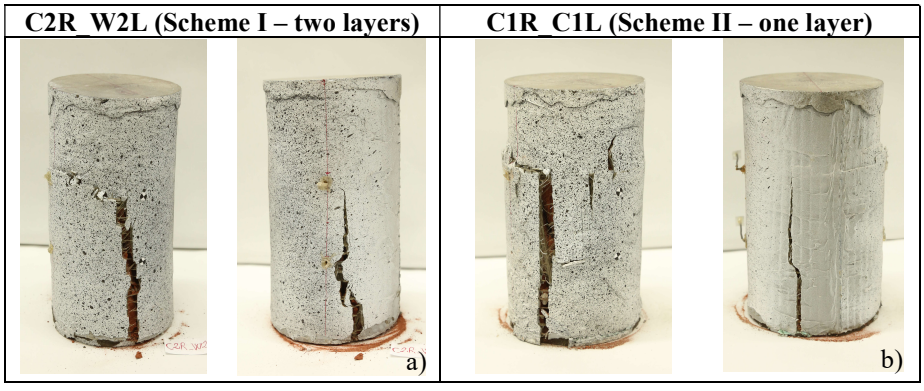

Figure 4.42 Comparison between the failure mode of FRP-wrapped cylinders from Scheme I and Scheme II: a) specimen C2R_W2L; b) specimen C1R_C1L

After testing, a visual examination of the cylinders revealed a strong bond between the BFRP jacket and the external masonry substrate. There was not debonding between BFRP layers at the overlapping zone and this means the overlapping length was sufficient to avoid this premature failure. Moreover, it was observed that the inner masonry core of wrapped cylinders was seriously crushed, more than unconfined masonry cylinders (Figure 4.41f).

BFRCM-confined cylinders

Figure 4.43 and Figure 4.44 present the BFRCM-confined specimens at the end of the tests. In particular, one-layer wrapped cylinders from Scheme I and Scheme II respectively are shown in Figure 4.43, while specimens confined by using two textile layers are depicted in Figure 4.44.

There were not marked differences in the failure mode of specimens from different schemes and the ultimate condition was reached by failure of the basalt textile at the cracks developed in the mortar. The crack pattern was characterized by vertical cracks which developed for the entire length of the samples, producing detachment of the external mortar layer of the jacket and the loss of material in some areas.

Apart from these zones, the jacket was solid, with the grid and the two mortar layers very tight, and it was well linked to the inner masonry core. Cracks in the external mortar layer coincided with the failure of the grid and of the internal mortar layer in that point (Figure 4.44g).

The main difference in the failure mode of one and two-layer wrapped cylinders was the amount of detached material from the jacket and the location of these detachments. In the case of one-layer wrapped specimens, the detachment of the external mortar layer was concentrated in a part of the lateral surface, while the remaining area was affected by some cracks or almost undamaged. In the case of two-layer wrapped cylinders, the areas with loss of material were smaller, but distributed along the sample surface.

This behaviour was connected with the development of the cracks. For one-layer wrapped cylinders, cracks were limited in number, developing along the entire length of the samples and they were well defined in their vertical trend. For two-layer wrapped cylinders, there were more cracks which hardly covered whole the length of specimens. Sometimes, they developed for a length portion

and combined with horizontal cracks due to a non-uniform bulging of the jacket at different heights of the cylinders.

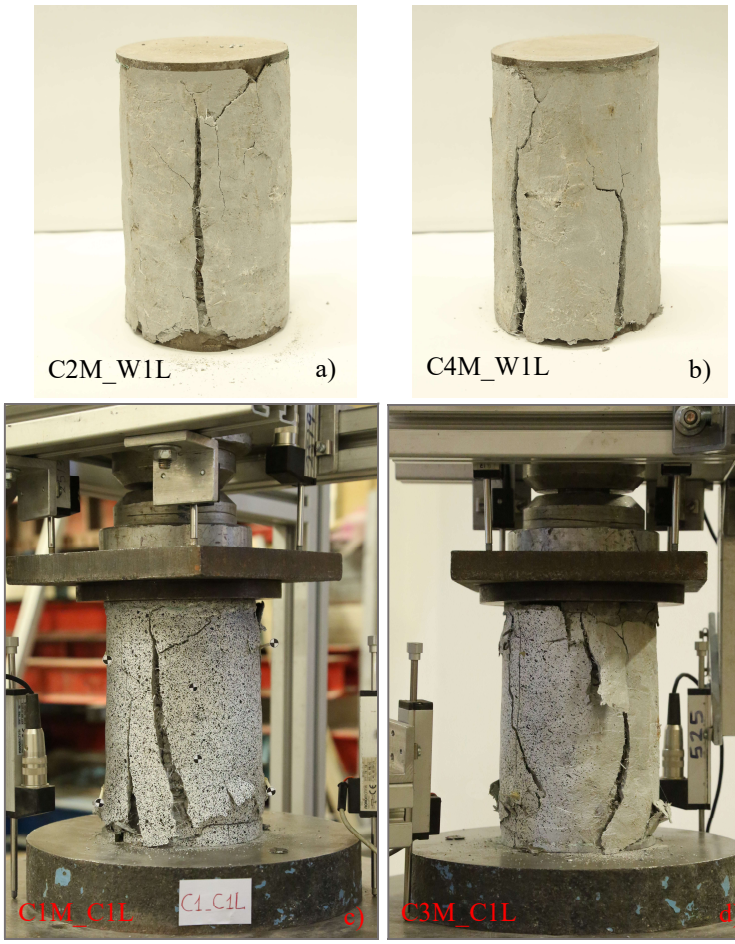

Figure 4.43 Failure modes of BFRCM-confined cylinders: a) b) Scheme I-1 layer; c) d) Scheme II-1 layer

4.4.5 Effective strain in the wrap

As discussed in Chapter 2, several literature studies proposed analytical models based on the calculation of the confinement pressure due to the external wrap, under the assumption that this last reaches its maximum stress in correspondence of the axial peak load.

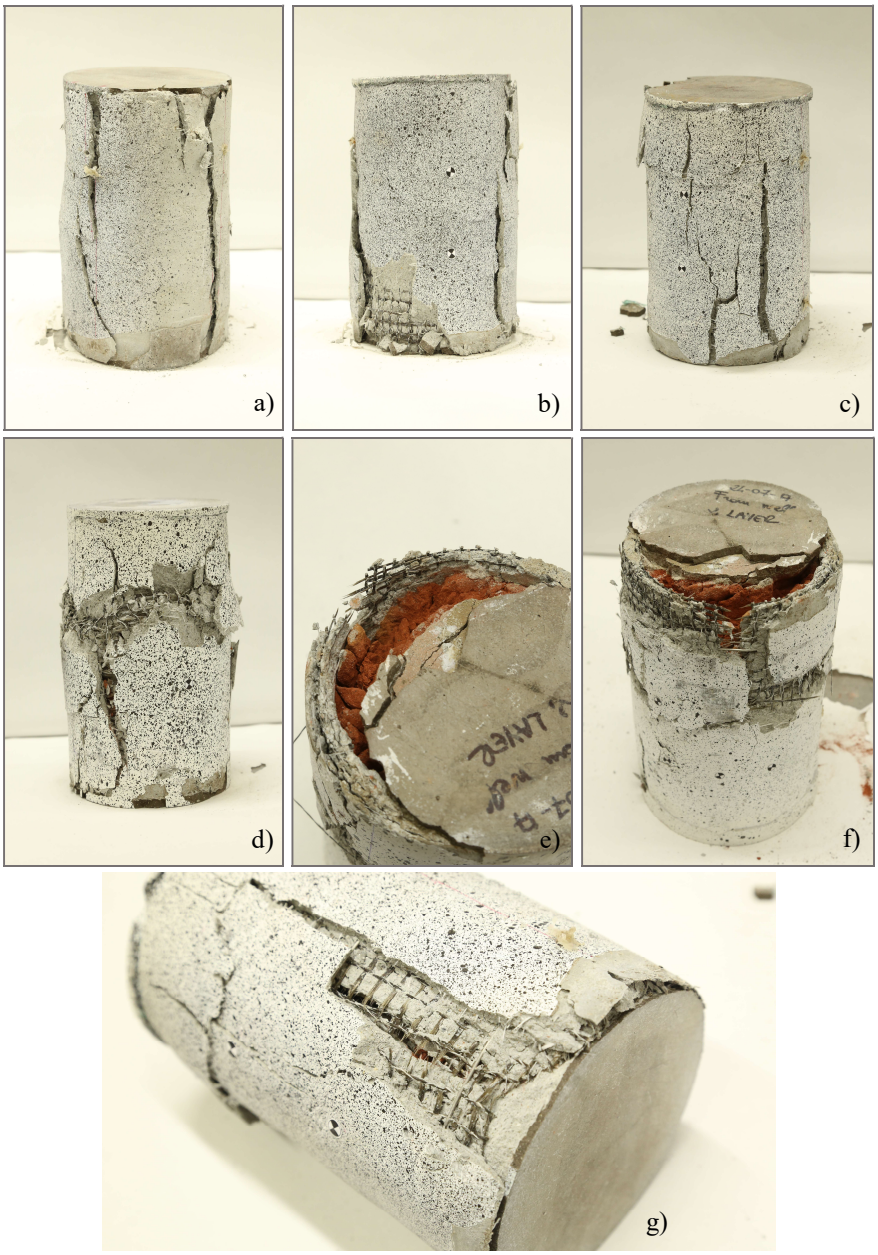

Figure 4.44 Failure modes of BFRCM-confined cylinders: a) b) c) Scheme II-2 layer; d) Scheme I-2 layers; e) BFRCM-masonry strong bond and severely crushed masonry core; f) g) failure of BFRCM jacket

Aiming to verify this assumption, the DIC system was employed in order to measure the hoop strains in confined cylinders and to compare the recorded values with the mechanical properties of the jacket.

As an example, Figure 4.45 shows the 2D field of hoop strains in the cylinder C1R_W1L, which was wrapped by one layer of BFRP. In particular, the record of the strains is plotted for two stages of the loading process, corresponding to the peak stress (Figure 4.45a) and to the failure of the external wrap (Figure 4.45b). These two stages can be identified at Points 1 and 2 of the stress-strain curve of the confined specimen represented in Figure 4.45c.

It is evident that the strain in the composite when the specimen reaches the peak stress is almost uniform and substantially lower than its ultimate value. The colorplot (Figure 4.45a) indicates a tensile strain in the BFRP of about 0.6%, which is substantially lower than the failure strain detected in the fabric by tensile tests (i.e. 2.7%). This fact means that masonry reached its peak load in correspondence of internal crushing, while the external BFRP jacket was still elastic. In fact, the ultimate stress of the composite was reached only in a successive stage (Figure 4.45b). It is worth to note that the strain field at failure is not uniform, but strain is localized along a subvertical zone.

A different behaviour was recorded in BFRCM-confined specimens. Figure 4.46 shows the colorplot of hoop strains for specimen C2M_C2L, which was tested without the use of the external ring for allowing a wider monitoring area. This choice was made due to the fact that, differently from BFRP-confined specimens, the crack pattern at failure in BFRCM-confined specimens was more diffused.

It is evident that the first drop in the axial stress-strain curve of confined masonry (Point 1 in Figure 4.46d) corresponded to the formation of the first cracks in the top zone of the specimen (Figure 4.46a) for very low values of strain. This stage did not correspond to the peak load; in fact, cracks propagated at the extremities of the monitoring area (Figure 4.46b and Point 2 of Figure 4.46d) and the load increased up to its maximum value.

The maximum load was reached in correspondence of Point 3 (Figure 4.46c and Point 3 of Figure 4.46d), when cracks were formed and opened in the top and bottom part of the cylinder. It is worth to note that in this stage, the maximum value of strain recorded in correspondence of cracks was already close to the

strain at failure of dry textile, even if this condition was not reached yet. This result point out the presence of slipping phenomena between the basalt grid and the matrix at cracks, as already shown by tensile tests on FRCM coupons.

After this point, the load decreased and cracks developed to the central part of the specimen. After cracks were all formed, hoop strain was localized in the fibre and this process ended when its value exceeded the ultimate strain of the fabric (Figure 4.46e and Point 4 in Figure 4.46d). After this point, the stress in the masonry decreased drastically and the cylinder could be considered at its ultimate stage.

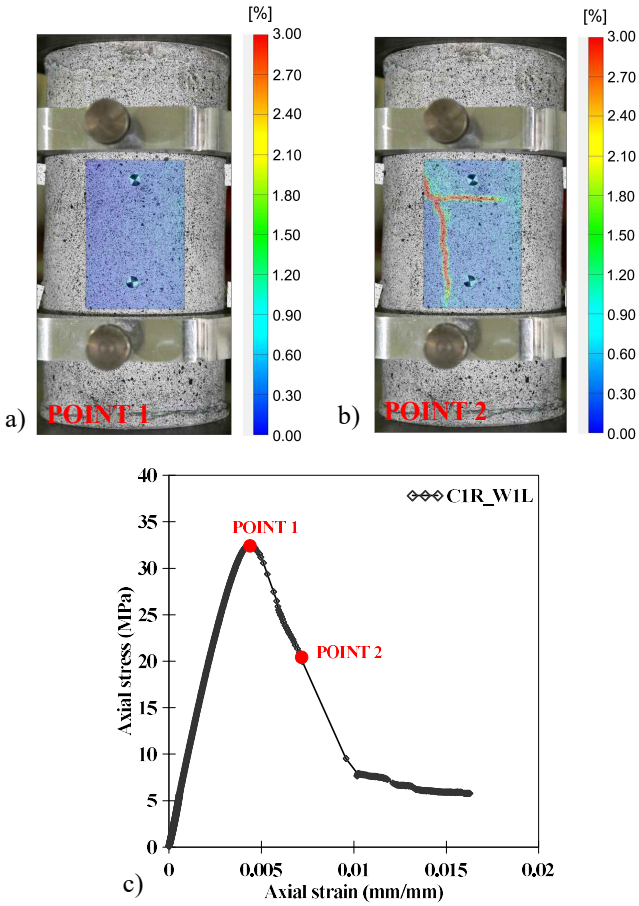

Figure 4.45 Strain measurement in a BFRP-confined cylinder (C1R_W1L): a) 2D strain field measured by DIC at peak stress of masonry; b) 2D strain field measured by DIC at failure of the wrap; c) axial stress-strain curve of the cylinder;

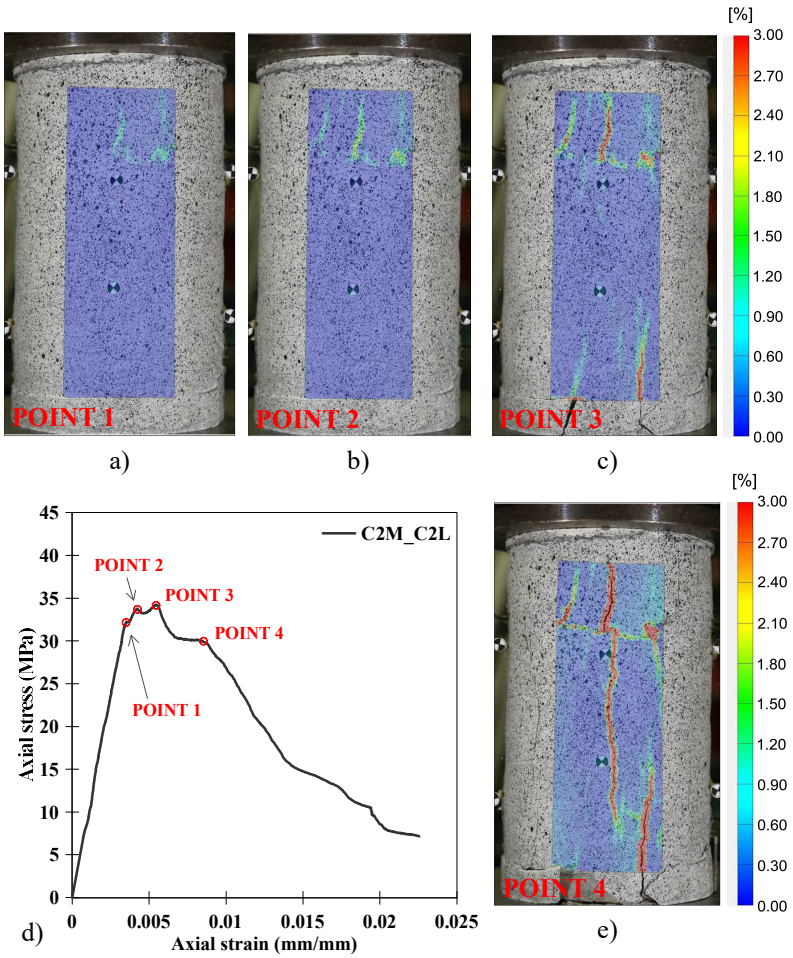

Figure 4.46 Strain measurement in a BFRP-confined cylinder (C2M_C2L): a) 2D strain field measured by DIC at first cracking of the jacket; b) 2D strain field measured by DIC at second drop of load; c) 2D strain field measured by DIC at peak stress of masonry; d) 2D strain field measured by DIC at failure of the fabric; e) axial stress-strain curve of the cylinder;

4.4.6 Evaluation of volumetric strain

In Figure 4.47 the variation of axial stress vs. volumetric strain is presented for unconfined and BFRP-confined specimens from Scheme I and Scheme II respectively. The volumetric strain ε_v was evaluated as it follows:

$$\varepsilon_v = \varepsilon_a + 2\varepsilon_h \tag{4.1}$$

where ε_a is the axial strain obtained from the average of the twenty extensometers considered in the axial direction and ε_h is the hoop strain obtained from the average of the forty-five extensometers in the transversal direction.

The first zone of the curves is almost linear and all the specimens (except specimen C2R_W1L) exhibit the same behaviour in terms of volumetric strain with the increase of the axial stress. This first branch of the curves is characterized by an increasing negative volumetric strain, which indicates a volume compaction. After a certain point, the behaviour changes and ε_v starts to increase, entering in a transition zone. When the volumetric strain becomes zero, it means that the volume of the cylinder is equal to the initial volume and it starts a third zone. At this point the jacket was fully activated since the cylinders entered to volume expansion, showing a non-linear behaviour.

For unconfined specimens from Scheme I the volume expansion was not pronounced because of the brittle failure of the cylinders. After the transition zone, in which the volume of the cylinders returns equal to the initial volume, the curve of C3R_WUn develops for a very short length, while for specimen C2R_WUn the volume expansion is almost completely inexistent. Results from Scheme II unconfined specimens are not available because of the lack of data about the hoop strain.

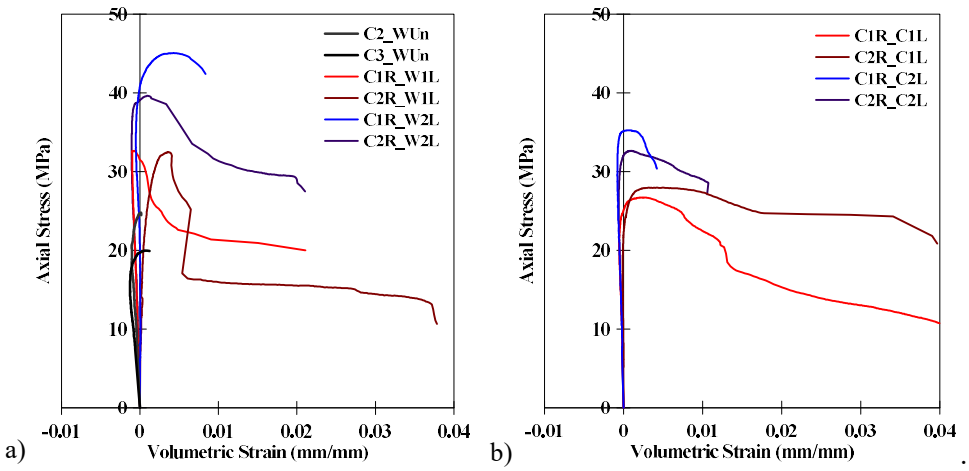

Figure 4.47 Variation of volumetric strain for BFRP-confined cylinders: a) Scheme I specimens; b) Scheme II specimens

Comparing one and two-layer wrapped cylinders, it can be observed that specimens with one BFRP layer experienced a larger average volume expansion which indicate a lower stiffness of the wrap. The increase of BFRP layers caused a significant gain in strength and a lower volume expansion; this is true for both Scheme I and Scheme II.

Figure 4.48 shows the variation of hoop strain vs. axial strain for Scheme I and Scheme II specimens respectively. Technically, the hoop-axial strain ratio is the Poisson's ratio of the masonry at the first zone of stress-strain curves (i.e. linear behaviour). All the cylinders exhibit an initial linear behaviour with Poisson's ratio of about 0.3, followed by a non-linear trend, except for unconfined cylinders which arrest after the linear stage. The non-linear branches show different slopes for both Scheme I and Scheme II, but for the latter it is clear as two layers of BFRP wraps are more effective to control the dilatation rate, with restrained hoop strains.

The same analysis was not carried out in the case of BFRCM-confined masonry cylinders because, as shown in Section 4.4.2, the hoop strain values registered by DIC were affected by the progressive crack and detachment of the jacket

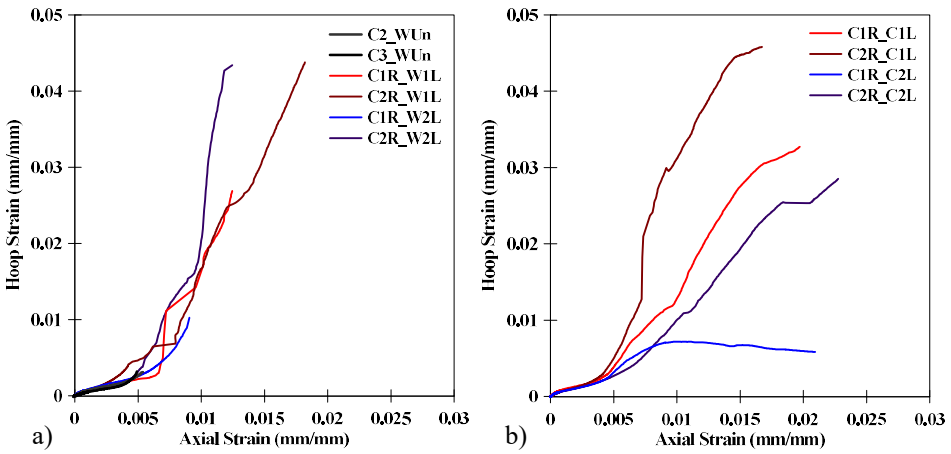

Figure 4.48 Variation of hoop strain vs. axial strain for BFRP-confined cylinders: a) Scheme I specimens; b) Scheme II specimens

5. THEORETICAL INVESTIGATIONS

5.1 Introduction

In order to predict the behaviour of confined masonry under monotonic compression, the modelling through analytical expressions constitutes a reliable and easy-to-manage provisional tool.

In the present chapter the analytical models presented in Chapter 2 are employed in order to evaluate the compressive strength of FRP/FRCM-confined masonry and to predict the stress-strain response in compression of these members.

First, some experimental-theoretical comparisons are made using experimental data available in the literature on FRP-confined masonry columns, in order to evaluate the reliability of existing theoretical models.

Then, the predictions provided by theoretical models on masonry columns confined by FRP and FRCM are compared with the experimental outcomes obtained in the framework of this thesis and their reliability is validated in terms of strength increments. Finally, the compressive law of BFRP and BFRCM-confined cylinders is defined by proposing new possible approaches.

5.2 FRP-confined masonry columns: evaluation of available analytical models

The literature review has shown that a unified approach for the definition of the compressive behaviour of FRP-confined masonry is still missing. Despite the large amount of research, some theoretical results seem actually to be in contrast with the experimental outcomes available in literature, due to the different key variables arising in the application of FRP jackets.

With the aim of evaluating their reliability, the main existing theoretical models to predict the compressive response of FRP-confined masonry columns are revised and analyzed in the following. In particular, five different approaches

are considered: Campione and Miraglia (2003) (C&M), Krevaikas and Triantafillou (2005) (KRE), Corradi et al. (2007) (CO), Di Ludovico et al. (2010) (DIL) and finally Italian CNR-DT 200/2013 Guidelines (CNR). Criteria to obtain the strength increase are initially analyzed and compared with a wide range of experimental data, evaluating the match between theoretical and experimental outcomes. In a second step, the combination of expressions by different models is adopted for predicting the compressive stress-strain response of masonry columns wrapped by FRP and quantitative comparisons are made with a wide database of experimental data. The average error is evaluated for each model in order to estimate his the reliability.

5.2.1 Strength increase due to FRP confinement

As mentioned above, the formulations providing the strength of confined masonry are initially studied and compared. Table 5.1 shows the expressions, already presented in Chapter 2, for calculating the compressive strength of FRP-confined masonry f_{mc} as a function of the effective confinement pressure f'_l and unconfined masonry strength f_{m0}.

In order to clarify their reliability, the results achieved by using the formulations in Table 5.1 were compared with experimental results available in the literature. In particular, an experimental database of forty-seven results was recorded, listing the main geometrical and mechanical features and the results achieved in terms of ultimate stress, strain and complete compressive axial force-shortening curve. Table 5.2 shows the main geometrical features and the characteristics of the external wrap for the analyzed specimens.

Figure 5.1 shows graphically the comparison between the formulas of Table 5.1 and experimental results. In particular, it plots the strength increase f_{mc}/f_{m0} as a function of the effective confinement pressure f'_l normalized by the strength of unconfined masonry f_{m0}.

Points in Figure 5.1 refer to the experimental data reported in Table 5.2. Specifically, the confinement pressure was assumed equal to its maximum value, which means that it was calculated for each specimen as:

$$f_l^{'} = k_e \cdot f_l \tag{5.1}$$

Table 5.1: Formulations for calculating the compressive strength of FRP-confined masonry

Model	Compressive strength of FRP-confined masonry
Campione and Miraglia, 2003 (C&M)	$f_{mc} = f_{m0} + k_1 \cdot f_l^{'}$ $k_1 = 2$
Krevaikas and Triantafillou, 2005 (KRE)	$\begin{cases} f_{mc} = f_{m0} & if \ \frac{f_l^{'}}{f_{m0}} \le 0.24 \\ f_{mc} = f_{m0} \cdot \left(0.6 + 1.65 \cdot \frac{f_l^{'}}{f_{m0}} \right) & if \ \frac{f_l^{'}}{f_{m0}} \ge 0.24 \end{cases}$
Corradi et al., 2007 (CO)	$f_{mc} = f_{m0} + k_1 \cdot f_l^{'}$ $k_1 = 2.4 \cdot \left(\frac{f_l^{'}}{f_{m0}} \right)^{-0.17}$
Di Ludovico et al., 2010 (DIL)	$f_{mc} = f_{m0} + k_1 \cdot f_l^{'}$ $k_1 = 1.53 \cdot \left(\frac{f_l^{'}}{f_{m0}} \right)^{-0.10}$
CNR-DT 200/2013, (CNR)	$f_{mc} = f_{m0} + k_1 \cdot \left(\frac{f_l^{'}}{f_{m0}} \right)^{\alpha_1}$ *where* $\alpha_1 = 0.5$ $k_1 = \alpha_2 \cdot \left(\frac{g_m}{1000} \right)^{\alpha_3}$ *where* g_m : *mass density of masonry* $\alpha_2 = \alpha_3 = 1$

$$k_e = 1 - \frac{(b^{'2} + d^{'2})}{3 \cdot A_m} \tag{5.2}$$

$$f_l = \frac{(b+d)}{b \cdot d} \cdot t_f \cdot f_r \tag{5.3}$$

and assuming that the external wrap reaches its maximum stress at failure:

$$f_r = f_{fu} = \varepsilon_{fu} \cdot E_f \tag{5.4}$$

where f_{fu} is the tensile strength of the FRP, ε_{fu} is its ultimate tensile strain and E_f is the elastic modulus.

Table 5.2: Geometrical features of specimens considered in the experimental database.

	Specimen	Geometry				External wrap					
		n	b (mm)	d (mm)	r_c (mm)	b' (mm)	d' (mm)	t_f (mm)	f_{fu} (MPa)	E_f (MPa)	ε_{fu}
DIL (2010)	B-G-1	1	264	265	20	224	225	0.48	1371	68740	0.0209
	B-G-2	1	265	265	20	227	225	0.48	1371	68740	0.0209
	B-G-3	1	266	265	20	226	225	0.48	1371	68740	0.0209
	B-B-1	1	266	266	20	226	226	0.24	1814	91000	0.0199
	B-B-2	1	265	264	20	225	224	0.24	1814	91000	0.0199
	B-B-3	1	265	264	20	225	224	0.24	1814	91000	0.0199
KRE (2005)	C1_1_R10	3	115	115	10	95	95	0.12	3500	230000	0.0152
	C2_1_R10	2	115	115	10	95	95	0.23	3500	230000	0.0152
	C3_1_R10	3	115	115	10	95	95	0.35	3500	230000	0.0152
	G5_1_R10	2	115	115	10	95	95	0.75	2000	70000	0.0286
	C1_1_R20	2	115	115	20	75	75	0.12	3500	230000	0.0152
	C2_1_R20	2	115	115	20	75	75	0.23	3500	230000	0.0152
	C3_1_R20	2	115	115	20	75	75	0.35	3500	230000	0.0152
	G5_1_R20	2	115	115	20	75	75	0.75	2000	70000	0.0286
	C2_1.5_R10	3	115	172.5	10	95	152.5	0.23	3500	230000	0.0152
	C3_1.5_R10	3	115	172.5	10	95	152.5	0.35	3500	230000	0.0152
	G5_1.5_R10	3	115	172.5	10	95	152.5	0.75	2000	70000	0.0286
	C2_2_R10	2	115	230	10	95	210	0.23	3500	230000	0.0152
	C3_2_R10	2	115	230	10	95	210	0.35	3500	230000	0.0152
	G5_2_R10	2	115	230	10	95	210	0.75	2000	70000	0.0286
CO (2007)	S-HT-2-n°1	5	245	250	20	245	250	0.33	3388	417625	0.0081
	S-VHM-2-n°1	3	245	250	20	245	250	0.286	1955	673200	0.0029

As it can be noted from Figure 5.1, wide dispersion of experimental points with respect to the theoretical predictions is observed. The CO model seems to be the most overestimating, while the KRE model gives the lowest strength increases, even if several points are also overestimated.

The lacking match between experimental results and theoretical predictions is due to different key parameters: - the variability of basic masonry properties; -

the evaluation of the effective confining stress, the latter depending on the corner radius. The first issue is related to the wider scattering of compressive strength of masonry with respect to that of concrete. It is well known that for a given kind of masonry (i.e. clay brick units and hydraulic mortar) the compressive strength is influenced by arrangement of units, thickness of mortar joints and size of the tested member.

However, the most critical issue is related to the effective confinement pressure. Figure 5.1 shows that some specimens with similar maximum confinement pressure, which means similar external wraps in terms of thickness and mechanical properties, gain very different strength increases. As an example, specimens with effective normalized confinement pressure equal to 1.3 could reach a maximum strength increase equal to about 3.7 and a minimum of 2.8. This is due to the fact that the stress in the external wrap can be noticeably lower than its tensile strength due to the stress intensification at the corners of the section and consequent weak failure. It has been widely demonstrated (Corradi et al. 2007, Campione and Miraglia 2003, Di Ludovico et al. 2010) that in this case the effective stress in the wrap is related to the adopted corner radius smoothing the corners. Therefore, confinement pressure should be calculated considering a stress intensification factor at the edge in order to achieve more reliable prediction, as discussed in the following sections.

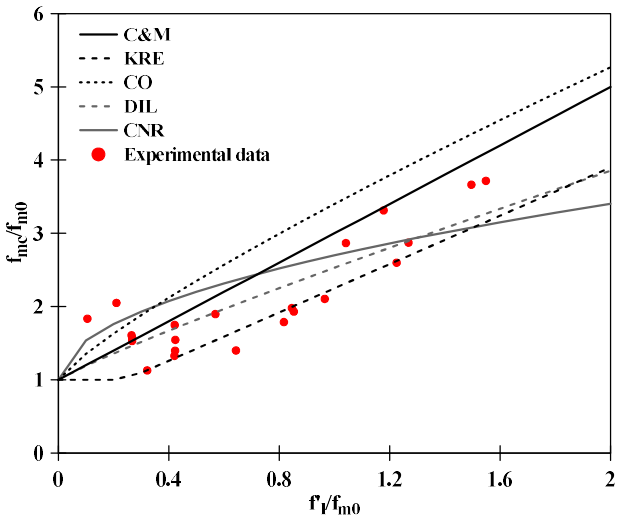

Figure 5.1 Compressive strength increase as a function of normalized effective confinement pressure

5.2.2 Definition of the stress-strain law in compression

As discussed above, five "models" were considered to predict the stress-strain law of FRP-confined masonry in compression, by combining expressions provided by the five analytical studies here considered. For each "model", confinement pressure and efficiency coefficient are calculated by means of Eqs. (5.1)-(5.3), but varying the expression of f_r. Moreover, the ultimate stress, strain and shape of the analytical stress-strain law are defined for each model.

C&M model (Campione and Miraglia, 2003)

In this model the effective stress in the wrap is evaluated through Eq. (2.7) introduced in Chapter 2.

The strength of FRP-confined masonry is calculated by the expression given in the first row of Table 5.1, while the ultimate strain ε_{mc} is defined by Eqs. (2.9) and (2.10).

After defining these parameters, the compressive response of FRP-confined masonry columns is obtained by means of Eqs. (2.11)-(2.13).

KRE model (Krevaikas and Triantafillou, 2005)

The KRE model considers the effective confinement pressure calculated by assuming $f_r = f_{fu}$.

The maximum stress of the FRP-confined masonry is calculated as indicated in Table 5.1 for the KRE model, while the ultimate strain is deduced by the expression reported in Eq. (2.15) of Chapter 2.

The overall stress-strain curve in compression is calculated by Eqs. (2.11)-(2.13) proposed by Campione and Miraglia (2003), assuming $R = 3$.

CO model (Corradi et al., 2007)

In the model of Corradi et al. (2007) the effective stress in the external wrap is calculated by Eq. (2.17) presented in Chapter 2.

The strength of confined masonry is calculated as indicated in Table 5.1 for the CO model, while the ultimate strain is calculated by means of Eqs. (2.9) and (2.10), since no expression is given in Corradi et al. 2007 for this.

The trend of the compressive stress-strain curve is defined by Eqs. (2.11)-(2.13), but the R parameter is here assumed equal to 5, as indicated in Corradi et al. 2007.

DIL model (Di Ludovico et al., 2010)

The model of Di Ludovico et al. (2010) evaluates the effective confinement pressure by assuming $f_r = f_{fu}$.

The maximum stress is calculated by the expression provided in Table 5.1 for the DIL model. The ultimate strain is evaluated by employing Eqs. (2.9) and (2.10).

Even in this case, the trend of the compressive stress-strain curve is defined by Eqs. (2.11)-(2.13), assuming $R = 3$.

CNR model (CNR-DT 200/2013)

The model deduced from the Italian CNR-DT 200/2013 Guidelines considers the stress in the external FRP wrap as reported in Eqs. (2.21) and (2.22) of Chapter 2.

The strength increase is calculated as indicated in Table 5.1 for the CNR model and the ultimate strain is defined through the formulation provided by Campione and Miraglia (2003) (Eqs. 2.9, 2.10).

The constitutive law of FRP-confined masonry is evaluated by means of the expressions given in CNR-DT 200/2013 and presented in Eqs. (2.23)-(2.27) of Chapter 2.

5.2.3 Comparisons with experimental data

Firstly, comparison between the models is made in terms of predicted strength gain. As discussed in the previous section, neglecting the effective stress in the wrap could lead to a wide dispersion of experimental results. Conversely, Figure

5.2 shows that different results are achieved if a reduced confinement pressure is calculated.

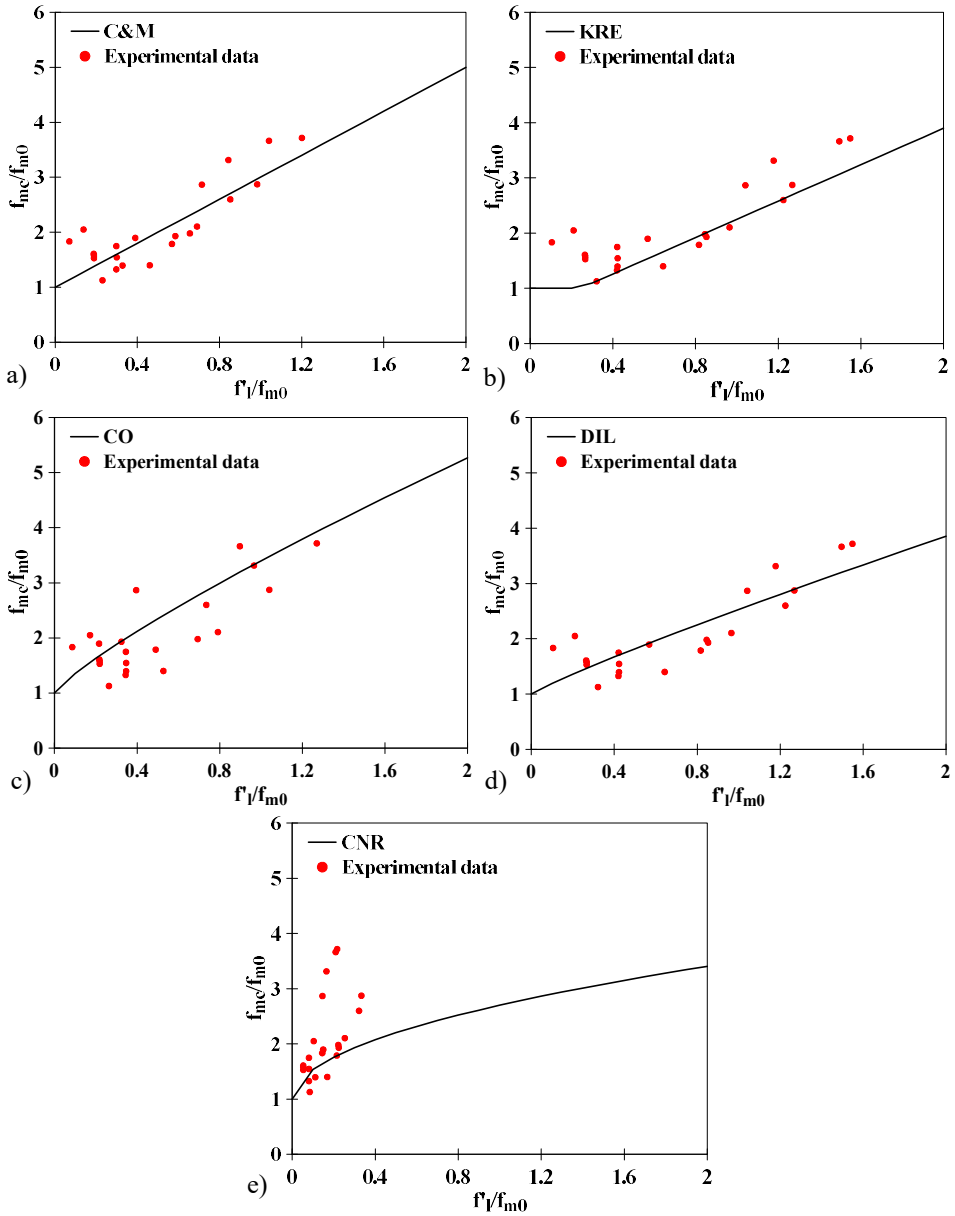

Figure 5.2 Strength increase as a function of normalized effective confinement pressure for the considered models: a) C&M; b) KRE; c) CO; d) DIL; e) CNR

The results are also expressed in terms of statistical parameters in Table 5.3, which shows the average ratio between the theoretical prediction of the compressive strength $f_{mc,th}$ and the experimental result $f_{mc,\exp}$. The Coefficient of Variation (COV) (the ratio between the standard deviation and the average value) is also given, in order to measure the dispersion of the prediction with respect to the average value.

It is evident that the C&M model is the most conservative (Figure 5.2a), underestimating confinement pressure and strength gains. This result could be due to the fact the equation expressing the strength increase was originally based on results obtained from concrete specimens.

The CO model shows good theoretical predictions (Figure 5.2c), unlike those obtained using the maximum confinement pressure. However, a quite wide dispersion of results is still observed, since the authors adopted only their own results to work out the equation expressing the strength increase.

The model which better fits the experimental outcomes is DIL model (Figure 5.2d), which shows the average ratio $(f_{mc,th}/f_{mc,exp})_{\mathrm{AV}}$ close to 1 and the lowest COV. This result was probably achieved because the authors calibrated the equation reported in Table 5.1 by best fitting many experimental points adopted in the present study.

The KRE model (Figure 5.2b) predicts slightly lower results. Most of the experimental points are on the curve expressing the theoretical prediction and reduced dispersion is observed with a low COV value.

Table 5.3: Reliability of each model in terms of predicted strength

Model	$(f_{mc,th}/f_{mc,exp})_{AV}$	COV
Campione and Miraglia, 2003 (C&M)	0.74	0.21
Krevaikas and Triantafillou, 2005 (KRE)	0.87	0.19
Corradi et al., 2007 (CO)	1.16	0.22
Di Ludovico et al., 2010 (DIL)	1.05	0.18
CNR-DT 200/2013 (CNR)	0.88	0.26

Finally, the CNR model (Figure 5.2e) proves to be conservative. Normalized confinement pressure is fairly similar for all the specimens since the model provides a maximum strain in the wrap equal to 0.004, as discussed in Chapter 2. Consequently, the model is in good accordance with the experimental results only for very low values of the FRP reinforcement ratio and tends to underestimate experimental outcomes for highly reinforced specimens or ones with larger corner radius.

A further analysis was carried out by comparing results in terms of compressive axial stress-strain curves. Analytical predictions were made by considering the equations given in the previous section for each specimen listed in Table 5.2 and for two different values of ε_{m0}. In the first analysis the axial strain corresponding to the peak stress of unconfined masonry ε_{m0} was set equal to 0.003, while in the second study ε_{m0}=0.002 was assumed.

As an example, Figure 5.3 shows four comparisons between the theoretical curves and experimental data, referring to some specimens tested by Krevaikas and Triantafillou (2005) and Di Ludovico et al. (2010). It is to be stressed that very different theoretical predictions can be obtained by adopting the different models. In order to quantify the capability of each predictive model, an error index was calculated in terms of stress. In particular, this parameter was defined as the ratio between the predicted and the experimentally measured stress (σ_{th}/σ_{exp}) for a fixed value of axial strain. This parameter made it possible to evaluate the accuracy of the prediction for each point of the stress-strain curve and it was evaluated for forty values of axial strain for each analyzed experimental curve. Therefore, an average value was calculated for each specimen over the forty points.

Figure 5.4 shows the average error calculated for each analyzed specimen and adopting ε_{m0}=0.003 for the five considered models. As resuming parameters, the mean value of the error ratio $(\sigma_{th}/\sigma_{exp})_{AV}$ between all the specimens examined and its COV are shown in Table 5.4 for the five theoretical models.

It is evident that the C&M and CO models tend to overestimate the experimental stress-strain curves. Some experimental results are overestimated with a ratio of over 3 and wide dispersion of the predictions is also observed.

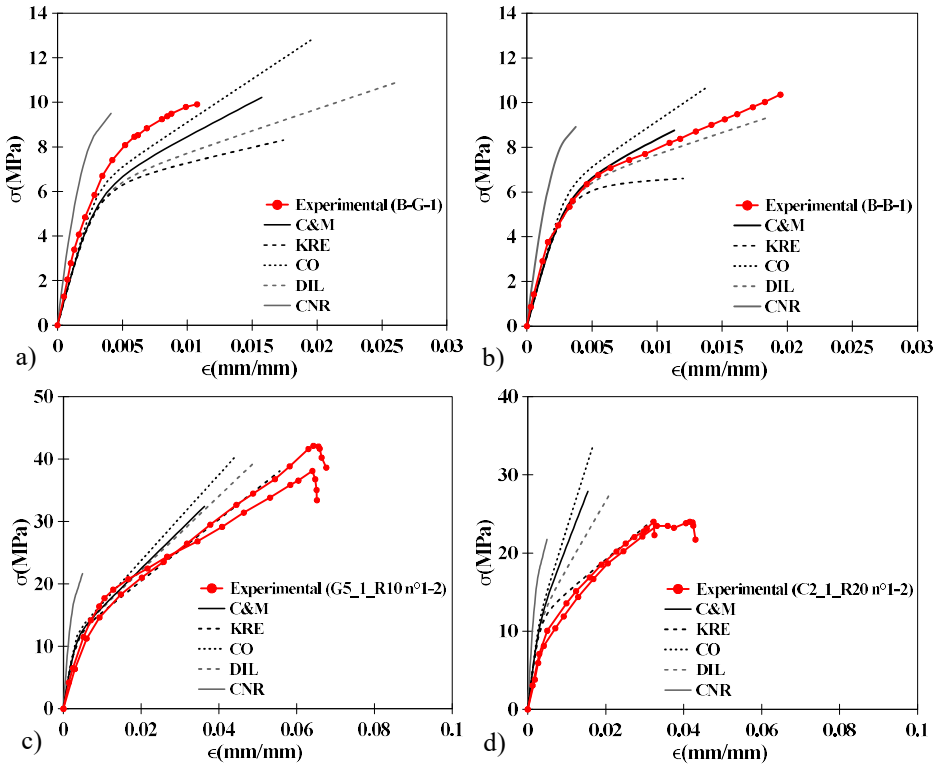

Figure 5.3 Comparison between experimental and theoretical stress-strain curves: a) Specimen B-G-1 (Di Ludovico et al. 2010); b) Specimen B-B-1 (Di Ludovico et al. 2010); c) Specimen G5_1_R10_ n°1 and 2 (Krevaikas and Triantafillou 2005); d) Specimen C2_1_R20 n°1 and 2 (Krevaikas and Triantafillou 2005)

The KRE and DIL models give better results. The former is the only model with an error ratio of less than 1, meaning that it is on average the most conservative. The DIL model is the best model in terms of average error ratio (1.08). Conversely, the KRE model has the lowest COV (0.26), confirming the reliability of this approach, while greater dispersion is observed for the DIL model.

Finally, the CNR model, which proved to be conservative in terms of predicted strength (Figure 5.2e), is the most overestimating model for the prediction of stress-strain curves. This result is probably due to the fact that it is the only approach adopting a different shape of the constitutive law, which tends

to predict stiffer curves with respect to those predicted by Eqs. (2.11)-(2.13), as can be also observed in Figure 5.3.

Figure 5.5 shows the average error calculated adopting ε_{m0}=0.002 and the statistical coefficients are presented in Table 5.5. It is worth to note that this value was selected since suggested in most codes as the design value for the compressive axial strain of masonry corresponding to the peak stress.

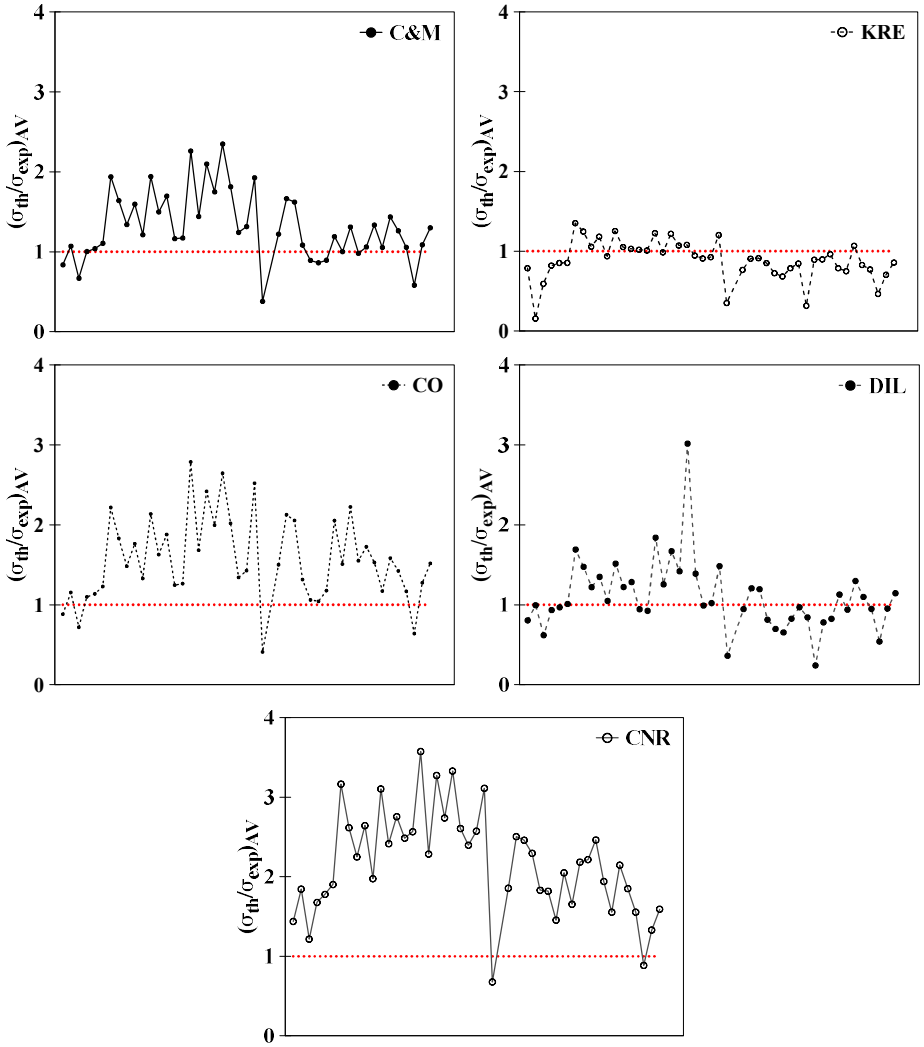

Figure 5.4 Average stress error for the considered models (ε_{m0}=0.003)

Similar considerations can be applied to the case of ε_{m0}=0.002, but with greater average errors. However, although all the models tend to be far from the experimental results, the KRE approach gives the best result of all the cases analyzed, in terms of both average stress ratio and COV.

It should be noted that this result is mainly due to the fact that the KRE approach provides a formulation to obtain the ultimate strain in compression that was calibrated on experimental points, while other models adopt the analytical expression of Campione and Miraglia (2003), which was developed for concrete members. Further studies should be addressed to the derivation of new formulations giving the ultimate strain in compression as a function of confinement pressure.

Table 5.4: Reliability of each model in terms of average stress error (ε_{m0} = 0.003)

Model	$(\sigma_{th}/\sigma_{exp})_{AV}$	COV
Campione and Miraglia, 2003 (C&M)	2.06	0.33
Krevaikas and Triantafillou, 2005 (KRE)	0.88	0.26
Corradi et al., 2007 (CO)	1.62	0.33
Di Ludovico et al., 2010 (DIL)	1.08	0.41
CNR-DT200/2013 (CNR)	2.15	0.30

Table 5.5: Reliability of each model in terms of average stress error (ε_{m0}=0.002)

Model	$(\sigma_{th}/\sigma_{exp})_{AV}$	COV
Campione and Miraglia, 2003 (C&M)	2.23	0.32
Krevaikas and Triantafillou, 2005 (KRE)	0.94	0.25
Corradi et al., 2007 (CO)	1.74	0.30
Di Ludovico et al., 2010 (DIL)	1.16	0.39
CNR-DT 200/2013 (CNR)	2.54	0.30

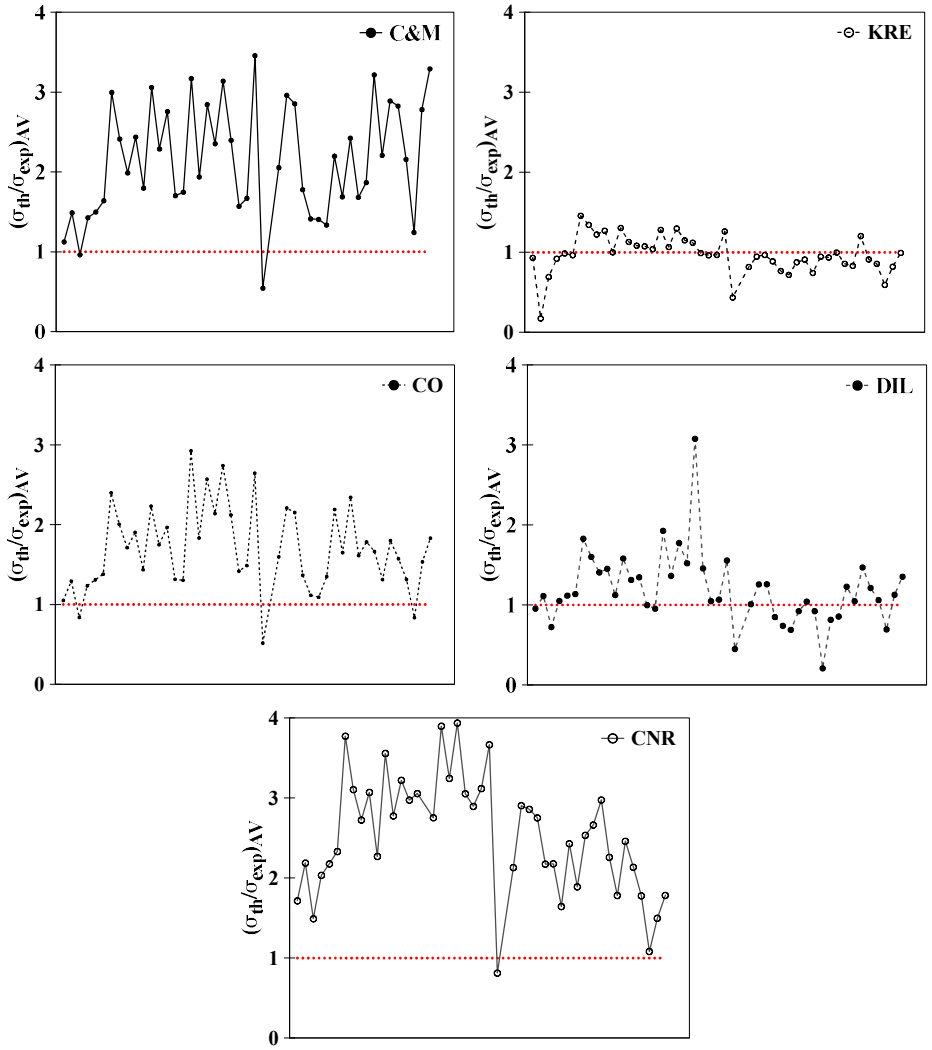

Figure 5.5 Average stress error for the considered models (ε_{m0}=0.002)

5.3 Theoretical predictions for tested BFRP-confined clay brick masonry cylinders

In this section, existing literature formulations and a modified version of CNR-DT 200/2013 model are adopted for evaluating the strength increase due to FRP confinement and results are compared with the experimental outcomes

produced in the framework of this thesis, in order to identify the most reliable analytical model.

The strain corresponding to the peak stress is evaluated through available formulations and a modified version of the formula proposed by Krevaikas and Triantafillou (2005) is proposed.

Finally, a possible approach is suggested for predicting the compressive stress-strain law in compression of FRP-confined masonry columns.

5.3.1 Strength previsions

Lateral confinement pressure

As it was introduced in Chapter 2 and according to traditional formulations available in literature, in the case of circular section the ultimate lateral confinement pressure can be evaluated using the rigid body equilibrium of the section:

$$f_l = \frac{2 \cdot t_f \cdot f_r}{D} \tag{5.5}$$

where t_f is the equivalent thickness of the fibres and D is the diameter of the section. The term f_r refers to the effective stress in the FRP at failure and, in the case of circular cross-section, it can be assumed equal to:

$$f_r = f_{fu} = \varepsilon_{fu} \cdot E_f \tag{5.6}$$

where ε_{fu} is the ultimate tensile strain corresponding to the rupture of the fibres and E_f is the Young's modulus of the fibres.

Moreover, the evaluation of the effective confinement pressure f'_l is made through the formulation:

$$f_l^{'} = k_e \cdot f_l \tag{5.7}$$

assuming that the in-plane efficiency coefficient k_e is equal to 1 (circular section). Thus, the confinement pressure f_l coincides with the effective confinement pressure f'_l.

The effective confinement lateral pressure f'_l estimated in this way is involved for the evaluation of the strength increase by all the models adopted in the following, except the model provided by the CNR-DT 200/2013 Guidelines, which takes account of a reduction of the maximum strain in the composite. In this case the stress in the external wrap is calculated as:

$$f_r = \varepsilon_{fu,rid} \cdot E_f \tag{5.8}$$

being $\varepsilon_{fu.rid}$ the reduced maximum strain in the wrap, expressed as:

$$\varepsilon_{fd,rid} = \min\left\{\eta_a \cdot \varepsilon_{fk} / \gamma_f ; 0.004\right\} \tag{5.9}$$

where η_a is the environmental conversion factor, ε_{fk} is the characteristic value of the ultimate tensile strain of the FRP and γ_f the partial safety factor.

Axial strength increase

The five different approaches discussed in the previous section are here employed to predict the compressive strength enhancement due to FRP confinement. In particular, the considered models are: Campione and Miraglia (2003) (C&M), Krevaikas and Triantafillou (2005) (KRE), Corradi et al. (2007) (CO), Di Ludovico et al. (2010) (DIL) and Italian CNR-DT 200/2013 Guidelines (CNR). The expressions for calculating the compressive strength of the FRP-confined masonry f_{mc} as function of the effective confinement pressure f'_l and unconfined masonry strength f_{m0} are reported for each model in Table 5.1.

In order to evaluate the reliability of the above-mentioned formulations, the results achieved using the five adopted criteria were compared with the experimental results obtained from compression tests on confined masonry cylinders. Table 5.6 presents the experimental results and theoretical predictions, the latter in terms of strength increase f_{mc}/f_{m0} and effective confinement pressure normalized by unconfined masonry strength f'_l/f_{m0}. In Table 5.7 the ratio between the theoretical predictions of the compressive strength $f_{mc,th}$ and the experimental results $f_{mc,exp}$ is calculated for each group of specimens belonging to the same type. Additionally, the average of the ratios between theoretical and experimental values is calculated for each model, along with the COV in order to measure the dispersion of the predictions with respect to the average values.

Table 5.6: Comparison of experimental results with theoretical predictions in terms of strength for BFRP-confined specimens

Specimen	Experimental results		Theoretical predictions						
	(f_{mc}/f_{m0})	Av.	C&M	KRE	CO	DIL	(f'_l/f_{m0})	CNR	(f'_l/f_{m0})
			(f_{mc}/f_{m0})					(f_{mc}/f_{m0})	
C1R_W1L	1.30	1.29	1.13	1.00	1.26	1.13	0.07	1.18	0.011
C2R_W1L	1.29								
C1R_W2L	1.79	1.68	1.27	1.00	1.45	1.25	0.13	1.25	0.022
C2R_W2L	1.57								
C1R_C1L	1.35	1.38	1.17	1.00	1.31	1.17	0.09	1.20	0.014
C2R_C1L	1.41								
C1R_C2L	1.78	1.71	1.34	1.00	1.55	1.31	0.17	1.28	0.027
C2R_C2L	1.64								

Table 5.7: Reliability of each model in terms of predicted strength for BFRP-confined specimens

Specimen	$(f_{mc,th}/ f_{mc,exp})$					
	C&M	KRE	CO	DIL	CNR	CNR_{mod}
C1R_W1L	0.88	0.77	0.97	0.88	0.91	1.12
C2R_W1L						
C1R_W2L	0.75	0.59	0.87	0.74	0.74	0.97
C2R_W2L						
C1R_C1L	0.85	0.73	0.95	0.85	0.87	1.09
C2R_C1L						
C1R_C2L	0.78	0.58	0.91	0.77	0.75	1.00
C2R_C2L						
AVERAGE	**0.82**	**0.67**	**0.92**	**0.81**	**0.82**	**1.04**
COV (%)	**(6.98)**	**(14.13)**	**(5.15)**	**(7.88)**	**(10.38)**	**(6.87)**

A graphical comparison between the adopted formulations is shown in Figure 5.6, which plots the strength increase f_{mc}/f_{m0} as a function of the effective confinement pressure normalized by unconfined masonry strength f'_l/f_{m0}. Points in the graphs refer to the experimental data of cylinders from Scheme I and Scheme II, reinforced with one or two layers. The comparison between experimental outcomes and the model provided by Italian Guidelines (CNR) is

reported in a different graph, because in this case the analytical prediction takes into account a reduced value of the lateral confinement pressure f_l (Figure 5.6b).

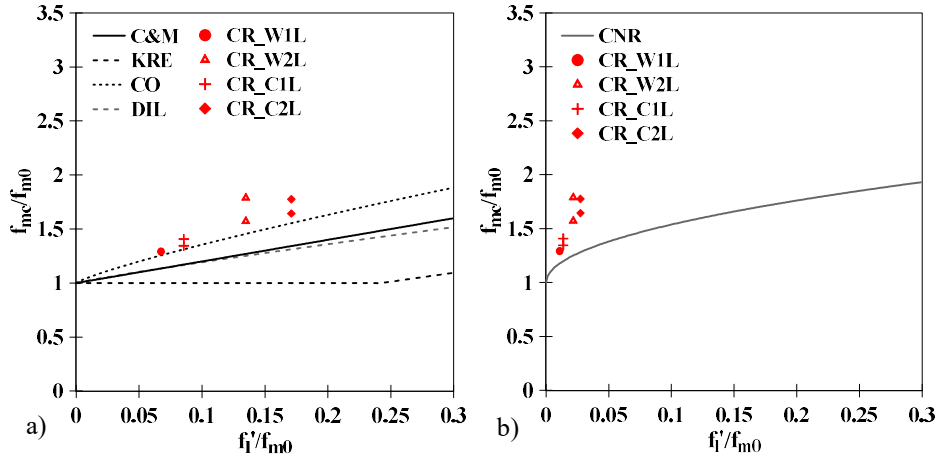

Figure 5.6 Compressive strength increase as a function of normalized effective confinement pressure for BFRP-confined cylinders: a) C&M, KRE, CO, DIL; b) CNR

Figure 5.6a shows a limited dispersion of the experimental data with respect to the theoretical predictions. In particular, all the models underestimate the experimental values and the KRE model is the most conservative.

A very reliable collation between experimental data and theoretical prediction is provided by the analytical model of Corradi at al. (2017) (CO), which shows the average ratio $(f_{mc,th}/f_{mc,exp})_{AV}$ close to the unit (0.92), as well as the lower COV (5.15%).

Reliable outcomes are obtained from C&M and DIL models, which present a ratio between theoretical and experimental values equal to 0.82 and 0.81 respectively, with a COV of 6.98% and 7.88%.

The CNR-DT 200/2013 model provides trustworthy results. However, the model proves to be conservative and this is due to the evaluation of the strain in the wrap, imposed equal to 0.004. Then, the normalized confinement pressure is quite similar for all the specimens and the model is in quite good accordance with the experimental outcomes only for low values of reinforcement ratio in the FRP (specimens confined using one FRP layer), while tends to underestimate the

experimental results for highly reinforced specimens (specimens strengthened with two FRP layers).

A modification of the CNR-DT 200/2013 model is proposed, neglecting the reduction of the lateral pressure and calculating this last by means of Eqs. (5.5) and (5.6). The modified model is named CNR_{mod} in Table 5.7, which reports the comparison between experimental results and the theoretical predictions provided by the model.

Evaluating the lateral pressure using the general expression employed by the other models improves the accuracy of the model and the average ratio $(f_{mc,th}/f_{mc,exp})_{AV}$ results to be very close to the unit (1.04). The refined model slightly overestimates the increased strength of one-layer confined cylinders, with an average ratio of theoretical predictions to experimental data of 1.12 and 1.09 for specimens from Scheme I and Scheme II respectively; while very good predictions are reached in the case of two-layer confined specimens, with the ratio $f_{mc,th}/f_{mc,exp}$ equal to 0.97 and 1 respectively for Scheme I and Scheme II cylinders .

The comparison between experimental results and the theoretical predictions of the modified CNR-DT 200/2013 is graphically shown in Figure 5.7. The experimental points are almost on the curve expressing the theoretical prediction and a limited dispersion is observed (COV= 6.87%).

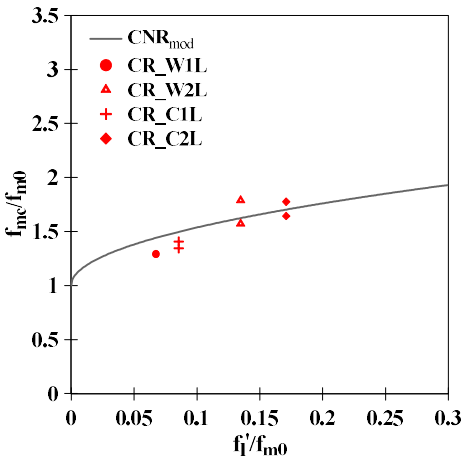

Figure 5.7 Compressive strength increase as a function of normalized effective confinement pressure for BFRP-confined cylinders: modified CNR model.

5.3.2 Evaluation of strain at peak stress

The strain at peak stress of BFRP-reinforced specimens was evaluated taken into account three different equations proposed respectively by Campione and Miraglia (2003) (C&M), Krevaikas and Triantafillou (2005) (KRE), Cascardi et al. (2017a) (CAS). Table 5.8 presents the used formulations. Moreover, a modification of the equation provided by Krevaikas and Triantafillou (2005) is here proposed, in which the coefficient k_2 is modified adopting the value 0.015 instead of the value 0.034 proposed by the authors.

With the aim of evaluating the suitability of the considered approaches, experimental results and analytical previsions are presented in Table 5.9. The ratio between theoretical and experimental outcomes ($\varepsilon_{mc,th}/\varepsilon_{mc,exp}$) is reported in Table 5.10 for specimens of the same type. Additionally, Table 5.10 reports the average ratio between theoretical and experimental values for each model, along with the COV.

Results presented in Table 5.10 point out that the formulations proposed by Campione and Miraglia (2003) and Krevaikas and Triantafillou (2005) overestimate the experimental results. On the other hand, the formulation of Cascardi et al. (2017a) slightly underestimates the experimental data, providing a ratio between theoretical provisions and experimental outcomes equal to 0.93.

Table 5.8: Formulations for calculating the strain at peak stress of FRP-confined masonry

Model	Strain at peak stress of FRP-confined masonry
Campione and Miraglia, 2003 (C&M)	$\frac{\varepsilon_{mc}}{\varepsilon_{m0}} = 1 + \rho_f \cdot \frac{1}{\varepsilon_{m0}} \cdot \frac{f_r^2}{E_f} \cdot \frac{1}{f_{m0} + k_e \cdot f_l}$ $where \quad \rho_f = \frac{2 \cdot \left[2 \cdot (b - 2r_c) + \pi r_c \right] \cdot t_f}{b^2 - 4 \cdot \left[r_c^2 - (\pi r_c^2 / 4) \right]}$
Krevaikas and Triantafillou, 2005 (KRE)	$\frac{\varepsilon_{mc}}{\varepsilon_{m0}} = 1 + \frac{k_2}{\varepsilon_{m0}} \cdot \frac{f_l'}{f_{m0}} \qquad where \quad k_2 = 0.034$
Cascardi et al., 2017a (CAS)	$\frac{\varepsilon_{mc}}{\varepsilon_{m0}} = 1 + \left(\frac{f_l}{f_{m0}} \right)^{0.5}$

Table 5.9: Comparison between experimental results and theoretical predictions in terms of strain at peak stress for BFRP-confined specimens

Specimen	Experimental results		Theoretical predictions			
	ε_{mc}	Av.	C&M	KRE	CAS	KRE_{mod}
C1R_W1L	0.0044	0.0042	0.0072	0.0063	0.0050	0.0050
C2R_W1L	0.0040					
C1R_W2L	0.0080	0.0065	0.0099	0.0086	0.0055	0.0060
C2R_W2L	0.0051					
C1R_C1L	0.0053	0.0051	0.0073	0.0063	0.0044	0.0047
C2R_C1L	0.0049					
C1R_C2L	0.0051	0.0058	0.0107	0.0092	0.0048	0.0060
C2R_C2L	0.0065					

Table 5.10: Reliability of each model in terms of predicted strain at peak stress for BFRP-confined specimens

Specimen	$(\varepsilon_{mc,th}/\varepsilon_{mc,exp})$			
	C&M	KRE	CAS	KRE_{mod}
C1R_W1L	1.71	1.50	1.19	1.19
C2R_W1L				
C1R_W2L	1.52	1.32	0.85	0.93
C2R_W2L				
C1R_C1L	1.43	1.24	0.86	0.92
C2R_C1L				
C1R_C2L	1.84	1.59	0.83	1.03
C2R_C2L				
AVERAGE	**1.63**	**1.41**	**0.93**	**1.02**
COV (%)	**(11.44)**	**(11.37)**	**(18.58)**	**(12.60)**

Reliable results are reached when the modified model of Krevaikas and Triantafillou (2005) is adopted. Indeed, the refined model allows obtaining an average ratio $(\varepsilon_{mc,th}/\varepsilon_{mc,exp})_{AV}$ equal to 1.02.

5.3.3 Stress-strain curves

In the present study, the trend of the axial stress as function of the longitudinal strain for BFRP-confined cylinders is obtained by adopting the constitutive law proposed by la Mendola and Papia (2002) for calcarenite masonry members, described by the following relation:

$$\frac{\sigma}{f_{mc}} = \frac{A \cdot \bar{\varepsilon} + (U+1) \cdot \bar{\varepsilon}^2}{1 + (A-2) \cdot \bar{\varepsilon} + U \cdot \bar{\varepsilon}^2} \tag{5.10}$$

$$\bar{\varepsilon} = \frac{\varepsilon}{\varepsilon_{mc}}; \qquad A = \frac{E_{m0}}{E^*_{\text{sec}}}; \qquad E^*_{\text{sec}} = \frac{f_{mc}}{\varepsilon_{mc}} \tag{5.11}$$

where f_{mc} and ε_{mc} are respectively the strength and the corresponding strain of FRP-confined masonry, E_{m0} is the Young's modulus of unconfined masonry and U is a parameter which rules the slope of the softening branch. Here two values of U are proposed, equal to 0.75 and 1 for Scheme I and Scheme II respectively, in order to catch the more or less steep post-peak behaviour of cylinders from different schemes.

On the base of the strength predictions presented above, the proposed modified CNR-DT 200/2013 model (CNR_{mod}) is adopted in the following to determine the peak stress f_{mc} of BFRP-confined cylinders.

The strain at peak stress ε_{mc} of the FRP-confined masonry corresponding to an assigned value of lateral confinement pressure is evaluated employing the modified equation of Krevaikas and Triantafillou (2005) proposed in this study, in which the value of 0.015 is adopted for the coefficient k_2.

5.3.4 Experimental-analytical comparison

Figure 5.8 shows the comparison between experimental results and analytical predictions, in order to test the accuracy and the precision of the theoretical outcomes.

The stress-strain results obtained from the analytical model are in good agreement with the experimental results. The adopted model is able to predict the average compressive response in terms of peak stress, corresponding strain and slope of ascending and softening branches. The compressive strength of BFRP-confined masonry is predicted with enough accuracy, although predictions slightly underestimate the average values of experimental data in the case of two-layer reinforced specimens. In particular, percentage differences between the average experimental values of compressive strength and predicted quantities are equal to 11.5% and 8.7% for one-layer reinforced specimens from Scheme I and Scheme II respectively. In the case of specimens confined with two BFRP layers,

there is almost no scatter between predicted and experimental average strength values.

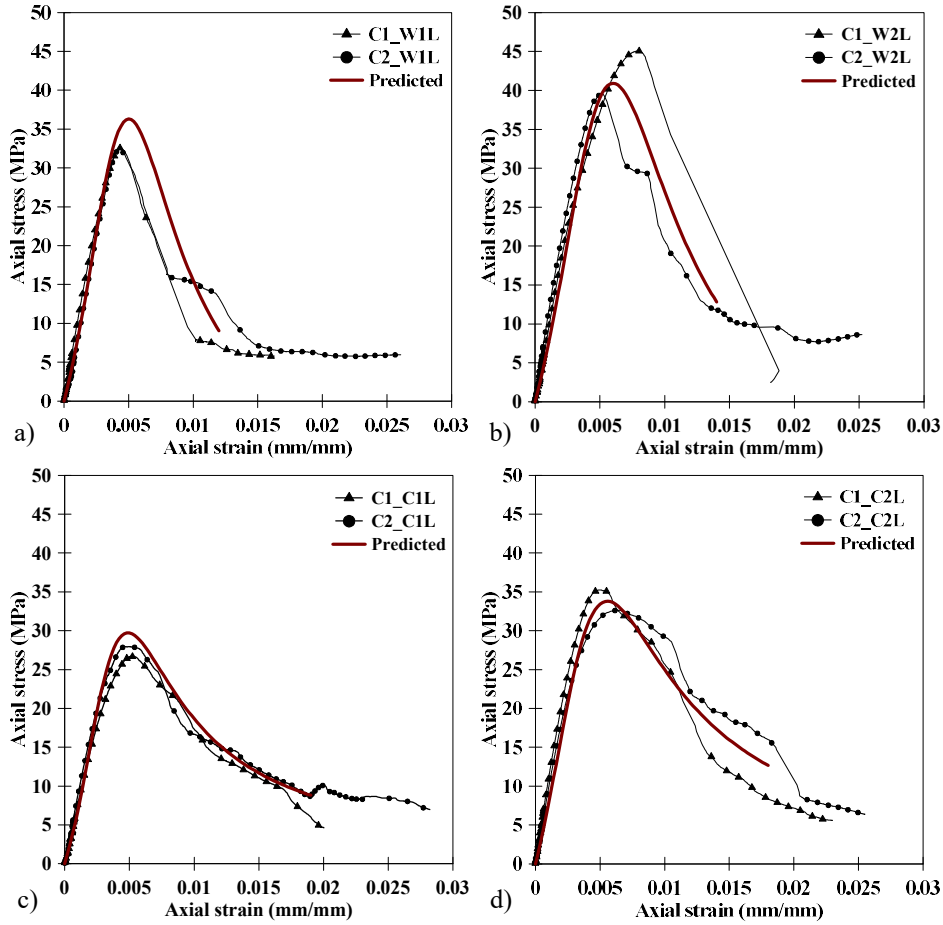

Figure 5.8 Comparison between experimental and theoretical compressive response of BFRP-confined cylinders: a) CR_W1L series; b) CR_W2L series; c) CR_C1L series; d) CR_C2L series

5.4 Theoretical predictions for tested BFRCM-confined clay brick masonry cylinders

The literature review has shown that a unified analytical model aimed at evaluating the strength enhancement due to FRCM confinement of masonry is

still missing, as well as a model to predict the compressive stress-strain law of FRCM-confined masonry columns.

Here, the well-known analytical models to predict the strength increase of FRP-confined masonry columns are employed, in order to assess the reliability of these formulations when used for columns strengthened by FRCM. Then, the analytical models proposed by Cascardi et al. (2017b) and by Balsamo et al. (2018) for columns confined by FRCM are applied to predict the enhancement in strength. The analytical outcomes are compared with the experimental data, assessing the reliability of the used formulations.

Finally, a modification of the parameters of the analysis-oriented stress-strain model provided by Cascardi et al. (2017a) is presented to reproduce the experimental results. In particular, the strength criterion, the evaluation of strain at peak stress and the axial stress-strain law are modified to obtain better prediction of the compressive behaviour of FRCM-confined cylinders.

5.4.1 Strength previsions

Lateral confinement pressure

The evaluation of the effective lateral confinement pressure has been already defined with regard to the formulations about FRP (Eqs. 5.5-5.7).

Considering the models proposed for FRCM-confined columns, the lateral confinement pressure evaluated according to Cascardi et al. (2017b) assumes the form:

$$f_l = \frac{n \cdot t_f \cdot E_f \cdot \varepsilon_{fu}}{D} \tag{5.12}$$

being t_f, E_f and ε_{fu} the thickness, Young's modulus and ultimate strain of the textile respectively, n is the number of reinforcing layers and D the diameter of the cross-section.

In Balsamo et al. (2018) the following formulations are assumed:

$$f_l^{'} = k_e \cdot k_{mat} \cdot f_l \tag{5.13}$$

$$f_l = \frac{2 \cdot n \cdot t_f \cdot E_f \cdot \varepsilon_{fu}}{D} \tag{5.14}$$

$$k_{mat} = \alpha_4 \left(\rho_{mat} \frac{f_{c,mat}}{f_{m0}} \right)^2 \tag{5.15}$$

$$\rho_{mat} = \frac{4 \cdot t_{mat}}{D} \tag{5.16}$$

where the effective confinement pressure f'_l is evaluated based on the confinement pressure f_l, the matrix effectiveness coefficient k_{mat} and the cross-section shape factor k_e.

Axial strength increase

In a first step, the experimental results in terms of axial strength enhancement were compared with the theoretical predictions achieved by using the expressions introduced in Section 5.3.1 for FRP-confined columns.

Results are presented in Table 5.11, which shows the experimental and analytical strength increases f_{mc}/f_{m0}, along with the effective confinement pressure normalized by the unconfined masonry strength f'_l/f_{m0}.

In order to assess the reliability of the above-mentioned formulations, the ratio $f_{mc,th}/f_{mc,exp}$ between analytical and experimental outcomes was calculated for cylinders belonging to the same scheme (Scheme I or Scheme II) and having the same strengthening characteristics (one or two reinforcing layers) (Table 5.12). Moreover, the average ratio $(f_{mc,th}/f_{mc,exp})_{AV}$ is evaluated for each model, along with the COV.

The adopted criteria are depicted in Figure 5.9, which plots the strength increase f_{mc}/f_{m0} as a function of the effective confinement pressure normalized by unconfined masonry strength f'_l/f_{m0}. The experimental data are represented by points in the graphs.

Figure 5.9 points out a good agreement between experimental values and theoretical predictions. As found about FRP-confined specimens, even in this case the used formulations tend to slightly underestimate experimental data.

Table 5.11: Comparison of experimental results with theoretical predictions in terms of strength for BFRCM-confined specimens

Specimen	Experimental results		Theoretical predictions						
	(f_{mc}/f_{m0})	Av.	C&M	KRE	CO	DIL	(f'_l/f_{m0})	CNR	(f'_l/f_{m0})
			(f_{mc}/f_{m0})					(f_{mc}/f_{m0})	
C1M_W1L	1.00	1.27	1.13	1	1.26	1.13	0.07	1.18	0.011
C2M_W1L	1.42								
C3M_W1L	1.48								
C4M_W1L	1.18								
C1M_W2L	1.34	1.38	1.27	1	1.45	1.25	0.13	1.25	0.022
C2M_W2L	1.26								
C3M_W2L	1.54								
C1M_C1L	1.55	1.66	1.17	1	1.31	1.17	0.09	1.20	0.014
C2M_C1L	1.84								
C3M_C1L	1.59								
C1M_C2L	1.98	1.85	1.34	1	1.55	1.31	0.17	1.28	0.027
C2M_C2L	1.73								

Table 5.12: Reliability of each model in terms of predicted strength for BFRCM-confined specimens

Specimen	($f_{mc,th}/f_{mc,exp}$)					
	C&M	KRE	CO	DIL	CNR	CNR_{mod}
C1M_W1L	0.89	0.79	0.99	0.89	0.93	1.13
C2M_W1L						
C3M_W1L						
C4M_W1L						
C1M_W2L	0.92	0.72	1.05	0.91	0.91	1.18
C2M_W2L						
C3M_W2L						
C1M_C1L	0.70	0.60	0.79	0.70	0.72	0.90
C2M_C1L						
C3M_C1L						
C1M_C2L	0.73	0.54	0.84	0.71	0.69	0.92
C2M_C2L						
AVERAGE COV (%)	**0.81 (13.70)**	**0.66 (16.90)**	**0.92 (13.46)**	**0.80 (13.95)**	**0.81 (14.91)**	**1.03 (13.76)**

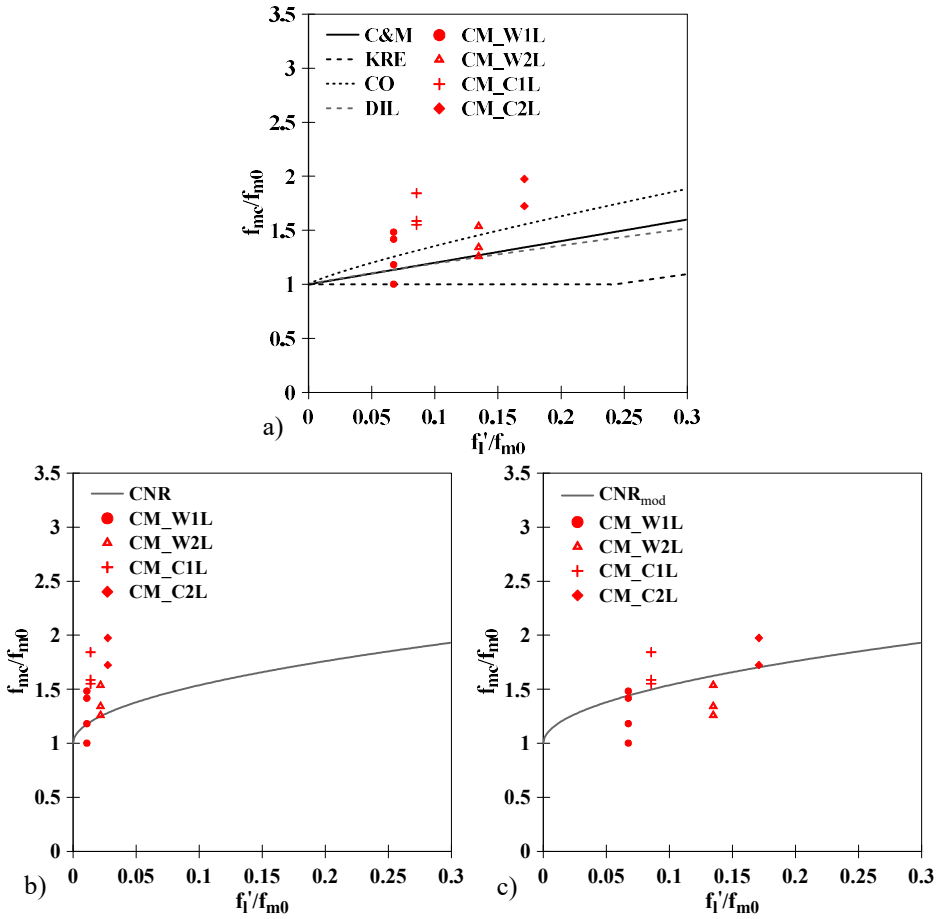

Figure 5.9 Compressive strength increase as a function of normalized effective confinement pressure for BFRCM-confined cylinders: a) C&M, KRE, CO, DIL; b) CNR; c) CNR_{mod}

Similarly to the case of FRP confinement, the KRE model proves to be the most conservative, because it predicts no strength enhancement for specimens with confinement pressure lower than 0.24 f_{mc0} and this occurs for all the tested cylinders.

Reliable results are given by (C&M), (DIL) and (CNR) models, which show an average ratio $(f_{mc,th}/f_{mc,exp})_{AV}$ equal to 0.81, 0.80 and 0.81 respectively.

Trustworthy prediction in terms of strength is provided by the analytical model of Corradi et al. (2007) (CO), which presents a ratio between theoretical and experimental values of 0.92.

The modified CNR-DT 200/2013 model is also applied, allowing the achievement of very good results. Indeed, Table 5.12 shows the average ratio $(f_{mc,th}/f_{mc,exp})_{AV}$ to be almost equal to the unit (1.03). The theoretical prediction lightly overestimates the strength enhancement of specimens from Scheme 1, with the ratio of theoretical values to experimental data equal to 1.13 and 1.18 respectively for one and two-layer confined specimens. In the case of cylinders from Scheme II, the ratio $f_{mc,th}/f_{mc,exp}$ results to be equal to 0.90 for specimens wrapped using one layer and 0.92 for samples wrapped with two layers.

In a second step, the analytical models proposed by Cascardi et al. (2017b) and by Balsamo et al. (2018) were employed in order to predict the strength increase of BFRCM-confined cylinders. The models have been introduced and discussed in Chapter 2 and the formulations for evaluating the strength of confined masonry are here reported in Table 5.13.

Table 5.13: Formulations for calculating the compressive strength of FRCM-confined masonry

Model	Strain at peak stress of FRP-confined masonry
Cascardi et al., 2017b (CAS)	$f_{mc} = f_{m0}\left[1 + k_1\left(\frac{f_l}{f_{m0}}\right)^{0.5}\right]$ $k_1 = 6\rho_{mat}\frac{f_{c,mat}}{f_{m0}}; \quad \rho_{mat} = \frac{4 \cdot t_{mat}}{D}$
Balsamo et al., 2018 (BAL)	$f_{mc} = f_{m0} \cdot \left[1 + k_1 \cdot \left(\frac{f_l'}{f_{m0}}\right)^{0.5}\right]$ $k_1 = \alpha_2 \cdot \left(\frac{g_m}{1000}\right)^{\alpha_3}$ *where* g_m : *mass density of masonry* $\alpha_2 = \alpha_3 = 1$

Table 5.14 present experimental data and theoretical outcomes in terms of strength enhancement f_{mc}/f_{m0}, as well as the theoretical-to-experimental ratio ($f_{mc,th}/f_{mc,exp}$). In Figure 5.10 the strength increases are represented, plotting the ratio f_{mc}/f_{m0} as function of the effective confinement pressure normalized by unconfined masonry strength f'_l/f_{m0}. In particular, the theoretical predictions of the two adopted models are shown in different graphs because of the different way to evaluate the confinement lateral pressure. Moreover, the adoption of the model of Cascardi et al. (2017b) involves the definition of parameter k_1, which is not constant for all the specimens, depending on the strength of unconfined masonry and strength and thickness of the mortar. Then, once k_1 value is set, four different graphs depict the comparison between experimental points and theoretical previsions.

Both the analytical approaches slightly underestimate the experimental results, with almost the same scatter between experimental and analytical outcomes (Table 5.14).

Table 5.14: Comparison between experimental results and theoretical predictions in terms of strength for BFRCM-confined specimens

Specimen	Experimental results		Theoretical predictions				Comparison	
			BAL		CAS		BAL	CAS
	(f_{mc}/f_{m0})	Av.	(f_{mc}/f_{m0})	(f'_l/f_{m0})	(f_{mc}/f_{m0})	(f'_l/f_{m0})	($f_{mc,th}/f_{mc,exp}$)	
C1M_W1L	1.00	1.27	1.10	0.0035	1.19	0.0337	0.87	0.93
C2M_W1L	1.42							
C3M_W1L	1.48							
C4M_W1L	1.18							
C1M_W2L	1.34	1.38	1.21	0.0157	1.39	0.0674	0.88	1.01
C2M_W2L	1.26							
C3M_W2L	1.54							
C1M_C1L	1.55	1.66	1.14	0.0071	1.27	0.0427	0.69	0.76
C2M_C1L	1.84							
C3M_C1L	1.59							
C1M_C2L	1.98	1.85	1.30	0.0320	1.56	0.0855	0.70	0.85
C2M_C2L	1.73							
					AVERAGE		**0.78**	**0.89**
					COV (%)		**(12.95)**	**(12.10)**

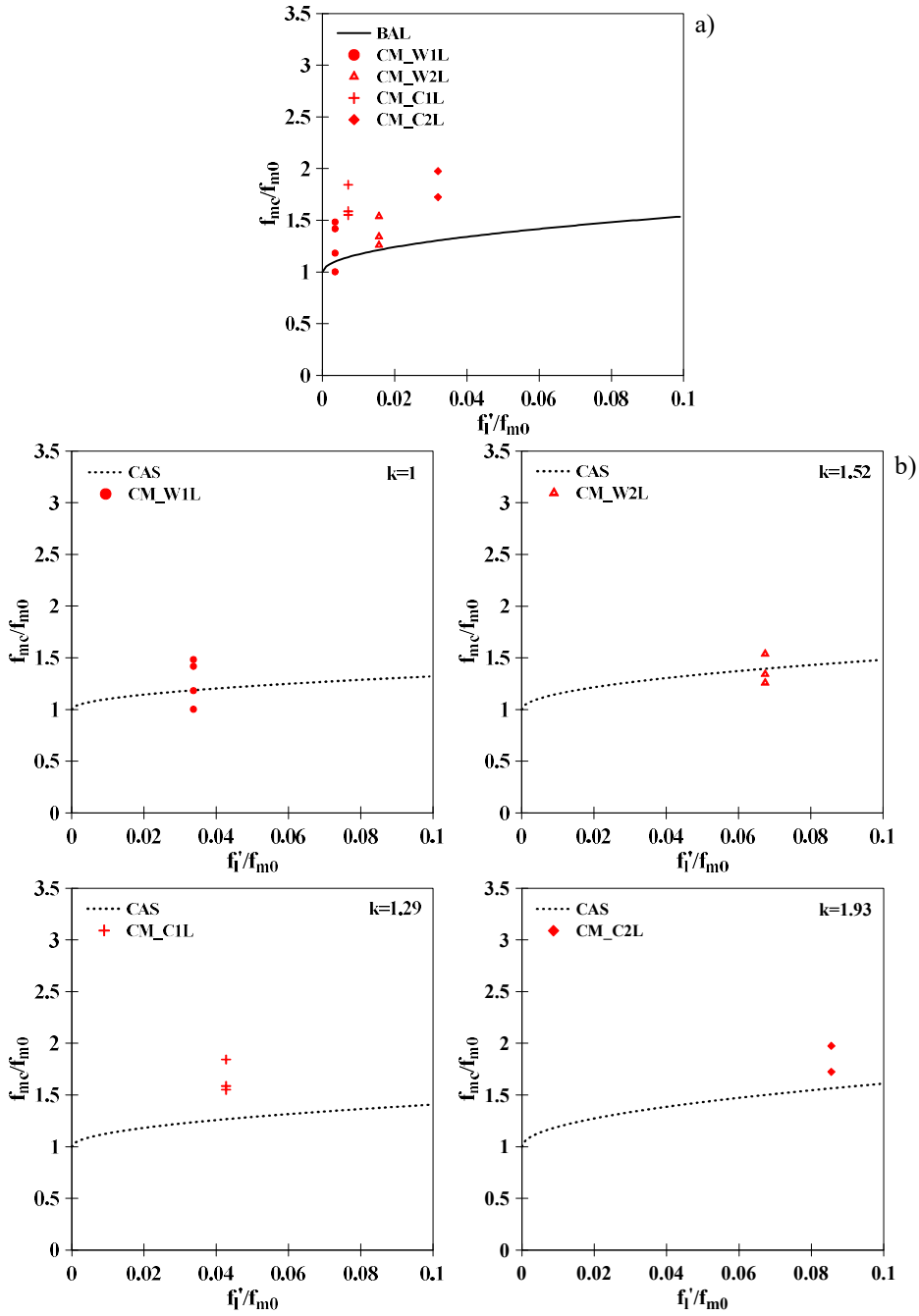

Figure 5.10 Compressive strength increase as a function of normalized effective confinement pressure for BFRCM-confined cylinders: a) BAL; b) CAS

The average ratio $(f_{mc,th}/f_{mc,exp})_{AV}$ is equal to 0.78 and 0.89 for BAL and CAS models respectively, with a coefficient of variation of 12.95% and 12.10%. Then, the model of Cascardi et al. (2017b) proved to be more accurate, allowing the achievement of very good predictions for Scheme I specimens, with a ratio of experimental to theoretical outcomes equal to 0.93 and 1.10 for one and two-layer confined cylinders from Scheme I respectively, while the strength enhancement of cylinders from Scheme II was slightly underestimated.

5.4.2 Evaluation of strain at peak stress

The evaluation of the strain at peak stress for BFRCM-confined cylinders was carried out by employing the same formulations used in the case of FRP and reported in Table 5.8.

In Table 5.15 experimental data and theoretically predicted values are reported, while Table 5.16 presents the ratio between theoretical and experimental results ($\varepsilon_{mc,th}/\varepsilon_{mc,exp}$) for each tested cylinder, in order to evaluate the reliability of the considered formulations in evaluating the strain. The average ratio for each model is also reported, considering all the specimens.

As it can be noted from the formulas presented in Table 5.8, the evaluation of the strain at peak stress is dependent from the mechanical characteristics of unconfined masonry (f_{mc0}, ε_{mco}) and from the lateral confinement pressure. Because the basic characteristics of masonry were the same for both BFRP and BFRCM-confined cylinders and since the evaluation of the strength for specimens confined with FRCM was made by using the same model adopted in the case of FRP (modified CNR-DT 200/2013 model), then the theoretical values of Table 5.15 are the same of those reported in Table 5.9.

From the results presented in Table 5.15 it is clear that, even for FRCM-confined cylinders the best previsions are achieved by employing the modified model of Krevaikas and Triantafillou (2005), obtaining an average theoretical-experimental ratio $(\varepsilon_{mc,th}/\varepsilon_{mc,exp})_{AV}$ equal to 0.94. As it was found for cylinders wrapped using FRP, even in this case the formulations of Campione and Miraglia (2005) and the original formulation of Krevaikas and Triantafillou (2005) tended to overestimate the experimental outcomes. The strain at peak stress predicted from Cascardi et al. (2017a) is reliable, even if it slightly underestimates the experimental results.

Table 5.15: Comparison between experimental results and theoretical predictions in terms of strain at peak stress for BFRCM-confined specimens

Specimen	Experimental results	Theoretical predictions				
	ε_{mc}	Av.	C&M	KRE	CAS	KRE_{mod}
C1M_W1L	0.0045	0.0058	0.0072	0.0063	0.0050	0.0050
C2M_W1L	0.0068					
C3M_W1L	0.0068					
C4M_W1L	0.0050					
C1M_W2L	0.0061	0.0062	0.0099	0.0086	0.0055	0.0060
C2M_W2L	0.0064					
C3M_W2L	-					
C1M_C1L	0.0058	0.0050	0.0073	0.0063	0.0044	0.0047
C2M_C1L	0.0051					
C3M_C1L	0.0040					
C1M_C2L	0.0065	0.0060	0.0107	0.0092	0.0048	0.0060
C2M_C2L	0.0055					

5.4.3 Stress-strain curves

The compressive stress-strain behaviour of FRCM-confined columns was predicted by adopting an iterative procedure similar to the one proposed in Cascardi et al. (2017a) and modified as proposed in Minafò and La Mendola (2018). The procedure involves an input phase opening the k-iteration and a calculation phase leading to the failure criterion, which can stop the process or allow passing to the upgrading phase and to the (k+1) iteration.

The input data (k=0) of the used procedure were represented by the unconfined properties of the columns, namely diameter D_0, the elastic modulus E_{m0}, the Poisson coefficient v_0 and the values of the compressive strength and corresponding strain (f_{m0} and ε_{m0} respectively). Initial information about the FRCM system involved the thickness of the jacket t_f, as well as the knowing of the complete tensile constitutive law of the FRCM, in terms of tangent moduli relative to the stages characterizing its tensile behaviour and tensile ultimate strains of the different stages.

Table 5.16: Reliability of each model in terms of predicted strain at peak stress for BFRCM-confined specimens

Specimen	$(\varepsilon_{mc,th}/\varepsilon_{mc,exp})$			
	C&M	**KRE**	**CAS**	**KRE_{mod}**
C1M_W1L	1.24	1.09	0.86	0.86
C2M_W1L				
C3M_W1L				
C4M_W1L				
C1M_W2L	1.60	1.39	0.89	0.97
C2M_W2L				
C3M_W2L				
C1M_C1L	1.46	1.26	0.88	0.94
C2M_C1L				
C3M_C1L				
C1M_C2L	1.78	1.53	0.80	0.99
C2M_C2L				
AVERAGE	**1.52**	**1.32**	**0.86**	**0.94**
COV (%)	**(15.02)**	**(14.43)**	**(4.62)**	**(6.04)**

The calculation process started by imposing a value of longitudinal strain $\varepsilon_{a,k}$ to the FRCM-confined column, which induced a lateral expansion. The equivalent diameter was calculated by using the following expression, proposed in Cascardi et al. (2017a):

$$D_i = D_0 \sqrt{\frac{1}{1-\varepsilon_{a,k}}} \tag{5.17}$$

The FRCM jacket was subjected to a tensile elongation equal to the circumferential strain, the latter evaluable as the product between the Poisson's coefficient and the longitudinal strain:

$$\varepsilon_{h,k} = \upsilon_{mc,k-1} \cdot \varepsilon_{a,k} \tag{5.18}$$

The circumferential strain allowed the activation of the FRCM jacket and the lateral confinement pressure could be evaluated employing the rigid body equilibrium of the section, as it follows:

$$f_{l,k} = \frac{2 \cdot E_{f,k} \cdot \varepsilon_{h,k} \cdot t_f}{D_k} \tag{5.19}$$

where $E_{f,k}$ is the tensile Young's modulus of the FRCM composite at the k-th step.

Because the tensile constitutive law of FRCM in tension is defined by a discontinuous function, the elastic modulus $E_{c,k}$ needed to be evaluated in a proper way. Making a simplification, a bi-linear constitutive law was adopted to describe the tensile behaviour of FRCM composite. Then, the elastic modulus had to be defined in two stages, corresponding to the situation of undamaged and full damaged matrix respectively. In simplified manner, it can be assessed as:

$$\text{if} \quad \varepsilon_{h,k} \le \varepsilon_{cr} \rightarrow E_{c,k} = E_m \cdot V_m + E_f \cdot V_f \tag{5.20a}$$

$$\text{if} \quad \varepsilon_{h,k} > \varepsilon_{cr} \rightarrow E_{c,k} = E_f \cdot V_f \tag{5.20b}$$

where E_m and E_f indicate the Young's modulus of mortar and fibres respectively, while V_m and V_f refer to the volume fraction of the two constituent materials.

Based on the evaluation of the strength and the corresponding strain of BFRCM-confined specimens carried out in the previous sections, the peak stress of FRCM-confined cylinders f_{mc} was evaluated by using the modified expression of CNR-DT 200/2013, while the strain at peak stress ε_{mc} was obtained through the modified model of Krevaikas and Triantafillou (2005).

For the evaluation of the Poisson's coefficient of the confined masonry column, the following equation proposed in Cascardi et al. (2017a) was adopted:

$$\frac{\upsilon_{mc,k}}{\upsilon_{m0}} = 1 + \frac{\varepsilon_{a,k}}{\varepsilon_{mc,k}} \left(0.719 + 1.914 \frac{f_{l,k}}{f_{m0}} \right) \le 0.5 \tag{5.21}$$

At the first step, the lateral confinement pressure $f_{l,i}$ was supposed null and the ν_{m0} value, here assumed equal to 0.2, was adopted.

Finally, the trend of the stress-strain curve of FRCM-confined cylinders under uniaxial compression was obtained by employing the constitutive relationship of La Mendola and Papia (2002), as done in the case of cylinders reinforced using FRP wraps (Eqs. 5.10, 5.11).

5.4.4 Experimental-analytical comparison

The comparison between experimental outcomes and theoretical predictions is presented in Figure 5.11 for all the cylinders confined by using BFRCM jackets.

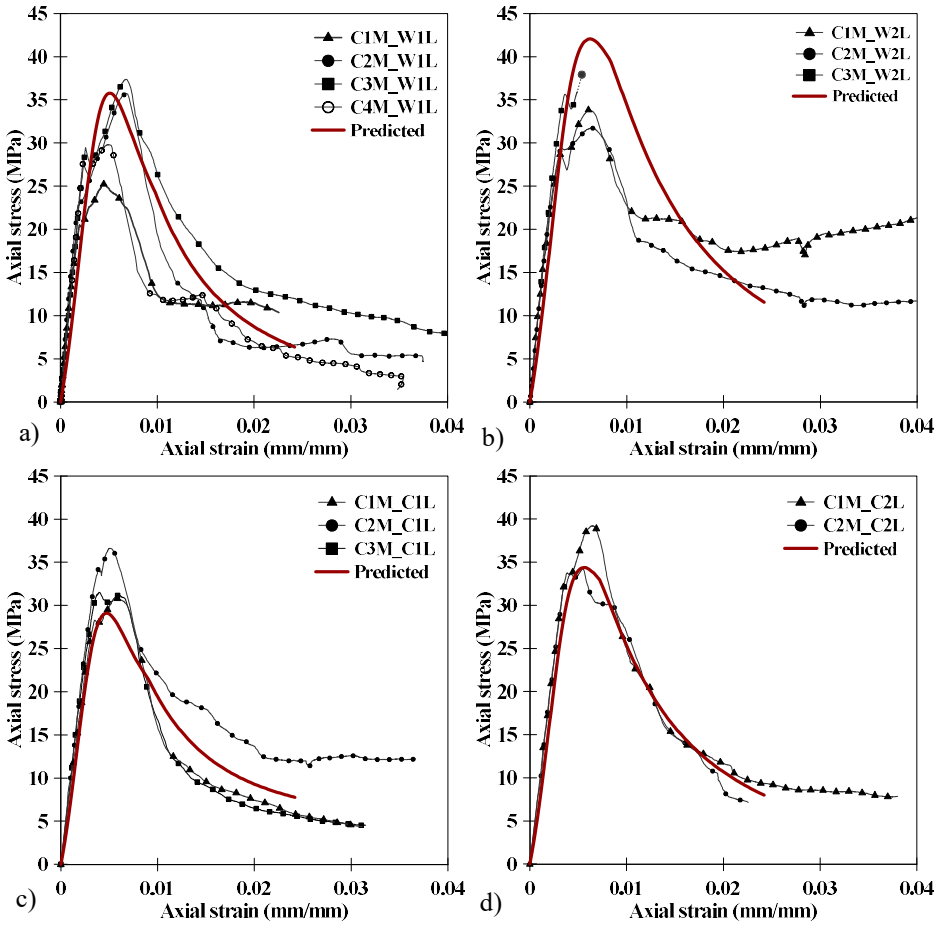

Figure 5.11 Comparison between experimental and theoretical compressive response of BFRCM-confined cylinders: a) CM_W1L series; b) CM_W2L series; c) CM_C1L series; d) CM_C2L series

The analytical modelling shows to be able to reproduce the experimental results with good accuracy. The theoretical stress-strain curves are in good agreement with the experimental ones in terms of stiffness of the initial branch,

up to the peak load. Also the softening branch of the curves is reproduced suitably. Predicted strengths and corresponding strains are evaluated with enough precision. In the case of Scheme I cylinders the strength results to be overestimated of 17% and 13% for specimens wrapped with one and two layers respectively. For Scheme II cylinders, a slight underestimation of the experimental peak load values can be observed; in particular, the theoretical values are 10% and 8% reduced compared to experimental results, for one and two-layer confined specimens respectively. However, for all the series the predicted values are very close to the maximum (CM_W1L series) or the minimum (CM_C1L and CM_C2L series) experimental values, except for CM_W2L series, for which all the experimental strength values are overestimated.

6. CONCLUSIONS AND FUTURE WORKS

Fibre Reinforced Cementitious Matrix (FRCM) materials have started to be employed during the last years with the aim of overcoming the drawbacks related to the use of Fibre Reinforced Polymer (FRP) composites, proving to be potentially suitable for strengthening masonry structures. Moreover, the will to develop materials able to guarantee a certain degree of sustainability without renounce to adequate mechanical properties has drawn the attention on the use of basalt fibres, which appear to be a material that could offer interesting opportunities in the future as alternative to carbon or glass fibres.

However, the literature review has shown that few research studies have been carried out on the use of basalt fibres for the confinement of masonry and an experimental comparative study on the performance of BFRP and BFRCM is still missing.

The main objective of this thesis was thus the investigation of the capability of FRP and FRCM composites involving the use of basalt fibres in improving the mechanical characteristics of masonry columns confined using these systems. With this aim, a detailed experimental study was carried out, supported by an analytical investigation.

6.1 Summary and conclusions

An experimental investigation was designed and performed with the goal of studying the compressive behaviour of clay brick masonry cylinders confined by using BFRP or BFRCM jackets. The experimental programme was divided in the following parts: - tests on components of the masonry and the composite; - tensile tests on BFRCM coupons; - compressive tests on unconfined and confined masonry cylinders. All the tests were monitored by using the technique of the Digital Image Correlation (DIC) in order to obtain more detailed information on the strain and displacement field and the evolution of crack patterns.

An in-deep discussion was made on the details of the performed investigation in terms of used materials, manufacturing procedures and test methods. Tests on BFRCM composite were preceded by an extensive study on the tensile behaviour of the basalt textile and tests on the mortar matrix, in order to relate the mechanical properties of constituent materials to the behaviour of the composite. Before characterisation tests on the basalt grid, a detailed study aimed at understanding the best setup configuration to be used during the tensile tests was presented, with reference to different clamping methods, loading rates and geometries of the samples. The use of aluminium tabs at the ends of the basalt textile strips proved to be the best solution in order to ensure a uniform load distribution and to avoid the slipping of the specimens inside the gripping area during the test. Moreover, the introduction of the use of the videoextensometer allowed obtaining more reliable results in terms of strain, avoiding the tests to be affected by the lack of rigidity of the testing system.

Because of its complex mechanical behaviour, BFRCM composite was subjected to an appropriate tensile characterisation. Tensile tests were carried out on three series of specimens reinforced respectively by using one, two or three layers of basalt grid with the aim of investigating on the influence of the textile reinforcement ratio on the tensile stress-strain response of the composite strips. The use of the DIC technique allowed the strain/displacement full-field analysis on the surface of the BFRCM coupons, highlighting differences in the strain distribution occurring in specimens reinforced with different reinforcement ratios and allowing considerations regarding the crack pattern evolution during tests. Results obtained from tensile tests on the BFRCM composite underlined the following outcomes:

- the maximum tensile stress of BFRCM specimens decreased with the increase of the number of reinforcing basalt textile layers and the maximum average strength was reached by the series characterized by the lowest reinforcement ratio (SP_1L);
- the average peak stresses of the three series of specimens were found always lower compared to the peak stress of the dry basalt grid, with a decrease equal to 28%, 38% and 46% respectively for one, two and three-layer reinforced specimens. Similarly, the stiffness of the BFRCM series (SP_1L, SP_2L, SP_3L) in the third stage of the tensile curves proved to be lower than the Young's modulus of the dry basalt fibre;

- the crack pattern was influenced by the reinforcement ratio. The higher the number of textile layers, the higher the number of cracks, which were closer together. Moreover, the crack opening during the tests was found to be influenced by the volume fraction of fibres, with tighter cracks in the case of over-reinforced specimens. The tensile failure of the grid was always recorded.

Subsequently, the attention was focused on the compressive behaviour of the cylinders manufactured by using two different schemes with the aim of evaluating the influence of the number of vertical mortar joints. The BFRP and BFRCM reinforced cylinders were wrapped using one or two basalt grid layers, in order to assess the enhancements of strength and deformation capacity in relation to the number of reinforcing layers. Unconfined and confined specimens were subjected to uniaxial compressive loads and results were discussed in terms of stress-strain curves and failure modes. The results in the axial direction obtained through traditional monitoring systems were compared with those achieved through the use of DIC. The latter allowed also recording the hoop strains on the surface of the cylinders and investigating on their circumferential behaviour. From results of compressive tests on masonry cylinders the following outcomes can be drawn:

- unconfined cylinders with three vertical joints (Scheme II) showed an average strength reduction of about 27% compared with cylinders having one vertical joint only (Scheme I), pointing out the detrimental effect of vertical joints;
- failure of cylinders reinforced by BFRP and BFRCM occurred always by tensile rupture of the jacket. Debonding phenomena between reinforcement layers at the overlapping zone were not observed. The inner masonry core of wrapped cylinders showed to be crushed, more than unconfined masonry cylinders;
- the strength enhancement due to confinement with both BFRP and BFRCM systems proved to be influenced by the number of vertical joints. The confinement revealed to be more effective in the case of weaker masonry, namely the scheme involving three vertical joints (Scheme II), and this is evident considering strength gains of wrapped cylinders compared to control specimens. In particular, in the case of

BFRP-confined cylinders, strength increases of 29% and 68% were obtained respectively for one-layer and two-layer wrapped specimens from Scheme I, while the strength was enhanced of 38% and 71% for Scheme II cylinders reinforced with one and two layers respectively;

- for BFRCM-confined cylinders, the strength gains for one and two-layer reinforced specimens from Scheme I were equal to 27% and 38% respectively. Enhancements of 66% and 85% were obtained in the case of cylinders from Scheme II strengthened respectively with one and two textile layers;
- the number of vertical joints had strong influence on the strength of confined cylinders, especially in those wrapped by BFRCM. In particular, the maximum load sustained by specimens of Scheme II wrapped with one and two layers of BFRP was greater of 27% and 3% with respect to same specimens belonging to Scheme I. Similarly, BFRCM-reinforced specimens of Scheme II gained a strength increase of 145% and 124% for one and two-layer wrapped cylinders with respect to same cylinders of Scheme I;
- the strength enhancement due to the addition of a second layer of fabric was more pronounced in the case of BFRP-confined cylinders. In particular, the strength gain due to the increase of the number of layers in BFRP-wrapped specimens of Scheme I was equal to 130%, while it was equal to 110% for specimens of Scheme II. The same increase evaluated for BFRCM-wrapped specimens was equal to 37% for Scheme I and 63% for Scheme II;
- confining cylinders through BFRP wraps was effective in terms of ultimate strain gains, with higher increments for cylinders involving three vertical joints (Scheme II). In particular, Scheme I cylinders showed an average ultimate strain increase of 30% and 81% for one and two-layer confined specimens respectively, compared to control samples. For cylinders from Scheme II, the average enhancement of ultimate strain was 93% and 146% for specimens confined by one and two layers respectively;
- in the case of BFRCM-wrapped cylinders, the average ultimate strain enhanced of 72% and 97 % for cylinders from Scheme I reinforced with

one and two layers respectively. Scheme II specimens showed average increments equal to 96% and 121% respectively for one and two-layer confined samples;

- the compressive stress-strain curves of BFRP and BFRCM-confined masonry cylinders were characterized by a softening descending branch, which was negligible for unconfined specimens. In the case of BFRP-wrapped cylinders, Scheme II specimens showed a more ductile behaviour, with a less steep softening branch than Scheme I specimens;
- comparing unconfined and BFRP-reinforced specimens for Scheme I and Scheme II respectively, the trend of the axial stress as a function of the hoop strain did not present slope variations in the ascending branch. Scheme I cylinders wrapped with two layers gave an average hoop strain increase of 67% compared to control specimens. One-layer reinforced cylinders showed an average strain increase next to zero.

It is evident that both BFRP and BFRCM jackets significantly increased the performance of reinforced cylinders, with considerable gains in term of strength and ultimate strain compared to unreinforced specimens. The above-mentioned results highlight that the use of BFRP and BFRCM wraps is an effective method for confining brick masonry columns.

Finally, the experimental results from compressive tests on BFRP and BFRCM-confined cylinders were compared with the theoretical predictions obtained by modifying some available formulations in order to better reproduce the behaviour of reinforced specimens. The comparison between theoretical predictions and experimental results pointed out a good correlation in terms of average compressive response, peak stress, corresponding strain and slope of ascending and softening branches, allowing some conclusions to be drawn on the predictive models:

- a modified version of the model provided in the CNR-DT 200/2013 Italian Guidelines allowed obtaining good strength predictions for both BFRP and BFRCM-wrapped masonry, with average differences lower than 3% with respect to experimental data;
- the proposed modified formulation of the model of Krevaikas and Triantafillou (2005) provided good predictions of the strain

corresponding to peak stress, with differences lower than 6% with respect to values obtained experimentally from both BFRP and BFRCM-wrapped specimens;

- the trend of the axial stress as a function of the axial strain could be predicted by adopting the analytical relationship provided by La Mendola and Papia (2002), which was able to plot the overall curve by means of a unique law.

6.2 Future works

- Further investigations are suggested to evaluate the effectiveness of basalt fibres in confining masonry columns in relation to parameters that were not taken into account in the framework of this thesis. The influence of the kind of masonry, the shape of the cross-section and the type of mortar used as matrix of the external strengthening system are parameters to investigate.
  Moreover, it is interesting to extend the experimental study here presented on BFRP/BFRCM-confined cylinders to the case of large-scale masonry columns, in order to understand the possible occurrence of scale effects.
- The definition of a unified analytical model aimed at evaluating the strength increase due to confinement of masonry by FRCM is of central importance, as well as the evaluation of a model able to predict the constitutive law in compression of masonry columns reinforced by FRCMs. Therefore, further studies on the analytical modelling of this strengthening system are suggested.
- One unsolved issue about the application of FRCMs for the confinement of masonry columns is the evaluation of the ultimate strain reached by the composite subjected to the lateral expansion of the compressed columns. Therefore, investigations are recommended aimed at defining this parameter. In order to reach this goal, the use of the DIC could be a useful tool. In particular, the 2D-DIC analyses developed in this research work could be extended to the case of 3D analyses, with the possibility to achieve better results in the study of the continuous strain field on the surface of the specimens.

REFERENCES

ACI 549.4R-13. (2013). "Guide to Design and Construction of Externally Bonded Fabric-Reinforced Cementitious Matrix (FRCM) Systems for Repair and Strengthening Concrete and Masonry Structures". Farmington Hills, MI, USA: American Concrete Institute.

Aiello, M. A., Micelli, F., Valente, L. (2007). Structural upgrading of masonry columns by using composite reinforcements. *Journal of Composites for Construction, 11(6)*, 650-658.

Aiello, M. A., Micelli, F., Valente, L. (2009). FRP confinement of square masonry columns. Journal of composites for construction, 13(2), 148-158.

Alecci, V., Bati, S. B., Ranocchiai, G. (2009). Study of brick masonry columns confined with CFRP composite. Journal of Composites for Construction, 13(3), 179-187.

Alecci, V., De Stefano, M., Luciano, R., Rovero, L., Stipo, G. (2015). Experimental investigation on bond behaviour of cement-matrix–based composites for strengthening of masonry structures. Journal of Composites for Construction, 20(1), 04015041.

Alotaibi, K. S. and Galal, K. (2017). Axial compressive behaviour of grouted concrete block masonry columns confined by CFRP jackets. Composites Part B: Engineering, 114, 467-479.

Arboleda, D. (2014). Fabric reinforced cementitious matrix (FRCM) composites for infrastructure strengthening and rehabilitation: Characterization methods.

Arboleda, D., Carozzi, F. G., Nanni, A., Poggi, C. (2015). Testing procedures for the uniaxial tensile characterization of fabric-reinforced cementitious matrix composites. Journal of Composites for Construction, 20(3), 04015063.

Ascione, L., de Felice, G., De Santis, S. (2015). A qualification method for externally bonded Fibre Reinforced Cementitious Matrix (FRCM) strengthening systems. Composites Part B: Engineering, 78, 497-506.

Atkinson, R. H., Noland, J. L., Abrams, D. P., McNary, S. (1985, February). A deformation failure theory for stack-bond brick masonry prisms in compression. In Proceedings 7th International Brick Masonry Conference (pp. 577-592).

Balsamo, A., Cascardi, A., Di Ludovico, M., Aiello, M. A., Morandini, G. (2018). Analytical study on the effectiveness of the FRCM-confinement of masonry columns. Construction Pathology, Rehabilitation Technology and Heritage Management, Cáceres, Spain

Banholzer, B., Brockmann, T., Brameshuber, W. (2006). Material and bonding characteristics for dimensioning and modelling of textile reinforced concrete (TRC) elements. Materials and structures, 39(8), 749.

Bellini, A., Bovo, M., Mazzotti, C. (2019). Experimental and numerical evaluation of fibre-matrix interface behaviour of different FRCM systems. Composites Part B: Engineering, 161, 411-426.

Bilotta, A., Ceroni, F., Nigro, E., Pecce, M. (2017a). Experimental tests on FRCM strengthening systems for tuff masonry elements. Construction and Building Materials, 138, 114-133.

Bilotta, A., Ceroni, F., Lignola, G. P., Prota, A. (2017b). Use of DIC technique for investigating the behaviour of FRCM materials for strengthening masonry elements. Composites Part B: Engineering, 129, 251-270.

Bisby, L. A. and Stratford, T. J. (2011). The ultimate condition of FRP confined concrete columns: New experimental observations and insights. In Advances in FRP composites in civil engineering (pp. 599-602). Springer, Berlin, Heidelberg.

Bisby, L. A. and Take, W. A. (2009). Strain localisations in FRP-confined concrete: new insights. Proceedings of the Institution of Civil Engineers-Structures and Buildings, 162(5), 301-309.

Bisby, L. A., Chen, J. F., Li, S. Q., Stratford, T. J., Cueva, N., Crossling, K. (2011). Strengthening fire-damaged concrete by confinement with fibre-reinforced polymer wraps. Engineering Structures, 33(12), 3381-3391.

Borri, A., Castori, G., Corradi, M. (2011). Masonry columns confined by steel fibre composite wraps. Materials, 4(1), 311-326.

Bournas, D. A., Lontou, P. V., Papanicolaou, C. G., Triantafillou, T. C. (2007). Textile-reinforced mortar (TRM) versus FRP confinement in reinforced concrete columns. ACI Structural Journal, 104(6), 740-748.

Branston, J. S. (2015). Properties and applications of basalt fibre reinforced concrete. Electronic Theses and Dissertations, University of Windsor.

Caggegi, C., Lanoye, E., Djama, K., Bassil, A., & Gabor, A. (2017a). Tensile behaviour of a basalt TRM strengthening system: influence of mortar and reinforcing textile ratios. Composites Part B: Engineering, 130, 90-102.

Caggegi, C., Carozzi, F. G., De Santis, S., Fabbrocino, F., Focacci, F., Hojdys, Ł., ... & Zuccarino, L. (2017b). Experimental analysis on tensile and bond properties of PBO and aramid fabric reinforced cementitious matrix for strengthening masonry structures. Composites Part B: Engineering, 127, 175-195.

Callister Jr, W. D., & Rethwisch, D. G. (2012). Fundamentals of materials science and engineering: an integrated approach. John Wiley & Sons.

Campione, G. and Miraglia, N. (2003). Strength and strain capacities of concrete compression members reinforced with FRP. Cement and Concrete Composites, 25(1), 31-41.

Campione, G., La Mendola, L., Monaco, A., Valenza, A., Fiore, V. (2015). Behaviour in compression of concrete cylinders externally wrapped with basalt fibres. Composites Part B: Engineering, 69, 576-586.

Caporossi, P., Mazzanti, P., Bozzano, F. (2018). Digital Image Correlation (DIC) Analysis of the 3 December 2013 Montescaglioso Landslide (Basilicata, Southern Italy): Results from a Multi-Dataset Investigation. ISPRS International Journal of Geo-Information, 7(9), 372.

Carloni, C., Mazzotti, C., Savoia, M., Subramaniam, K. V. (2014). Confinement of Masonry Columns with PBO FRCM Composites. Key Engineering Materials, 624.

Carozzi, F. G. and Poggi, C. (2015). Mechanical properties and debonding strength of Fabric Reinforced Cementitious Matrix (FRCM) systems for masonry strengthening. Composites Part B: Engineering, 70, 215-230.

Carozzi, F. G., Bellini, A., D'Antino, T., de Felice, G., Focacci, F., Hojdys, Ł., ... & Poggi, C. (2017). Experimental investigation of tensile and bond properties of Carbon-FRCM composites for strengthening masonry elements. Composites Part B: Engineering, 128, 100-119.

Cascardi, A., Aiello, M. A., Triantafillou, T. (2017b). Analysis-oriented model for concrete and masonry confined with fibre reinforced mortar. Materials and Structures, 50(4), 202.

Cascardi, A., Longo, F., Micelli, F., Aiello, M. A. (2017a). Compressive strength of confined column with Fibre Reinforced Mortar (FRM): New design-oriented-models. Construction and Building Materials, 156, 387-401.

Cascardi, A., Micelli, F., Aiello, M. A. (2018). FRCM-confined masonry columns: experimental investigation on the effect of the inorganic matrix properties. Construction and Building Materials, 186, 811-825.

Ceroni, F. and Salzano, P. (2018). Design provisions for FRCM systems bonded to concrete and masonry elements. Composites Part B: Engineering, 143, 230-242.

Cevallos, O. A. and Olivito, R. S. (2015). Effects of fabric parameters on the tensile behaviour of sustainable cementitious composites. Composites Part B: Engineering, 69, 256-266.

Chakinala, S. (2013). A Study of Algorithms Based on Digital Image Correlation for Embedding in a Full-Fiield Displacement Sensor with Subpixel Resolution(Doctoral dissertation, University of Akron).

Chu, T. C., Ranson, W. F., Sutton, M. A. (1985). Applications of digital-image-correlation techniques to experimental mechanics. Experimental mechanics, 25(3), 232-244.

CNR-DT 200 R1 (2013). Guide for the Design and Construction of externally bonded FRP Systems for Strengthening Existing Structures. Italian Council of Research (CNR), Roma, Italy.

Codispoti, R., Oliveira, D. V., Olivito, R. S., Lourenço, P. B., Fangueiro, R. (2015). Mechanical performance of natural fibre-reinforced composites for the strengthening of masonry. Composites Part B: Engineering, 77, 74-83.

Corradi, M., Grazini, A., Borri, A. (2007). Confinement of brick masonry columns with CFRP materials. Composites Science and Technology, 67(9), 1772-1783.

Dalalbashi, A., Ghiassi, B., Oliveira, D. V., Freitas, A. (2018a). Fibre-to-mortar bond behaviour in TRM composites: effect of embedded length and fibre configuration. Composites Part B: Engineering.

Dalalbashi, A., Ghiassi, B., Oliveira, D. V., Freitas, A. (2018b). Effect of test setup on the fibre-to-mortar pull-out response in TRM composites: Experimental and analytical modeling. Composites Part B: Engineering, 143, 250-268.

D'Antino, T. and Papanicolaou, C. (2017). Mechanical characterization of textile reinforced inorganic-matrix composites. Composites Part B: Engineering, 127, 78-91.

D'Antino, T. and Papanicolaou, C. C. (2018). Comparison between different tensile test set-ups for the mechanical characterization of inorganic-matrix composites. Construction and Building Materials, 171, 140-151.

De Felice, G., De Santis, S., Garmendia, L., Ghiassi, B., Larrinaga, P., Lourenço, P. B., ... & Papanicolaou, C. G. (2014). Mortar-based systems for externally bonded strengthening of masonry. Materials and structures, 47(12), 2021-2037.

De Felice, G., Aiello, M. A., Caggegi, C., Ceroni, F., De Santis, S., Garbin, E., ... & Leone, M. (2018). Recommendation of RILEM Technical Committee 250-CSM: Test method for Textile Reinforced Mortar to substrate bond characterization. Materials and Structures, 51(4), 95.

De Santis, S. and de Felice, G. (2015a). Tensile behaviour of mortar-based composites for externally bonded reinforcement systems. Composites Part B: Engineering, 68, 401-413.

De Santis, S. and de Felice, G. (2015b). Tensile Behaviour and Durability of Mortar-Based Strengthening Systems with Glass-Aramid Textiles. Key Engineering Materials, 624, 346-353.

De Santis, S., Carozzi, F. G., de Felice, G., Poggi, C. (2017a). Test methods for textile reinforced mortar systems. Composites Part B: Engineering, 127, 121-132.

De Santis, S., Ceroni, F., de Felice, G., Fagone, M., Ghiassi, B., Kwiecień, A., ... & Viskovic, A. (2017b). Round Robin Test on tensile and bond behaviour of Steel Reinforced Grout systems. Composites Part B: Engineering, 127, 100-120.

De Santis, S., Hadad, H. A., De Caso y Basalo, F., De Felice, G., Nanni, A. (2018). Acceptance Criteria for Tensile Characterization of Fabric-Reinforced Cementitious Matrix Systems for Concrete and Masonry Repair. Journal of Composites for Construction, 22(6), 04018048.

Deák, T. and Czigány, T. (2009). Chemical composition and mechanical properties of basalt and glass fibres: A comparison. Textile Research Journal, 79(7), 645-651.

Di Ludovico, M., D'Ambra, C., Prota, A., Manfredi, G. (2010). FRP confinement of tuff and clay brick columns: Experimental study and assessment of analytical models. Journal of Composites for Construction, 14(5), 583-596.

Di Ludovico, M., Fusco, E., Prota, A., Manfredi, G. (2008, October). Experimental behaviour of masonry columns confined using advanced materials. In The 14th world conference on earthquake engineering.

Donnini, J. and Corinaldesi, V. (2017). Mechanical characterization of different FRCM systems for structural reinforcement. Construction and Building Materials, 145, 565-575.

Donnini, J., Lancioni, G., Corinaldesi, V. (2018). Failure modes in FRCM systems with dry and pre-impregnated carbon yarns: Experiments and modeling. Composites Part B: Engineering, 140, 57-67.

Donnini, J., Chiappini, G., Lancioni, G., Corinaldesi, V. (2019). Tensile behaviour of glass FRCM systems with fabrics' overlap: experimental results and numerical modeling. Composite Structures, 212, 398-411.

EN 1015-11, (1999). "Methods of test for mortar for masonry – Part 11: Determination of flexural and compressive strength of hardened mortar".

EN 772-1, (2011). "Method of test for masonry units – Part 1: Determination of compressive strength".

Faella, C., Martinelli, E., Camorani, G., Aiello, M. A., Micelli, F., Nigro, E. (2011b). Masonry columns confined by composite materials: Design formulae. Composites Part B: Engineering, 42(4), 705-716.

Faella, C., Martinelli, E., Paciello, S., Camorani, G., Aiello, M. A., Micelli, F., Nigro, E. (2011a). Masonry columns confined by composite materials: Experimental investigation. Composites Part B: Engineering, 42(4), 692-704.

Fiore, V., Scalici, T., Di Bella, G., Valenza, A. (2015). A review on basalt fibre and its composites. Composite Parte B: Engineering, 74, 74-94.

Fossetti, M. and Minafò, G. (2017). Comparative experimental analysis on the compressive behaviour of masonry columns strengthened by FRP, BFRCM or steel wires. Composites Part B: Engineering, 112, 112-124.

Fossetti, M., Minafò, G., Giacchino, C. (2016). Experimental investigation on the compressive behaviour of clay brick masonry columns confined by BFRP or steel wires. Applied Mechanics & Materials, 847.

Francis, A. J., Horman, C. B., Jerrems, L. E. (1971, April). The effect of joint thickness and other factors on the compressive strength of brickwork. In Proceedings of 2nd international brick masonry conference, stoke-on-trent (pp. 31-37).

Galal, K., Farnia, N., Pekau, O. A. (2012). Upgrading the seismic performance of reinforced masonry columns using CFRP wraps. Journal of Composites for Construction, 16(2), 196-206.

Garbin, E., Panizza, M., Valluzzi, M. R. (2018). Experimental Characterization of Glass and Carbon FRCMs for Masonry Retrofitting. Special Publication, 324, 3-1.

Ghiassi, B., Razavizadeh, A., Oliveira, D. V., Marques, V., Lourenço, P. B. (2016a). Tensile and Bond Characterization of Natural Fibres Embedded in Inorganic Matrices. In Natural Fibres: Advances in Science and Technology Towards Industrial Applications (pp. 305-314). Springer, Dordrecht.

Ghiassi, B., Oliveira, D. V., Marques, V., Soares, E., Maljaee, H. (2016b). Multi-level characterization of steel reinforced mortars for strengthening of masonry structures. Materials & Design, 110, 903-913.

GOM GmbH. GOM Testing—Technical Documentation as of V8 SR1, Digital Image Correlation and Strain Computation Basics; GOM mbH: Braunschweig, Germany, 2016.

Grédiac, M. and Hild, F. (Eds.). (2012). Full-field measurements and identification in solid mechanics. John Wiley & Sons.

Hendry, A. W. (1998). Structural masonry. Macmillan International Higher Education.

Hilsdorf, H. K. (1969). Investigation into the failure mechanism of brick masonry loaded in axial compression. Designing engineering and constructing with masonry products (pp. 34-41).

ICC. AC434. (2013). "Proposed Acceptance Criteria for Masonry and Concrete Strengthening Using Fibre-reinforced Cementitious Matrix (FRCM) Composite Systems". Whittier, CA: ICC-Evaluation Service.

Incerti, A., Vasiliu, A., Ferracuti, B., Mazzotti, C. (2015). Uni-Axial compressive tests on masonry columns confined by FRP and FRCM. In Proceedings of the 12th international symposium on fibre reinforced polymers for reinforced concrete structures and the 5th Asia-Pacific conference on fibre reinforced polymers in structures, joint conference, Nanjing (pp. 14-16).

Iorfida, A., Verre, S., Candamano, S., Ombres, L. (2017). Tensile and Direct Shear Responses of Basalt-Fibre Reinforced Mortar Based Materials. In International Conference on Strain-Hardening Cement-Based Composites (pp. 544-552). Springer, Dordrecht.

ISO 13934-1, (April 2013). "Textiles – Tensile properties of fabrics – Part 1: Determination of maximum force and elongation at maximum force using the strip method". CEN – European Committee for Standardization.

Khoo, C. L. (1972). Failure criterion for brickwork in axial compression. In: Proc 3rd Int brick and block masonry Conf, Essen, Germany (pp. 139–45).

Koutsomitopoulou, A. F. (2013). Manufacturing and Experimental Investigation of Green Composites Materials (Doctoral dissertation, Ph. D. thesis, University of Patras).

Krevaikas, T. D. (2015). Textile reinforced mortar system as a means for confinement of masonry structures. In Proc. In: the 12th International Symposium on Fibre Reinforced Polymers for Reinforced Concrete Structures (FRPRCS-12) & the 5th Asia-Pacific Conference on Fibre Reinforced Polymers in Structures (APFIS-2015) Joint Conference (Vol. 14, p. 16).

Krevaikas, T. D. and Triantafillou, T. C. (2005). Masonry confinement with fibre-reinforced polymers. Journal of Composites for Construction, 9(2), 128-135.

La Mendola, L. and Papia, M. (2002). General stress-strain model for concrete or masonry response under uniaxial cyclic compression. Structural Engineering and Mechanics, 14(4), 435-454.

Larrinaga, P., Chastre, C., Biscaia, H. C., San-José, J. T. (2014). Experimental and numerical modeling of basalt textile reinforced mortar behaviour under uniaxial tensile stress. Materials & Design, 55, 66-74.

Lava, P., Cooreman, S., Debruyne, D. (2010). Study of systematic errors in strain fields obtained via DIC using heterogeneous deformation generated by plastic FEA. Optics and Lasers in Engineering, 48(4), 457-468.

Leone, M., Aiello, M. A., Balsamo, A., Carozzi, F. G., Ceroni, F., Corradi, M., ... Mazzotti, C. (2017a). Glass fabric reinforced cementitious matrix: Tensile properties and bond performance on masonry substrate. Composites Part B: Engineering, 127, 196-214.

Leone, M., Rizzo, V., Micelli, F., Aiello, M. A. (2017b). Experimental Analysis on Bond Behaviour of GFRCM Applied on Clay Brick Masonry. In Key Engineering Materials (Vol. 747, pp. 542-549). Trans Tech Publications.

Lignola, G. P., Angiuli, R., Prota, A., Aiello, M. A. (2014). FRP confinement of masonry: analytical modeling. Materials and structures, 47(12), 2101-2115.

Lignola, G. P., Caggegi, C., Ceroni, F., De Santis, S., Krajewski, P., Lourenço, P. B., ... & Zuccarino, L. (2017). Performance assessment of basalt FRCM for retrofit applications on masonry. Composites Part B: Engineering, 128, 1-18.

Lu, H. and Cary, P. D. (2000). Deformation measurements by digital image correlation: implementation of a second-order displacement gradient. Experimental mechanics, 40(4), 393-400.

Maddaloni, G., Cascardi, A., Balsamo, A., Di Ludovico, M., Micelli, F., Aiello, M. A., Prota, A. (2017). Confinement of full-scale masonry columns with FRCM systems. In Key Engineering Materials(Vol. 747, pp. 374-381). Trans Tech Publications.

McCormick, N. and Lord, J. (2010). Digital Image Correlation. Materialstoday, 13(12), 52-54.

Mercedes, L., Gil, L., Bernat-Maso, E. (2018). Mechanical performance of vegetal fabric reinforced cementitious matrix (FRCM) composites. Construction and Building Materials, 175, 161-173.

Mezrea, P. E., Yilmaz, I. A., Ispir, M., Binbir, E., Bal, I. E., Ilki, A. (2016). External jacketing of unreinforced historical masonry piers with open-grid basalt-reinforced mortar. Journal of Composites for Construction, 21(3), 04016110.

Micelli, F., Angiuli, R., Corvaglia, P., Aiello, M. A. (2014b). Passive and SMA-activated confinement of circular masonry columns with basalt and glass fibres composites. Composites Part B: Engineering, 67, 348-362.

Micelli, F., De Lorenzis, L., La Tegola, A. (2004). FRP-confined masonry columns under axial loads: analytical model and experimental results. Masonry International Journal, Ed., British Masonry Society, 17(3), 95-108.

Micelli, F., Di Ludovico, M., Balsamo, A., Manfredi, G. (2014a). Mechanical behaviour of FRP-confined masonry by testing of full-scale columns. Materials and structures, 47(12), 2081-2100.

Minafò, G. and La Mendola, L. (2018). Experimental investigation on the effect of mortar grade on the compressive behaviour of FRCM confined masonry columns. Composites Part B: Engineering, 146, 1-12.

Montesi, M. (2015). Investigation of interlaminar shear behaviour of fabric reinforced cementitious matrix (FRCM) composite systems.

Murgo, F. S. and Mazzotti, C. (2019). Masonry columns strengthened with FRCM system: Numerical and experimental evaluation. Construction and Building Materials, 202, 208-222.

Nanni, A. (2012). A new tool for concrete and masonry repair. Concrete international, 34(4).

Olivito, R. S., Codispoti, R., Cevallos, O. A. (2016). Bond behaviour of Flax-FRCM and PBO-FRCM composites applied on clay bricks: experimental and theoretical study. Composite Structures, 146, 221-231.

Ombres, L. (2015). Confinement effectiveness in eccentrically loaded masonry columns strengthened by fibre reinforced cementitious matrix (FRCM)

jackets. In Key Engineering Materials (Vol. 624, pp. 551-558). Trans Tech Publications.

Ombres, L. and Verre, S. (2018a). Masonry columns strengthened with Steel Fabric Reinforced Cementitious Matrix (S-FRCM) jackets: experimental and numerical analysis. Measurement, 127, 238-245.

Ombres, L., Mancuso, N., Mazzuca, S., Verre, S. (2018b). Bond between Carbon Fabric-Reinforced Cementitious Matrix and Masonry Substrate. Journal of Materials in Civil Engineering, 31(1), 04018356.

Ouyang, L. J., Gao, W. Y., Zhen, B., Lu, Z. D. (2017). Seismic retrofit of square reinforced concrete columns using basalt and carbon fibre-reinforced polymer sheets: A comparative study. Composite Structures, 162, 294-307.

Pan, B., Qian, K., Xie, H., Asundi, A. (2009). Two-dimensional digital image correlation for in-plane displacement and strain measurement: a review. Measurement science and technology, 20(6), 062001.

Pino, V. and Nanni, A. (2015). FRCM and FRP composites for the repair of damaged PC girders(No. 00042134-04).

Rao, K. N. and Pavan, G. S. (2014). FRP-confined clay brick masonry assemblages under axial compression: Experimental and analytical investigations. Journal of Composites for Construction, 19(4), 04014068.

RILEM Technical Committee 232-TDT (Wolfgang Brameshuber) Mater Struct (2016) 49: 4923. doi:10. 1617/s115270160839z.

Roscini, F., De Santis, S., de Felice, G. (2016), Structural Analysis of Historical Constructions - Anamnesis, diagnosis, therapy, controls. Proceedings of the 10th International Conference on SACH, Leuven, Belgium, 384–390.

Sadeghian, P. and Fillmore, B. (2018). Strain distribution of basalt FRP-wrapped concrete cylinders. Case Studies in Construction Materials, 9.

Sandoli, A., Ferracuti, B., Calderoni, B. (2019). FRP-CONFINED tuff masonry columns: Regular and irregural stone arrangement. Composites Part B: Engineering, 162, 621-630.

Santandrea, M., Quartarone, G., Carloni, C., Gu, X. L. (2017). Confinement of masonry columns with steel and basalt FRCM composites. In Key Engineering Materials (Vol. 747, pp. 342-349). Trans Tech Publications.

Santandrea, M., Baietti, G., Shahreza, S. K., Carloni, C. (2019). A Comparison Between the Bond Behaviour of SRP and SRG Strengthening Systems Applied to a Masonry Substrate. In Structural Analysis of Historical Constructions (pp. 1743-1750). Springer, Cham.

Shrive, N. G. and Jessop, E. L. (1982). An examination of the failure mechanism of masonry piers, prisms and walls subjected to compression. In Proc. Br. Ceram. Soc. (No. 30, p. 110).

Sim, J. and Park, C. (2005). Characteristics of basalt fibre as a strengthening material for concrete structures. Composites Part B: Engineering, 36(6-7), 504-512.

Sneed, L. H., Carloni, C., Baietti, G., Fraioli, G. (2017). Confinement of clay masonry columns with SRG. In Key Engineering Materials (Vol. 747, pp. 350-357). Trans Tech Publications.

Take, W. A. and Kemp, J. (2006). Application of digital image-based deformation measurements to geotechnical testing. In 59th Canadian Geotechnical Conference, Vancouver (pp. 313-318).

Tekieli, M., De Santis, S., de Felice, G., Kwiecień, A., Roscini, F. (2017). Application of Digital Image Correlation to composite reinforcements testing. Composite Structures, 160, 670-688.

Talreja, R. (2005). Composites: Polymer–Polymer. In Encyclopedia of Condensed Matter Physics, Editors-in-Chief: Franco, B.; Gerald, L. L.; Peter, W., Eds. Elsevier: Oxford, 2005; pp 208-211

Valdés, M., Concu, G., De Nicolo, B. (2014). FRP Strengthening of Masonry Columns: Experimental Tests and Theoretical Analysis. Key Engineering Materials, 624.

Witzany, J. and Zigler, R. (2016). Stress state analysis and failure mechanisms of masonry columns reinforced with FRP under concentric compressive load. Polymers, 8(5), 176.

Witzany, J., Čejka, T., Zigler, R. (2014). Failure mechanism of compressed short brick masonry columns confined with FRP strips. Construction and Building materials, 63, 180-188.

Xavier, J., Sousa, A. M., Morais, J. J., Filipe, V. M., Vaz, M. A. (2012). Measuring displacement fields by cross-correlation and a differential technique: experimental validation. Optical Engineering, 51(4), 043602.

Yilmaz, I., Mezrea, P., Ispir, M., Binbir, E., Bal, I., Ilki, A. (2013, December). External confinement of brick masonry columns with open-grid basalt reinforced mortar. In Proceedings of the Fourth Asia-Pacific Conference on FRP in Structures (APFIS 2013), Melbourne, Australia (pp. 11-13).

Yoneyama, S. and Murasawa, G. (2009). Digital image correlation. Experimental mechanics.

Zucchini, L. (2010). Experimental analysis of Fibre Reinforced Cementitious Matrix (FRCM) confined masonry columns. Master Thesis, City University of New York.

Zwick/Roell Group, Germany - Austria. (2015). Zwick/Roell VideoXtens, Manual No. 255.